

TECHNISCHE UNIVERSITÄT MÜNCHEN

Lehrstuhl für Technische Chemie II

**Elucidation of reaction pathways of the
photoreforming and overall water splitting reaction
over precious metal decorated semiconductors**

Tobias Friedrich Berto

Vollständiger Abdruck der von der Fakultät für Chemie der
Technischen Universität München zur Erlangung des akademischen Grades eines

Doktors der Naturwissenschaften (Dr. rer. nat.)

genehmigten Dissertation.

Vorsitzender: Prof. Dr. Thomas Brück

Prüfer der Dissertation:

1. Prof. Dr. Johannes A. Lercher
2. Prof. Dr. Tom Nilges

Die Dissertation wurde am 24.08.2016 bei der Technischen Universität München eingereicht und durch die Fakultät für Chemie am 10.10.2016 angenommen.

Dedicated to my parents

*“Doch Forschung strebt und ringt, ermüdend nie,
Nach dem Gesetz, dem Grund, Warum und Wie.”*

Johann Wolfgang von Goethe (1749-1832)

Statutory Declaration

I declare that I have authored this thesis independently and that I have solely used the declared (re)sources and that I have marked all material, which has been quoted either literally or by content from the used sources. At the end of each chapter all collaborators are named and their specific contribution is addressed. Published content of this thesis is clearly marked.

_____ , _____

Acknowledgements

First of all I wish to express my full gratitude to Professor Johannes A. Lercher. In 2011 he decided to start with photocatalysis research and placed his trust in me to build up the required equipment and to establish appropriate experimental methods. Thank you very much for this great opportunity. Guided by your trust, patience, visions and enthusiasm I could learn a lot about building setups of any kind, heterogeneous (photo)catalysis and science itself. I deeply appreciate these possibilities of self-fulfillment. I am thankful that you enabled me to visit research groups in the USA and Saudi Arabia. I am going to miss your intellectuality and perception, which raised the quality of my research.

Dr. Oliver Gutierrez was the most mindful co-advisor I could imagine. Besides being an academic teacher you tenderly improved my social and methodological competences. Today, I enjoy the fruits of your labor. Your non-subject-specific input helped me to find a position in industry! Moreover, thanks for improving the design and the comprehensibility of manuscripts and presentations.

My special thanks go to my hard working labmate Kai Sanwald. I deeply enjoyed doing and discussing research with you. I am very happy that I could experience your intellectual capacity and grasp and that you accepted my decisions and ideas, once you joined, even the situation was extremely tough and desperate. I am going to miss you - a reliable, ambitious and gentle partner.

Every day, while doing my experiments, I kept Professor Kazuhiro Takanabe and Dr. Ela Nurlaela from the King Abdullah University of Science and Technology in mind. Thank you so much for everything you taught me! Ela kindly introduced me to experimental photocatalysis and I deeply appreciate the lasting friendship!

I also want to express my gratitude to Professor Wolfgang Eisenreich and his technician Christine Schwarz. We would have had no chance to perform our photoreforming studies without you! I appreciate your efforts to improve the water suppression pulse sequence and solving conflicts caused by expanded measurement times.

I am also very grateful to Dr. Maricruz Sanchez-Sanchez for a short but very fruitful collaboration.

Dedication, knowledge and experience of Xaver Hecht are indispensable for TC2. Therefore, special thanks go particularly to Xaver Hecht but also to Martin Neukamm, Andreas Marx and to the members of the mechanical, glass and electronic work shop. You all helped me to apply my knowledge gained during my chemistry studies.

I want to thank the administrative staff, Steffi Seibold, Bettina Federmann and Uli Sanwald, for their support.

I am grateful to the Federal Ministry of Education and Research and the Clariant AG for the financial support and to Professor Richard Fischer and Dr. Andreas Geisbauer for fruitful discussions and their continual interest in my research.

I am proud of my students, who achieved great results. I am thankful to Pablo Rodriguez, Sebastian Helmbrecht, Patrick Bretzler, Elisabeth Bauer, Bezaleel Yahya, Theresa Zach, Benjamin Strehle, Sarah Bohrmann, José Moya Cancino, Martina Aigner, Thomas Obereisenbuchner, Berin Kaçkar and Miriam Wehrle. I especially thank José, Sarah and Miriam for their excellent input.

I want to thank my colleagues for their help, discussions, encouragements and all the joyful moments, when we were hanging out or hiking in the mountains.

I want to thank my friends, who share my life with me, for cheerful hours and their support. Thanks for keeping me in mind, when I “appeared to be dead” for weeks because I struggled in the lab. Special thanks go to Basti, Tobi, Simon, Klaus, Michael, Lei and Lisl. I am happy to be your friend ☺.

Last but not least I want to mention my family, especially my parents, my sisters and my grandfather. I would like to thank them for all their love and indispensable support they gave me so far every day of my life.

Thanks a lot. Tobi

Abbreviations

Unit prefixes

Y	Yotta (10^{24})
T	Tera (10^{12})
G	Giga (10^9)
M	Mega (10^6)
k	Kilo (10^3)
m	Milli (10^{-3})
μ	Micro (10^{-6})
n	Nano (10^{-9})

Units

m	Meter
m ²	Square meter
Å	Ångström, 0.1 nm
L	Liter
Nm ³	Normal cubic meter
M	Molar (mol per liter)
t	Ton
g	Gram
d	Day
h	Hour
min	Minute
eV	Electron volt
J	Joule
W	Watt
Pa	Pascal
K	Kelvin
V	Volt
A	Ampere
Hz	Hertz
Ω	Ohm

Other abbreviations

%	Percentage
(HR)SEM	(High resolution) scanning electron microscopy
(HR)TEM	(High resolution) transmission electron microscopy
ΔG	Change of Gibbs free energy
AAS	Atomic absorption spectroscopy
ATR	Attenuated total reflection
BET	Brunauer Emmett Teller

CM	Cold mirror
DR	Diffuse reflectance
e^-	Electron
e.g.,	<i>Exempli gratia</i> , 'for example'
E^0	Standard electrode potential
E_{BG}	Band gap energy
e_{cb}^-	Conduction band electron
E_{CB}	Energy of the conduction band edge
E_{VB}	Energy of the valence band edge
EG	Ethylene glycol
E_{Ox}	Oxidation potential
E_{Red}	Reduction potential
E_{VB}	Energy of the valence band edge
FID	Flame ionization detector
FTIR	Fourier transform infrared spectroscopy
GC	Gas chromatography
h_{vb}^+	Valence band hole
HER	Hydrogen evolution reaction
i.e.,	<i>Id est</i> , 'in other words'
I_0	Intensity of incident light
ICP	Inductively coupled plasma
LC ₅₀	Lethal concentration, 50%
MS-5Å	Molecular sieve 5Å
NHE	Normal hydrogen electrode
NMR	Nuclear magnetic resonance
ppm	parts per million
STH	Solar to hydrogen
TCD	Thermal conductivity detector
UV	Ultraviolet
Vis	Visible
Wt.%	Weight percentage
XANES	X-ray absorption near edge structure
XRD	X-Ray diffraction
Q.E.	Quantum efficiency
OER	Oxygen evolution reaction
L42	Long pass filter with an absorption edge at 420 nm
Φ	Work function
λ	Wavelength
γ	Photon

Abstract

H₂ was produced *via* photocatalysis in aqueous phase using two approaches: Photoreforming and overall water splitting on semiconductors decorated with Rh. Oxidation of ethylene glycol in photoreforming *via* direct or indirect hole transfer depends on the surface properties and band gap of the semiconductors. In overall water splitting, the performance of the photocatalyst is greatly enhanced by blocking the sites catalyzing the reverse reaction with a controlled CO-coverage on the Rh co-catalyst.

Kurzzusammenfassung

H₂ wurde photokatalytisch in wässriger Phase in zwei Verfahren dargestellt: Photoreformierung und Wasserspaltung über Rh dekorierten Halbleitern. In der Photoreformierung ist die Oxidation von Ethylenglykol über direkten oder indirekten Lochtransfer von Oberflächeneigenschaften und Bandlücke der Halbleiter abhängig. In der Wasserspaltung wird die Aktivität des Photokatalysators bedeutend erhöht, indem die katalytischen Zentren der Rückreaktion mittels kontrollierter CO-Bedeckung des Rh Co-Katalysators blockiert werden.

Table of Contents

Acknowledgements	i
Abbreviations.....	iii
Abstract	v
Table of Contents.....	vi
1. Introduction	1
1.1. Principle of Heterogeneous Photocatalysis.....	1
1.2. Hydrogen – Importance and Synthesis	2
1.3. Comparison of Overall Water Splitting and Photoreforming	5
1.4. Description of Used Semiconductors	9
1.4.1. UV-Light Absorbing SrTiO ₃ and Aeroxide [®] TiO ₂ P 25	9
1.4.2. UV-Vis-Light Absorbing GaN:ZnO.....	10
1.5. Polyol Photoreforming	11
1.5.1. Definition and Kinetics.....	11
1.5.2. State of C1-/C2-Oxygenates in Aqueous Phase	16
1.5.3. Mode of Adsorption of Aqueous C1-/C2-Oxygenates on TiO ₂	18
1.5.4. Reaction Network and Mechanism.....	24
1.6. HER Co-Catalysts for the Overall Water Splitting Reaction.....	32
1.6.1. Physicochemical Requirements	32
1.6.2. First HER Co-Catalysts for Overall Water Splitting.....	34
1.6.3. WC – HER Electrocatalyst as Co-Catalyst for Water Splitting	34
1.6.4. Core–Shell-Type Co-catalysts.....	35
1.6.5. Core–Shell-Type Photocatalyst	36
1.7. Scope of the Thesis	39
1.8. References	41
1.9. Supporting Information.....	48
2. Photocatalytic Ethylene Glycol Reforming over Rh/TiO ₂ and Rh/GaN:ZnO	51
2.1. Abstract	51
2.2. Introduction.....	52

2.3. Experimental Section	54
2.3.1. Materials.....	54
2.3.2. Catalyst Preparation.....	54
2.3.3. Photocatalytic Test.....	55
2.3.4. Catalyst Characterization	58
2.3.5. Light Intensity Measurements.....	59
2.4. Results and Discussion.....	60
2.4.1. Synthesis Procedure and Physicochemical Properties.....	60
2.4.2. Reaction Network of EG Photoreforming on 1 wt.% Rh/TiO ₂	62
2.4.3. Determination of Adsorption Constants by Kinetic Modeling	72
2.4.4. On the Elementary Steps of the Reaction Network	77
2.4.5. Origin of CO Formation	81
2.4.6. EG Photoreforming on 1 wt.% Rh/GaN:ZnO	82
2.4.7. Challenges for a Clean EG Photoreforming Process.....	86
2.5. Conclusions.....	88
2.6. Acknowledgements	90
2.7. References	91
2.8. Supporting Information.....	94
3. Overall Water Splitting over Photocatalysts with CO-Covered Nobel Metals: an Alternative to Core-Shell Approaches	105
3.1. Introduction.....	106
3.2. Experimental Section	108
3.2.1. Materials.....	108
3.2.2. Synthesis of the Photocatalysts.....	108
3.2.3. Photocatalytic Tests	109
3.2.4. Catalyst Characterization	110
3.2.5. Light Intensity Measurements.....	112
3.3. Results and Discussion.....	113
3.3.1. Photocatalyst Synthesis and Characterization.....	113
3.3.2. Influence of CO on Water Splitting over Rh/GaN:ZnO.....	115
3.3.3. Comparison of Rh@Cr ₂ O ₃ and Rh-CO Co-Catalysts	117
3.3.4. Influence of CO Partial Pressure on Overall Water Splitting Rate ...	118
3.3.5. Deduction of CO-Coverage	119

3.3.6. Elucidation of Reaction Mechanism.....	122
3.3.7. Water Splitting over Various Co-Catalysts.....	127
3.4. Conclusions.....	129
3.5. Acknowledgements.....	130
3.6. References.....	131
3.7. Supporting Information.....	133
4. Summary and Conclusions.....	143
5. Zusammenfassung.....	146
6. Appendix.....	151
Curriculum Vitae.....	161
List of Publications.....	162

CHAPTER 1

*Yes, my friends, I believe that water will one day be employed as fuel, that hydrogen and oxygen which constitute it, used singly or together, will furnish an inexhaustible source of heat and light, of an intensity of which coal is not capable...
Water will be the coal of the future."*

Jules Verne, *The Mysterious Island* (1874)

1. Introduction

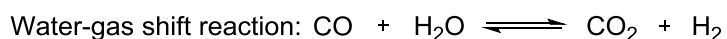
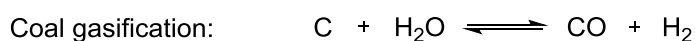
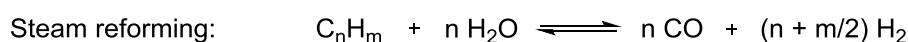
1.1. Principle of Heterogeneous Photocatalysis

Heterogeneous photocatalysis is a pathway to use charge carriers (electrons and holes), generated through photons absorbed by a photoabsorber, for driving electrochemical reactions, which are exergonic or endergonic.¹ Potential photoabsorbers can be organic or inorganic semiconductors.²⁻⁴ If the energy of a photon is equal or larger than the band gap of the photoabsorber, a valence band electron is excited to a vacant conduction band state, whereas a hole (h_{vb}^+) remains in the valence band.^{1,5} The energy level of the bottom of the conduction band and of the top of the valence band determines the electrochemical potential of a conduction band electron (e_{cb}^-) to drive a reduction reaction and of a hole (h_{vb}^+) to perform an oxidation reaction.^{1,5} In respect to thermodynamics, a surface adsorbate is reduced, if the corresponding standard electrode potential is more anodic than the bottom of the conduction band and is oxidized, if the corresponding standard electrode potential is more cathodic than the top of the valence band.¹ If both half reactions occur on one semiconductor surface, the heterogeneous photocatalyst can be described as a micro-electrochemical cell.^{6,7}

As in any electrochemical cell, chemical charge transfer has to be ensured. Accordingly, heterogeneous photocatalysis is preferably performed in aqueous systems.⁸ Protons serve here as a chemical charge transfer agent and as a reducible reactant to the energy carrier H_2 , if O_2 is absent.^{8,9}

1.2. Hydrogen – Importance and Synthesis

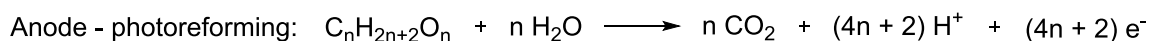
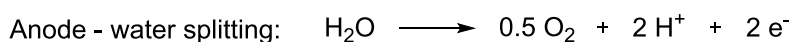
H₂ is an important reactant in the chemical and petroleum industry and is considered as an (intermediate) energy carrier having the potential to replace fossil fuels. Nowadays, the annual production capacity represents approximately 170 Mtons of oil equivalents, which is less than 2% of the global primary energy demand.¹⁰ These 700 GNm³ (~ 60 Mt) of H₂ are almost exclusively converted in (petro-)chemical processes (e.g., NH₃ and methanol production, refining), whereas 96% are produced from fossil fuels.¹¹ Water electrolysis accounts for the remaining 4%. Current fossil feedstocks are natural gas (48%), liquid hydrocarbons (30%) and coal (18%) and are converted preferable *via* steam reforming or coal gasification (Scheme 1-1). H₂ is mainly produced from CH₄ possessing the highest H₂ to carbon ratio (4:1) of all hydrocarbons. The production yield is increased by water-gas shift reaction after adding steam to the generated synthesis gas (Scheme 1-1). These pathways demand harsh reaction conditions and lack sustainability by diminishing non-regenerative resources, i.e., hydrocarbons, and by emitting CO₂.^{12,13}



Scheme 1-1. Common reaction pathways to generate H₂ from fossil resources (hydrocarbons, carbon) and applied water-gas shift reaction to increase H₂ yield.¹³

Despite great efforts during the last decades, processes of sustainable H₂ production currently lack of economical feasibility compared to conventional production methods.¹² Alternative routes using water or biomass as a feedstock, developed to various stages of feasibility, comprise thermal, electrochemical and photolytic processes.^{13,14} Thermal pathways include cleavage of water *via* thermochemical cycles as well as gasification or pyrolysis of biomass coupled with catalytic steam reforming. Extensive investigations on photolytic water splitting using enzymes have also been reported. Approaches based on electrochemical reduction of protons complete the picture and can be considered as a promising route due to the abundance of sun light and (waste) water.^{13,15} Here, H₂ generation (cathodic half reaction) can be coupled with oxidation of water (anodic half reaction) to O₂ or with

oxidation of organic molecules, a constituent of waste water streams, to CO₂ (Scheme 1-2).⁹ The latter pathway creates added value as cleaning of waste water by valorization of contaminants and energy carrier generation is coupled.



Scheme 1-2. Anodic and cathodic half reactions of the electrochemical water splitting and polyol reforming reaction generating H₂/O₂ or H₂/CO₂ mixtures, respectively.

The required potential can be generated by means of electrochemistry or photocatalysis. In the former pathway, electricity generation and electrochemical half reactions, e.g., water electrolysis, are spatially separated, whereas for the latter build-up of electrochemical potential and charge carrier driven half reactions occur on the same catalyst particle and in one reaction chamber. Note that additional approaches like ‘two photon processes’ (Z-scheme)¹⁶ or photoelectrochemistry¹³ are also known. In case of these latter two technologies, generation of the charge carriers with appropriate potential and the electrochemical reactions are locally (and temporally) separated, whereas in ‘one photon processes’ both steps occur simultaneously within one solid matrix and one reactor. The latter technology is focus of this thesis in respect to overall water splitting and photoreforming of alcohols (C_nH_{2n+2}O_n).

The potential of photon-driven technologies is enormous. The anthropogenic energy consumption is four orders of magnitude smaller than the total photon energy absorbed by the planet, which is approximately 3.85 YJ year⁻¹.¹⁷ Based on an air mass of 1.5 global and 7.6 h of sun irradiation per day, the irradiance is estimated as 27 TJ km⁻² at the terrestrial equatorial area.¹⁸ There, an overall water splitting plant, with 25 km² in size and using a photocatalyst with 10% solar to hydrogen (STH) efficiency, would produce 570 t H₂ d⁻¹. 10000 of such solar plants would cover 1% of the world’s desert area and provide 30% of the projected global energy demand in 2050. In order to reach 10% STH efficiency photoabsorbers with band gaps of 1.8 to 2.0 eV (700 to 600 nm) and quantum efficiencies from 40% (at 700 nm) to 60% (at 600 nm) are necessary.¹⁸ Current systems are far from technological realization due

to low efficiency (smaller than 1% STH).^{19,20} Considering the tremendous abundance of solar energy, heterogeneous photocatalysis can replace traditional H₂ production routes and fossil fuels once efficient photocatalysts composed of abundant elements are developed.

1.3. Comparison of Overall Water Splitting and Photoreforming

Overall water splitting and photoreforming contrast in respect to their anodic half reactions. In the former case water and in the latter case an oxygenate serves as reducing agent producing H_2/O_2 and H_2/CO_2 mixtures, respectively. H_2/O_2 mixtures are explosive and difficult to separate. Moreover, they show high reactivity in the presence of noble metals, which are commonly applied as H_2 evolution reaction (HER) co-catalysts (chapter 1.6.1),⁷ at ambient conditions in contrast to H_2/CO_2 mixtures. Therefore, co-catalyst design (chapter 1.6.2-1.6.5), separation and safety design are less constraining for photoreforming plants than for plants adequate for overall water splitting. The gas products of photoreforming reactions (e.g., glycerol photoreforming: 69% H_2 , 30% CO_2 , 1% CH_4/CO) equal in composition typical reformer off-gas, which comprises 77% H_2 , 22% CO_2 and further impurities (1%).²¹ Therefore, several technologies, e.g., membranes²², pressure swing adsorption^{21,23} and amine wash²³, are commercialized for the separation of H_2/CO_2 mixtures, whereas these technologies remain to be developed for H_2/O_2 mixtures.

The oxidation potential of oxygenates and CO, which is sometimes proposed as intermediate of alcohol and polyol photoreforming (chapter 1.5.4.1), is less positive (referred to normal H_2 electrode (NHE)) compared to the oxidation potential of water (Table 1-1). Thus, semiconductors meet the thermodynamic requirements more easily for photoreforming than for the overall water splitting reaction as depicted in Figure 1-1. Exemplarily, we consider a semiconductor with a band gap of 1.6 eV (absorption edge: 775 nm) for the Figure 1-1. In respect to methanol reforming, the edges of valence and of conduction band (E_{VB} , E_{CB}) are located between 1.19 eV and -0.38 eV, and between -0.41 eV and -1.98 eV vs. NHE (pH = 7), respectively. For the overall water splitting reaction, the range of possible energy levels is narrowed (E_{VB} : 1.19 eV to 0.82 eV, and E_{CB} : -0.41 eV to -0.78 eV vs. NHE (pH = 7)). Therefore, a higher number of materials is suitable for the photoreforming reaction compared to the overall water splitting reaction as depicted in Figure-SI 1-1.²⁴

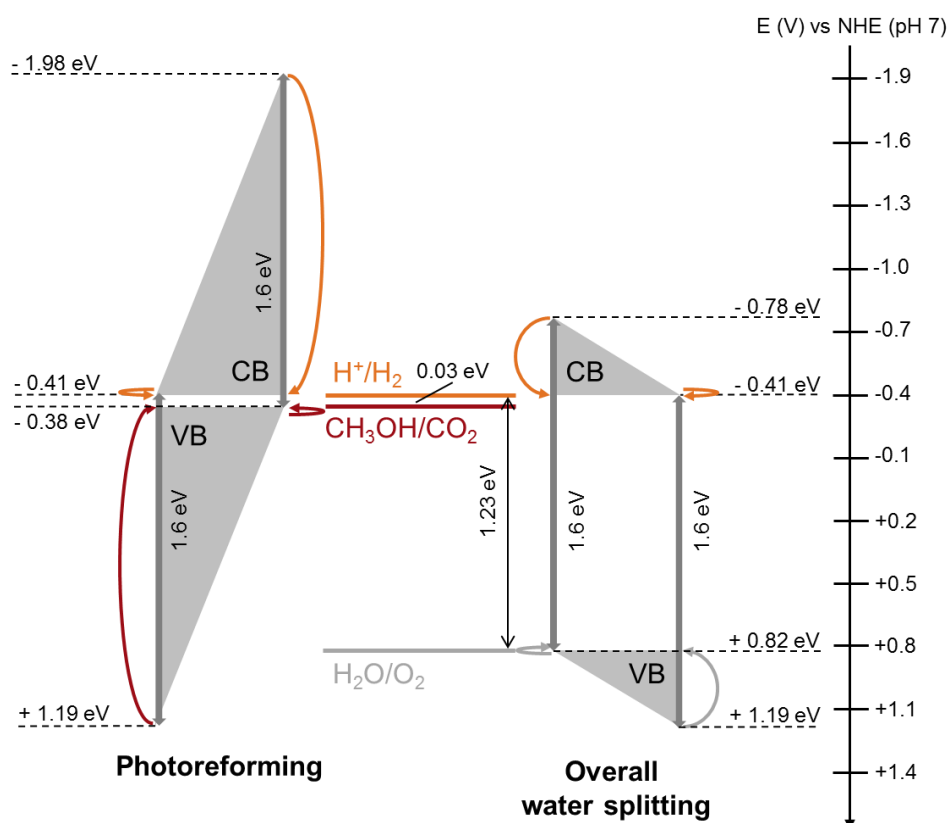


Figure 1-1. Graphical illustration of possible conduction and valence band edge positions (exemplified by grey triangles; versus NHE, pH = 7) for the methanol photoreforming and the overall water splitting reaction considering a semiconductor with a band gap of 1.6 eV (absorption edge: 775 nm) and resulting overpotentials for the respective half reactions (exemplified by bent arrows).

If a semiconductor fulfills the thermodynamic prerequisites for the overall water splitting reaction, the available overpotential of the anodic half reaction is always larger for the photoreforming reaction (Figure 1-2). Moreover many semiconductors are not active for the overall water splitting reaction, although they fulfill the thermodynamic requirements as exemplified in Figure-SI 1-1.²⁴

Table 1-1 lists the change of Gibbs free energy (ΔG_{298K}^0) of the overall water splitting reaction and various photoreforming reactions. The overall water splitting is a strongly endergonic reaction ($\Delta G_{298K}^0 = 237 \text{ kJ mol}^{-1}$), whereas photoreforming of oxygenates is slightly endergonic or exergonic.^{9,25,26} In the former case, the energy of photons is converted into chemically stored energy, i.e., H_2 and O_2 , and in the latter case photons are used to convert chemical energy, stored in aqueous oxygenates, into the energy carrier H_2 . The share of stored photon energy is small

(e.g., ethylene glycol) or non-existing (e.g., formic acid) and is predominantly lost in the large overpotentials (Figure 1-2).

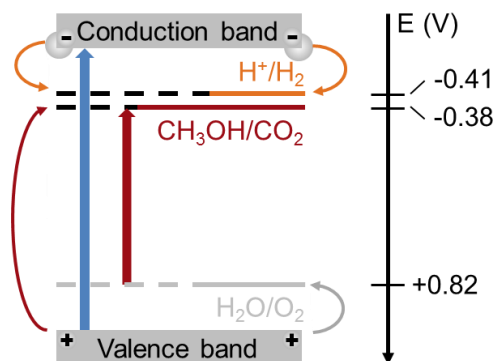


Figure 1-2. Graphical description of potentials (versus NHE, pH=7) of half reactions of the photoreforming and overall water splitting reaction and comparison of available overpotentials for the half reactions. (exemplified by bent arrows).

Table 1-1. Oxidation potentials (versus NHE, pH = 7) of various oxygenates, CO and water as well as reduction potential of protons to H₂.

Reactant	Formula	Reaction equation for half reaction	E _{Ox/Red} (V)	ΔG _{298K} ⁰ (kJ mol ⁻¹) [*]
Carbon monoxide	CO	CO + H ₂ O + 2h ⁺ → CO ₂ + 2H ⁺	-0.53 ^a	-29 ^{c,**}
Formic acid	HCOOH	CHOO ⁻ + H ₂ O + 2h ⁺ → CO ₂ + H ⁺	-0.49 ^a	-43 ^{c,**}
Formaldehyde	CH ₂ O	CH ₂ O + H ₂ O + 4h ⁺ → CO ₂ + 4H ⁺	-0.48 ^a	-63 ^{c,**}
Glycerol	C ₃ H ₈ O ₃	C ₃ H ₈ O ₃ + 3H ₂ O + 14h ⁺ → 3CO ₂ + 14H ⁺	-0.41 ^b	5.1 ^b
Ethylene glycol	C ₂ H ₆ O ₂	C ₂ H ₆ O ₂ + 2H ₂ O + 10h ⁺ → 2CO ₂ + 10H ⁺	-0.40 ^b	8.6 ^b
Methanol	CH ₄ O	CH ₄ O + H ₂ O + 6h ⁺ → CO ₂ + 6H ⁺	-0.38 ^a	9.3 ^b
Ethanol	C ₂ H ₆ O	C ₂ H ₆ O + 3H ₂ O + 12h ⁺ → 2CO ₂ + 12H ⁺	-0.33 ^b	97.4 ^b
Water	H ₂ O	H ₂ O + 2h ⁺ → 0.5O ₂ + 2H ⁺	+0.82 ^a	237 ^{c,***}
Proton	H ⁺	2H ⁺ + 2e ⁻ → H ₂	-0.41 ^a	

* Change of Gibbs free energy of overall water splitting and various photoreforming reactions.

** gas phase, *** liquid phase (gas phase: 229 kJ mol⁻¹).

(a) reference 25, (b) reference 26, (c) reference 9.

At a first glance, the STH efficiencies of overall water splitting and photoreforming reaction can be regarded as equivalent, because the number of required photons to generate one equivalent of H₂ is equivalent irrespective of the reaction (Scheme 1-2) (the author considers the conversion of oxygenates from waste water streams). If current doubling is part of a photoreforming mechanism (chapter 1.5.4.2), the STH efficiency of the photoreforming reaction is up to twice of the STH efficiency of the overall water splitting H₂ reaction.^{27,28} Current doubling occurs, if the unpaired electron

of a carbon radical, generated *via* an one-hole oxidation process, is injected into the conduction band of the semiconductor. Accordingly, a single photon excitation results in the formation of two conduction band electrons and a doubled STH efficiency compared to overall water splitting.

The main appeal of the photoreforming reaction is the combination of H₂ production and simultaneous removal of organic contaminants from waste water streams. This feedstock is widely available and multiple in source as well as nature (e.g., glycerol – side-product from bio-diesel production, ethylene glycol – de-icing agent). The author has the opinion that photoreforming would constitute a ‘facilitated’ start into a solar H₂ economy for the following reasons: band gap design of the photocatalyst is simplified due to the small required potential (Table 1-1), co-catalyst and safety plant design can be kept simple due to missing reactivity of the gaseous product mixtures (H₂ and CO₂), whose separation is well-known in the petro-chemical industry. Small STH efficiencies in case of low oxygenate surface coverage (Figure 1-3A) are compensated by added value resulting from purified waste water streams. Given the nature of the feedstock, small and decentralized solar plants are required. They could serve as a starting point to design large-scale, centralized overall water splitting plants, which require efficient photocatalysts (due to missing added value effects) and sophisticated safety design.

1.4. Description of Used Semiconductors

1.4.1. UV-Light Absorbing SrTiO₃ and Aeroxide[®] TiO₂ P 25

SrTiO₃ and TiO₂ are wide band gap metal oxide photocatalysts based on d⁰ metal cations.²⁹ The valence band of both semiconductors predominantly comprises O_{2p} orbitals, whose potential is located around 2.6 eV vs. NHE (pH = 7). In contrast to SrTiO₃ photoelectrodes, TiO₂ based ones are not active for the overall water splitting reaction without external bias.²⁹ Powdered, co-catalyst modified TiO₂ possesses none or little activity for the overall water splitting reaction³⁰ in contrast to the corresponding SrTiO₃ based photocatalysts.³¹ In this thesis, TiO₂ and SrTiO₃ were applied as photoabsorber for the photoreforming and overall water splitting reaction, respectively.

SrTiO₃ - Properties and Synthesis

SrTiO₃ crystallizes in a perovskite cubic structure and possesses an indirect band gap value of 3.25 eV.³² The top of the valence band consists mainly of O_{2p} and Sr_{4p} states, whereas the bottom of the conduction band is made of Ti_{3d} orbitals.³² The E_{VB} is 2.4 V vs. NHE (pH = 7) and the E_{CB} is located at -0.85 V vs. NHE (pH = 7).³³ SrTiO₃, which has been used for this thesis, was synthesized *via* a SrCl₂ flux synthesis method from commercial SrTiO₃ powder in an Al₂O₃-crucible.³¹ The flux treatment enables crystallization from a supersaturated solution of dissolved SrTiO₃, so that particles with high crystallinity and controlled morphology (here: truncated cubes) are obtained. In this particular case, additional aliovalent doping occurs due to the incorporation of dissolved Al³⁺-cations in the SrTiO₃ lattice. Note that the surface of the Al₂O₃-crucible is etched by the SrCl₂ melt under the applied synthesis conditions. This doping diminishes the presence of Ti³⁺-sites, whose existence is believed to increase electron hole recombination rates.³¹

TiO₂ P 25

Aeroxide[®] TiO₂ P 25 is a widely applied powdered photoabsorber in photocatalysis research because it is a highly active and commercial available semiconductor. Accordingly it enables comparability and serves as a reference material. TiO₂ P 25 is synthesized *via* flame spray pyrolysis and is obtained as a powder (50 m² g⁻¹) of aggregated anatase (E_{BG} = 3.3 eV, particle size: 25 nm) and rutile particles

($E_{BG} = 3.1$ eV, particle size: 85 nm).³⁴ The anatase to rutile ratio varies between 3 : 1 and 4 : 1.^{34,35} The absolute and relative position of the valence and conduction band edges of the two polymorphs and their intrinsic band alignment has been controversially discussed.³⁶ Nevertheless, it is generally accepted that band alignment between the two polymorphs promotes efficient charge separation and evokes the high photocatalytic activity of (co-catalyst modified) TiO_2 P 25.³⁵

1.4.2. UV-Vis-Light Absorbing GaN:ZnO

Gallium zinc oxynitrides ($Ga_{1-x}Zn_x)(N_{1-x}O_x)$ are prepared by nitridation of ZnO/ Ga_2O_3 -mixtures under elevated temperatures.³⁷ ($Ga_{1-x}Zn_x)(N_{1-x}O_x)$ is an UV-Vis-light absorbing solid solution of GaN and ZnO. It crystallizes in a wurtzite-type structure with lattice parameters located between those of GaN and ZnO. The band gap energy is minimized with increasing zinc content x (e.g., $x = 0.05$: $E_{BG} = 2.82$ eV and $x = 0.22$: $E_{BG} = 2.60$ eV).³⁷ Due to the reductive environment during the synthesis reduction of ZnO and Zn sublimation causes formation of GaN-enriched ($Ga_{1-x}Zn_x)(N_{1-x}O_x)$ solid solutions. Zn^0 -centers (negative for activity) can be removed by a post-calcination treatment in synthetic air at elevated temperatures.³⁸ Fraction of absorbed visible light and photocatalytic activity do not correlate as maximal activities for the overall water splitting reaction around 9 atom% Zn ($x = 0.18$) have been observed.^{38,39} The narrowed band gap energy of ($Ga_{1-x}Zn_x)(N_{1-x}O_x)$ compared to those of GaN ($E_{BG} = 3.4$ eV)³⁷ and ZnO ($E_{BG} = 3.2$ eV)³⁷ was explained by shifted conduction (e.g., repulsion of empty conduction band states) or valence band edges (Zn species as doping bands), respectively.^{40,41} However, the determined E_{CB} of a GaN:ZnO photoelectrode (ca. -1.19 V vs. NHE (pH = 7)) is comparable to the E_{CB} of GaN and supports the latter hypothesis as the reason of visible light absorption.⁴²

1.5. Polyol Photoreforming

1.5.1. Definition and Kinetics

Photoreforming of polyols is a slightly endergonic or exergonic pathway to CO₂ / H₂-mixtures (see chapter 1.3), which is solely driven by photons under ambient conditions. Photogenerated charge carriers with appropriate chemical potential drive H₂ evolution and the conversion of the alcohol to CO₂. The required C–C-cleavage steps were suggested to take place *via* decarboxylation or decarbonylation of aldehydes (light-driven) or alcohols (thermal) with subsequent photon-driven water-gas shift reaction (chapter 1.5.4.1). The polyol oxidation can be considered as a multi-step reaction sequence *via* 2e⁻ oxidation intermediates, e.g., aldehydes or carboxylic acids.

Numerous studies demonstrated successful H₂ evolution by photoreforming of oxygenates on various semiconductor materials. Little focus has been directed to the reaction network and the mechanism of the oxidation of oxygenates to CO₂.⁴³⁻⁴⁷ Knowledge about the nature of intermediates and its formation is urgently required, as technical relevance only arises, if any intermediate possesses equivalent or reduced toxicity compared to the reactant. The necessity is underlined by the identification of toxic formaldehyde and acetaldehyde as intermediates with low reactivity as indicated by deviating H₂ to CO₂-ratios or missing CO₂ formation during methanol^{6,48-52} and ethanol photoreforming⁵³⁻⁵⁷, respectively. Although quantitative photoreforming for various oxygenates, including alcohols (C_nH_{2n+2}O_n, n = 1-3)^{52,58-60}, acetic acid^{58,59} and saccharides⁵⁸ has been demonstrated, it does not eliminate the consideration about the formation of toxic intermediates.

The kinetics of various oxygenate photoreforming reactions^{52,61-68} were shown to follow linearized⁶⁹ Langmuir adsorption models, so that they can be described by a Langmuir based rate equation (equation (1-1) with n = 1) as illustrated in Figure 1-3.⁷⁰ At high reactant concentrations, the saturation limit of adsorption is reached and the reaction order is zero (Figure 1-3A, blue dotted line). In case of low reactant concentrations, a first order dependence is observed because the amount of adsorbed reactant correlates in this regime linearly to the concentration of reactant in the solution (Figure 1-3A, orange dotted line). Therefore, reaching full conversion is connected to declining rates evoked by decreasing surface coverages. If a

photocatalyst is active for the photoreforming as well as for the overall water splitting reaction, the H₂ evolution rate is expected to be independent of oxygenate concentration. At small oxygenate concentrations, H₂ evolution rate is maintained as holes oxidize water to O₂ (Figure 1-3A). Note that the current doubling phenomena is not considered (chapter 1.5.4.2) and that the reaction order of the overall water splitting reaction is zero because the activity of water is assumed to be unity.⁷¹ Aerobic photooxidation studies revealed that the rate constant, in most cases, is invariant to the nature of chemical bond transformation and predominantly depends on the adsorption constant of the reactant.⁷²

In order to describe an entire photoreforming reaction network competitive adsorption of the liquid phase intermediates has to be considered according to equation (1-1).

$$\frac{dc_i}{dt} = \frac{k \cdot K_i^{L,app} \cdot c_i}{1 + \sum_{i=1}^n K_i^{L,app} \cdot c_i} = k \cdot \theta_i \quad (1-1)$$

Where dc_i/dt denotes the reaction rate of reactant i (mM h⁻¹), k is the maximum intrinsic rate constant of any reactant i (mM h⁻¹), K_i is the apparent Langmuir adsorption constant of reactant i (L mM⁻¹), c_i is the concentration of reactant i (mM L⁻¹) and θ_i is the surface coverage (percentage) of reactant i . Competition for adsorption sites during progression of photoreforming of species i by n intermediates is accounted for in the denominator of equation (1-1).

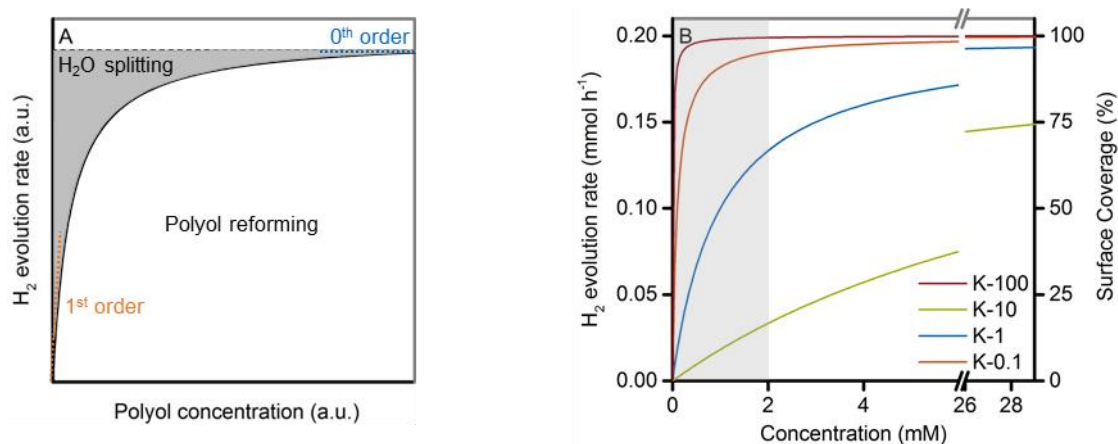


Figure 1-3. (A) Proportion of water splitting (grey area) and polyol reforming (white area) to H₂ evolution rate in dependence of polyol concentration. Current doubling phenomenon is not considered. (B) Course of H₂ evolution rate following Langmuir adsorption based kinetics in dependence of various adsorption strengths ($K = 0.1, 1, 10, 100$). Maximal intrinsic rate constant k : 0.2 mmol h⁻¹.

The larger the adsorption constant K , the smaller the required minimal concentration to reach full surface coverage and consequently maximal H_2 evolution rates as depicted in Figure 1-3B.

In the following, diverse scenarios, relevant for the results presented in this work, are described, where reactants and products have varying affinities for adsorbing on the photocatalyst. We assume a reactant A (2 mM) being consecutively converted *via* two intermediates, named B and C , to CO_2 on a photocatalyst, e.g., Pt/TiO₂, which cannot oxidize water to O₂. Using equation (1-1) the appropriate rate equation of each individual species can be defined. Four different combinations of adsorption constants K_A , K_B and K_C (Table 1-2) should reveal the impact of adsorption strength on the reaction time and on the course of concentration of liquid phase species A , B and C . K_A was set to one in all cases.

Table 1-2. Selected combination of adsorption constants for a photoreforming reaction, which follows a reaction sequence starting from a reactant A *via* two consecutive intermediates B and C to CO_2 .

Combination	Adsorption constant (L mmol ⁻¹)		
	K_A	K_B	K_C
I	1	1	1
II	1	0.1	0.1
III	1	10	10
IV	1	100	10

In combination I (Table 1-2) the adsorption constants of the reactant A and the intermediates B and C are identical. The proportion of reactant A decreases with ongoing conversion, whereas the share of reactant C increases continuously (Figure 1-4-V). Nevertheless, all species are present at any time of the reaction. Compared to combination I, the adsorption constants of the intermediates B and C are reduced by an order of magnitude for combination II. Consequently, prolonged reaction times (Case I: 77 min, Case II: 410 min; Figure 1-4-I, -II) are obtained. A small adsorption constant evokes a reduced surface coverage resulting in a lower overall H_2 evolution rate as depicted in Figure 1-3B. However, quantitative conversion (99%) of reactant A is reached after 37 min for combination II compared to 51 min for combination I (Figure 1-4-I, -II). Thus, the intermediates B and C are the dominant species for combination II. The opposite occurs, if the adsorption constant

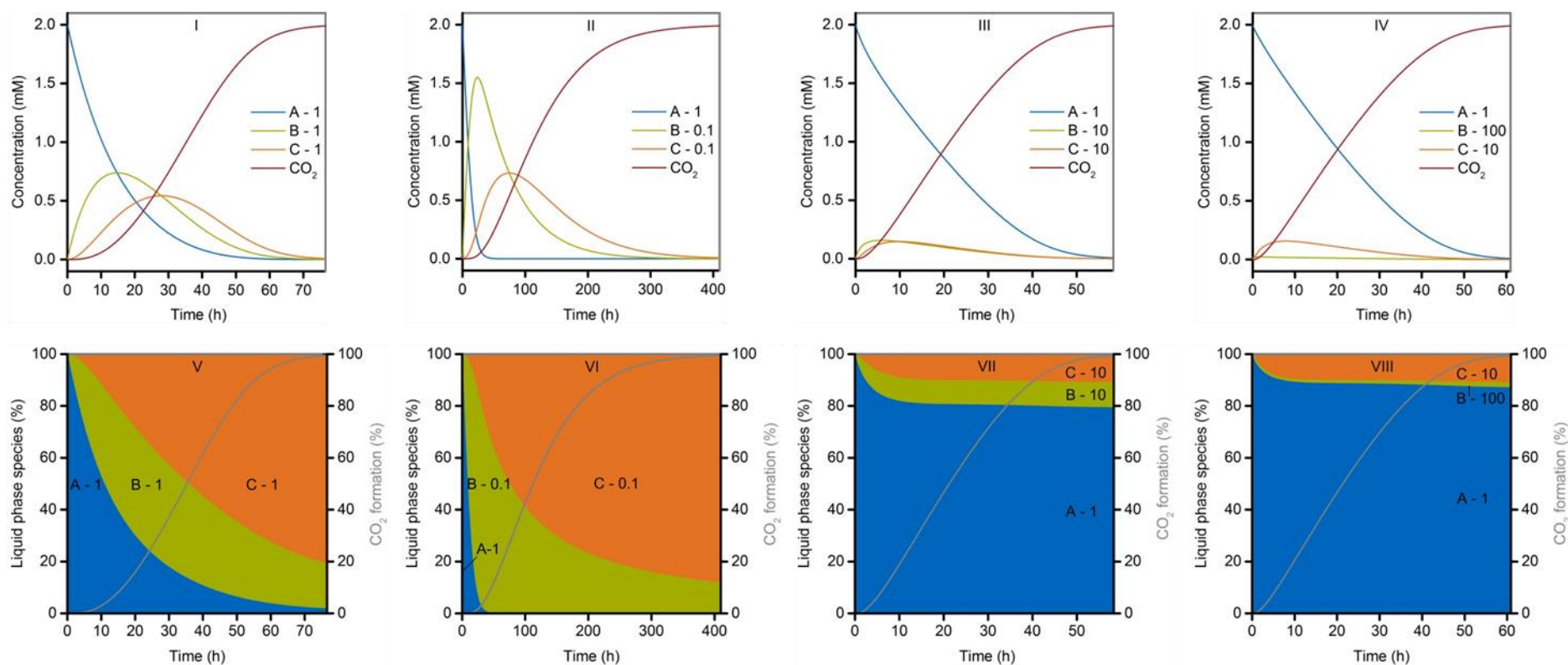


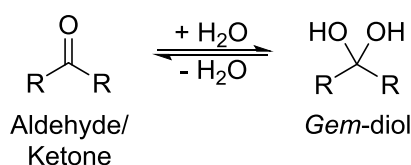
Figure 1-4: Influence of individual adsorption constants on the course of concentration of a reactant *A* (2 mM) and of the consecutive intermediates *B* and *C*, which is converted to CO₂ (I-IV). Proportion of liquid phase species *A*, *B* and *C* as a function of the reaction time (V-VIII). Comparison of four sets of adsorption constants (I – $K_A = K_B = K_C = 1$; II – $K_A = 1, K_B = K_C = 0.1$; III – $K_A = 1, K_B = K_C = 10$; IV – $K_A = 1, K_B = 100, K_C = 10$). Applied kinetic model: Langmuir adsorption based rate equation, consideration of competitive adsorption of *A*, *B* and *C* as well as a substrate independent maximal intrinsic rate constant (0.2 mM h^{-1}), CO₂ formation: 99.5%.

of the intermediates *B* and *C* is larger than of the reactant *A* (Table 1-2, combination **III** and **IV**). Independent of the conversion, reactant *A* is the dominant species (Figure 1-4-VII, -VIII). Moreover, maximum reaction rates are preserved over large concentration regimes as the low coverage Henry-like regime is shifted to small concentration (Figure 1-3B, compare K-0.1 and K-100). In general, short reaction times are highly desirable, however also the individual toxicity of reactant *A* as well as of intermediates *B* and *C* has to be considered. If reactant *A* possesses high toxicity in contrast to the intermediates *B* and *C*, the adsorption strength of *A*, *B* and *C* should correspond to combination **II**. Here, reactant *A* is rapidly converted to intermediate *B* and the toxicity of the waste water is reduced, although prolonged reaction times have to be accepted. If the toxicity of reactant *A* is negligible in contrast to the intermediates *B* and *C*, combination **II** is highly undesirable in respect to toxicological and economic considerations. Combinations **III** and **IV** guarantee small proportion of intermediates *B* and *C*, so that their specific toxicity plays a minor role. In addition short reaction times are obtained. The toxicity of polyols like ethylene glycol (e.g., 96-h LC₅₀ is 22800-50800 mg L⁻¹ for rainbow trout, *Onocrhynchus mykiss*)⁷³ is minor compared to potential intermediates like formaldehyde (e.g., 48-h LC₅₀ is 42.3-86 mg L⁻¹ for rainbow trout, *Onocrhynchus mykiss*)⁷⁴. Accordingly, combinations **III** and **IV** should be targeted in respect to polyol photoreforming. The polyol would be the dominating reactant in the liquid phase and a constant small proportion of the intermediates is obtained, which approximates close to zero if the adsorption strength of a single intermediate, is one order of magnitude larger than any other (Figure 1-4-IV, here *B*). Thus, an efficient polyol photoreforming process is based on a reaction network with intermediates exhibiting increased adsorption strengths compared to the polyol.

The design of such a network requires knowledge about the molecular state of oxygenates in aqueous phase and the nature of hole transfer (direct or indirect *via* radical oxygen species) channeling the reaction pathway. Selective transfer of holes (direct or indirect) premises defined functionality of the semiconductor surface and a uniform adsorption strength of the adsorbates (chemi- or physisorption).

1.5.2. State of C1- / C2-Oxygenates in Aqueous Phase

The nature of the solvent (e.g., protic or aprotic) influences the molecular state of an organic molecule in solution. In case of a protic solvent (e.g., water), the molarity and the pH influence the molecular state. Alcohols do not noticeably deprotonate in aqueous phase, as they are very weak Brønsted acids with typical pK_a -values between 15 and 18 (Table 1-3).^{75,76} Aldehydes possess very similar pK_a -values like alcohols. However they are (partially) hydrated because they undergo keto *gem*-diol tautomerism in aqueous phase as depicted in Scheme 1-3.⁷⁷ An overview of the keto *gem*-diol tautomerism of the C1- / C2-oxygenates bearing a formyl group is given in Scheme-SI 1-1.



Scheme 1-3. Keto *gem*-diol tautomerism of aldehydes / ketones in aqueous phase.

The position of the equilibrium of the tautomerism is described by the hydration constant K_H , which is defined as the quotient of *gem*-diol- and keto-form.⁷⁷ Knowledge about the position of the equilibrium K_H of an oxygenate is of high importance as its adsorption properties are influenced by the degree of keto *gem*-diol tautomerism. The resulting adsorption complex may determine reactivity and mechanism of oxidation. In addition, the concentration of the oxygenate has to be considered because oligomerization of aqueous aldehydes is a well-known phenomenon.^{78,79}

The photoreforming studies presented in this thesis have been performed in a concentration range (< 20 mM) in which aldehydes solely appear as monomeric species with the exception of acetaldehyde,⁸⁰ which is present in its keto, *gem*-diol form and as dimer at concentrations equal or smaller than 20 mM. Table-SI 1-1 lists the critical concentrations required to induce self-oligomerization or dimer formation of the relevant C1- and C2-aldehydes.

Table 1-3. Hydration constants K_H and dissociation constants (pK_a) for C1- and C2-oxygenates (298 K).

Name	Formula	Chemical state	K_H	pK_a
Methanol	CH ₄ O			15.5 ^d -16 ^e
Ethanol	C ₂ H ₆ O			15.9 ^d -18 ^e
Ethylene Glycol	C ₂ H ₆ O ₂			15.1 ^f
Formaldehyde in H ₂ O	CH ₂ O		2530 ^a	13.3 ^g
Acetaldehyde	C ₂ H ₄ O		1.2 ^a	13.6 ^g
Glycolaldehyde	C ₂ H ₄ O ₂		9 ^a	-
Glyoxal	C ₂ H ₂ O ₂		22000 ^b	-
Formic acid	HCOOH			3.77 ^h
Glycolic acid	C ₂ H ₄ O ₃			3.83 ^h
Acetic acid	C ₂ H ₄ O ₂			4.76 ⁱ
Glyoxylic acid	C ₂ H ₂ O ₃	-CH(OH) ₂	300 ^c 15.1-19.2 ^c	2.98-3.46 ^c
		-CHO		1.89 ^c
		-CO ₂ H		
		-CO ₂ ⁻		
Oxalic acid	C ₂ H ₂ O ₄	HOCCOO ⁻		1.27 ⁱ
		⁻ OCCOO ⁻		4.27 ⁱ

$pK_a = -\log_{10} K_a$, whereas K_a (acid ionization constant) is the equilibrium constant for the dissociation reaction in context of the carboxy group.

K_H (keto-*gem*-diol equilibrium) is defined as the ratio of *gem*-diol- divided by the keto-form.

Determination of the acidity of alcohols is attended with uncertainties due to similar equilibrium constants compared to water.⁸¹

References: (a) ⁷⁷, (b) ⁸², (c) ⁸³, (d) ⁷⁵, (e) ⁷⁶, (f) ⁸⁴, (g) ⁸⁵, (h) ⁸⁶, (i) ⁸⁷.

The degree of *gem*-diol formation depends predominantly on the polarity and not on the sterics of the substituent. Substituents with increasing electron withdrawing effect shift the equilibrium towards the *gem*-diol form.⁷⁷ Aqueous formaldehyde and glyoxal solutions equilibrate almost quantitatively in *gem*-diol form as indicated by large K_H constants.⁷⁷ This is in line with the absence of carbonyl signals for aqueous glyoxal solutions, which prove negligible concentrations of monohydrate and aldehyde form.⁷⁹ In contrast, hydration of glycolaldehyde and acetaldehyde occurs to a lower extent.⁷⁷ Carboxylic acids, e.g., formic acid, are weak acids (Table 1-3) and their dissociation depends on the pH according to the Henderson-Hasselbach equation. The pK_a value is defined as the negative decadic logarithm of the acid dissociation constant K_A , which describes the equilibrium of an aqueous acid AH and its conjugate base A^- . Quantitative dissociation of a carboxylic acid occurs solely, if the pH is two units larger than its pK_a value as depicted in Figure 1-5. The dissociation of a diprotic acid is described by two pK_a constants due to two equilibrium reactions (Scheme1-4).

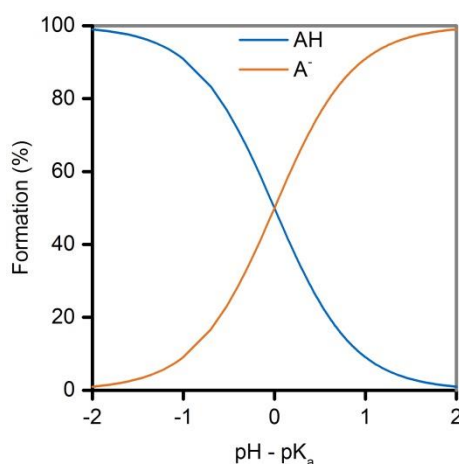


Figure 1-5. Percentage dissociation of a monoprotic acid AH to its conjugate base A⁻ in dependence of the difference between the pH and the pK_a of the acid.



Scheme 1-4. Dissociation equilibria of a diprotic acid (e.g., oxalic acid).

1.5.3. Mode of Adsorption of Aqueous C1- / C2-Oxygenates on TiO₂

In this thesis, photoreforming of aqueous oxygenate solutions was studied in depth on TiO₂ as it is the most used system in photocatalysis. Therefore, the adsorption of water and aqueous C1- / C2-oxygenates is summarized in respect to TiO₂ and insertions are given, if studies of other materials are available and considered as relevant.

1.5.3.1. Adsorption of Water on Powdered TiO₂

Powdered TiO₂ contains surface defects appearing as undercoordinated titanium surface atoms, which act as Lewis acid sites, whereas bridged surface oxygen atoms behave as Lewis basic sites. Solid state ¹H NMR (nuclear magnetic resonance) studies⁸⁸ of wetted TiO₂ revealed three different layers of adsorbed water. The first layer, which is three water molecules thick, comprises strongly coordinated or surface bounded water. Binding occurs either coordinatively (Scheme 1-5 (II)) and/or dissociatively (Scheme 1-5 (III)). Independent of its defined surface interaction, this first layer shows low mobility due to its rigid structure. Water molecules of the second layer are physisorbed and show increased mobility, which is

over TiO_2 , SnO_2 , ZnO , WO_3 or V_2O_5 , the water contact angle did not change over SrTiO_3 .⁹⁵ Nevertheless, SrTiO_3 was shown to be a highly active photocatalyst for (an)aerobic photocatalyzed reactions in contrast to WO_3 and V_2O_5 (Z-scheme applications are not considered).⁹⁵ Thus, photoinduced hydrophilicity is not a prerequisite for photocatalytic activity, although a different reaction pathway might occur on a light-altered surface (due to formation or increased density of terminal hydroxy groups).

1.5.3.2. Adsorption of Primary Alcohols ($\text{C}_n\text{H}_{2n+2}\text{O}$; $n = 1,2$)

Methanol and ethanol are present as molecular (physisorbed) or dissociated (chemisorbed) adsorbates on TiO_2 (rutile and anatase) in the absence of condensed water.^{89,96-98} Here, terminal hydroxy groups or (water coordinatively bound to) undercoordinated Ti-sites are replaced by the alcohol forming a methoxy or ethoxy group and releasing one molecule of water or a proton. The chemisorption capacity of TiO_2 for primary alcohols depends on the density of undercoordinated Ti-centers. Platinum decorated TiO_2 showed significantly diminished methanol adsorption capacity, explained by consumed undercoordinated Ti-sites serving as nucleation sites for (platinum) nanoparticles.⁹⁷ Physisorption of methanol occurs at non-vacancy sites⁹⁸ *via* electrostatic effect or displacement of water on the surface.⁸⁹ Sum frequency and ^1H solution NMR spectroscopy studies revealed that methanol and ethanol, chemisorbed on TiO_2 , hydrolyzes in the presence of water (excess; e.g., water to methanol ratio: 300) and are stabilized *via* H-bonding in surface-near physisorbed water layers.^{99,100} The experimental studies are supported by density functional theory calculations showing that chemisorption of methanol in aqueous phase is minor or can be neglected as calculated adsorption energies are predominantly positive.¹⁰¹ It is worth to note, that water preferable evaporates under vacuum and the alcohol re-chemisorbs.⁹⁹

1.5.3.3. Adsorption of Polyols on TiO_2 ($\text{C}_n\text{H}_{2n+2}\text{O}_n$; $n = 2,3$)

The adsorption of polyols on semiconductors in aqueous phase has been scarcely studied. One of the few studies¹⁰² revealed that glycerol adsorbs *via* bidentate α - γ -complexes on anatase in presence of co-adsorbed water. Both primary alcohol

groups interact with terminal surface hydroxy groups (formed *via* the interaction of water with Lewis acid sites). One primary alcohol adsorbs dissociatively, whereas the other adsorbs molecularly. H-bond interaction of the secondary alcohol group with basic surface oxygen was not observed as soon as water was present.¹⁰² XANES (X-ray absorption near edge structure) studies¹⁰³ suggested a similar mode of adsorption in form of a bidentate chelating chemisorption. Here a change to octahedral coordination was observed, when small Ti particles (19 Å) with undercoordinated Ti-surface atoms¹⁰⁴ were exposed to an aqueous ethylene glycol or glycerol solution. Whereas chemisorption of monodentate primary alcohols is thermodynamically unfavorable in aqueous phase, polyols form non hydrolysable complexes due to chelation.

1.5.3.4. (Oxo-functionalized) C1- / C2-Aldehydes

Chemisorption of aqueous formaldehyde (0.2 M) on TiO₂ P 25 was not observed. Instead interaction of formaldehyde and TiO₂ occurs *via* weak hydrogen-bonding.¹⁰⁵ One computational study¹⁰⁶ revealed that formaldehyde and acetaldehyde adsorb *via* the interaction of carbonyl oxygen and Lewis acidic Ti-centers on the TiO₂ polymorphs rutile and anatase. As calculated adsorption energies of the aldehydes (70 – 170 kJ mol⁻¹) are comparable to the adsorption energy of water, competitive adsorption occurs causing decreasing surface coverage of the aldehyde with increasing proportion of water. The author notes, that the *gem*-diol forms of formaldehyde and acetaldehyde (existing in aqueous phase) and potential oligomerization were not considered (Chapter 1.5.2). Neither experimental nor theoretical studies were found for glyoxal and glycolaldehyde.

1.5.3.5. (Oxo-functionalized) C1- / C2-Carboxylic Acid

The adsorption of aqueous (oxo-functionalized) C1- / C2-carboxylic acids was extensively investigated on TiO₂ by ATR-FTIR-spectroscopy. Carboxylic acids adsorb in general as dissociated acids, i.e., with their carboxylate anion, on metal oxides.¹⁰⁷ Bi-functionalized carboxylic acids (0.1 mM) adsorbed dissociatively with both functional groups.¹⁰⁷⁻¹⁰⁹ Spectroscopically identical complexation can occur on one or two adjacent Ti-centers (Figure 1-6).¹¹⁰

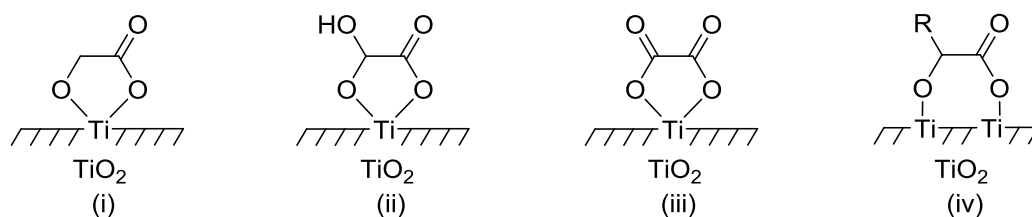


Figure 1-6. Schematic illustration of bidentate adsorption complex of α -oxygen functionalized C2-carboxylic acids, i.e., (i) glycolic acid, (ii) glyoxylic acid, (iii) oxalic acid to (i-iii) one (chelating) or (iv) two adjacent (bridging) Ti-centers in aqueous phase on a TiO_2 polymorph.¹⁰⁷⁻¹⁰⁹

Irrespectively if it is a 5-ring bidentate chelating and/or 6-ring bidentate bridging (both forms are reported),¹¹¹ the adsorption complex is formed from the OH-group of the carboxylic group and another OH-group of the second functional oxo-group, i.e., hydroxy, hydrated formyl, carboxylic group as depicted in Figure 1-6. In case of CdS, glycolic acid adsorbed *via* an electrostatic interaction with its carboxylate ion and could be replaced by water in contrast to oxo-functionalized C2-carboxylic acids chemisorbed on TiO_2 .¹⁰⁹

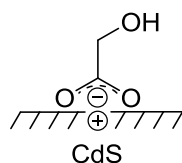


Figure 1-7. Schematic illustration of electrostatic interaction of carboxylate group of glycolic acid with CdS in aqueous phase.¹⁰⁹

If a second anchoring group is missing, different modes of adsorption were observed for linear acids. In several studies, no stable interaction of the respective linear carboxylic acid, i.e., $\text{C}_n\text{H}_{2n}\text{O}_2$ with $n = 1,^{107} 2,^{107} 3^{109}$, was observed on TiO_2 . In contrast, a sum frequency generation spectroscopy study revealed that acetic acid interacts solely *via* chemisorption with anatase and cannot not be replaced by co-adsorbed water.⁹⁰ Systematic perturbation of the pH of aqueous oxalic acid (2.3-11.7) demonstrated that chemisorption of oxalic acid ($\text{pK}_{a1} = 1.27$, $\text{pK}_{a2} = 4.27$)⁸⁷ requires a positively charged surface ($\text{pH}_{\text{IEP-TiO}_2} \approx 5^{112}$), whereas the adsorption capacity rises with increasing pH.¹¹³ Various modes of adsorption were suggested for the diprotic C2-acids. An experimental adsorption isotherm of oxalic acid was described by a superposition of three Langmuir isotherms adopted for surface species with different Langmuir adsorption constants. The strongest one was

ascribed to a chelating and the two other ones to monodentate binding modes.¹¹⁰ However measurements of desorption kinetics, monitored by ATR-FTIR spectroscopy, suggested only two chemisorbed and one physisorbed species, whereas the strongest one presumably represents a bidentate chelating oxalate and the weakest one physisorbed oxalate.¹¹⁴ Acetic acid ($pK_a = 4.75$)⁸⁷ is a weak monoprotic acid and the degree of dissociation (HAc/Ac^-) depends on pH as described in chapter 1.5.2. The adsorption isotherm of acetic acid (pH=4.5) on TiO_2 P 25 comprised one Langmuir and one linear component, whereas the subtracted spectra of the linear component agreed well with the liquid phase spectrum, i.e. protonated and deprotonated form, of acetic acid at pH 4.6.¹¹⁰ The comparison of the deduced Langmuir adsorption constants of acetic acid and oxalic acid ($K_{L_HAc} = 137 \text{ M}^{-1}$, $K_{L1_H2Ox} = 1.3 \cdot 10^6 \text{ M}^{-1}$, $K_{L2_H2Ox} = 3.9 \cdot 10^5 \text{ M}^{-1}$, $K_{L3_H2Ox} = 3.2 \cdot 10^3 \text{ M}^{-1}$, pH = 3)¹¹⁰ confirmed higher adsorption strength of the diprotic carboxylic acid compared to the monoprotic one. It was shown that acetic acid follows the adsorption modes of formic acid.¹¹⁵ Accordingly, interaction of aqueous formic acid with anatase and rutile occurs *via* physisorption as well as chemisorption^{115,116} following a Langmuir saturation behavior.¹¹⁷ Comparison of calculated and experimental vibrational frequencies of possible adsorption complexes of formic acid on rutile (110) revealed that formate chemisorbs *via* μ -coordination as depicted in Figure 1-8.¹¹⁵

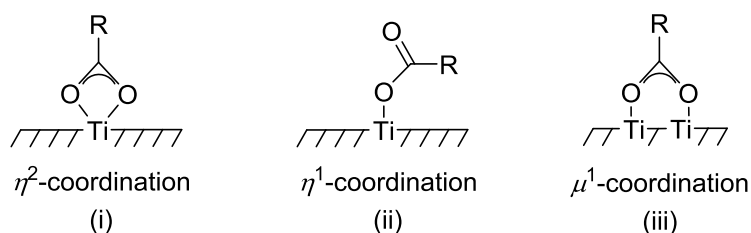


Figure 1-8. Suggested adsorption complexes of formic acid ($\text{R} = \text{-H}$) and acetic acid ($\text{R} = \text{-CH}_3$) on TiO_2 polymorphs.¹¹⁵

Hexa-coordinated η^1 -formate is an additional stable adsorption complex, which is formed at tetra-coordinated Ti^{IV} -centers (e.g., edges, corners) as shown by computational¹¹⁵ and experimental¹¹⁷ studies. Hepta-coordinated η^2 -formate can be ruled out on anatase as well as rutile, whereas the μ -coordination may not occur on anatase due to the particular Ti-Ti -distances on the two polymorphs (110, anatase:

3.785 Å¹¹⁸, rutile: 2.96 Å¹¹⁹).¹¹⁵ The suggested adsorption complexes are summarized in Figure 1-8.

1.5.4. Reaction Network and Mechanism

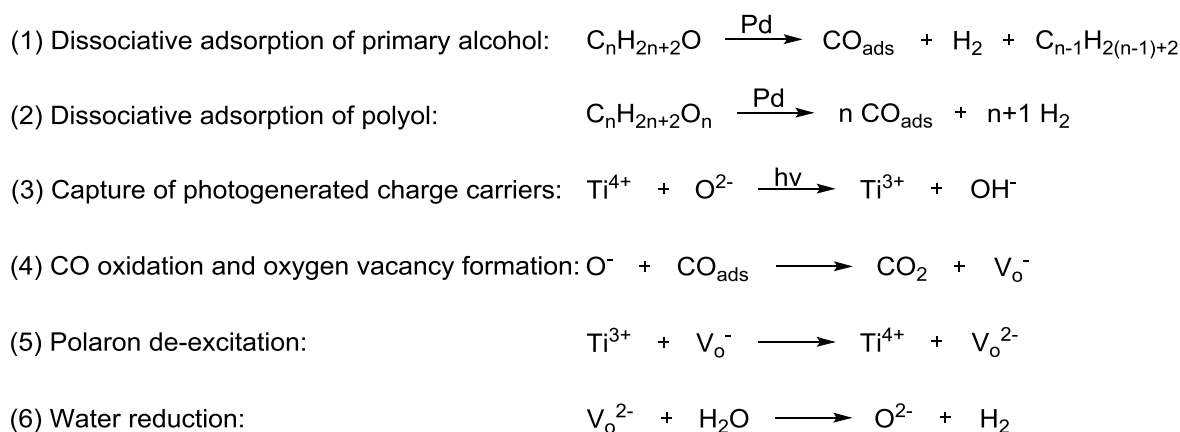
1.5.4.1. Primary Alcohols ($C_nH_{2n+2}O$, $n = 2-4$) or Polyols ($C_nH_{2n+2}O_n$, $n = 2-3$)

Reaction pathway analysis of alcohol photoreforming was performed almost exclusively on TiO₂ based systems. The analysis of gaseous products, evolved during photoreforming of primary alcohols or polyols, revealed the formation of the expected reaction products CO₂ and H₂ beside CO and alkanes (C1-C3).^{46,120} The observed product spectrum was rationalized by several reaction pathways, which are subsequently named according to their reaction pathway directing mechanistic feature.

A. Co-catalyst assisted alcohol decarbonylation.^{44,63,121,122}

This route comprises thermal decarbonylation of an alcohol (Scheme 1-7 (1), (2)) adsorbed on a Pd co-catalyst and a subsequent light-driven water-gas shift reaction (Figure 1-10A).^{44,123} Careful analysis of product gas mixtures of primary linear alcohol ($C_nH_{2n+2}O$, $n = 2-4$) and polyol ($C_nH_{2n+2}O_n$, $n = 2-3$) photoreforming revealed that the amount of evolved H₂ does not necessarily correspond to the chain length of the alcohol.⁴⁴ Instead, the amount of evolved H₂ correlates to the number of α -hydrogen atoms. Accordingly, polyols ($C_nH_{2n+2}O_n$, $n = 2-3$), dehydrogenate under formation of two or three equivalents of CO, whereas linear alcohols ($C_nH_{2n+2}O$, $n = 2-4$) decompose to one equivalent of CO and the corresponding (n-1) alkane.⁴⁴ Light-driven water-gas shift reaction (Scheme 1-7 (3), (4)) liberates the decarbonylation sites from chemisorbed CO and rationalizes CO₂ formation.¹²⁴ Water-gas shift has been proven to occur efficiently over the respective photoreforming photocatalysts, i.e., Pd/TiO₂¹²⁵, and is regarded as the rate determining step. Removal of CO is considered to occur at the semiconductor metal interface.⁶³ Here, water or a surface oxygen atom of TiO₂ is oxidized to an oxygen species of unknown nature (Scheme 1-7 (3)), which reacts with CO, chemisorbed on the co-catalyst, to CO₂ (Scheme 1-7 (4)). After polaron de-excitation an oxygen vacancy is created which is healed by the decomposition of water generating one

equivalent of H_2 (Scheme 1-7 (5), (6)). Note, on Au/TiO_2 , the dehydrogenation intermediates of an alcohol are considered to form stable adsorbates, e.g., methoxy, formate,¹²⁶ and are directly oxidized to CO_2 by a light-driven reaction pathway.¹²⁴ Moreover other reports about the activity of Au/TiO_2 for the water-gas shift reaction question CO as a key intermediate.^{127,128}



Scheme 1-7. Proposed mechanism for photoreforming of primary linear alcohols ($\text{C}_n\text{H}_{2n+2}\text{O}$, $n = 2-4$) and polyols ($\text{C}_n\text{H}_{2n+2}\text{O}_n$, $n = 2-3$) via dissociative alcohol decarbonylation on Pd/TiO_2 .^{63,121,122}

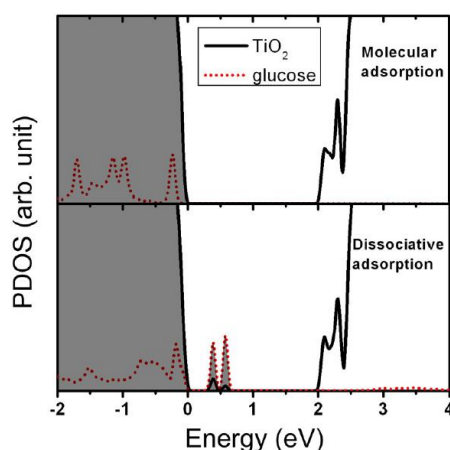


Figure 1-9. Projected density of states (PDOS) for molecularly (upper panel) and dissociatively (lower panel) adsorbed glucose. The density of states of the TiO_2 surface and that of the adsorbed glucose are shown by solid black and dashed red lines, respectively. Shaded areas indicate occupied states.¹²⁹ (Copyright © 2007, American Publish Society.)

Time-resolved spectroscopy studies evidence rapid scavenging of photogenerated trapped holes by alcohols, e.g., methanol, propan-2-ol, on pristine¹³⁰⁻¹³² or metal decorated¹³²⁻¹³⁴ TiO_2 . First principle calculations showed that dissociative adsorption of (poly)hydroxy compounds (e.g., ethylene glycol, glucose) yields intra band gap

states (Figure 1-9), which act as efficient hole traps (direct hole transfer).¹²⁹ The oxidation of alkoxy to formyl species, monitored by *in-situ* spectroscopy, confirmed direct hole transfer and the existence of intra band gap states.¹³⁴ In addition, indirect hole transfer mechanisms *via* $\cdot\text{OH}$ or $\cdot\text{OOH}$ -radicals can occur (*vide infra*).

B. Light driven aldehyde decarbonylation.

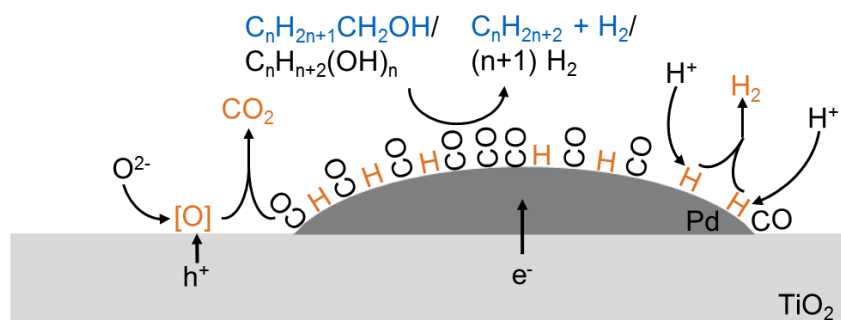
Glycerol is considered to adsorb on the semiconductor surface as described in chapter 1.5.3.3. Upon band gap irradiation the polyol is oxidized to glyceraldehyde by direct (h_{vb}^+) or indirect ($\cdot\text{OH}$ -radical) hole transfer (Figure 1-10B).⁴³ First principle calculations provided insight into the mechanism of glycerol oxidation by direct hole transfer.¹²⁹ The oxygenate chemisorbs on TiO_2 forming a surface ester. After hole capture a carbon centered radical is formed. The potential of its singly occupied carbon dangling-bond is more cathodic than the conduction band minimum of TiO_2 . Thus, the single electron is injected into the conduction band of TiO_2 and subsequently the ionic Ti–O-bond is weakened due to simultaneous carbonyl bond formation.¹²⁹

The intermediate glyceraldehyde decarbonylates to ethylene glycol after a second radical attack. CO_2 formation is considered to occur *via* photocatalytic driven water-gas shift reaction according to the formerly described mechanism (*vide supra*). Ethylene glycol undergoes transformations identical to that of the C3-polyol. Note that additional pathways like dehydration or hydrogenation might be operable but will not be discussed for simplicity.⁴³

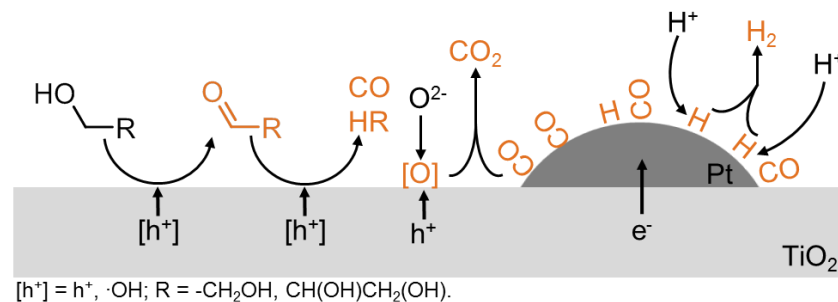
C. Decarboxylation of intermediate formed carboxylic acids.

Decarboxylation of carboxylic acids was suggested for the photoreforming of alcohols, e.g., glycerol, ethanol, over co-catalyst decorated semiconductors, e.g., Pt/TiO_2 , Pt/CdS , $\text{Au}/\epsilon\text{-Fe}_2\text{O}_3$.^{45,46,57,135,136} The co-catalyst serves only as H_2 evolution site, whereas the oxidation of the alcohol to CO_2 takes place on the semiconductor surface. Upon illumination, $\cdot\text{OH}$ -radicals are formed, which oxidize the alcohol *via* $2e^-$ steps to the carboxylic acid, which subsequently undergoes a light-driven decarboxylation (Figure 1-10C).^{46,137} Thus, ethanol is oxidized to acetic acid, which decarboxylates to CH_4 and CO_2 (so-called Photo-Kolbe reaction).^{46,137} In case of glycerol photoreforming, the intermediate glyceric acid decomposes to glycolalde-

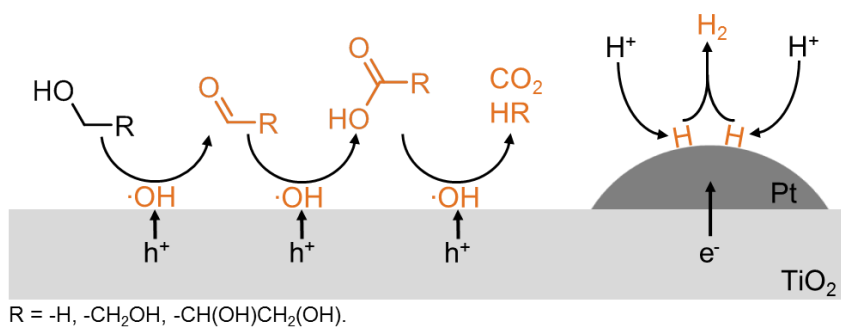
A. Co-catalyst assisted alcohol decarbonylation



B. Light driven aldehyde decarbonylation



C. Decarboxylation of carboxylic acids



D. Peroxo radical driven C-C-cleavage over rutile {110}

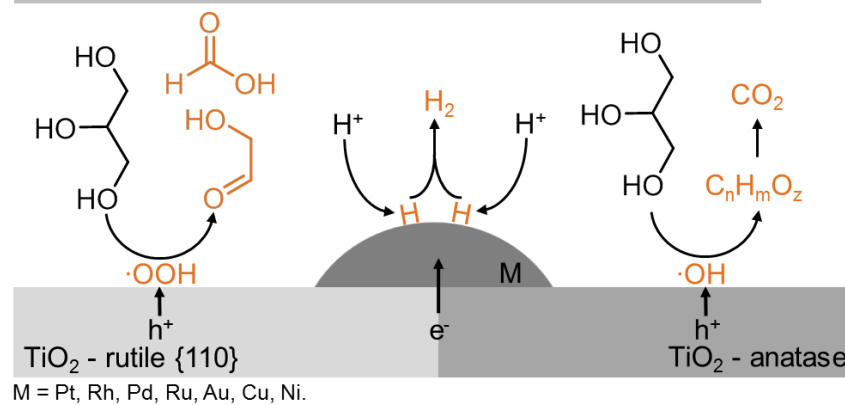


Figure 1-10. Graphical illustration of proposed reaction mechanism for alcohol ($C_nH_{2n+1}CH_2OH$) and polyol ($C_nH_{n+2}(OH)_n$) reforming. References: A⁶³, B⁴³, C^{45,46}, D¹³⁸.

hyde and CO₂.⁴⁵ The oxidation of the corresponding C2- and C1-intermediates (see chapter 1.5.4.2) pursues the described mechanism.⁴⁵ Specifically, ethylene glycol is oxidized *via* glycolaldehyde to glycolic acid prior decarboxylation, whereas methanol is converted to formic acid which dehydrogenates. Note that intermediate formed CH₃C[•]HOH-radical ($E^0(\text{CH}_3\text{COH}/\text{CH}_3\text{C}^{\bullet}\text{HOH}) = -1.3 \text{ V vs. NHE, pH} = 7$)¹³⁹ can be oxidized *via* the current doubling process as discussed in chapter 1.5.4.2 in detail.

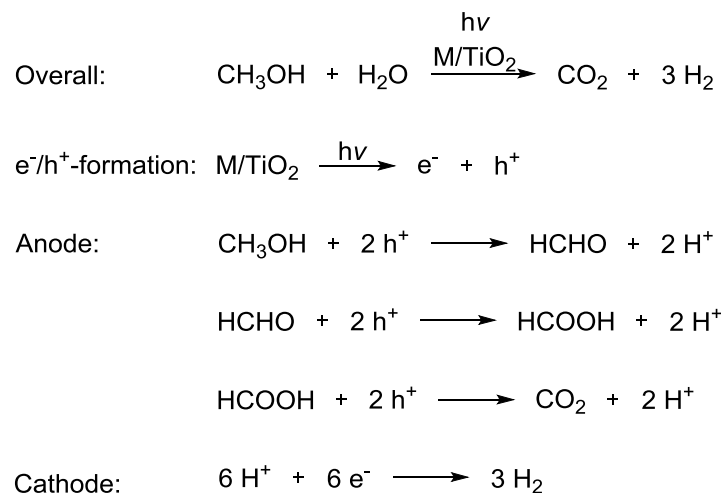
D. Peroxo-radical driven C–C-cleavage over rutile (110).

The surface structure of a TiO₂ polymorph determines the nature of reactive oxygen species.¹³⁸ Morphology of anatase, i.e., (001) and (101) facet, promotes ·OH-radical generation, whereas surface bound peroxo-radicals are formed on the rutile (110) facet due to efficient coupling of adjacent Ti–O[•]-radicals. The different oxidation potential of these two radicals influences the oxidative degradation pathway of an oxygenate like glycerol.¹³⁸ The large oxidative strength of an ·OH-radical (+2.18 V vs. NHE, pH = 7)¹³⁹ causes transformation of any functional group as explained in the latter two mechanisms. Here, oxidation of the primary hydroxy group *via* formyl to carboxy group and multiple C–C-cleavage pathways were suggested (*vide supra*). In contrast, ·OOH-radicals (+0.94 V vs. NHE, pH = 7)¹³⁹ cause selective C–C-cleavage of C2- / C3-oxygenates. Glycerol is converted to glycolaldehyde and formic acid, which further decomposes to CO₂ (Figure 1-10D).¹³⁸ In absence of glycerol, glycolaldehyde undergoes oxidative C–C-cleavage upon formation of formaldehyde and formic acid. Note that the nature of the co-catalyst does not influence the selectivity and solely serves as H₂ evolution site.¹³⁸

1.5.4.2. Methanol

Two different reaction networks have been suggested for the photoreforming of methanol. Over Pd/TiO₂, Pd-catalyzed decarbonylation of methanol was suggested to take place, whereas chemisorbed CO is removed by a photocatalytic water-gas shift reaction (for mechanistic details see Chapter 1.5.4.1).⁶³ The second pathway comprises only light-driven steps and methanol is oxidized in 2e⁻ steps *via* formaldehyde and formic acid to CO₂ as depicted in Scheme 1-8.⁶ The mechanism of this pathway was discussed to proceed *via* direct or indirect hole transfer, which requires chemisorbed or physisorbed methanol, respectively (Figure 1-9).¹⁴⁰ An ·OH-

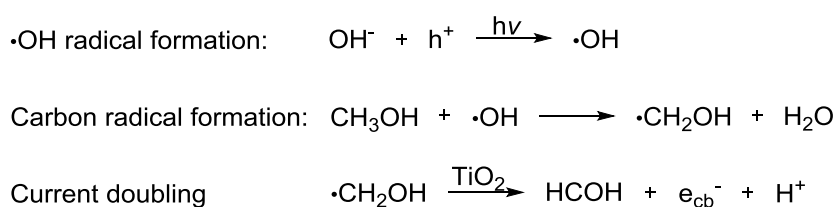
radical, i.e., indirect hole transfer, driven pathway is dominant in aqueous methanol solutions (< 0.2 M) due to the absence of chemisorbed methanol as outlined in chapter 1.5.3.2.⁹⁹



Scheme 1-8. Proposed anodic and cathodic half reactions for photoreforming of methanol on metal decorated TiO₂.¹⁴¹ Note: Current doubling mechanism is not considered in the particular anodic half reactions (*vide infra*).

High H₂ evolution rates for linear alcohols under alkaline conditions correlate with the ability of the alcohol to undergo an indirect hole transfer.⁶⁷ In contrast, the H₂ evolution rate of chemisorbing ethylene glycol in aqueous phase is independent of pH.⁶⁷ Note, that an indirect hole transfer can also be considered for formaldehyde due to its weak interaction strength with TiO₂ (chapter 1.5.3.4). ·OH-radicals abstract H-atoms of C–H-bonds, e.g., methanol, formaldehyde, with high selectivity, e.g., methanol (93%).¹⁴² The resulting hydroxymethyl-radical (·CH₂OH, E⁰(HCOH / ·CH₂OH) = -1.3 V vs. NHE, pH = 7)¹³⁹ has a strong reduction potential and is consequently more cathodic than the bottom of the conduction band of TiO₂ and other semiconductors.^{24,27} This is an immanent property of almost any carbon centered radical.^{139,143} Accordingly, the generated carbon centered radicals, i.e., ·CH₂OH, ·CH(OH)₂, act as a reducing intermediate injecting their unpaired electron into the conduction band of TiO₂ and being oxidized to formaldehyde and formic acid, respectively.²⁸ This process is called current doubling and occurs on various semiconductors.²⁷ The mechanism is exemplarily depicted for methanol in Scheme 1-9. Current doubling is not restricted to indirect hole transfer because it also has been observed for formic acid, which chemisorbs on TiO₂ (chapter 1.5.3.5).

It decomposes *via* a $\cdot\text{CO}_2^-$ radical anion ($E^0(\text{CO}_2 / \cdot\text{CO}_2^-) = -2.0 \text{ V vs. NHE, pH} = 7$)¹³⁹ by a direct hole transfer mechanism.²⁸ The co-catalyst acts exclusively as a H_2 evolution site. Accordingly proton reduction and oxidation of methanol to CO_2 proceed independent of each other at separate sites of the photocatalyst confirmed by missing HD and D_2 formation during photoreforming of aqueous CD_3OD .^{51,140} The deuterium atoms of CD_3OD are transferred into the aqueous phase by H-atom abstraction due to indirect hole transfer ($\cdot\text{OH}$ -radical) or by proton release due to the current doubling process. Therefore, the anodic half reaction is considered to proceed on the semiconductor surface. The same mechanism is considered to occur for methanol photoreforming over platinized CdS .¹⁴⁴

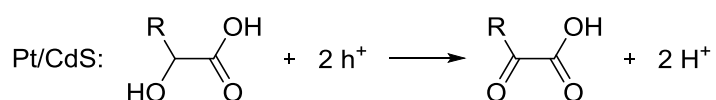
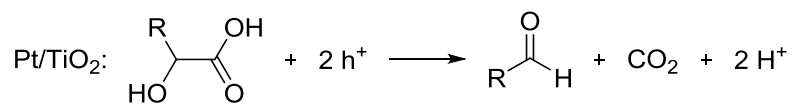


Scheme 1-9. Mechanism of anodic oxidation of methanol to formaldehyde assumed to proceed *via* indirect hole transfer and current doubling process over co-catalyst decorated TiO_2 (M/TiO_2).¹⁴³

1.5.4.3. Anaerobic Oxidation of α -Hydroxycarboxylic Acids on TiO_2 and CdS

During the anaerobic oxidation of α -hydroxycarboxylic acids, e.g., glycolic acid, lactic acid, over Pt decorated TiO_2 and CdS ,²⁷ H_2 / CO_2 mixtures or just H_2 evolve, respectively. Further, liquid phase analysis revealed that the latter material selectively transforms the hydroxy group of the α -hydroxycarboxylic acids to a carbonyl group, whereas TiO_2 promotes the selective oxidative C–C-cleavage to CO_2 and the corresponding aldehyde, which is further oxidized (chapter 1.5.4.1., pathway C). Further transformations were not observed over Pt/CdS corroborating the incapability of CdS to convert (α -oxo-functionalized) carboxylic acids *via* oxidative C–C-cleavage. The difference in selectivity is not caused by the less anodic valence band position of CdS (1.33 V vs. NHE, $\text{pH} = 7$) compared to TiO_2 because the oxidative C–C-cleavage is catalyzed over a glassy C carbon electrode at a potential of 1.13 V vs. NHE, $\text{pH} = 7$. Instead, it is the mode of adsorption (chapter 1.5.3.5) what directs the reaction pathway. Oxidative C–C-cleavage of

(α -hydroxy)carboxylic acids requires (chelating) chemisorption (TiO_2) and is prevented in case of electrostatic interaction (CdS).²⁷



R = -H, -CH₃, -CH(CH₃)₂

Scheme 1-10. Oxidation of α -hydroxycarboxylic acids (first $2e^-$ transfer) causes decarboxylation and aldehyde formation over Pt/TiO_2 and generation of the corresponding α -ketocarboxylic acids over Pt/CdS .²⁷ Note, the reaction equations do not reflect the current doubling mechanism.

1.6. HER Co-Catalysts for the Overall Water Splitting Reaction

1.6.1. Physicochemical Requirements

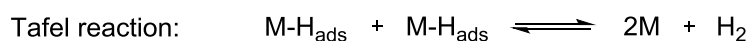
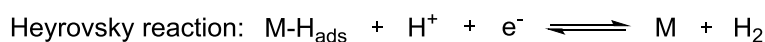
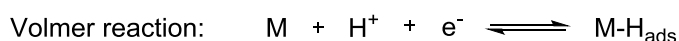
In 1976, platinum decorated TiO₂ was demonstrated to split water into H₂ and O₂ under band gap illumination by Bulatov *et al.*¹⁴⁵ and four years later by Sato *et al.*¹⁴⁶ However, reaction products were not observed over illuminated pristine TiO₂. The necessity of the platinum co-catalyst was explained by its ability to catalyze the HER and an improved electron-hole separation due to the formation of a Schottky barrier at the Pt-TiO₂ interface.¹⁴⁶⁻¹⁴⁸

The properties of a co-catalyst for the HER should be optimized according to the following points:⁷¹

- (1) Minimized Schottky barrier or enabled ohmic contact between the semiconductor and the co-catalyst
- (2) Reduced activation energy for the HER
- (3) Lack of active sites for the back reaction, i.e., H₂ and O₂ to water

Whereas points (1) and (2) are relevant for the photoreforming reaction, all points have to be considered for the overall water splitting reaction. As this thesis does not offer any contribution to item (1) it is not further covered in this chapter.

HER is initiated by a proton reduction step (Volmer reaction) and continues with subsequent H₂ desorption, which can proceed according to the Heyrovsky or Tafel mechanism as depicted in Scheme 1-11.⁷¹



Scheme 1-11. Possible mechanisms of HER, which is introduced by the Volmer reaction, whereas the H₂ desorption can occur *via* an electrochemical (Heyrovsky reaction) or catalytic (Tafel reaction) desorption.⁷¹

The Sabatier principle states that a reaction is efficiently catalyzed, if intermediate binding energies between the reactant and the catalytic surface are present. Accordingly, maximum rates for the (electrochemical) HER are obtained, if the free energy of H₂ adsorption (ΔG_{H}) is close to 0.^{125,126} In case of positive ΔG_{H} values, metal-hydrogen bond strength is too weak and the proton reduction is kinetically

hindered, whereas at negative ΔG_H values the reaction sites are blocked due to decelerated release of strongly binding hydrides.^{125,126} Comparison of numerous metals revealed that precious metals, e.g., Pd, Pt or Rh, or alloys of them are most suitable candidates for the electrochemical HER.^{149,150} As semiconductors (exceptions¹⁵¹⁻¹⁵⁴ are neglected) do not show catalytic activity for the HER, transition metal elements or their equivalently performing oxides are commonly applied as HER co-catalysts.¹⁵⁵ Note that activity trends of electrochemical and photocatalytic HER for different metals coincide and confirm the transferability of the described relationships from electrochemical catalysts to photocatalytic systems.¹⁷

HER active co-catalysts, e.g., Rh, Pt, Pd, Ir or Cu, loaded on a semiconductor, which is able to oxidize water, e.g., GaN:ZnO, shows negligible activity for the overall water splitting reaction.¹⁵⁶ Thus, the thermodynamically preferred back reaction is catalyzed over HER active co-catalysts¹⁵⁷ with almost identical activity trends as exemplarily depicted in Figure 1-11. The back reaction can occur *via* thermal and photocatalytic routes. Photoreduction of O_2 is well known from aerobic photocatalysis studies (Scheme 1-12). Neglecting some exceptions,^{146,158-163} co-catalyst modification is mandatory in order to diminish the back reaction by introducing kinetic control.

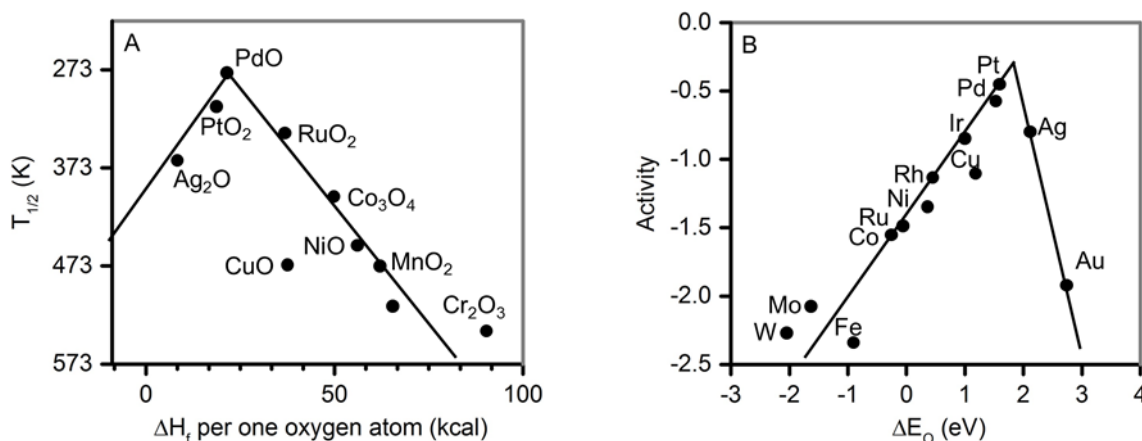
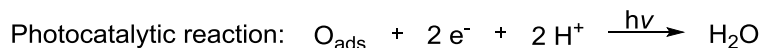
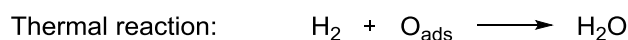
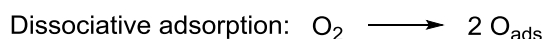


Figure 1-11. (A) Catalytic activity of metal oxides for H_2 oxidation as a function of their heat of formation per one O_2 atom. $T_{1/2}$ is the temperature for 50% conversion of H_2 obtained by fixed bed flow reaction in a stream of 1 vol.% H_2 in air under a space velocity of $2 \cdot 10^4 \text{ h}^{-1} \text{ g}_{\text{cat}}$. (B) Volcano plot of O_2 reduction reaction plotted as a function of the O_2 binding energy. The activity of non-activated electron/proton transfer is defined as zero. (Reprinted/Adapted with permission from references (A)¹⁶⁴ and (B)¹⁶⁵. Copyright © 2003 John Wiley and Sons and 2004 American Chemical Society.)



Scheme 1-12. Proposed thermal and light-driven pathways for the back reaction over co-catalyst decorated semiconductors.

1.6.2. First HER Co-Catalysts for Overall Water Splitting

Ni based materials were the first successful examples of stable and active overall water splitting co-catalysts.¹⁵⁸ In contrast to Pt, the reverse reaction is kinetically decelerated on NiO (Figure 1-11).^{146,158} Different proposals have been given for the detailed mode of action. Domen *et al.* suggested occurrence of Ni@NiO core-shell particles formed by a subsequent hydrogenation oxidation heat treatment.¹⁶⁶ The nickel core enables facilitated electron transfer from the semiconductor to the hydrated NiO shell, where the HER takes place.¹⁶⁶ In another study, parallel existence of Ni and NiO particles were suggested catalyzing H₂ and O₂ evolution, respectively.¹⁶⁷ Later, Hisatomi *et al.* stated that both models are likely and the state of Ni particles depend on the synthesis conditions as well as on the properties of the semiconductor.⁷¹

In addition, RuO₂ was identified to promote the overall water splitting reaction,³⁷ whereas detailed investigations revealed that it can catalyze H₂ and O₂ evolution.¹⁶⁸⁻¹⁷⁰ Optimal activities for overall water splitting were obtained if an appropriate loading of RuO₂ co-catalyst is crystallized to nanoparticles with the size of 30 nm.¹⁷¹ RuO₂ acts as a H₂ evolution catalyst, if it is deposited on a n-doped semiconductor, like CdS or TiO₂.¹⁶⁸

1.6.3. WC – HER Electrocatalyst as Co-Catalyst for Water Splitting

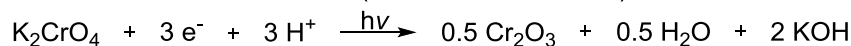
Numerous new electrocatalysts, e.g., sulfides or carbides, are active for the HER reaction.^{172,173} These HER electrocatalysts can be applied as co-catalysts for the overall water splitting, if they do not possess concurrent activity for the O₂ reduction reaction. Indeed, nanoparticulate WC decorated on Na-doped SrTiO₃ was shown to be active for the overall water splitting reaction.¹⁷⁴ Electrochemical studies revealed

large overpotentials for the O₂ reduction reaction, whereas the HER reaction was well catalyzed on the same material.¹⁷⁴

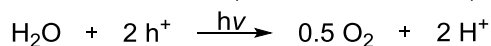
1.6.4. Core–Shell-Type Co-catalysts

Deposition of an oxidic layer onto HER co-catalysts decorating GaN:ZnO imparted stable overall water splitting activities to these systems.¹⁵⁶ Here, redox inactive chromium oxides¹⁷⁵ and lanthanide oxides, e.g., La, Sm, Dy,¹⁷⁶ have been successfully tested, whereas the transition metal based shell performed best. Thus, the back reaction was effectively suppressed as further confirmed by missing reactivity of H₂/O₂ mixtures over these core-shell co-catalysts.¹⁵⁰ Note that, nanoparticulate Cr₂O₃ itself is not active for proton reduction but might serve as a water oxidation co-catalyst on some semiconductors.¹⁷⁷⁻¹⁷⁹ Potential dependent subtractively normalized interfacial FTIR spectra and voltammogram studies revealed that the HER occurs at the core-shell interface.¹⁸⁰ Thus, the Cr₂O₃ shell serves as a molecular sieve, which allows selective permeation of protons to the HER active core, e.g., Rh, and efficient release of H₂ as depicted in Figure 1-12. The required diffusion properties cannot be explained by the corundum structure of Cr₂O₃, in lieu a hydration to a microporous chromium oxyhydroxide (CrO_(1.5-m)(OH)_{2m}·xH₂O) is considered. The confinement of this structure prevents diffusion of O₂, which has a larger kinetic diameter compared to H₂, to the HER active core.¹⁸⁰ Cr₂O₃ shells may be synthesized by a method related to electroplating as depicted in Scheme 1-13, which requires toxic, water-soluble Cr(VI)-precursors, e.g., K₂CrO₄. The thickness of the Cr₂O₃ layer is restricted to a few nanometers because missing electron tunneling through the formed Cr₂O₃ shell prohibits further Cr(VI)-reduction.^{177,180} This photodeposition method is compatible to numerous HER active cores, e.g., Rh, Pt, Ni or Cu, independent of the synthesis method and the oxidation state of the core component.^{178,181,182} Cu-Cr or Rh-Cr mixed oxide nanoparticles were synthesized *via* co-impregnation^{183,184} or co-photodeposition^{178,185}. In case of the Rh-Cr system, a solid solution (Rh_{2-y}Cr_yO₃)¹⁸⁶ is obtained which does not display any reactivity for the back reaction and demonstrates similar performance like the analogue core–shell systems.¹⁸⁷ It is worth to note that less harmful Cr(III)-precursors are used for the co-impregnation method.¹⁸⁷

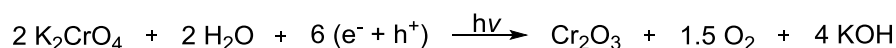
(A) Photoreduction of Cr^{VI} to Cr^{III} (cathodic half reaction):



(B) Oxidation of water (anodic half reaction):



(C) Overall reaction:



Scheme 1-13. Half reactions during photodeposition of K₂CrO₄ resulting in the formation of M@Cr₂O₃ core-shell co-catalysts.¹⁸⁸

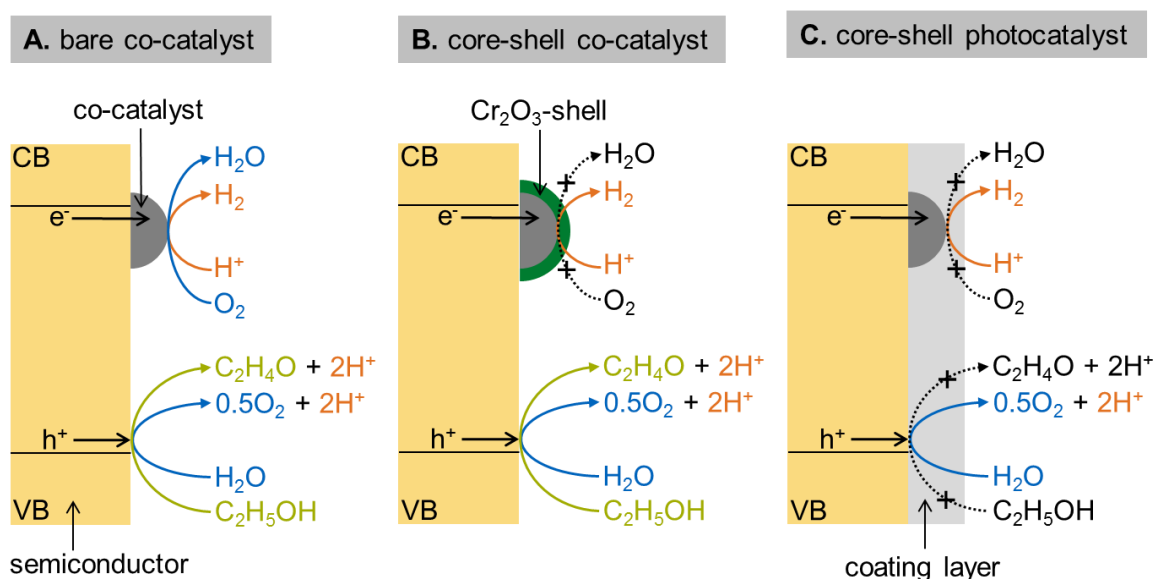


Figure 1-12. Schematic of occurring surface reactions on a photocatalyst decorated (A) with a bare co-catalyst, (B) with a core-shell-structured co-catalyst, respectively or (C) on a core-shell-structured photocatalyst and function of shells. (Adapted with permission from references¹⁸⁰ and¹⁸⁸. Copyright © 2009, 2015 American Chemical Society.)

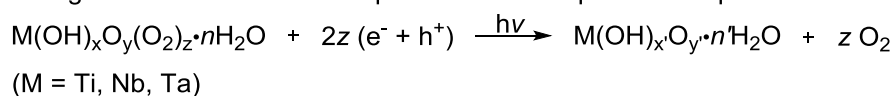
1.6.5. Core-Shell-Type Photocatalyst

This sub-chapter exclusively summarizes a publication from Takata *et al.*¹⁸⁸, if it is not otherwise declared.

The entire semiconductor, decorated with a co-catalyst, is coated with a shell preventing the reverse reaction by acting as a selective molecular sieve. The shell consists of an amorphous, few nanometer thick oxyhydroxide of a group IV and V transition metal (i.e., Ti, Nb, Ta) formed *via* photodeposition from the corresponding water-soluble peroxy complexes¹⁸⁹ (Scheme 1-14 A). A shell covering the entire photocatalyst is presumably formed because the standard electrode potential for the

reduction and oxidation of hydrogen peroxide (1.36, 0.27 V vs. NHE, pH = 7)¹⁹⁰ is more anodic or cathodic than the standard electrode potential for the reduction and oxidation of water (-0.41 eV, 0.82 eV vs. NHE, pH = 7), respectively (Scheme 1-14B-D). Accordingly, decomposition of the peroxo complex is considered to occur on the semiconductor surface and on the co-catalyst. Decomposition *via* direct photoexcitation of the peroxo complexes was shown to play a minor role. Among the three investigated metals, i.e., Ti, Nb and Ta, the TiO₂-photodeposited samples were the most active one for the overall water splitting reaction.

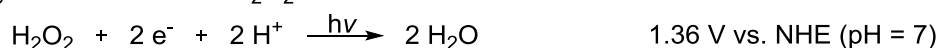
(A) Charge carrier assisted decomposition of metal peroxo complexes:



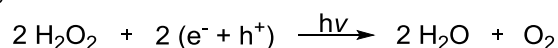
(B) Photooxidation of H₂O₂:



(C) Photoreduction of H₂O₂:



(D) Overall reaction:



Scheme 1-14. Photodeposition of group IV and V transition metal oxyhydroxides from their peroxo precursors *via* their oxidative and reductive decomposition by photogenerated charge carriers.¹⁸⁸

Note that other deposition methods, e.g., impregnation, are possible, however the obtained photocatalysts showed lower performance and / or stability compared to the photodeposition method. The resulting core-shell-structured photocatalyst enabled stable overall water splitting, but was inactive for the (ethanol) photoreforming and reverse reaction, i.e., water formation. Accordingly, the shell allows selective penetration of water and release of the products H₂ and O₂, whereas O₂ cannot reach the cathode, i.e., co-catalyst, as depicted in Figure 1-12C. Diffusion of ethanol is likely disrupted by the hydrophilic character of the shell, while direction of O₂ diffusion is directed by partial pressure differences. Due to restricted space at the semiconductor-shell interface, water oxidation results in locally, strongly enhanced O₂ partial pressures, which entails its directed diffusion into the aqueous phase with low O₂ partial pressures. It is worth to note that an additional effect of a photocatalyst

coating layer can be a prevented photooxidation of the semiconductor, e.g., $\text{LaMg}_{1/3}\text{Ta}_{2/3}\text{O}_2\text{N}$.²⁰

Summarizing, both types of shell, i.e., core–shell co-catalyst and core–shell-structured photocatalyst, enable overall water splitting by serving as a molecular sieve preventing the diffusion of O_2 to the cathodic acting co-catalyst. Thus, molecular sieve like layers represent a tool of kinetic control, which defeats a thermodynamic limitation.

1.7. Scope of the Thesis

Anaerobic heterogeneous photocatalysis represents a sustainable pathway to generate H_2 . Therefore, the photoreforming of alcohols ($C_nH_{2n+2}O_n$) and the overall water splitting have been extensively investigated. Both reactions occur in principle on the same co-catalyst decorated semiconductors and require defined surface speciation and coverage for selective photocatalytic and thermal reactions in order to display efficient and sustainable H_2 production:

The anodic oxidation of a polyol ($C_nH_{2n+2}O_n$) to CO_2 requires $(4n+2)$ h^+ -transfers to adsorbates of reactants and intermediates. The nature of the adsorbate complexes determine the hole transfer mechanism, which influences kinetics and reaction network.

Efficient overall water splitting demands prevented adsorption of O_2 on the HER-active co-catalyst because activated O_2 initiates the thermodynamically preferred reverse reaction.

These two items have been rarely investigated because most studies have focused on band gap, low defect site density and interface engineering in order to obtain photocatalysts with high STH efficiencies.

The first part of this thesis addresses the elucidation of the anodic reaction mechanism of ethylene glycol photoreforming over Rh/TiO₂. Quantitative liquid and gas phase analysis is applied in order to elucidate the reaction network. Kinetic modeling, using a set of Langmuir adsorption based rate equations, reveals the impact of adsorption strength of reactant and intermediates on the photoreforming kinetics. Using the deduced reaction network and the gained insights from kinetic modeling, conclusions on the mechanisms of hole transfer are drawn. Comparison of Rh/TiO₂ with Rh/GaN:ZnO emphasizes the impact of band gap position and an additional water splitting activity on the overall reaction mechanism of ethylene glycol photoreforming.

The second part of this thesis demonstrates that an adsorbate, i.e., CO, on a precious metal based co-catalyst hinders the activation of O_2 for the back reaction while preserving the H_2 evolution reaction with comparable performance to the known core-shell systems. CO oxidation occurs in parallel to O_2 evolution reaction. The CO pressure range, which guarantees selective blocking of the back reaction

sites without affecting the H₂ evolution reaction, is determined. The stability of the CO shell is examined by co-dosing H₂ and O₂. Isotope experiments and varied photon flux disclose the reaction mechanism of competing H₂ evolution reaction, O₂ evolution reaction, back reaction and CO oxidation. Finally, alternatives to diminish undesired side reactions, i.e., back reaction and CO oxidation, are presented.

1.8. References

- (1) Ohtani, B. *Phys. Chem. Chem. Phys.* **2014**, *16*, 1788-1797.
- (2) Takanahe, K.; Domen, K. *ChemCatChem* **2012**, *4*, 1485-1497.
- (3) Zhang, Y.; Mori, T.; Ye, J. *Sci. Adv. Mater.* **2012**, *4*, 282-291.
- (4) Martin, D. J.; Reardon, P. J. T.; Moniz, S. J. A.; Tang, J. *J. Am. Chem. Soc.* **2014**, *136*, 12568-12571.
- (5) Ohtani, B. *J. Photochem. Photobiol., C* **2010**, *11*, 157-178.
- (6) Kawai, T.; Sakata, T. *J. Chem. Soc. Chem. Comm.* **1980**, 694-695.
- (7) Yang, J. H.; Wang, D. G.; Han, H. X.; Li, C. *Acc. Chem. Res.* **2013**, *46*, 1900-1909.
- (8) Kisch, H. *Angew. Chem., Int. Ed.* **2013**, *52*, 812-847.
- (9) Shimura, K.; Yoshida, H. *Energy Environ. Sci.* **2011**, *4*, 2467-2481.
- (10) Pant, K. K.; Gupta, R. B. In *Hydrogen Fuel: Production, Transport, and Storage*; Gupta, R. B., Ed.; CRC Press: New York, 2009, p 4-29.
- (11) Ball, M.; Wietschel, M. *Int. J. Hydrogen Energy* **2009**, *34*, 615-627.
- (12) Ball, M.; Weeda, M. *Int. J. Hydrogen Energy* **2015**, *40*, 7903-7919.
- (13) Armaroli, N.; Balzani, V. *ChemSusChem* **2011**, *4*, 21-36.
- (14) Navarro, R. M.; Sanchez-Sanchez, M. C.; Alvarez-Galvan, M. C.; del Valle, F.; Fierro, J. L. G. *Energy Environ. Sci.* **2009**, *2*, 35-54.
- (15) Pinaud, B. A.; Benck, J. D.; Seitz, L. C.; Forman, A. J.; Chen, Z. B.; Deutsch, T. G.; James, B. D.; Baum, K. N.; Baum, G. N.; Ardo, S.; Wang, H. L.; Miller, E.; Jaramillo, T. F. *Energy Environ. Sci.* **2013**, *6*, 1983-2002.
- (16) Maeda, K. *ACS Catal.* **2013**, *3*, 1486-1503.
- (17) Takanahe, K.; Domen, K. *Green* **2011**, *1*, 313-322.
- (18) Maeda, K.; Domen, K. *J. Phys. Chem. Lett.* **2010**, *1*, 2655-2661.
- (19) Wang, Q.; Hisatomi, T.; Jia, Q.; Tokudome, H.; Zhong, M.; Wang, C.; Pan, Z.; Takata, T.; Nakabayashi, M.; Shibata, N.; Li, Y.; Sharp, I. D.; Kudo, A.; Yamada, T.; Domen, K. *Nat. Mater.* **2016**, *15*, 611-615.
- (20) Pan, C.; Takata, T.; Nakabayashi, M.; Matsumoto, T.; Shibata, N.; Ikuhara, Y.; Domen, K. *Angew. Chem., Int. Ed.* **2015**, *54*, 2955-2959.
- (21) Kim, W.-G.; Yang, J.; Han, S.; Cho, C.; Lee, C.-H.; Lee, H. *Korean J. Chem. Eng.* **1995**, *12*, 503-511.
- (22) Ismail, A. F.; Khulbe, K. C.; Matsuura, T. *Gas Separation Membranes: Polymeric and Inorganic*; Springer: Cham a.o., 2015.
- (23) Krishnamurthy, R.; Malik, V. A.; Stokley, A. G.; BOC GROUP INC, 1990; US 4963339 A.
- (24) Marschall, R. *Adv. Funct. Mater.* **2014**, *24*, 2421-2440.
- (25) Indrakanti, V. P.; Kubicki, J. D.; Schobert, H. H. *Energy Environ. Sci.* **2009**, *2*, 745-758.
- (26) Al-Azri, Z. H. N.; Chen, W.-T.; Chan, A.; Jovic, V.; Ina, T.; Idriss, H.; Waterhouse, G. I. N. *J. Catal.* **2015**, *329*, 355-367.
- (27) Harada, H.; Ueda, T.; Sakata, T. *J. Phys. Chem.* **1989**, *93*, 1542-1548.
- (28) Hykaway, N.; Sears, W. M.; Morisaki, H.; Morrison, S. R. *J. Phys. Chem.* **1986**, *90*, 6663-6667.
- (29) Kudo, A.; Miseki, Y. *Chem. Soc. Rev.* **2009**, *38*, 253-278.
- (30) Maeda, K. *Chem. Commun.* **2013**, *49*, 8404-8406.

-
- (31) Ham, Y.; Hisatomi, T.; Goto, Y.; Moriya, Y.; Sakata, T.; Yamakata, A.; Kubota, J.; Domen, K. *J. Mater. Chem. A* **2016**, 3027-3033.
- (32) Liu, P.; Nisar, J.; Pathak, B.; Ahuja, R. *Int. J. Hydrogen Energy* **2012**, 37, 11611-11617.
- (33) Bolts, J. M.; Wrighton, M. S. *J. Phys. Chem.* **1976**, 80, 2641-2645.
- (34) Ohno, T.; Sarukawa, K.; Tokieda, K.; Matsumura, M. *J. Catal.* **2001**, 203, 82-86.
- (35) Komaguchi, K.; Nakano, H.; Araki, A.; Harima, Y. *Chem. Phys. Lett.* **2006**, 428, 338-342.
- (36) Nosaka, Y.; Nosaka, A. Y. *J. Phys. Chem. Lett.* **2016**, 7, 431-434.
- (37) Maeda, K.; Takata, T.; Hara, M.; Saito, N.; Inoue, Y.; Kobayashi, H.; Domen, K. *J. Am. Chem. Soc.* **2005**, 127, 8286-8287.
- (38) Maeda, K.; Teramura, K.; Domen, K. *J. Catal.* **2008**, 254, 198-204.
- (39) Ohno, T.; Bai, L.; Hisatomi, T.; Maeda, K.; Domen, K. *J. Am. Chem. Soc.* **2012**, 134, 8254-8259.
- (40) Yoshida, M.; Hirai, T.; Maeda, K.; Saito, N.; Kubota, J.; Kobayashi, H.; Inoue, Y.; Domen, K. *J. Phys. Chem. C* **2010**, 114, 15510-15515.
- (41) McDermott, E. J.; Kurmaev, E. Z.; Boyko, T. D.; Finkelstein, L. D.; Green, R. J.; Maeda, K.; Domen, K.; Moewes, A. *J. Phys. Chem. C* **2012**, 116, 7694-7700.
- (42) Hashiguchi, H.; Maeda, K.; Abe, R.; Ishikawa, A.; Kubota, J.; Domen, K. *Bull. Chem. Soc. Jpn.* **2009**, 82, 401-407.
- (43) Panagiotopoulou, P.; Karamerou, E. E.; Kondarides, D. I. *Catal. Today* **2013**, 209, 91-98.
- (44) Bahruji, H.; Bowker, M.; Davies, P. R.; Pedrono, F. *Appl. Catal., B* **2011**, 107, 205-209.
- (45) Lalitha, K.; Sadanandam, G.; Kumari, V. D.; Subrahmanyam, M.; Sreedhar, B.; Hebalkar, N. Y. *J. Phys. Chem. C* **2010**, 114, 22181-22189.
- (46) Sakata, T.; Kawai, T. *Chem. Phys. Lett.* **1981**, 80, 341-344.
- (47) Cargnello, M.; Gasparotto, A.; Gombac, V.; Montini, T.; Barreca, D.; Fornasiero, P. *Eur. J. Inorg. Chem.* **2011**, 4309-4323.
- (48) Chiarello, G. L.; Forni, L.; Selli, E. *Catal. Today* **2009**, 144, 69-74.
- (49) Chiarello, G. L.; Aguirre, M. H.; Selli, E. *J. Catal.* **2010**, 273, 182-190.
- (50) Chiarello, G. L.; Ferri, D.; Selli, E. *J. Catal.* **2011**, 280, 168-177.
- (51) Kandiel, T. A.; Ivanova, I.; Bahnemann, D. W. *Energy Environ. Sci.* **2014**, 7, 1420-1425.
- (52) Nomikos, G. N.; Panagiotopoulou, P.; Kondarides, D. I.; Verykios, X. E. *Appl. Catal., B* **2014**, 146, 249-257.
- (53) Yang, Y. Z.; Chang, C. H.; Idriss, H. *Appl. Catal., B* **2006**, 67, 217-222.
- (54) Gallo, A.; Montini, T.; Marelli, M.; Minguzzi, A.; Gombac, V.; Psaro, R.; Fornasiero, P.; Dal Santo, V. *ChemSusChem* **2012**, 5, 1800-1811.
- (55) Gallo, A.; Marelli, M.; Psaro, R.; Gombac, V.; Montini, T.; Fornasiero, P.; Pievo, R.; Dal Santo, V. *Green Chem.* **2012**, 14, 330-333.
- (56) Simon, Q.; Barreca, D.; Gasparotto, A.; Maccato, C.; Montini, T.; Gombac, V.; Fornasiero, P.; Lebedev, O. I.; Turner, S.; Van Tendeloo, G. *J. Mater. Chem.* **2012**, 22, 11739-11747.
- (57) Carraro, G.; Gasparotto, A.; Maccato, C.; Gombac, V.; Rossi, F.; Montini, T.; Peeters, D.; Bontempi, E.; Sada, C.; Barreca, D.; Fornasiero, P. *RSC Adv.* **2014**, 4, 32174-32179.

- (58) Kondarides, D. I.; Daskalaki, V. M.; Patsoura, A.; Verykios, X. E. *Catal. Lett.* **2008**, *122*, 26-32.
- (59) Daskalaki, V. M.; Kondarides, D. I. *Catal. Today* **2009**, *144*, 75-80.
- (60) Patsoura, A.; Kondarides, D. I.; Verykios, X. E. *Catal. Today* **2007**, *124*, 94-102.
- (61) Fu, X. L.; Long, J. L.; Wang, X. X.; Leung, D. Y. C.; Ding, Z. X.; Wu, L.; Zhang, Z. Z.; Li, Z. H.; Fu, X. Z. *Int. J. Hydrogen Energy* **2008**, *33*, 6484-6491.
- (62) Li, Y. X.; Wang, J. X.; Peng, S. Q.; Lu, G. X.; Li, S. B. *Int. J. Hydrogen Energy* **2010**, *35*, 7116-7126.
- (63) Dickinson, A.; James, D.; Perkins, N.; Cassidy, T.; Bowker, M. *J. Mol. Catal. A: Chem.* **1999**, *146*, 211-221.
- (64) Peng, S. Q.; Peng, Y. J.; Li, Y. X.; Lu, G. X.; Li, S. B. *Res. Chem. Intermed.* **2009**, *35*, 739-749.
- (65) Peng, S. Q.; Ding, M.; Yi, T.; Zhan, Z. K.; Li, Y. X. *Environ. Prog. Sustainable Energy* **2016**, *35*, 141-148.
- (66) Zheng, X. J.; Wei, L. F.; Zhang, Z. H.; Jiang, Q. J.; Wei, Y. J.; Xie, B.; Wei, M. B. *Int. J. Hydrogen Energy* **2009**, *34*, 9033-9041.
- (67) Nishimoto, S. I.; Ohtani, B.; Kagiya, T. *J. Chem. Soc. Farad. T 1* **1985**, *81*, 2467-2474.
- (68) Li, Y. X.; Lu, G. X.; Li, S. B. *Appl. Catal., A* **2001**, *214*, 179-185.
- (69) Foo, K. Y.; Hameed, B. H. *Chem. Eng. J.* **2010**, *156*, 2-10.
- (70) Mills, A.; O'Rourke, C.; Moore, K. *J. Photochem. Photobiol., A* **2015**, *310*, 66-105.
- (71) Hisatomi, T.; Takanebe, K.; Domen, K. *Catal. Lett.* **2015**, *145*, 95-108.
- (72) Turchi, C. S.; Ollis, D. F. *J. Catal.* **1990**, *122*, 178-192.
- (73) Staples, C. A.; Williams, J. B.; Craig, G. R.; Roberts, K. M. *Chemosphere* **2001**, *43*, 377-383.
- (74) Tišler, T.; Zagorc-Končan, J. *Water, Air, Soil Pollut.* **1997**, *97*, 315-322.
- (75) Stewart, R. In *The Proton: Applications to Organic Chemistry*; Wassermann, H. H., Ed.; Academic Press: New York, 1986; Vol. 46 of Organic Chemistry, A Series of Monographs, p 9-86.
- (76) McEwen, W. K. *J. Am. Chem. Soc.* **1936**, *58*, 1124-1129.
- (77) Buschmann, H.-J.; Földner, H.-H.; Knoche, W. *Ber. Bunsen-Ges. Phys. Chem.* **1980**, *84*, 41-44 and cited references therein.
- (78) Le Botlan, D. J.; Mechin, B. G.; Martin, G. J. *Anal. Chem.* **1983**, *55*, 587-591.
- (79) Avzianova, E.; Brooks, S. D. *Spectrochim. Acta, Part A* **2013**, *101*, 40-48.
- (80) Scheithauer, A.; von Harbou, E.; Hasse, H.; Grützner, T.; Rijksen, C.; Zollinger, D.; Thiel, W. R. *AIChE J.* **2015**, *61*, 177-187.
- (81) Silva, C. O.; da Silva, E. C.; Nascimento, M. A. C. *J. Phys. Chem. A* **2000**, *104*, 2402-2409.
- (82) Betterton, E. A.; Hoffmann, M. R. *Environ. Sci. Technol.* **1988**, *22*, 1415-1418 and cited reference therein.
- (83) Olson, T. M.; Hoffmann, M. R. *J. Phys. Chem.* **1988**, *92*, 4246-4253 and cited references therein.
- (84) Ballinger, P.; Long, F. A. *J. Am. Chem. Soc.* **1960**, *82*, 795-798.
- (85) Kuo, M. H.; Moussa, S. G.; McNeill, V. F. *J. Phys. Chem. C* **2014**, *118*, 29108-29116.
- (86) Okada, T. *Anal. Chem.* **1988**, *60*, 1666-1669.

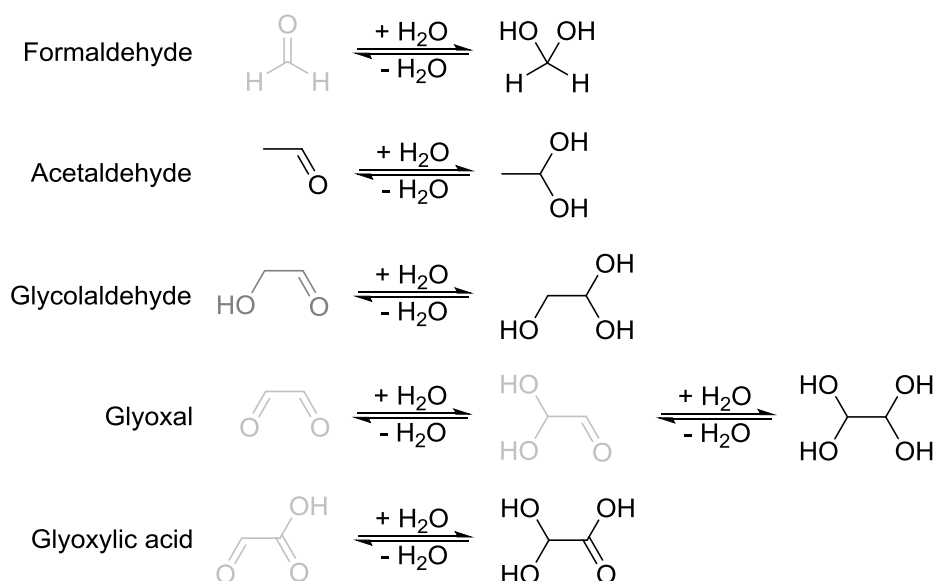
-
- (87) Goldberg, R. N.; Kishore, N.; Lennen, R. M. *J. Phys. Chem. Ref. Data* **2002**, *31*, 231-370.
- (88) Nosaka, A. Y.; Kojima, E.; Fujiwara, T.; Yagi, H.; Akutsu, H.; Nosaka, Y. *J. Phys. Chem. B* **2003**, *107*, 12042-12044.
- (89) Wang, C.-y.; Groenzin, H.; Shultz, M. J. *J. Phys. Chem. B* **2004**, *108*, 265-272.
- (90) Wang, C.-y.; Groenzin, H.; Shultz, M. J. *J. Am. Chem. Soc.* **2005**, *127*, 9736-9744.
- (91) Sun, R.-D.; Nakajima, A.; Fujishima, A.; Watanabe, T.; Hashimoto, K. *J. Phys. Chem. B* **2001**, *105*, 1984-1990.
- (92) Nakamura, R.; Ueda, K.; Sato, S. *Langmuir* **2001**, *17*, 2298-2300.
- (93) Wang, R.; Sakai, N.; Fujishima, A.; Watanabe, T.; Hashimoto, K. *J. Phys. Chem. B* **1999**, *103*, 2188-2194.
- (94) Zhang, L.; Dillert, R.; Bahnemann, D.; Vormoor, M. *Energy Environ. Sci.* **2012**, *5*, 7491-7507.
- (95) Miyauchi, M.; Nakajima, A.; Watanabe, T.; Hashimoto, K. *Chem. Mater.* **2002**, *14*, 2812-2816.
- (96) Wu, W.-C.; Chuang, C.-C.; Lin, J.-L. *J. Phys. Chem. B* **2000**, *104*, 8719-8724.
- (97) Chen, T.; Feng, Z.; Wu, G.; Shi, J.; Ma, G.; Ying, P.; Li, C. *J. Phys. Chem. C* **2007**, *111*, 8005-8014.
- (98) A. Henderson, M.; Otero-Tapia, S.; E. Castro, M. *Faraday Discuss.* **1999**, *114*, 313-329.
- (99) Wang, C.-y.; Groenzin, H.; Shultz, M. J. *J. Am. Chem. Soc.* **2004**, *126*, 8094-8095.
- (100) Nosaka, A. Y.; Fujiwara, T.; Yagi, H.; Akutsu, H.; Nosaka, Y. *Langmuir* **2003**, *19*, 1935-1937.
- (101) Sánchez, V. M.; de la Llave, E.; Scherlis, D. A. *Langmuir* **2011**, *27*, 2411-2419.
- (102) Copeland, J. R.; Santillan, I. A.; Schimming, S. M.; Ewbank, J. L.; Sievers, C. *J. Phys. Chem. C* **2013**, *117*, 21413-21425.
- (103) Shkrob, I. A.; Sauer, M. C.; Gosztola, D. *J. Phys. Chem. B* **2004**, *108*, 12512-12517.
- (104) Chen, L. X.; Rajh, T.; Jager, W.; Nedeljkovic, J.; Thurnauer, M. C. *J. Synchrotron Radiat.* **1999**, *6*, 445-447.
- (105) Li, Y. X.; Lu, G. X.; Li, S. B. *Chemosphere* **2003**, *52*, 843-850.
- (106) Koppen, S.; Langel, W. *Phys. Chem. Chem. Phys.* **2008**, *10*, 1907-1915.
- (107) Dobson, K. D.; McQuillan, A. J. *Spectrochim. Acta, Part A* **1999**, *55*, 1395-1405.
- (108) Ekström, G. N.; McQuillan, A. J. *J. Phys. Chem. B* **1999**, *103*, 10562-10565.
- (109) Awatani, T.; Dobson, K. D.; McQuillan, A. J.; Ohtani, B.; Uosaki, K. *Chem. Lett.* **1998**, *27*, 849-850.
- (110) Hug, S. J.; Sulzberger, B. *Langmuir* **1994**, *10*, 3587-3597.
- (111) Mendive, C. B.; Bredow, T.; Blesa, M. A.; Bahnemann, D. W. *Phys. Chem. Chem. Phys.* **2006**, *8*, 3232-3247.
- (112) Ardizzone, S.; Trasatti, S. *Adv. Colloid Interface Sci.* **1996**, *64*, 173-251.
- (113) Dobson, K. D.; Connor, P. A.; McQuillan, A. J. *Langmuir* **1997**, *13*, 2614-2616.
- (114) Young, A. G.; McQuillan, A. J. *Langmuir* **2009**, *25*, 3538-3548.

- (115) Rotzinger, F. P.; Kesselman-Truttmann, J. M.; Hug, S. J.; Shklover, V.; Grätzel, M. *J. Phys. Chem. B* **2004**, *108*, 5004-5017.
- (116) Savory, D. M.; McQuillan, A. J. *J. Phys. Chem. C* **2013**, *117*, 23645-23656.
- (117) Berger, T.; Delgado, J. M.; Lana-Villarreal, T.; Rodes, A.; Gómez, R. *Langmuir* **2008**, *24*, 14035-14041.
- (118) Cromer, D. T.; Herrington, K. *J. Am. Chem. Soc.* **1955**, *77*, 4708-4709.
- (119) Baur, W. *Acta Crystallogr.* **1961**, *14*, 209-213.
- (120) Bamwenda, G. R.; Tsubota, S.; Kobayashi, T.; Haruta, M. *J. Photochem. Photobiol., A* **1994**, *77*, 59-67.
- (121) Bowker, M.; Davies, P. R.; Al-Mazroai, L. S. *Catal. Lett.* **2009**, *128*, 253-255.
- (122) Bahruji, H.; Bowker, M.; Davies, P. R.; Al-Mazroai, L. S.; Dickinson, A.; Greaves, J.; James, D.; Millard, L.; Pedrono, F. *J. Photochem. Photobiol., A* **2010**, *216*, 115-118.
- (123) Bahruji, H.; Bowker, M.; Brookes, C.; Davies, P. R.; Wawata, I. *Appl. Catal., A* **2013**, *454*, 66-73.
- (124) Bowker, M.; Morton, C.; Kennedy, J.; Bahruji, H.; Greaves, J.; Jones, W.; Davies, P. R.; Brookes, C.; Wells, P. P.; Dimitratos, N. *J. Catal.* **2014**, *310*, 10-15.
- (125) Millard, L.; Bowker, M. *J. Photochem. Photobiol., A* **2002**, *148*, 91-95.
- (126) Outka, D. A.; Madix, R. J. *Surf. Sci.* **1987**, *179*, 361-376.
- (127) Sastre, F.; Oteri, M.; Corma, A.; Garcia, H. *Energy Environ. Sci.* **2013**, *6*, 2211-2215.
- (128) Al-Mazroai, L. S.; Bowker, M.; Davies, P.; Dickinson, A.; Greaves, J.; James, D.; Millard, L. *Catal. Today* **2007**, *122*, 46-50.
- (129) Du, M.-H.; Feng, J.; Zhang, S. B. *Phys. Rev. Lett.* **2007**, *98*, 066102.
- (130) Yoshihara, T.; Katoh, R.; Furube, A.; Tamaki, Y.; Murai, M.; Hara, K.; Murata, S.; Arakawa, H.; Tachiya, M. *J. Phys. Chem. B* **2004**, *108*, 3817-3823.
- (131) Tamaki, Y.; Furube, A.; Murai, M.; Hara, K.; Katoh, R.; Tachiya, M. *J. Am. Chem. Soc.* **2006**, *128*, 416-417.
- (132) Warman, J. M.; Matthijs P, d. H.; Pierre, P.; Theodorus P.M, K.; ETTY A, v. d. Z.-A.; Adri, M.; Ronald, C. *Radiat. Phys. Chem.* **1991**, *37*, 433-442.
- (133) Yamakata, A.; Ishibashi, T.-a.; Onishi, H. *J. Phys. Chem. B* **2002**, *106*, 9122-9125.
- (134) Yamakata, A.; Ishibashi, T.-a.; Onishi, H. *Chem. Phys. Lett.* **2003**, *376*, 576-580.
- (135) Majeed, I.; Nadeem, M. A.; Al-Oufi, M.; Nadeem, M. A.; Waterhouse, G. I. N.; Badshah, A.; Metson, J. B.; Idriss, H. *Appl. Catal., B* **2016**, *182*, 266-276.
- (136) Puga, A. V.; Forneli, A.; García, H.; Corma, A. *Adv. Funct. Mater.* **2014**, *24*, 241-248.
- (137) Kraeutler, B.; Bard, A. J. *J. Am. Chem. Soc.* **1978**, *100*, 5985-5992.
- (138) Chong, R. F.; Li, J.; Zhou, X.; Ma, Y.; Yang, J. X.; Huang, L.; Han, H. X.; Zhang, F. X.; Li, C. *Chem. Commun.* **2014**, *50*, 165-167.
- (139) Koppenol, W. H.; Butler, J. *Adv. Free Radical Biol. Med.* **1985**, *1*, 91-131.
- (140) Chen, J.; Ollis, D. F.; Rulkens, W. H.; Bruning, H. *Water Res.* **1999**, *33*, 669-676.
- (141) Chen, J.; Ollis, D. F.; Rulkens, W. H.; Bruning, H. *Water Res.* **1999**, *33*, 661-668.
- (142) Asmus, K. D.; Mockel, H.; Henglein, A. *J. Phys. Chem.* **1973**, *77*, 1218-1221.
- (143) Schneider, J.; Bahnemann, D. W. *J. Phys. Chem. Lett.* **2013**, *4*, 3479-3483.

- (144) Matsumura, M.; Hiramoto, M.; Iehara, T.; Tsubomura, H. *J. Phys. Chem.* **1984**, *88*, 248-250.
- (145) Bulatov, A. V.; Khidekel', M. L. *Bull. Acad. Sci. USSR, Div. Chem. Sci. (Engl. Transl.)* **1976**, *25*, 1794.
- (146) Sato, S.; White, J. M. *Chem. Phys. Lett.* **1980**, *72*, 83-86.
- (147) Linsebigler, A. L.; Lu, G.; Yates, J. T. *Chem. Rev.* **1995**, *95*, 735-758.
- (148) Anpo, M.; Takeuchi, M. *J. Catal.* **2003**, *216*, 505-516.
- (149) Trasatti, S. *J. Electroanal. Chem. Interfacial Electrochem.* **1972**, *39*, 163-184.
- (150) Greeley, J.; Jaramillo, T. F.; Bonde, J.; Chorkendorff, I. B.; Norskov, J. K. *Nat. Mater.* **2006**, *5*, 909-913.
- (151) Kato, H.; Kudo, A. *Catal. Lett.* **1999**, *58*, 153-155.
- (152) Kurihara, T.; Okutomi, H.; Miseki, Y.; Kato, H.; Kudo, A. *Chem. Lett.* **2006**, *35*, 274-275.
- (153) Sayama, K.; Arakawa, H. *J. Phys. Chem.* **1993**, *97*, 531-533.
- (154) Domen, K.; Kudo, A.; Shibata, M.; Tanaka, A.; Maruya, K.-I.; Onishi, T. *J. Chem. Soc., Chem. Commun.* **1986**, 1706-1707.
- (155) de la Peña O'Shea, V. A. In *Design of Advanced Photocatalytic Materials for Energy and Environmental Applications*; Coronado, M. J., Fresno, F., Hernández-Alonso, D. M., Portela, R., Eds.; Springer London a.o., 2013, p 195-216.
- (156) Maeda, K.; Domen, K. *Top. Curr. Chem.* **2011**, *303*, 95-119.
- (157) Dionigi, F.; Vesborg, P. C. K.; Pedersen, T.; Hansen, O.; Dahl, S.; Xiong, A. K.; Maeda, K.; Domen, K.; Chorkendorff, I. *J. Catal.* **2012**, *292*, 26-31.
- (158) Domen, K.; Naito, S.; Soma, M.; Onishi, T.; Tamaru, K. *J. Chem. Soc. Chem. Comm.* **1980**, 543-544.
- (159) Lehn, J. M.; Sauvage, J. P.; Ziessel, R.; Hilaire, L. *Isr. J. Chem.* **1982**, *22*, 168-172.
- (160) Inoue, Y.; Niiyama, T.; Asai, Y.; Sato, K. *J. Chem. Soc. Chem. Comm.* **1992**, 579-580.
- (161) Sayama, K.; Arakawa, H. *J. Chem. Soc. Chem. Comm.* **1992**, 150-152.
- (162) Kudo, A.; Sayama, K.; Tanaka, A.; Asakura, K.; Domen, K.; Maruya, K.; Onishi, T. *J. Catal.* **1989**, *120*, 337-352.
- (163) Domen, K.; Kudo, A.; Onishi, T. *J. Catal.* **1986**, *102*, 92-98.
- (164) Haruta, M. *Chem. Rec.* **2003**, *3*, 75-87.
- (165) Nørskov, J. K.; Rossmeisl, J.; Logadottir, A.; Lindqvist, L.; Kitchin, J. R.; Bligaard, T.; Jónsson, H. *J. Phys. Chem. B* **2004**, *108*, 17886-17892.
- (166) Domen, K.; Kudo, A.; Onishi, T.; Kosugi, N.; Kuroda, H. *J. Phys. Chem.* **1986**, *90*, 292-295.
- (167) Townsend, T. K.; Browning, N. D.; Osterloh, F. E. *Energy Environ. Sci.* **2012**, *5*, 9543-9550.
- (168) Sakata, T.; Hashimoto, K.; Kawai, T. *J. Phys. Chem.* **1984**, *88*, 5214-5221.
- (169) Kalyanasundaram, K.; Grätzel, M. *Angew. Chem., Int. Ed.* **1979**, *18*, 701-702.
- (170) Kawai, T.; Sakata, T. *Chem. Phys. Lett.* **1980**, *72*, 87-89.
- (171) Teramura, K.; Maeda, K.; Saito, T.; Takata, T.; Saito, N.; Inoue, Y.; Domen, K. *J. Phys. Chem. B* **2005**, *109*, 21915-21921.
- (172) Morales-Guio, C. G.; Stern, L.-A.; Hu, X. *Chem. Soc. Rev.* **2014**, *43*, 6555-6569.
- (173) Regmi, Y. N.; Waetzig, G. R.; Duffee, K. D.; Schmuecker, S. M.; Thode, J. M.; Leonard, B. M. *J. Mater. Chem. A* **2015**, *3*, 10085-10091.

-
- (174) Garcia-Esparza, A. T.; Cha, D.; Ou, Y.; Kubota, J.; Domen, K.; Takanabe, K. *ChemSusChem* **2013**, *6*, 168-181.
- (175) Maeda, K.; Teramura, K.; Lu, D. L.; Saito, N.; Inoue, Y.; Domen, K. *Angew. Chem., Int. Ed.* **2006**, *45*, 7806-7809.
- (176) Yoshida, M.; Maeda, K.; Lu, D. L.; Kubota, J.; Domen, K. *J. Phys. Chem. C* **2013**, *117*, 14000-14006.
- (177) Maeda, K.; Teramura, K.; Lu, D. L.; Saito, N.; Inoue, Y.; Domen, K. *J. Phys. Chem. C* **2007**, *111*, 7554-7560.
- (178) Busser, G. W.; Mei, B.; Pougine, A.; Strunk, J.; Gutkowski, R.; Schuhmann, W.; Willinger, M. G.; Schlogl, R.; Muhler, M. *ChemSusChem* **2014**, *7*, 1030-1034.
- (179) Soldat, J.; Busser, G. W.; Muhler, M.; Wark, M. *ChemCatChem* **2016**, *8*, 153-156.
- (180) Yoshida, M.; Takanabe, K.; Maeda, K.; Ishikawa, A.; Kubota, J.; Sakata, Y.; Ikezawa, Y.; Domen, K. *J. Phys. Chem. C* **2009**, *113*, 10151-10157.
- (181) Maeda, K.; Sakamoto, N.; Ikeda, T.; Ohtsuka, H.; Xiong, A. K.; Lu, D. L.; Kanehara, M.; Teranishi, T.; Domen, K. *Chem. Eur. J.* **2010**, *16*, 7750-7759.
- (182) Sakamoto, N.; Ohtsuka, H.; Ikeda, T.; Maeda, K.; Lu, D. L.; Kanehara, M.; Teramura, K.; Teranishi, T.; Domen, K. *Nanoscale* **2009**, *1*, 106-109.
- (183) Maeda, K.; Teramura, K.; Takata, T.; Hara, M.; Saito, N.; Toda, K.; Inoue, Y.; Kobayashi, H.; Domen, K. *J. Phys. Chem. B* **2005**, *109*, 20504-20510.
- (184) Maeda, K.; Ohno, T.; Domen, K. *Chem. Sci.* **2011**, *2*, 1362-1368.
- (185) Maeda, K.; Lu, D.; Teramura, K.; Domen, K. *J. Mater. Chem.* **2008**, *18*, 3539-3542.
- (186) Zhang, Y. C.; Kershaw, R.; Dwight, K.; Wold, A. *J. Less-Common Met.* **1988**, *142*, 155-161.
- (187) Maeda, K.; Teramura, K.; Lu, D.; Takata, T.; Saito, N.; Inoue, Y.; Domen, K. *J. Phys. Chem. B* **2006**, *110*, 13753-13758.
- (188) Takata, T.; Pan, C. S.; Nakabayashi, M.; Shibata, N.; Domen, K. *J. Am. Chem. Soc.* **2015**, *137*, 9627-9634.
- (189) Schwarzenbach, G.; Muehlebach, J.; Mueller, K. *Inorg. Chem.* **1970**, *9*, 2381-2390.
- (190) Krishnan, C. V.; Garnett, M.; Chu, B. *Int. J. Electrochem. Sci.* **2008**, *3*, 1348-1363.
- (191) Mattioda, G.; Christidis, Y. In *Ullmann's Encyclopedia of Industrial Chemistry*; Wiley-VCH Verlag GmbH & Co. KGaA: 2000; Vol. 17, p 89-92.

1.9. Supporting Information



Scheme-SI 1-1. Keto *gem*-diol tautomerism of formyl bearing C1-/C2-oxygenates. Formulas written in black indicate the predominant species.

Table-SI 1-1. Required minimal aqueous aldehyde concentration, which induces self-oligomerization under ambient conditions and non-adjusted pH.

Aldehyde	Lower concentration (M)
Formaldehyde	0.16 ⁷⁸
Glycolaldehyde	0.02*
Glyoxal	1.0 ⁷⁹
Glyoxylic acid	-** ¹⁹¹

* Own experiment: solely traces of dimer.

** The linear dimer exists in small proportion next to the *gem*-diol form.

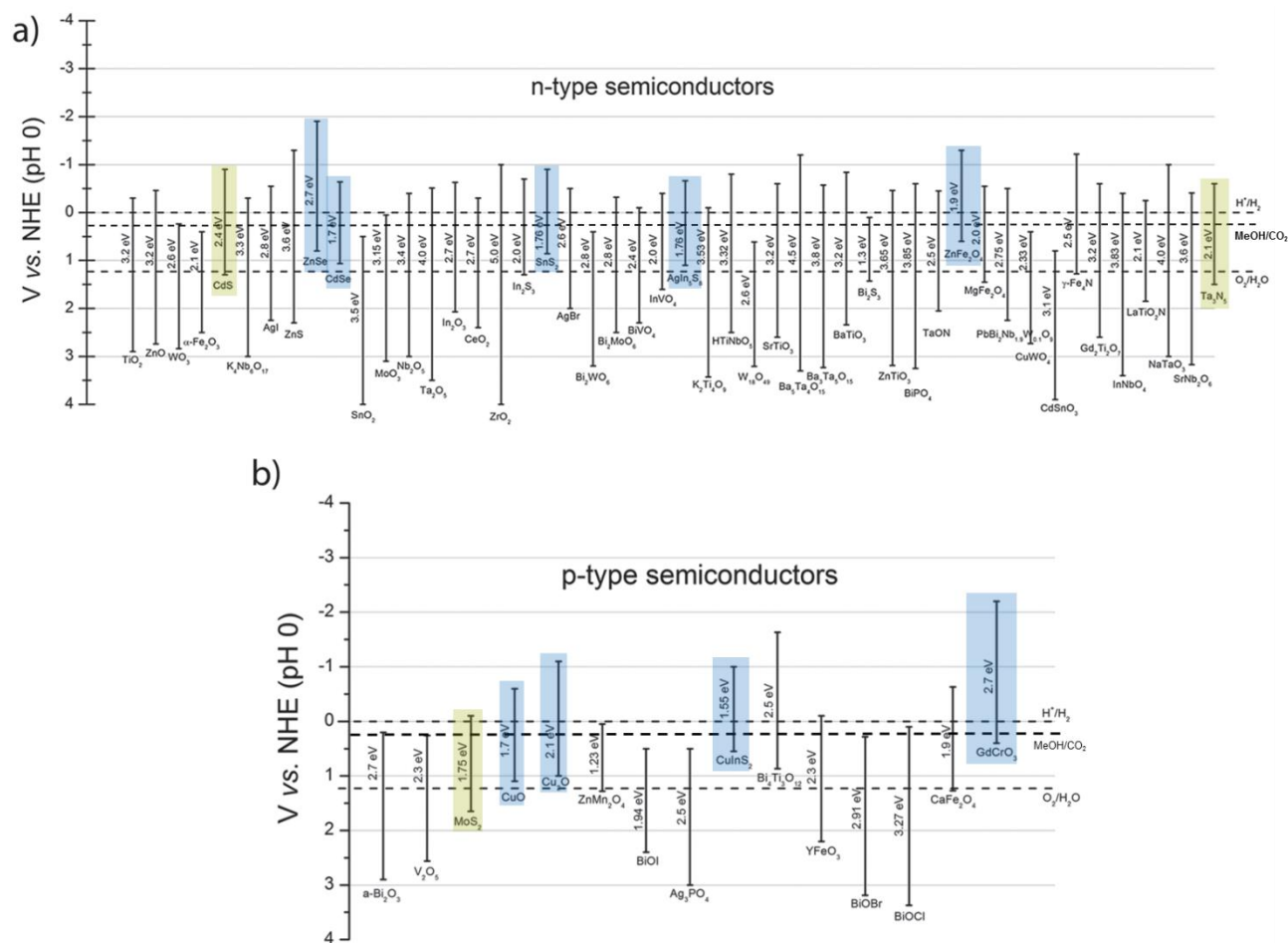
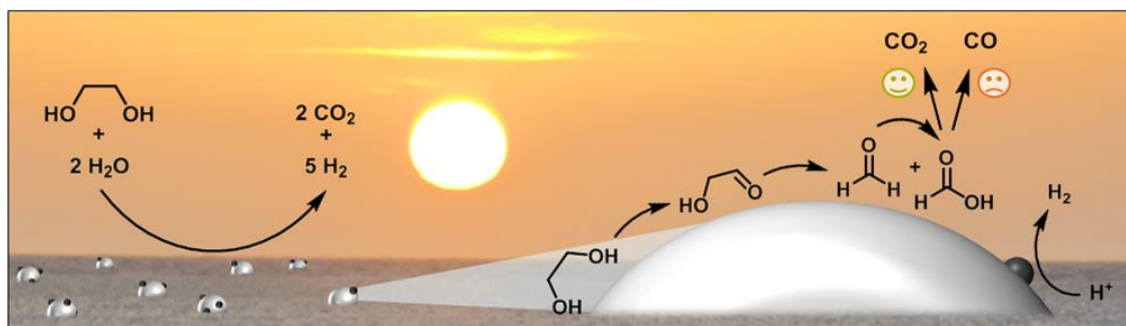


Figure-SI 1-1. Band gaps and band positions (referred to NHE (pH = 0)) of (a) n-type semiconductors and (b) p-type semiconductors. Blue marked semiconductors fulfill solely the thermodynamic prerequisites for photoreforming reactions (e.g., methanol photoreforming reaction). Exemplarily green marked semiconductors are currently not known to be active for the overall water splitting reaction, although the band edge positions fulfill the thermodynamic requirements. Reprinted and adapted with permission from reference 24. Copyright © 2013 John Wiley and Sons.

Photoreforming of Ethylene Glycol



Chapter 2

2. Photocatalytic Ethylene Glycol Reforming over Rh/TiO₂ and Rh/GaN:ZnO

This chapter is based on:

Berto, T.F.; Sanwald, K.E.; Eisenreich, W.; Gutiérrez, O.Y.; Lercher, J.A. *J.Catal.* **2016**, 338, 68-81.^{1,2}

2.1. Abstract

Photoreforming of diols, such as ethylene glycol, proceeds through a sequence of anodic oxidations, which enable the parallel formation of H₂ by reduction of H⁺ at the cathode. The anodic oxidation of ethylene glycol on Rh/TiO₂ leads to glycolaldehyde, formaldehyde and acetaldehyde as primary products. Glycolaldehyde is further converted *via* oxidative C–C-cleavage to formaldehyde and formic acid. The former is converted to formic acid forming CO₂ and H₂. Acetaldehyde is oxidized to acetic acid, which decarboxylates to CO₂ and CH₄. Two catalytically active sites are proposed. On terminal Ti^{IV}–OH groups, oxygenates are oxidized *via* direct hole transfer to alkoxy-radicals prior to β-C–C-bond cleavage. Bridged [Ti··O··Ti]⁺-sites, in contrast, cleave a C–H-bond, forming carbon centered radicals, which are further oxidized by transferring an electron to the conduction band of the semiconductor. On Rh/GaN:ZnO, glycolaldehyde is the main product, forming higher oxidized C₂-oxygenates in turn by reaction with free oxygen radicals formed as product of OH[•] photocatalytic oxidation. The overall rates of photoreforming and, hence, H₂ evolution, depend mainly on the surface concentration of the oxygenates, which are oxidized, while the nature of the oxygenate is of less importance.

¹ Reprinted or adapted from Journal of Catalysis, Copyright (2016), with permission from Elsevier. (license number: 3841800378601)

² T.F.B. designed and performed the experiments (if not otherwise stated at the end of the chapter), did the data analysis and wrote the manuscript. K.E.S., O.Y.G. and J.A.L. contributed with discussion of results and with correction of the manuscript. W.E. programmed the applied NMR measurement pulse sequence and proof-read the text.

2.2. Introduction

Photocatalytic reforming of polyols has been discussed as a promising route to carbon-neutral H₂.^{1,2} The technology may provide simpler pathways compared to overall water splitting, as the recombination of H₂ and O₂ is avoided³ and separation of H₂ and CO₂ is greatly facilitated. The wide abundance of oxygenate contaminants in water would make this even a preferred route, coupling water cleaning with storing photon energy in H₂. Methanol and polyols can be quantitatively photoreformed to CO₂/H₂-mixtures,⁴⁻⁶ while the overall H₂ evolution rates have been reported to depend on the nature of the oxygenate.^{7,8} Little agreement exists, however, on the evolution of intermediates and side products, as well as the kinetics of the associated overall processes and elementary steps.^{6,7,9-11}

In photoreforming of glycerol, the first oxidation step is proposed to be initiated by ·OH-radicals or holes.^{6,9,11} As expected from the corresponding Fenton's reagent chemistry, alcohols are oxidized to aldehydes⁶ or carboxylic acids.^{9,11} Subsequent C–C-cleavage is attributed to decarboxylation^{9,11} or decarbonylation, using water-gas shift to rationalize the observation of CO₂.⁶ The anodic half reactions during photooxidation of polyols on TiO₂ proceed *via* a different route.¹² Terminal OH-groups and surface lattice oxygen [Ti–O–Ti]-sites facilitate direct and indirect hole transfer, respectively. In both cases, the carbon radicals are oxidized by reacting with molecular O₂. The formation of CO has been attributed to the dehydration of formic acid formed intermediately during methanol reforming.¹³⁻¹⁶ The pathway to CO formation in reforming of higher oxygenates is unclear. The ambiguity in the reaction path analyses and the contradiction in the existing hypotheses require to probe photoreforming under well-defined conditions and to identify the nature and kinetics of transformations of reactants, intermediates, and products of photocatalytic reforming.

The reaction is catalyzed, in principle, by a variety of semiconductors in the presence of UV- or visible light, including TiO₂ or alkaline earth titanates with metal co-catalysts,^{1,2} as well as oxynitrides (e.g., TaON, LaTaON₂, Y₂Ta₂O₅N₂, and GaN:ZnO).^{1,2,17} Therefore, the chemistry on two typical representatives, namely, AEROXIDE® TiO₂ P 25 (in this chapter abbreviated as TiO₂) and GaN:ZnO as semiconductors, is explored using Rh as co-catalyst. It should be noted in passing

that the less positive valence band edge potentials of visible-light absorbing semiconductors, e.g., GaN:ZnO (band gap: 2.7 eV), lead to lower oxidation potentials compared to UV-light absorbing semiconductors, e.g., TiO₂ (band gap: 3.1 eV).^{18,19} The present study aims, therefore, to describe the elementary reactions involved in photoreforming using ethylene glycol (EG) as model reactant on a molecular level.^{20,21} The simplicity of EG allows unambiguous identification of the involved elemental steps. The reaction pathway analysis and kinetics are based on quantitative gas and liquid phase analysis linked in a kinetic model.²²⁻²⁴

2.3. Experimental Section

2.3.1. Materials

All chemicals were obtained from commercial suppliers and used as provided: AEROXIDE® TiO₂ P 25 (Evonik, LOT: 4162092398), sodium hexachlororhodate (III) (Alfa Aesar, Rh 17.1%), gallium oxide (ABCR, 99.99%, LOT: 1040437), zinc oxide (ABCR, 99.7%, LOT: 1121535), ammonia (NH₃, BASF, 5.0, anhydrous), synthetic air (Westfalen), hydrogen (H₂, Westfalen, 5.0), argon (Ar, Westfalen, 5.0), nitrogen (N₂, Westfalen, 5.0), ethanol (80 mg 100 mL⁻¹, European Reference Materials), glyoxal trimer dihydrate (Fluka, ≥ 95%), EG (VWR-Chemicals, 99.9%), glycolaldehyde dimer (Aldrich), glycolic acid (Aldrich, 99%), glyoxylic acid monohydrate (Aldrich, 98%), formaldehyde solution (Fluka, 1000 μg mL⁻¹ in H₂O, IC Standard), formic acid (Merck, 99-100%), methanol (Aldrich, 99.8%, anhydrous), phloroglucinol (Aldrich, ≥ 99%), acetaldehyde solution (Aldrich, 35 wt.%), D₂O (Euriso-Top, 98.85 atom%), deuterium chloride in D₂O (Acros Organics, 1 M, 99.8 atom%), gallium ICP-standard (Merck, Certipur, 1000 mg L⁻¹), zinc ICP-standard (Merck, Certipur, 1000 mg L⁻¹), Rh AAS-standard (Fluka, TraceCert, 999 mg L⁻¹ +/- 9 mg L⁻¹), Rh-foil (was provided by ESRF / BM25 station), rhodium(III)oxide (Fluka, anhydrous, puriss.).

2.3.2. Catalyst Preparation

2.3.2.1. Synthesis of 1.0 wt.% RhO_x/TiO₂

TiO₂ was dried under static air at 473 K for 2 hours prior to impregnation. The support (BET surface area: 53 m² g⁻¹ and pore volume of 0.11 mL g⁻¹) was treated with an aqueous solution of Na₃RhCl₆·12H₂O *via* incipient wetness impregnation. The reddish powder was kept at 383 K (5 K min⁻¹) for 1 h, and heat treated in synthetic air at 623 K (5 K min⁻¹) for 1 h (100 mL min⁻¹). After cooling to room temperature, the obtained RhO_x/TiO₂ material was treated by heating with an increment of 5 K min⁻¹ to 623 K in H₂ (100 mL min⁻¹) and cooled to room temperature. Subsequently, the sample was washed thoroughly to remove NaCl and dried in N₂ at 383 K overnight. Within the study used, parent TiO₂ was subjected to identical treatments as RhO_x/TiO₂. 1.0 wt.% Pt/TiO₂ was synthesized using H₂PtCl₆ as Pt precursor, following the synthesis procedure used to prepare RhO_x/TiO₂.

2.3.2.2. Synthesis of 1.0 wt.% RhO_x/(Ga_{1-x}Zn_x)(N_{1-x}O_x)

RhO_x/(Ga_{1-x}Zn_x)(N_{1-x}O_x) was synthesized according to a procedure reported by Domen *et al.*¹⁹ A physical mixture of 0.6 g (3.2 mmol) Ga₂O₃ and 0.520 g (6.4 mmol) ZnO was nitrated at 1098 K (10 K min⁻¹) for 16 h under NH₃ flow (200 mL min⁻¹). The obtained solid solution was cooled to room temperature under NH₃ flow and was subsequently treated at 873 K (5 K min⁻¹) for 1 h in synthetic air flow (50 mL min⁻¹). This procedure is defined as post-calcination in agreement to reference 19. Post-calcined (Ga_{1-x}Zn_x)(N_{1-x}O_x) (x = 0.14) was modified with RhO_x (denoted as a co-catalyst) by wet impregnation. In an evaporating dish 0.2 g of (Ga_{1-x}Zn_x)(N_{1-x}O_x) were dispersed in 1 mL of bidistilled water (σ = 18.2 MΩ cm) containing the appropriate amount of Na₃RhCl₆·12H₂O. The stirred suspension was evaporated to dryness. The obtained powder was kept in static air at 623 K (5 K min⁻¹) for 1 h in order to obtain the RhO_x-decorated (Ga_{1-x}Zn_x)(N_{1-x}O_x) solid solution. After cooling to room temperature the sample was washed to remove NaCl and dried in N₂ at 383 K overnight.

Different procedures of co-catalyst preparation were chosen in order to obtain photocatalysts with a maximum activity. Rh/(Ga_{1-x}Zn_x)(N_{1-x}O_x), which was obtained by reducing RhO_x-decorated (Ga_{1-x}Zn_x)(N_{1-x}O_x) in H₂ flow, possessed poor photocatalytic activity. We hypothesize that H₂ partially reduced Zn²⁺-centers to create oxygen vacancies and, thus, increased the electron-hole recombination rate. The best RhO_x/TiO₂ was obtained by treatment in synthetic air at 623 K (5 K min⁻¹) for 1 h and in H₂ at 623 K (5 K min⁻¹) for 1 h.

2.3.3. Photocatalytic Test

2.3.3.1. Photoreforming Experiments

Photocatalytic reactions were carried out in a photo-reactor connected to a gas-tight gas circulation system (leakage rate < 5·10⁻⁴ Pa s⁻¹ L⁻¹, V = 310 mL), the catalyst being exposed to light *via* top-irradiation through a quartz-window. 75 mg of photocatalyst were suspended in 100 mL of an aqueous solution containing the reactant (typically 20 mM). The reactor was kept at 288 K and the system was filled with Ar to 1 bar. The system was evacuated four times in order to remove O₂

(< 0.3 $\mu\text{mol O}_2$ /detection limit). Completeness of O_2 removal was verified by GC analysis. Subsequently, the suspension was illuminated with a 300 W Xenon lamp, equipped with a cold-mirror 1 (CM1) and a water filter tempered at 303 K. High EG conversion experiments were performed over Rh/TiO_2 using high power UV-LEDs instead of the 300 W Xe-lamp. The evolved gases were analyzed by an online gas chromatograph (Shimadzu, GC 2010 Plus with Ar as carrier gas and a Chromosorb 101 column connected with a MS-5Å column), equipped with a TCD, FID and a methanizer. The concentrations of dissolved gases, in particular CO_2 , were accounted for by applying Henry's law. H_2 production rates were determined by dividing the difference of H_2 amounts between two adjacent data points by the corresponding time interval. Concentrations in the liquid were determined by quantitative $^1\text{H-NMR}$ spectroscopy. Liquid samples were withdrawn *via* a sample valve, filtered with a nylon syringe filter and analyzed.

2.3.3.2. $^1\text{H-NMR}$ Analysis

A sample of 400 μL was mixed with 400 μL of pH-adjusted internal standard (20 mM 1,3,5-trihydroxybenzene in D_2O , pH adjusted with DCl to 2.7). All experiments were performed at 305 K using an Avance III 500 System (Bruker Biospin, Rheinstetten, Germany) with an UltraShield 500 MHz magnet and a SEI 500 S2 probe head (5 mm, inverse $^1\text{H}/^{13}\text{C}$ with Z-gradient). The measurements were conducted at a magnetic field of 11.75 T. The resonance frequency of ^1H was 500.13 MHz. For all samples, the $^1\text{H-NMR}$ spectra were acquired using the one-dimensional NOESY sequence "noesygppr1d.comp" with pre-saturation of the residual water signal during the relaxation delay and the mixing time using spoil gradients. The relaxation delay was 26 s, and the acquisition time was 4.1 s. Spectra were the result of 64 or 128 scans, with data collected into 32 k data points. Each FID was zero-filled to 64 k data points. Prior to Fourier transformation, an exponential window function with a line broadening factor of 0.2 Hz was applied. The resulting spectra were manually phased, baseline corrected, and integrated using Mestre-C 7.1.0 software package. Chemical shifts were referenced to the internal standard. T_1 , the longitudinal relaxation time, was determined by the inversion recovery pulse sequence method. The sum of acquisition time and relaxation delay in the quantitative analysis was

then adjusted to be equal to or higher than three times T_1 of the slowest relaxing molecule (formic acid). The reaction products were identified according to their specific $^1\text{H-NMR}$ chemical shifts verified with measurements of commercial references recorded under the same experimental conditions (Table 2-1). The amounts of products were determined on the basis of their signal intensities (integrals) referenced to the known molar amount of the internal standard. As the signal intensity of formaldehyde and glyoxal was affected by the water suppression, each compound was respectively calibrated using five to seven calibration solutions. Quantitative gas and liquid phase analysis (detection limit: 0.1 ppm) allowed obtaining closed hydrogen and carbon balances.

Table 2-1. Chemical shifts of various C1- and C2-oxygenates and the used internal standard 1,3,5-Trimethoxybenzene.

Compound	Chemical shift (ppm)	Integral (number of H-atoms)
Formic acid	8.23	1
1,3,5-Trimethoxybenzene	5.94	3
Glyoxylic acid	5.26	1
Glyoxal (diol)	4.77	2
Formaldehyde (diol)	4.75	2
Glycolaldehyde – formyl	4.38	2
Glycolaldehyde - diol	3.45	2
Glycolic acid	4.10	2
Ethylene glycol	3.60	4
Methanol	3.29	3
Ethanal - formyl	2.18	3
Ethanal - diol	1.33	3
Ethanal - dimer	1.25	6
Acetic acid	2.02	3

2.3.3.3. Photocatalytic Water-Gas Shift Reaction Experiments

75 mg of photocatalyst were suspended in 100 mL water, kept at 288 K. The system was evacuated four times in order to remove O_2 quantitatively and was subsequently filled with 8 mbar of CO and then with Ar up to atmospheric pressure 30 minutes prior illumination. All other experimental procedures correspond to the description in chapter 2.3.3.1.

2.3.4. Catalyst Characterization

Elemental analysis.

Ga and Zn concentrations were determined by inductively coupled plasma atomic emission spectroscopy (ICP-AES) using a spectroflame-ICP spectrometer (Spectro Analytical Instruments Inc.). Rh concentrations were analyzed by atomic absorption spectroscopy (AAS) using a Thermo Scientific – SOLAAR M Series AA Spectrometer. H-C-N elemental analyses were carried out by the Microanalytical Laboratory at the Technischen Universität München.

Textural properties.

Specific surface area and average pore diameter were determined by N₂ adsorption-desorption measurements carried out at 77 K using a PMI automated BET sorptometer. All samples were outgassed at 523 K for 20 h before the measurements. The specific surface area and the average pore diameter were calculated applying the BET and BJH (Barret-Joyner-Halenda) models, respectively.

X-ray diffraction (XRD).

XRD-patterns were collected on a STOE STADI-P diffractometer (Cu-K_{α1} radiation, $\lambda = 1.54051 \text{ \AA}$, Ge-monochromator) using a Dectric Mythen 1 K detector.

H₂ chemisorption.

The catalyst was collected after reaction in order to determine the particle size of the metallic Rh particles which are considered to be obtained by in situ photoreduction. Each sample was activated in H₂ at 473 K for 2 h. H₂ adsorption (physisorption and chemisorption) was measured over the pressure range from 1 kPa to 40 kPa at 313 K. The sample was outgassed at 313 K for 1 h and a second isotherm was measured in order to determine physisorbed H₂. The concentration of chemisorbed H₂ was determined by extrapolating the subtracted isotherm to zero H₂ pressure. Mean Rh particle size was calculated assuming half spheres and one atom of hydrogen chemisorbed on one surface atom of Rh.

Diffuse reflectance UV-Vis (DR UV-Vis) spectroscopy.

DR UV-Vis measurements were performed with an Avantes Avaspec 2048 spectrometer equipped with a reflection probe (FCR-7UV200-2-ME) and a

homemade sample holder. All DR UV-Vis spectra are plotted in the form of Kubelka-Munk function defined as $F(R) = (1-R)^2 \cdot (2R)^{-1}$ with $R = R_S/R_T$, where R_S is the reflectance of the sample and R_T is the reflectance of teflon used as a reference.

Transmission and scanning electron microscopy (TEM and SEM).

TEM images were recorded on a JEOL JEM-2010 transmission electron microscope operating at 120 kV with a magnification of 200 k. Before measurement, the catalyst sample was ground, suspended in ethanol, and ultrasonically dispersed. Droplets of the suspension were transferred to a copper grid-supported carbon film. The average Rh particle size was calculated from 300 measured particles. SEM images were taken on a JEOL REM 5900 LV microscope operating at 2.0 kV. The samples were measured without any pretreatment.

X-ray absorption spectroscopy (XAS).

X-ray absorption near edge structure (XANES) measurements at the Rh K-edge were conducted at the BM25 beamline of the European Synchrotron Radiation Facility (ESRF). The storage ring was operated at 6 GeV. A Si(111) double crystal monochromator was used and detuned to about 60% of maximum incident intensity in order to minimize contributions from higher harmonics. Experiments were conducted at room-temperature and in fluorescence mode using a 13-element Si(Li) solid-state detector. Photocatalyst samples collected after synthesis were examined in quartz capillaries (2 mm outer diameter, 0.05 mm wall thickness). A Rh foil was placed in between two ionization chambers as a reference for energy calibration of each spectrum, whereas the edge position of Rh(0) was set to 23220 eV. All spectra represented the average of at least three spectral scans and were normalized to an edge step height of one absorption unit.

2.3.5. Light Intensity Measurements

Light intensity measurements were performed with an Avantes Avaspec 2048 spectrometer equipped with a SMA terminated quartz fiber (FC-UV-200-1-ME-SR) equipped with a cosine corrector (CC-UV/Vis). The spectrometer was calibrated using a calibrated light source (AvaLight DH-BAL-CAL).

2.4. Results and Discussion

2.4.1. Synthesis Procedure and Physicochemical Properties

The Rh content, particle size and textural properties of the photocatalysts are compiled in Table 2-2. The solid solution $(\text{GaN})_{0.86}(\text{ZnO})_{0.14}$ (Figure 2-1, Table 2-3; denoted in the following as GaN:ZnO) exhibited a band gap of 2.7 eV (Figure 2-2), i.e., it is a visible light absorbing material. HR-SEM images show that primary nm-sized particles are agglomerated to μm -sized secondary particles (Figure-SI 2-1). The surface area of GaN:ZnO was $8\text{-}10\text{ m}^2\text{ g}^{-1}$. The averaged Rh particle size after photoreduction was 7.8 nm (determined from H_2 chemisorption).

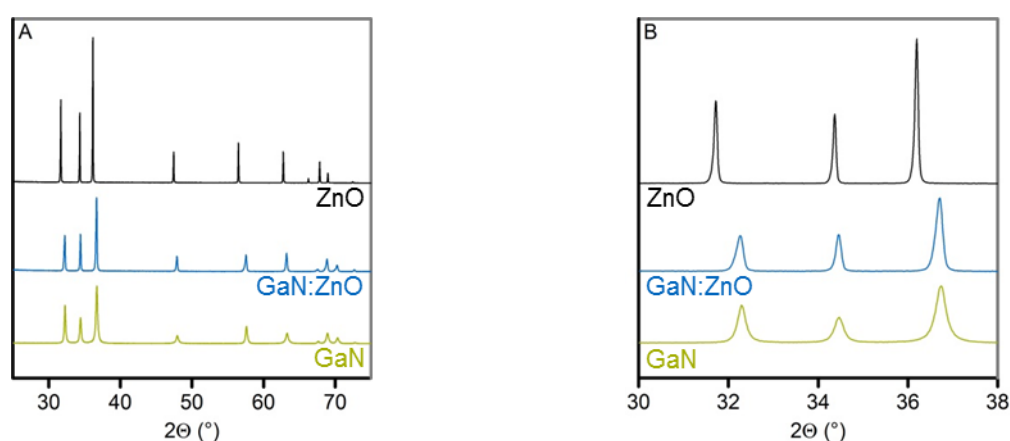


Figure 2-1. XRD patterns of $(\text{GaN})_{0.86}(\text{ZnO})_{0.14}$ obtained by nitriding a mixture of Ga_2O_3 and ZnO (atomic Zn/Ga-ratio = 1) at 1098 K for 16 h in comparison to GaN and ZnO. (A) complete diffractograms. (B) cutout.

Table 2-2. Chemical composition, band gap and textural properties of synthesized photocatalysts.

Photocatalyst	Rh content (wt.%)	Rh particle size (nm)	BET surface area ($\text{m}^2\text{ g}^{-1}$)	Pore diameter (nm)	Band gap (eV)
Rh/TiO ₂	1.0	1.5 [*] 1.7 (± 0.7) ^{**}	44	32	3.1
Rh/GaN:ZnO	1.0	7.8 [*]	8-10	-	2.7

^{*} H_2 chemisorption, ^{**} TEM (analysis of 300 particles).

Table 2-3. Results of elemental analysis of GaN:ZnO obtained by nitriding a mixture of Ga₂O₃ and ZnO (atomic Zn/Ga-ratio = 1) at 1098 K for 16 h.

Element	Technique	Ga/Zn-, N/O-ratio (%)
Gallium	ICP	86
Zinc	ICP	14
Nitrogen	CHN-analysis	82
Oxygen	-	18 ^a

a: calculated

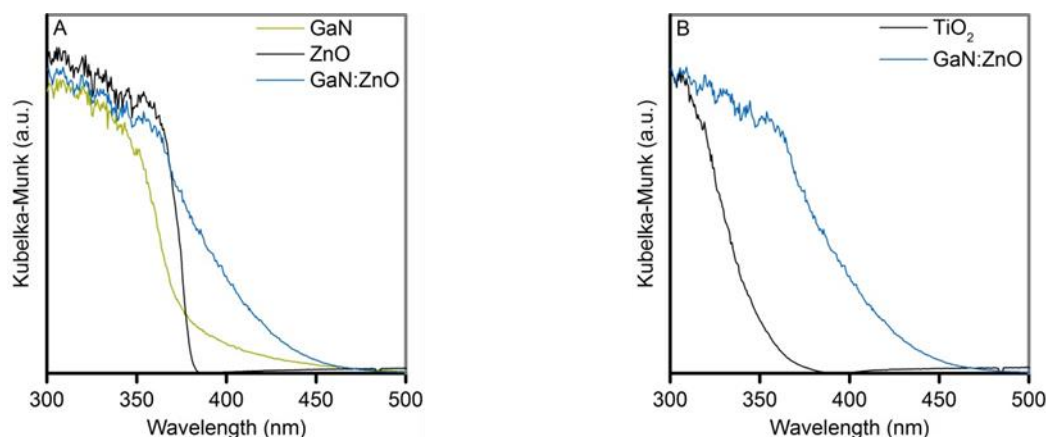


Figure 2-2. Diffuse reflectance UV-Vis spectra of photoabsorbers. (A) Spectra of GaN and ZnO references as well as (GaN)_{0.86}(ZnO)_{0.14}. (B) Spectra of TiO₂ and (GaN)_{0.86}(ZnO)_{0.14}.

AEROXIDE[®] TiO₂ P 25 (denoted as TiO₂) is a mixture of anatase (75%, 25 nm) and rutile (25%, 80 nm) and absorbs solely UV-light due to its band gap of 3.1 eV (Figure 2-2B). Deposition of Rh slightly reduced the pore volume and the specific surface area of the parent TiO₂, but did not influence the band gap and phase composition. The metal content was 1.0 wt.% and the particle size, derived from H₂ chemisorption was 1.5 nm in good agreement with TEM analysis (1.7 nm ± 0.7 nm, Figure-SI 2-2). Different sizes of Rh particles were obtained on TiO₂ and GaN:ZnO because of the differences in the available areas for dispersing the metal. TiO₂ is a mesoporous support with a surface area of 53 m²·g⁻¹, whereas GaN:ZnO is a non-porous support with surface area of 8-10 m²·g⁻¹.

Normalized XANES spectra obtained at the Rh K-edge for RhO_x/TiO₂ and RhO_x/GaN:ZnO as well as for the reference materials are shown in Figure 2-3. The Rh K-edges of the two samples indicate a similar oxidation state. The absorption edges as well as near edge absorption fine structure with absorption maxima at 23245 eV and 23300 eV resemble the Rh₂O₃ reference indicating a predominantly oxidized co-catalyst.²⁵ We conclude that the H₂ reduced Rh/TiO₂ oxidized under

ambient conditions. The near edge absorption fine structure absorption maxima around 23245 eV indicate that Rh on TiO_2 is less oxidized than on GaN:ZnO. Thus, the fresh catalysts consist of mixtures of Rh and RhO_x , the latter being the dominating phase. Under reaction conditions, however, it is hypothesized that RhO_x undergoes in situ photoreduction to form metallic Rh, which acts as site for hydrogen atom recombination to H_2 . Ongoing investigations address the oxidation state of Rh under reaction. For simplicity both catalysts are denoted as Rh/ TiO_2 and Rh/GaN:ZnO in the following.

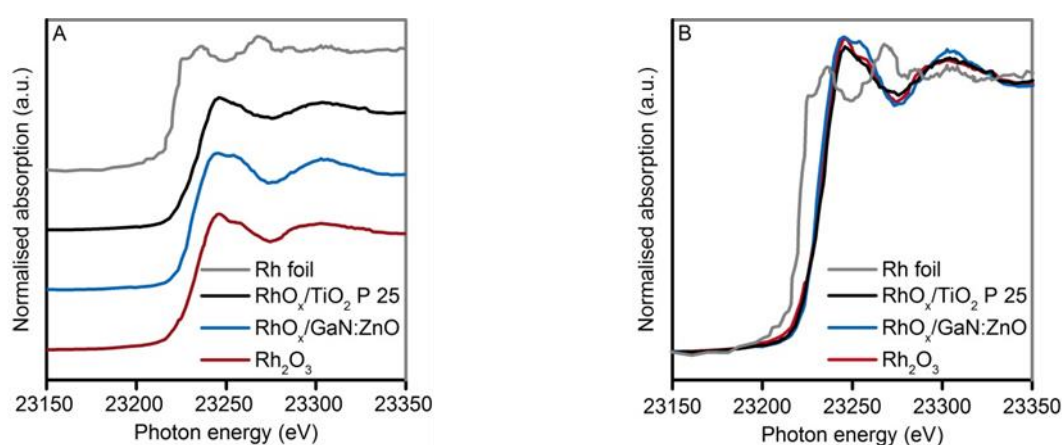


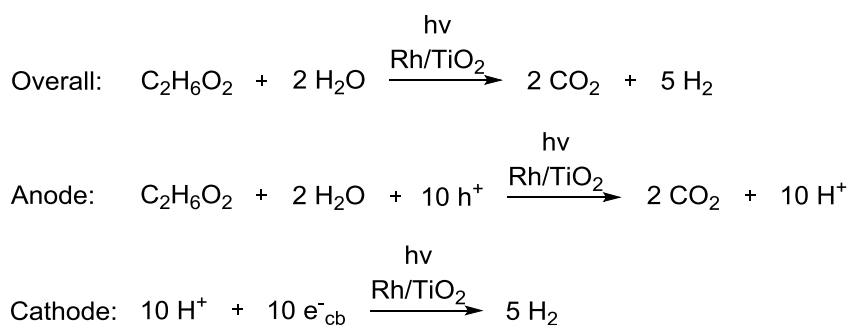
Figure 2-3. Rh K-edge XANES spectra for RhO_x decorated GaN:ZnO and TiO_2 after synthesis. (A) Stacked plotting, (B) Overlapped plotting.

2.4.2. Reaction Network of EG Photoreforming on 1 wt.% Rh/ TiO_2

2.4.2.1. Kinetics of EG Photoreforming

The change in standard free enthalpy of the reaction (ΔG^0) is $+8.6 \text{ kJ mol}^{-1}$ (Table 1-1). The complete reaction leads to two equivalents of CO_2 and five equivalents of H_2 (Scheme 2-1). In chapter 1.1 co-catalyst decorated photoabsorbers like Rh/ TiO_2 or Rh/GaN:ZnO were described to work as a micro-electrochemical cell. Accordingly, Rh co-catalyst acts as the cathode (H_2 evolution site), whereas EG and all intermediates are converted to CO_2 on the anodic semiconductor surface.

The expected reaction products of both redox half reactions H_2 ($1580 \mu\text{mol}$ after 12 h) and CO_2 ($573 \mu\text{mol}$ after 12 h) were detected (Figure 2-4A). Formation of small quantities of CH_4 ($1.3 \mu\text{mol}$ after 12 h) besides CO ($1.5 \mu\text{mol}$ after 12 h) were also observed (Figure 2-4B).



Scheme 2-1. Photocatalytic ethylene glycol reforming.

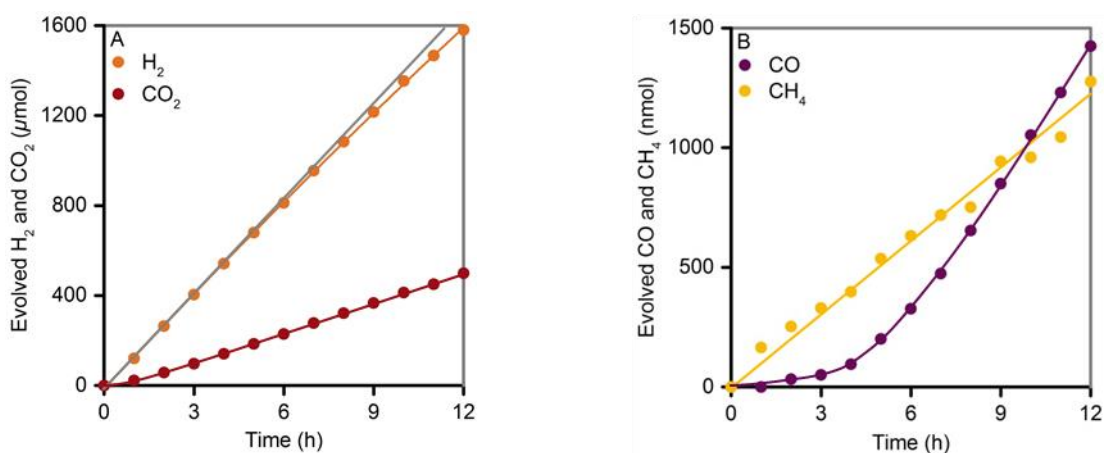


Figure 2-4. Analysis of evolved gaseous products during ethylene glycol photoreforming. **(A)** Course of expected reaction products H₂ and CO₂ and **(B)** of side products CO and CH₄. Colored lines serve to guide the eye. Grey line indicates course of constant H₂ evolution. Reaction conditions: 75 mg Rh/TiO₂, 100 mL aqueous ethylene glycol solution (20 mM), 288 K, 1 bar Ar, 300 W Xe-lamp (CM1).

The evolution of CO is distinctly retarded differently to all other gaseous products. The course of formation indicates that it is formed from a decomposing secondary product or due to structural changes of the photocatalyst surface under illumination. The H₂ evolution rate decreased with time on stream, which is attributed to the consumption of EG (Figure 2-5A). The H₂ to CO₂-ratio also decreased approaching asymptotically a H₂ to CO₂-ratio of 3.0 instead of the expected ratio of 2.5 (Figure 2-5A). Thus, EG is not stoichiometrically mineralized to CO₂ and one or more organic intermediates remain in the aqueous phase. As EG consumption was not observed in the dark, we conclude that any observed reactivity is caused by light induced reactions (Figure 2-5B).

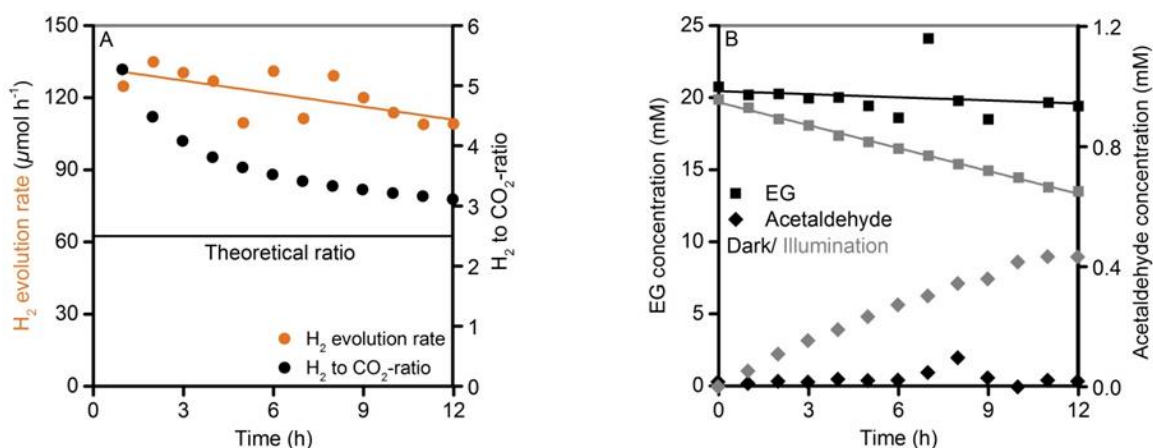
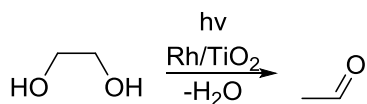


Figure 2-5. (A) Course of H₂ evolution rate and H₂ to CO₂-ratio during ethylene glycol photoreforming. (B) Comparison of ethylene glycol conversion (20 mM) and acetaldehyde formation with and without illumination. Sloping lines serve to guide the eye. Reaction conditions: 75 mg Rh/TiO₂, 100 mL aqueous ethylene glycol solution (20 mM), 288 K, 1 bar Ar, 300 W Xe-lamp (CM1) or no illumination.

Formaldehyde (478 μmol after 12 h, HCHO), glycolaldehyde (95 μmol after 12 h) and acetaldehyde (43 μmol after 12h) were the main intermediates. Acetic acid (3 μmol after 12 h), methanol (5 μmol after 12 h) and formic acid (6 μmol after 12 h, HCOOH) were present as minor products (Figure 2-6). The aqueous phase was enriched with HCHO with almost constant rate. In contrast, glycolaldehyde and HCOOH reached constant concentrations after five hours indicating that they were consumed by consecutive reactions. Acetaldehyde, the dehydration product of EG (Scheme 2-2), was also formed by a light-driven process, because its formation was not observed in absence of irradiation (Figure 2-5B).

The two C₂-intermediates, glycolaldehyde (2e⁻-oxidation product, Scheme 2-3) and acetaldehyde (dehydration product), formed directly from EG, indicated two parallel reaction pathways (Scheme 2-4). In order to identify the reaction network of each pathway, glycolaldehyde (Path 1) and acetaldehyde (Path 2) were photoreformed over Rh/TiO₂.



Scheme 2-2. Dehydration of ethylene glycol to acetaldehyde.

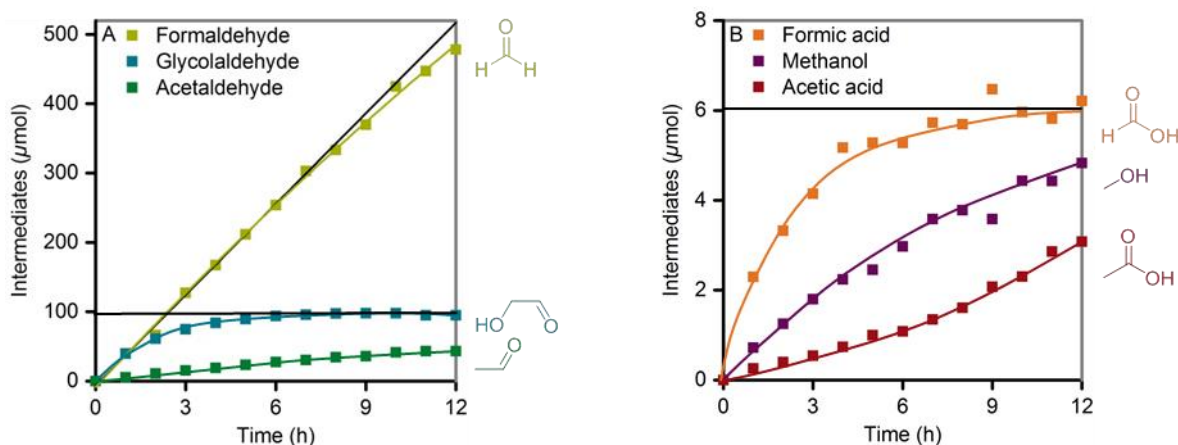
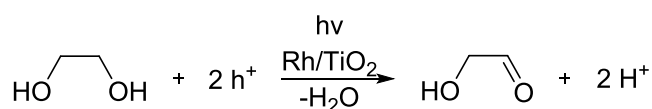
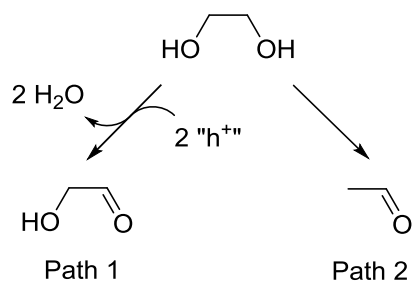


Figure 2-6. Analysis of species generated in anodic half reactions during ethylene glycol photoreforming. Course of (A) main and (B) side intermediate formation. Colored lines serve to guide the eye. Sloping black line indicates course of constant formaldehyde formation. Horizontal black line indicates equilibrium concentration of a species throughout the reaction period. Reaction conditions: 75 mg Rh/TiO₂, 100 mL aqueous ethylene glycol solution (20 mM), 288 K, 1 bar Ar, 300 W Xe-lamp (CM1).



Scheme 2-3. Oxidation of ethylene glycol to glycolaldehyde.

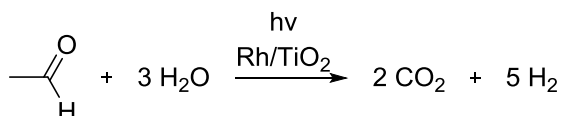


Scheme 2-4. Proposed reaction pathways for photocatalytic ethylene glycol reforming over Rh/TiO₂.

2.4.2.2. Photoreforming of Acetaldehyde over Rh/TiO₂

Photoreforming of acetaldehyde (Scheme 2-5) on Rh/TiO₂ was conducted under the same conditions than EG photoreforming. The expected reaction products of both half reactions, H₂ (312 μmol after 12 h) and CO₂ (81 μmol after 12 h), were detected (Figure 2-7). The low H₂ evolution rate ($\sim 30 \mu\text{mol h}^{-1}$ vs. $130 \mu\text{mol h}^{-1}$ for EG photoreforming) was attributed to a lower adsorption constant of acetaldehyde compared to EG. Acetic acid, a 2e⁻-oxidation product of acetaldehyde reforming, was detected in the liquid phase (197 μmol after 12 h, Scheme 2-6). Furthermore, the

formation of CH₄ (42 μmol after 12 h, Figure 2-7B) indicated that CH₃COOH photocatalytically decarboxylates (Photo-Kolbe reaction, Scheme 2-7).²⁶ Note that ethanol had been converted before to mixtures of H₂ and acetaldehyde with only traces of CO₂ and CH₄.^{10,27} Comparison with our results suggests that in that case the weak adsorption of acetaldehyde, compared to ethanol, hindered its conversion to acetic acid and subsequently to CO₂.



Scheme 2-5. Photocatalytic acetaldehyde reforming.

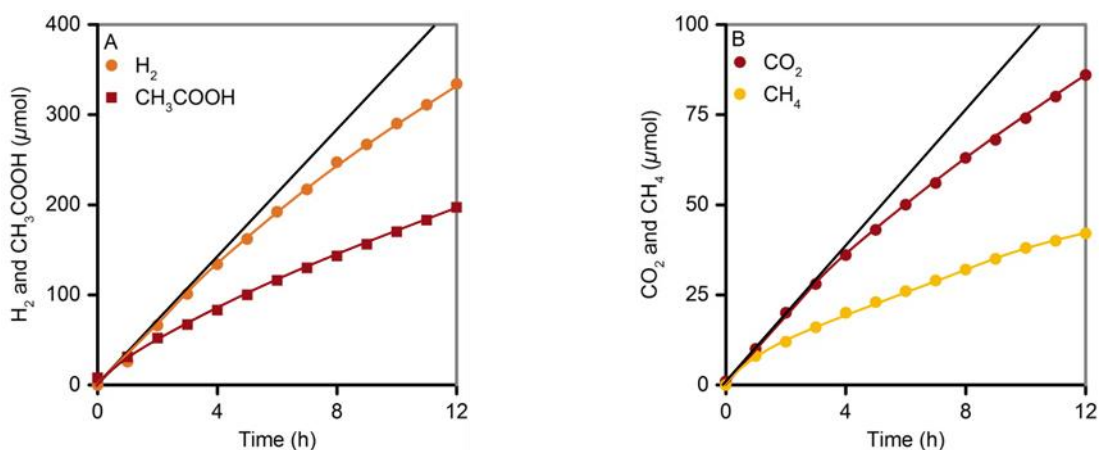
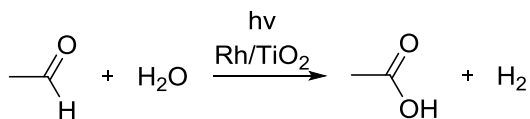


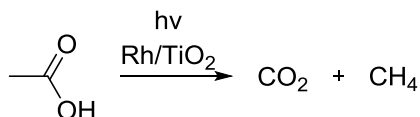
Figure 2-7. Analysis of evolved gaseous products during acetaldehyde photoreforming. Comparison of course of (A) H₂ and acetic acid as well as (B) CO₂ and CH₄ formation. Colored lines serve to guide the eye. Black lines indicate course of constant H₂ or CO₂ formation. Reaction conditions: 75 mg Rh/TiO₂, 100 mL aqueous acetaldehyde solution (20 mM), 288 K, 1 bar Ar, 300 W Xe-lamp (CM1).

CO₂ to CH₄- and H₂ to CH₃COOH-ratios of 1, within the first hour, correspond to those expected from the reactions of Scheme 2-6 and Scheme 2-7 (acetaldehyde oxidized to acetic acid, which in turn decarboxylates). With increasing reaction time the ratios of products changed, i.e., the CO₂ to CH₄-ratio was 2 and the H₂ to CH₃COOH-ratio was 1.6 after 12 h. Related to the amount of CH₄ formed, the amount of CO₂ was twice higher than expected, whereas the rates of acetic acid formation declined faster than expected only from the Photo-Kolbe reaction. The differences between the observed amounts of H₂ and CO₂ and the expected ones, based on the stoichiometry of Scheme 2-6 and Scheme 2-7 and on the amounts of CH₄ and CH₃COOH formed, gave the H₂ to CO₂-ratio of 2. This indicates that the

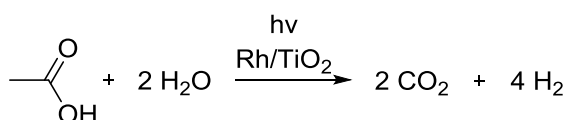
excess of H_2 and CO_2 is produced by oxidative C–C-bond cleavage of acetic acid as shown in Scheme 2-8.



Scheme 2-6. Anaerobic photo-oxidation of acetaldehyde to acetic acid.

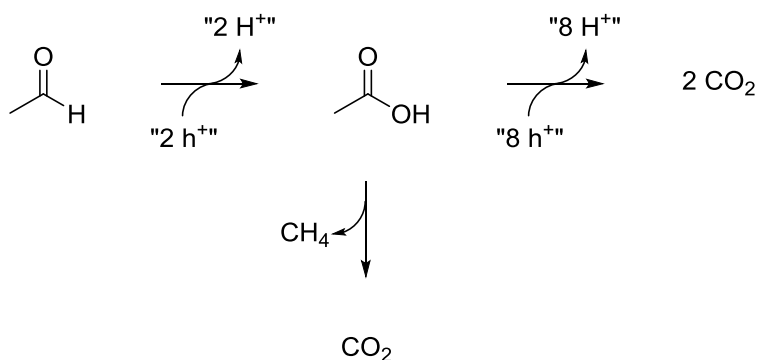


Scheme 2-7. Photo-Kolbe reaction of acetic acid.



Scheme 2-8. (Photocatalytic) acetic acid reforming.

The network for CH_3CHO oxidation is summarized in Scheme 2-9. CH_3CHO is oxidized with a low rate to CH_3COOH , which decomposes to CH_4 and CO_2 or is oxidized to CO_2 . Thus, the acetic acid and CH_4 observed in EG photoreforming stem from the photoreforming of acetaldehyde (Figure 2-4B). We cannot speculate on the routes for the photoreforming of acetic acid, because potential intermediates were not observed. It is hypothesized that these intermediates react much faster than acetaldehyde and acetic acid. The slow photoreforming rate of acetic acid indicates that an α -oxygen-functionalized carbon is needed for efficient hole transfer. The corresponding α -hydroxy functionalized acetic acid (glycolic acid) was photoreformed with high rate ($200 \mu\text{mol H}_2 \text{ h}^{-1}$ at 20 mM, Figure 2-8) without decarboxylation due to the absence of methanol formation.



Scheme 2-9. Deduced reaction network for the photocatalytic acetaldehyde photoreforming over Rh/TiO_2 .

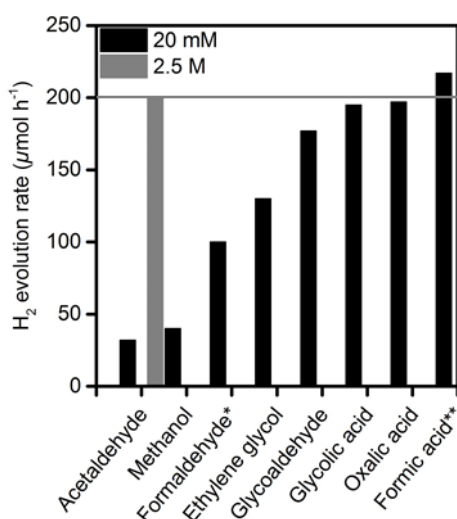
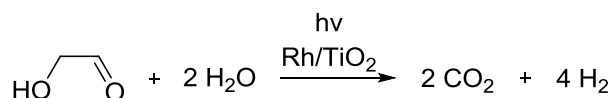


Figure 2-8. Comparison of H₂ evolution rates of various C1- and C2-oxygenates. *concentration of formaldehyde could not be exactly determined due to polymerization in the NMR-tube. **Concentration of formic acid was 10 mM in order to keep a pH of 3.

2.4.2.3. Photoreforming of Glycolaldehyde over Rh/TiO₂

Photoreforming of glycolaldehyde (Scheme 2-10, Figure 2-9), the primary product of EG photoreforming, yielded formaldehyde (1082 μmol after 12 h) and formic acid (65 μmol after 12 h) as main intermediates besides small quantities of acetaldehyde (41 μmol after 12 h) and acetic acid (3 μmol after 12 h) (Figure 2-9B).



Scheme 2-10. (Photocatalytic) glycolaldehyde reforming.

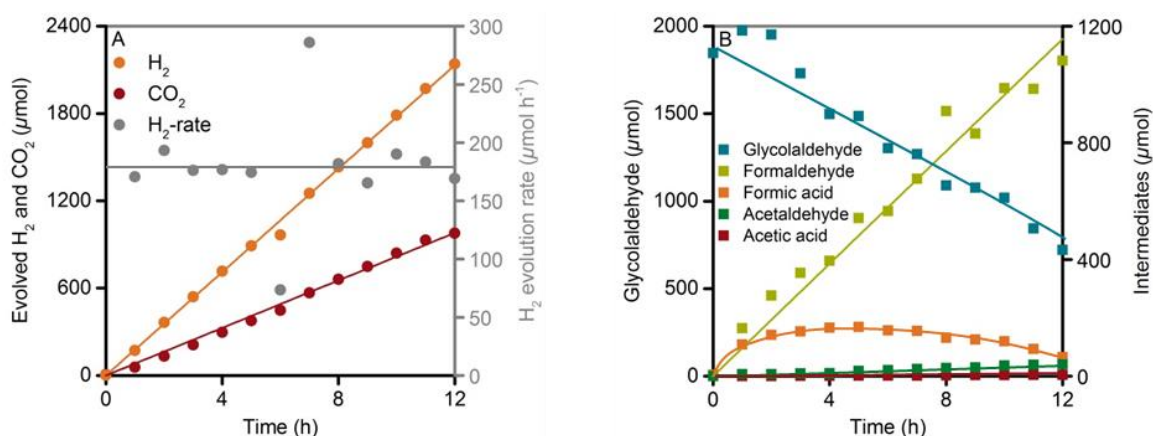


Figure 2-9. Analysis of gaseous and liquid species generated/transformed during glycolaldehyde photoreforming. Course of (A) gaseous and (B) liquid species. Lines serve to guide the eye. Reaction conditions: 75 mg Rh/TiO₂, 100 mL aqueous glycolaldehyde solution (20 mM), 288 K, 1 bar Ar, 300 W Xe-lamp (CM1).

As the amounts of acetaldehyde were very small, this path was considered as a side reaction and will not be discussed further at this point.

The formation of formaldehyde and formic acid, on the other hand, suggested that glycolaldehyde was preferentially oxidized *via* C–C-bond cleavage. Equimolar concentrations of formaldehyde and formic acid were, however, not observed, because HCOOH rapidly decomposed to CO₂ and H₂. Accordingly, the sum of CO₂ and HCOOH were equal to the amounts of HCHO (Figure 2-10). The high rate of HCOOH conversion is striking in the light of the negligible conversion of HCHO (see Scheme 2-11 for the reaction network). The H₂ evolution rate was higher for glycolaldehyde photoreforming (180 μmol H₂ h⁻¹, 20 mM, Figure 2-9) than for EG reforming (130 μmol H₂ h⁻¹, 20 mM, Figure 2-5). Differently to EG photoreforming, a constant H₂ evolution rate was observed during glycolaldehyde photoreforming and corresponds to a constant surface coverage of glycolaldehyde throughout the reaction period. This different kinetic behavior points to a higher adsorption strength of glycolaldehyde compared to ethylene glycol. As glycolaldehyde conversion is initiated by oxidative C–C-bond cleavage, while the OH-group of EG is oxidized to a formyl group, the higher rate of glycolaldehyde conversion than EG conversion suggests in addition that the rate of C–C-bond cleavage does not limit the forward rate of polyol photoreforming.

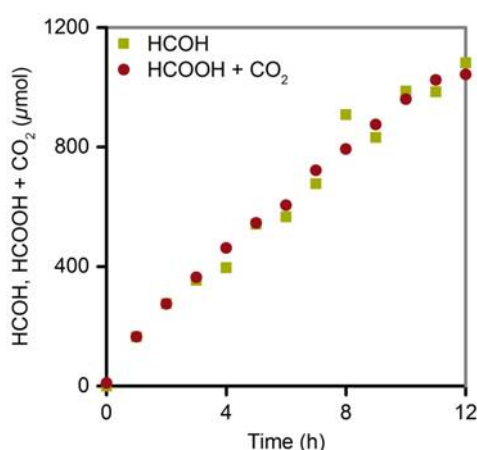
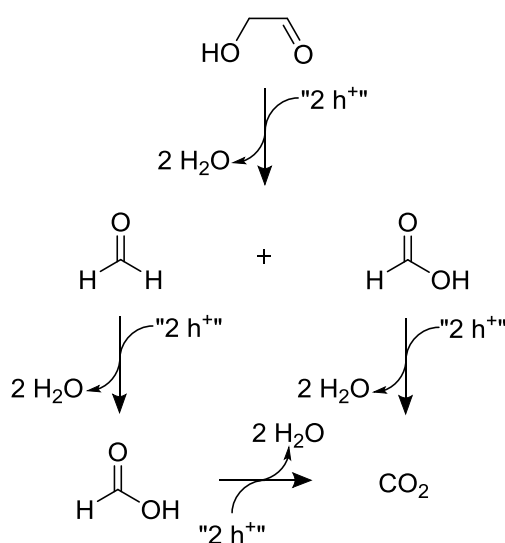


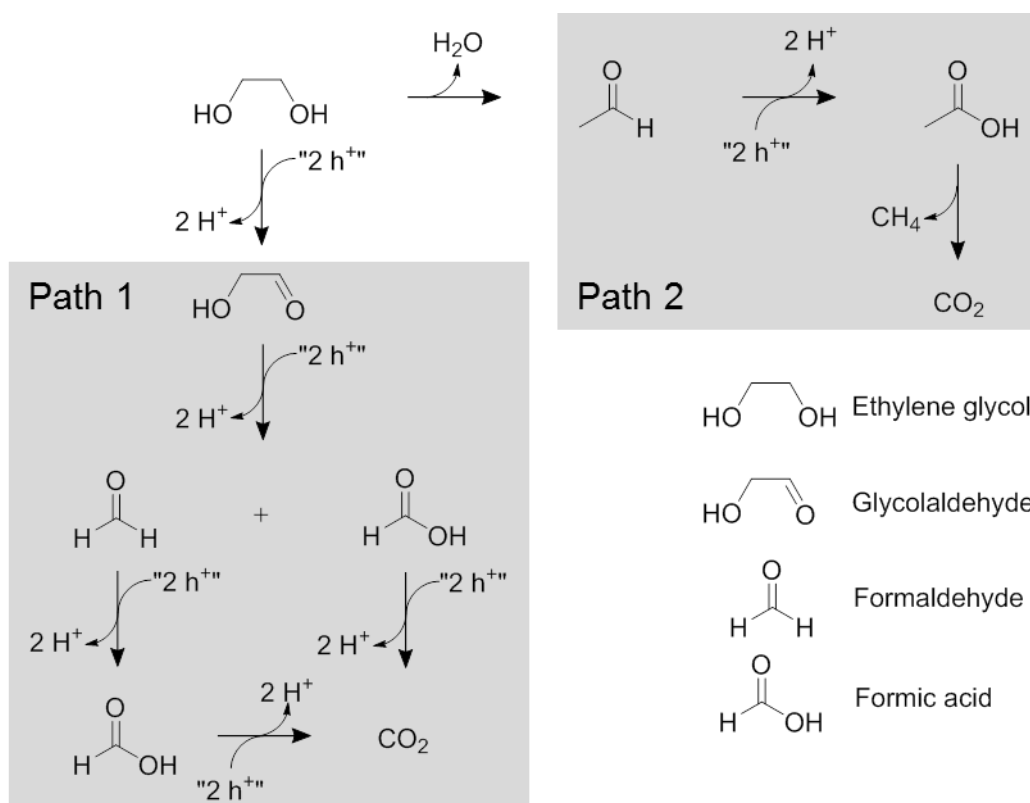
Figure 2-10. Comparison of amounts of detected formaldehyde (HCOH) and totalized amounts of detected formic acid (HCOOH) and CO₂ for the photocatalytic glycolaldehyde reforming. Reaction conditions: 75 mg Rh/TiO₂, 100 mL aqueous glycolaldehyde solution (20 mM), 288 K, 1 bar Ar, 300 W Xe-lamp (CM1).



Scheme 2-11. Deduced reaction network for the photocatalytic glycolaldehyde reforming (GlyAl#1) over Rh/TiO₂ based on quantitative liquid and gas phase analysis.

2.4.2.4. Overall Reaction Network of EG Photoreforming over Rh/TiO₂

Combining the individual reaction pathways allows deducing the overall reaction network of the photocatalytic EG reforming shown below in Scheme 2-12. Acetaldehyde was detected with a constant selectivity of 7.1% within 12 h reaction time considering only liquid phase intermediates (Figure-SI 2-3A). Because the reactivity of acetaldehyde was very low and only trace amounts of CH₄ (from decarboxylation of acetic acid) were detected, the formation of CO₂ *via* conversion of acetaldehyde to acetic acid and subsequent decarboxylation is concluded to be negligible. Thus, Path 2, dehydration of EG to acetaldehyde is only a side reaction. After 12 h, CO₂ accounted for 42% of all converted carbon, the remaining 58% in the liquid phase was predominantly formaldehyde with minor amounts of glycolaldehyde, acetaldehyde and formic acid (Figure-SI 2-3B). Thus, EG is concluded to react with a selectivity of approximately 93% *via* the formation of the intermediates glycolaldehyde, formaldehyde and formic acid to CO₂ (Path 1).



Scheme 2-12. Deduced reaction network for the photocatalytic ethylene glycol reforming (EG#1) over Rh/TiO₂ based on quantitative liquid and gas phase analysis.

These results suggest that the pathways proposed by Kondarides *et al.*⁶ for glycerol on 0.5 wt.% Pt/TiO₂ concerning the transformations of the intermediates acetaldehyde and glycolaldehyde are unlikely. The latter intermediate was suggested to oxidize *via* decarbonylation upon formation of one equivalent of methanol. The absence of CO was explained by photocatalytic water-gas shift, as suggested for alcohol photoreforming over Pd/TiO₂,²⁸ thermal reforming of EG,^{29,30} and electrochemical EG oxidation.³¹⁻³³

We can rule out this pathway because of the low rate of the photocatalytic water-gas shift reaction ($0.4 \mu\text{mol H}_2 \text{ h}^{-1}$) on 1 wt.% Rh/TiO₂, which is in agreement with the low quantum efficiency of 0.5% reported in literature.³⁴ In contrast, for the photocatalytic alcohol reforming typically quantum efficiencies between 20% to 40% for noble metal supported on TiO₂ have been reported and are confirmed in this study.¹ Thus, we conclude that in the present case the C–C-cleavage of glycolaldehyde occurs *via* a one electron release for each carbon atom leading to the formation of stoichiometric amounts of formaldehyde and formic acid that undergoes dehydrogenation.

2.4.2.5. Influence of the Co-catalyst on the Anodic Reaction Network

Rh nanoparticles, obtained by reduction with H₂, may undergo oxidative disruption after CO adsorption accompanied with the formation of Rh(I)-dicarbonyls, which may influence individual reaction steps.³⁵ In order to investigate their potential influence on the anodic reaction network, photocatalytic EG reforming was studied on 1 wt.% Pt/TiO₂. Comparison of the selectivities (Figure-SI 2-3, Table-SI 2-1) shows that the reaction pathways observed on Rh/TiO₂ (Scheme 2-12) are identical to the pathways on Pt/TiO₂. Both act only as sites for H₂ evolution.

2.4.3. Determination of Adsorption Constants by Kinetic Modeling

Systematic variation of the initial EG concentration led to H₂ evolution rates, which seemed to follow a Langmuir adsorption based rate equation (2-1) (Figure 2-11).

$$\frac{dc}{dt} = r^{app} \cdot \theta^{app} = r^{app} \cdot \frac{K^{L,app}c}{1 + K^{L,app}c} = r^{app'} \cdot I^n \cdot \frac{K^{L,app}c}{1 + K^{L,app}c}; \text{ with } n = 0.5 \text{ or } 1 \quad (2-1)$$

where dc/dt is the reaction rate of a reactant (mM min⁻¹), r^{app} is its maximal apparent rate constant (mM min⁻¹), θ^{app} is the apparent surface coverage (%), $K^{L,app}$ is the apparent Langmuir adsorption constant (L mmol⁻¹) and c is the concentration of the reactant (mmol L⁻¹), $r_i^{app'}$ is the maximal, light-intensity independent rate constant (mM min⁻¹) and I^n is the photon flux depending on the reaction order n of e⁻/h⁺-recombination. This kinetic behavior had been obtained for numerous (an)aerobic reactions as summarized in chapter 1.5.1. It had been further observed that the maximal apparent rate constants (r^{app}) of various reactants is identical.³⁶ Hence, the maximal apparent rate is independent of the chemical bond transformation, e.g., C–C-bond rupture or hydroxy group oxidation, purposing that the kinetics are predominantly governed by the apparent Langmuir adsorption constant $K^{L,app}$. At first glance, this fact seemed not to be applicable for the photoreforming of C1- and C2-oxygenates (20 mM) because different H₂ evolution rates were obtained (Figure 2-8).⁷ Here, formic acid, oxalic acid, glycolic acid and glyoxylic acid exhibited identical maximum activities of around 200 μmol H₂ h⁻¹, whereas an apparent H₂ evolution rate of 40 μmol h⁻¹ was obtained for methanol. However, when the concentration of methanol was increased to 2.5 M, also an activity of 200 μmol H₂ h⁻¹ was observed. Thus, it is hypothesized that the observed

H₂ evolution rates depend only on the surface coverage determined by the specific adsorption constant of the oxygenate. This implies that the intrinsic rate constants of the oxidations are only subtly influenced by the nature of the substrate and equation (2-1) considering an identical maximal apparent rate constant k^{app} (200 $\mu\text{mol H}_2 \text{ h}^{-1}$) is applicable.

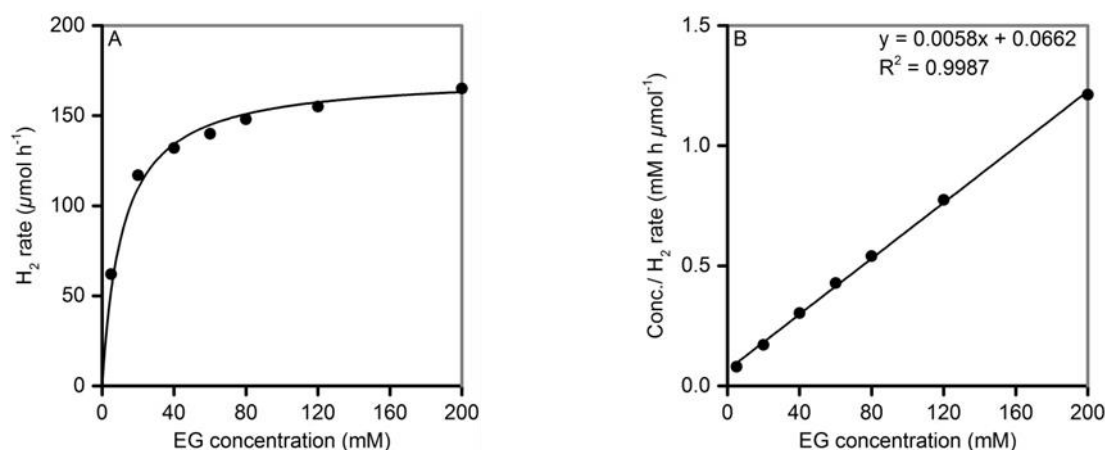


Figure 2-11. (A) Plot of H₂ evolution rates versus ethylene glycol concentrations and obtained Langmuir adsorption based rate curve. (B) Linearized plot for verification, that ethylene glycol photoreforming kinetics are governed by surface concentration of substrates adsorbed on the photocatalyst surface in a Langmuirian fashion. Reaction conditions: 75 mg Rh/TiO₂, 100 mL aqueous ethylene glycol solution (20 mM), 288 K, 1 bar Ar, 300 W Xe-lamp (CM1).

In order to describe an entire reaction network, competitive adsorption of n species has to be considered according to equation (2-2)

$$\frac{dc_i}{dt} = \frac{k^{app} \cdot K_i^{L,app} \cdot c_i}{1 + \sum_{i=1}^n K_i^{L,app} \cdot c_i} \quad (2-2)$$

where dc_i/dt is the reaction rate of reactant i (mM min^{-1}), k^{app} is the maximum apparent rate constant of the component i (mM min^{-1}), $K_i^{L,app}$ is the apparent Langmuir adsorption constant of component i (L mmol^{-1}) and c_i is the concentration of component i (mmol L^{-1}). The denominator describes competitive adsorption of n chemical species.

Recently, simultaneous systematic perturbation of reactant concentration c and of the light intensity I for the same photocatalytic system disclosed that the apparent rate constant r_i^{app} as well as the apparent Langmuir adsorption constant $K_i^{L,app}$ of equation (2-1) depend on the light intensity.³⁷⁻⁴⁰ A dependence on the light intensity is to be expected for r_i^{app} in contrast to $K_i^{L,app}$ according to equation (2-1). Ollis *et al.*²³

showed that a pseudo steady state hypothesis leads to a rate equation (2-3) in Langmuir-Hinshelwood form containing an apparent adsorption constant $K^{DA,app}$,

$$\frac{dc}{dt} = \frac{k^{app} \cdot K^{DA,app} \cdot c}{1 + K^{DA,app} \cdot c} \quad (2-3)$$

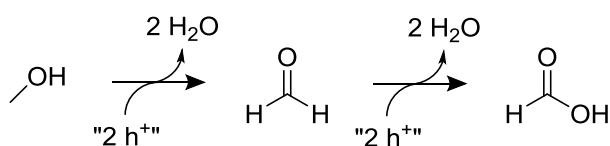
which can be easily transformed to a term considering competitive adsorption of multiple intermediates (equation (2-4)).⁴¹

$$\frac{dc_i}{dt} = \frac{k^{app} \cdot K_i^{DA,app} \cdot c_i}{1 + \sum_{i=1}^n K_i^{DA,app} \cdot c_i} \quad (2-4)$$

where dc_i/dt is the reaction rate of reactant i (mM min^{-1}), k^{app} is a maximal apparent rate constant for each component i (mM min^{-1}), $K_i^{DA,app}$ is the apparent adsorption constant of component i (L mmol^{-1}) and c_i is the concentration of component i (mmol L^{-1}). The denominator describes competitive adsorption of n chemical species, while i is the subscript to denote each of this n chemical species. The apparent adsorption constant K_i^{app} (dimensionless) can be obtained from $K_i^{DA,app} \cdot c_S$, where $K_i^{DA,app}$ is multiplied with the solvent molar concentration c_S (here: water, $55508 \text{ mmol L}^{-1}$).⁴²

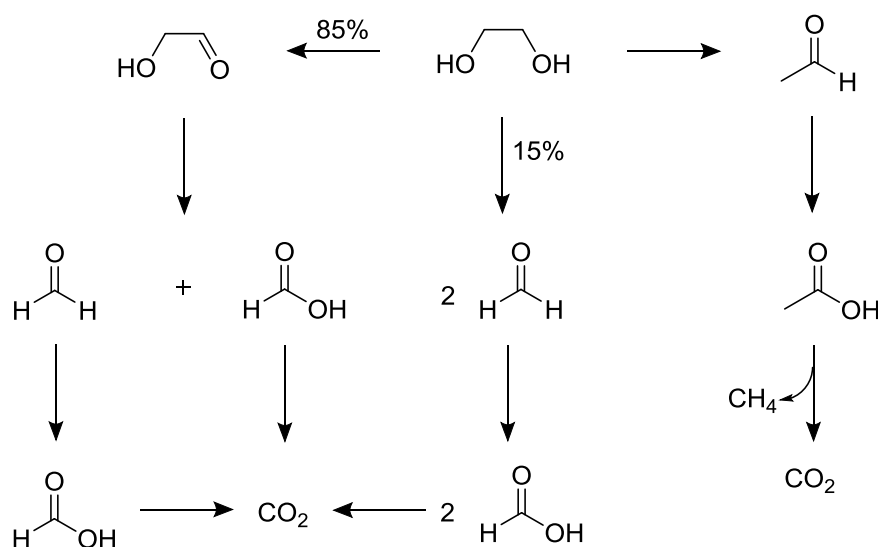
Experimental data were fitted using two built-in MATLAB subroutines. Minimization of the objective function was carried out with a CMA-ES algorithm and the numerical integration of the differential equations was carried out using ode45-function.

In order to obtain general and reliable fitting parameters, the apparent adsorption constants were determined by fitting the photoreforming kinetics of several compounds, namely ethylene glycol, glycolaldehyde and methanol. The methanol photoreforming reaction was chosen because the anodic oxidation proceeds *via* formaldehyde and formic acid.¹⁶ The maximum rate of $200 \mu\text{mol H}_2 \text{ h}^{-1}$ was used as constraint. The reaction networks of glycolaldehyde and EG photoreforming were taken as basis to establish the system of differential equations with the form of Equation (2-4). The reaction network in Scheme 2-13 was used for methanol reforming.



Scheme 2-13. Deduced reaction network for the photocatalytic methanol reforming (MeOH#1) over Rh/TiO₂ based on quantitative liquid and gas phase analysis.

These boundary conditions led to adsorption constants of the reactants and intermediates involved in methanol and glycolaldehyde photoreforming that agree very well with the experimental data (Figure 2-12C-E). In contrast, the introduction of an additional reaction pathway was required in order to obtain an acceptable agreement for the data of EG reforming (Figure 2-12A-B), i.e., oxidative C–C-cleavage of EG to two equivalents of formaldehyde (Scheme 2-14).



Scheme 2-14. Deduced reaction network for the photocatalytic ethylene glycol reforming (EG#2) over Rh/TiO₂ based on quantitative liquid and gas phase analysis and kinetic fitting.

Table 2-4 indicates the validity of this approach and the transferability of the results, as similar apparent adsorption constants, K^{app} , were obtained for each oxygenate in different photoreforming reactions. The determined values compare well with values reported in previous studies (Table-SI 2-2).⁴³⁻⁴⁵ The good fitting of the experimental data with the kinetic model confirms that the photocatalytic rates depend primarily on surface coverage. It should be highlighted that the apparent adsorption constant of formaldehyde is two orders of magnitude smaller than that of formic acid. Thus, we conclude that the low adsorption constant of formaldehyde causes its accumulation in the liquid phase during photoreforming reactions of EG, glycolaldehyde and methanol.

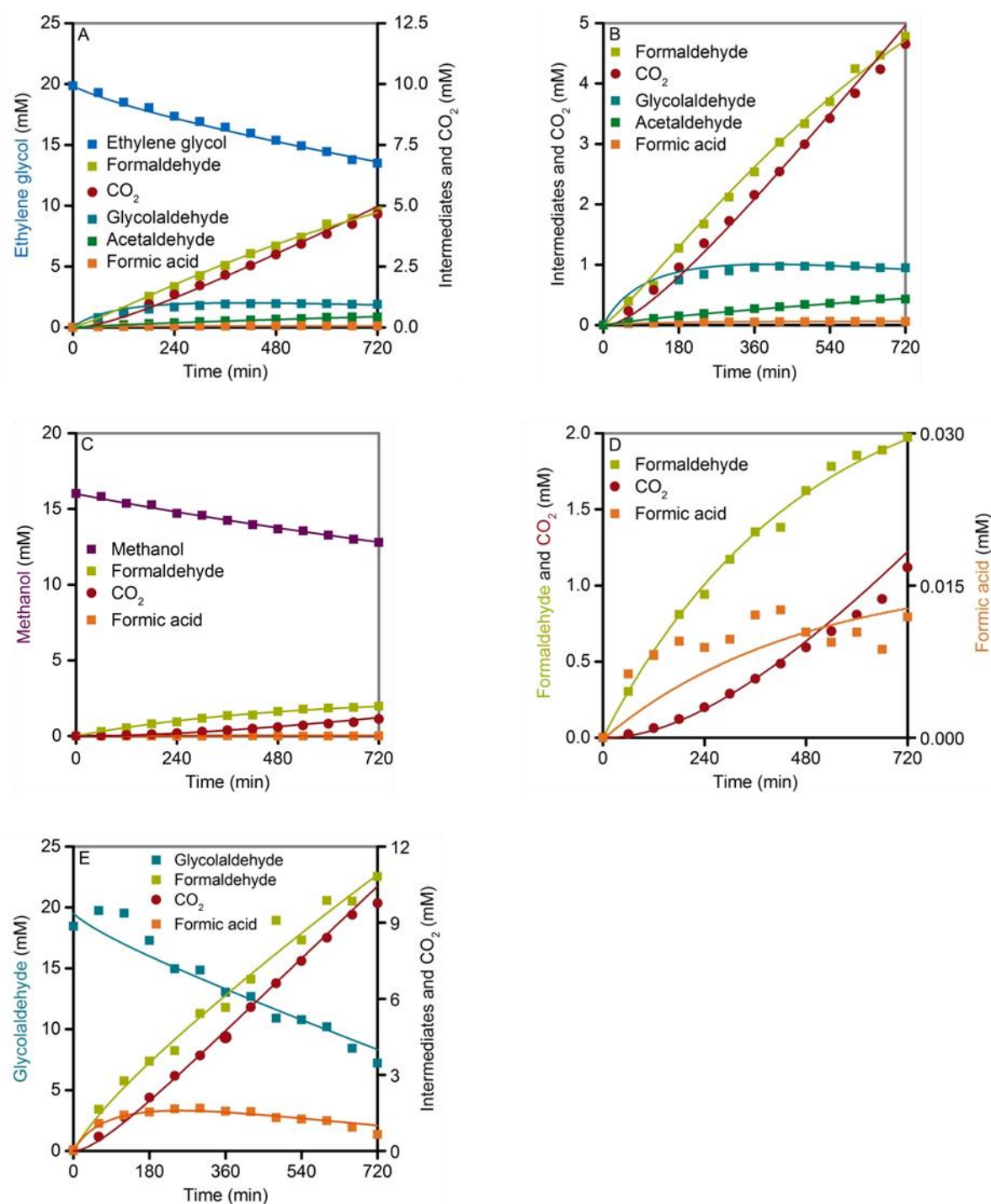


Figure 2-12. Experimental and predicted concentration profiles for various photoreforming reactions: ethylene glycol ((A) all anodic reactants and CO₂, (B) all anodic intermediates and CO₂); methanol ((C) all anodic reactants and CO₂, (D) all anodic intermediates and CO₂); glycolaldehyde (E). Assumptions: maximal apparent rate constant of 200 $\mu\text{mol H}_2 \text{ h}^{-1}$, proposed reaction networks for ethylene glycol, glycolaldehyde and methanol photoreforming shown in Scheme 2-14, Scheme 2-13 and Scheme 2-11, respectively.

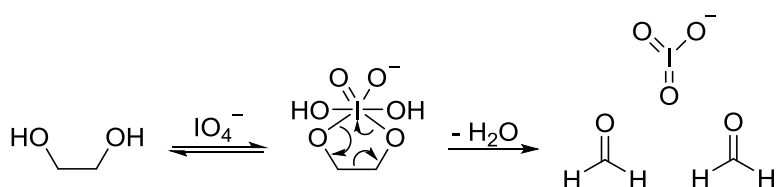
Table 2-4. Comparison of fitted adsorption constants (K^{app} , $\cdot 10^4$) of several C1- and C2-oxygenates from various photoreforming reactions at 288 K.

Probe molecule	Photoreforming reaction		
	Ethylene glycol	Glycolaldehyde	Methanol
Ethylene glycol	0.27	-	-
Glycolaldehyde	3.6	5.1	-
Methanol	-	-	0.068
Formaldehyde	0.34	0.26	0.32
Formic acid	77	49	48

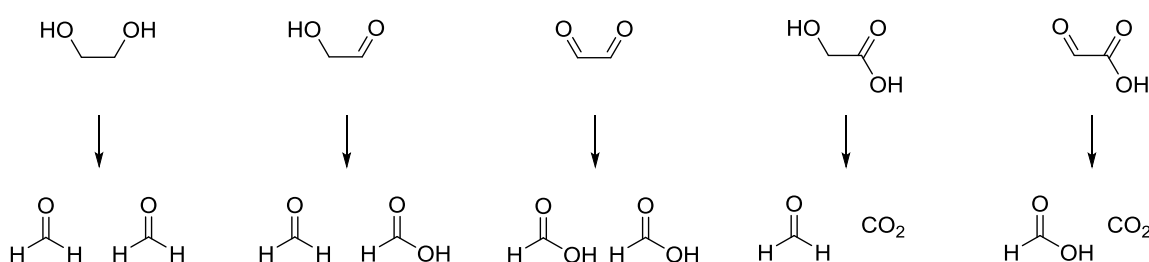
2.4.4. On the Elementary Steps of the Reaction Network

All anodic oxidations are attributed to direct electron transfer from the oxygenate to the hole and/or an indirect $\cdot\text{O}(\text{H})$ -radical driven oxidation. The existence and relative importance of these two pathways on TiO_2 has been extensively investigated.⁴⁶⁻⁵¹ Modeling of the oxidation kinetics in the present study shows that EG is oxidized to formaldehyde *via* C–C-bond cleavage (15%) as well as to glycolaldehyde (85%). The latter product is hypothesized to be generated *via* an $\cdot\text{O}(\text{H})$ -radical mediated mechanism following a Fenton's reagent like chemistry. $\cdot\text{O}(\text{H})$ -radicals, abstract a $\cdot\text{H}$ -atom in α -position; the resulting carbon centered radical is further oxidized to glycolaldehyde by losing a further $\cdot\text{H}$ atom. A Fenton's reagent mediated degradation of EG does not show HCHO formation, because the diol is gradually oxidized to oxalic acid before C–C-bond cleavage.^{52,53} Thus, oxidative C–C-bond rupture of EG to formaldehyde is concluded to be associated with a direct electron transfer in close resemblance to the reaction mechanism of a Malaprade periodic acid oxidation reaction. In this reaction, periodic acid ($E^0(\text{IO}_4^-/\text{IO}_3^-) = 1.60 \text{ V}$ at 298 K)⁵⁴ and EG form a five-membered cyclic ester. The C–C-bond is formally cleaved upon one electron transfer from each carbon atom to the iodine which is reduced to iodic acid (Scheme 2-15).⁵⁵ Photoreforming of any oxygenate functionalized with a sp^2 -hybridized α -oxygen over Rh/TiO_2 occurs exclusively *via* oxidative C–C-cleavage as neither hydroxy- nor formyl-groups are oxidized. The intermediates during photoreforming of these oxygenates, i.e., glyoxal, glycolic acid and glyoxylic acid, equaled the expected reactivity of the Malaprade oxidation reaction (Scheme 2-16). This implies that oxidation of sp^2 -hybridized α -oxygen functionalized C2-oxygenates occurs *via* direct hole-transfer. The α -carbon atom

must be functionalized with an oxygen containing group. In contrast, acetaldehyde is oxidized to acetic acid and C–C-cleavage occurs *via* photon induced decarboxylation (Photo-Kolbe reaction).



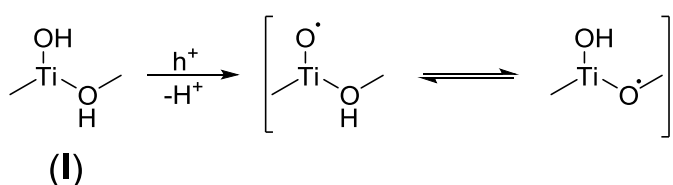
Scheme 2-15. Mechanism for cleavage of ethylene glycol with periodate.



Scheme 2-16. Expected products of the oxidation of C₂-oxygenate with periodate.

As oxygenates are oxidized *via* direct or indirect hole transfer, at least two different adsorption sites must exist. We hypothesize that these two active sites are (i) terminal OH-groups of Ti^{IV}-OH-sites and (ii) sites containing two Ti cations and a bridging oxygen in agreement with references 12 and 56.

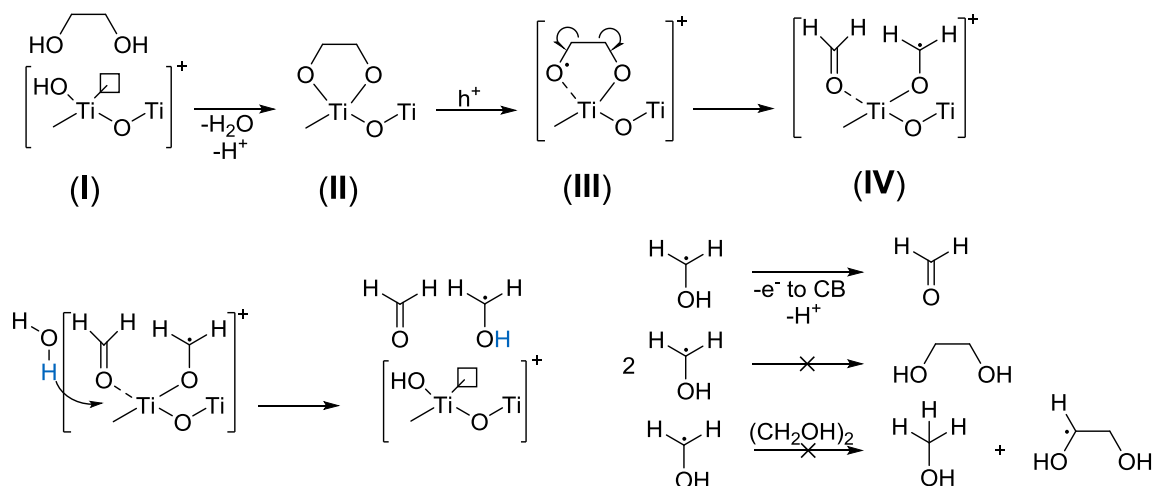
Scheme 2-17 schematically shows the surface structure of TiO₂ denoted as (I), which is subsequently described as Ti(OH)_T(O)_B (Scheme 2-17, Scheme 2-18).



Scheme 2-17. Schematic view of shallow surface trapped hole on TiO₂.

Titanium K-edge XANES studies⁵⁷ have shown that for small TiO₂ nanoparticles (~ 46 Å), dispersed in aqueous polyol solutions like EG, the coordination of unsaturated surface Ti atoms change almost quantitatively from square pyramidal to octahedral. These structural changes suggest that α -oxygen functionalized oxygenates chemisorb as chelating agents at the TiO₂-surface and this is discussed in detail in chapter 1.5.3.⁵⁷ Thus, the coordinatively unsaturated Ti(IV)-ion in the

$\text{Ti}(\text{OH})_{\text{T}}(\text{O})_{\text{B}}$ species is proposed to be a typical adsorption site for α -oxygen functionalized oxygenates, which catalyzes the selective C–C-cleavage of sp^2 -hybridized α -oxygen functionalized C2-oxygenates.



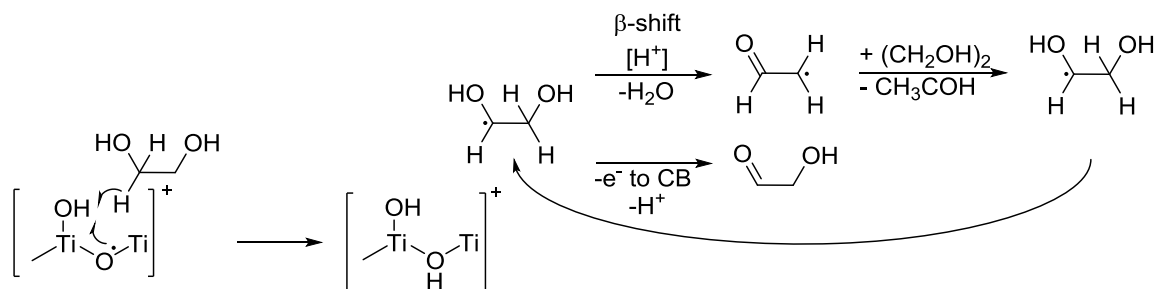
Scheme 2-18. Proposed anodic oxidation mechanism for C2-oxygenates adsorbing on $\text{Ti}^{\text{IV}}\text{-OH}$ -sites.

Upon coordination with EG the $\text{Ti}(\text{OH})_{\text{T}}(\text{O})_{\text{B}}$ site transforms to energetically deeper surface hole traps, $\text{Ti}(\text{OR})_{\text{T}}(\text{O})_{\text{B}}$ (II) (Scheme 2-18), which may allow direct hole transfer.¹² Upon occurrence, an alkoxy-radical (III) is formed, which may be oxidized by a second hole or may undergo direct β -C–C-cleavage. Under experimental conditions, the time between two photons reaching a TiO_2 particle ranges from 1 to 10 milliseconds (Figure-SI 2-4, Table-SI 2-3). For the least reactive *t*-alkoxy radical a rate constant for the β -scission of approximately $2 \cdot 10^3 \text{ s}^{-1}$ is determined at 313 K.⁵⁸ Further stabilization of the resulting $\cdot\text{CH}_x\text{O}_y(\text{H})$ -radical by adjacent lone-pairs of the oxygen would lead to even faster decomposition of species (III). Therefore, it is highly probable that the rate for β -scission is significantly higher than the rate for a second hole transfer. Indeed, preferential β -C–C-bond cleavage has been shown for free cyclic β -hydroxy alkoxide radicals upon formation of a linear di-aldehyde, demonstrating the rate enhancement by an adjacent oxygen lone pair stabilized radical.⁵⁹ In addition, rapid C–C-rupture has been observed for β -hydroxyalkoxy and other oxygen substituted alkoxy radicals with small activation energies ($29\text{-}40 \text{ kJ mol}^{-1}$) in the gas phase.⁶⁰

After β -C–C-cleavage of radical (III) (Scheme 2-18), formaldehyde and a $\cdot\text{CH}_2\text{O}(\text{H})$ -radical (IV) are formed. The latter is expected to readily hydrolyze under acidic conditions. Due to the large negative potential of the $\cdot\text{CH}_2\text{OH}$ -radical ($E^0(\text{CH}_2\text{O}/\cdot\text{CH}_2\text{OH}) = -0.97 \text{ V vs. NHE}$)⁶¹ an electron is injected into the conduction band of TiO_2 . This phenomenon (current-doubling) has been extensively studied for methanol as well as for various C1- and C2-oxygenates.⁶²⁻⁶⁴ It requires carbon-centered radicals, that in case of a direct hole transfer are only formed after β -C–C-cleavage.

For methanol and EG photoreforming, the same intermediate radical ($\cdot\text{CH}_2\text{OH}$) is formed. The absence of EG during glycolaldehyde photoreforming and the small rate of methanol photoreforming allows us to conclude that $\cdot\text{CH}_2\text{OH}$ -radicals are efficiently oxidized by current-doubling (Scheme 2-18). Our proposal is in line with aerobic oxidation studies of glycerol,¹² where a $\cdot\text{CHROH}$ -radical ($\text{R} = \text{H}$ or CH_2OH) is suggested as an intermediate. In the case of aerobic oxidation, the $\cdot\text{CHROH}$ -radical reduces oxygen.

The second site for the conversion of EG is postulated to be a $\text{Ti}(\text{OH})(\text{O}\cdot)$ shallow surface hole trap (Scheme 2-17 right, Scheme 2-19).



Scheme 2-19. Proposed anodic oxidation mechanism for C2-oxygenates interacting with $\text{Ti}(\text{OH})(\text{O}\cdot)$ shallow surface hole traps.

On these sites, a $\cdot\text{CHOHCH}_2\text{OH}$ -radical is formed upon H-atom abstraction. Because of its reductive potential, it can inject an electron into the conduction band of TiO_2 being oxidized to glycolaldehyde. Electron paramagnetic resonance experiments showed that $\cdot\text{CHOHCH}_2\text{OH}$ -radicals also can undergo acid-catalyzed β -H-shift ($\text{pH} < 3$) with subsequent dehydration upon formation of a carbon-centered acetaldehyde radical.⁶⁵ This carbon-centered radical can abstract an H-atom from another EG molecule leading to acetaldehyde. In homogeneous phase ($\text{pH} < 3$) the

rate constant of dehydration is determined as $7 \cdot 10^5 \text{ s}^{-1}$, which is orders of magnitude slower than the acid-catalyzed β -H-shift.⁶⁵

These studies show, that the light driven dehydration of EG (Scheme 2-12, pathway 2) is only a side reaction. Thus, e^- -injection of the $\cdot\text{CHOHCH}_2\text{OH}$ -radical into the conduction band is kinetically preferred compared to the acid-catalyzed β -H-shift of the radical connected with dehydration.

2.4.5. Origin of CO Formation

CO evolution was observed during C1- and C2-oxygenate photoreforming on Rh/TiO₂, with the exception of oxalic acid. The formation rate of CO strongly depended on the nature of the oxygenate (Figure-SI 2-5). High concentrations of CO evolved from oxygenates with formyl groups (e.g., glycolaldehyde) compared to those not containing formyl groups (e.g., EG) suggest that CO is formed by decarbonylation in agreement with proposals in the cases of electrocatalytic EG oxidation⁶⁶ and thermal aqueous phase reforming of EG.³⁰

In order to explore the origin of CO formation during photoreforming, each intermediate has been reacted over parent TiO₂. Due to the absence of the Rh co-catalyst, H₂ evolution was kinetically hindered. Thus, CO evolved from the reactant and not from an intermediate. Very little amounts of CO were detected from EG (1.4 μmol CO after 5 h), glycolaldehyde (9.0 μmol CO after 5 h) and formaldehyde (4.8 μmol CO after 5 h). In contrast, pronounced CO evolution occurred in case of formic acid photoreforming (216 μmol CO after 5 h). Thus, CO formation is concluded to be caused by dehydration of formic acid, in agreement with results from methanol photoreforming on Pt/TiO₂.^{13-16,67} In consequence, the CO evolution followed formic acid formation (Figure-SI 2-6). Indeed, there is a linear correlation between the surface coverage of formic acid (determined from the apparent adsorption constant) and the rate of CO formation (Figure 2-13). We emphasize at this point that both dehydrogenation and dehydration of formic acid are light-driven reactions. The active sites for the dehydration of formic acid are hypothesized to be formed only during the reaction, because an induction period was observed for CO evolution as discussed in chapter 2.4.2.1 (Figure 2-4B, Figure-SI 2-7B).

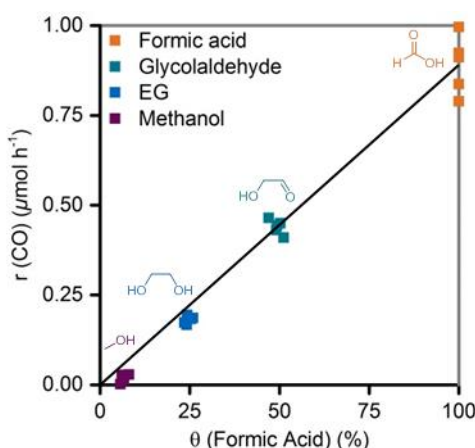


Figure 2-13. Origin of CO evolution. Correlation of rate of CO formation and calculated surface coverage of formic acid, using fitted apparent adsorption constants for various photoreforming reactions. Reaction conditions: 75 mg Rh/TiO₂, 100 mL aqueous oxygenation solution (20 mM), 288 K, 1 bar Ar, 300 W Xe-lamp (CM1).

2.4.6. EG Photoreforming on 1 wt.% Rh/GaN:ZnO

2.4.6.1. Kinetics of EG and Glycolaldehyde Photoreforming on Rh/GaN:ZnO

GaN:ZnO is much more labile against reduction than TiO₂. Thus, it had to be post-calcined in static air in order to remove Zn(0) surface defects, which act as electron-hole recombination centers.¹⁹ This led to a three-fold higher photocatalytic activity compared to non post-calcined GaN:ZnO. During the photoreforming experiments H₂ (698 μmol after 47 h) and CO₂ (237 μmol after 47 h) were detected (Figure 2-14A). A constant amount of O₂ (~ 2-4 μmol) was also observed during the experiments. This is attributed to the activity of Rh/GaN:ZnO for overall water-splitting (*vide infra*). The H₂ evolution rate, starting from 35 μmol H₂ h⁻¹, steadily decreased and stabilized at around 12 μmol H₂ h⁻¹. The lower level after this decrease corresponds to the photocatalytic activity of non post-calcined GaN:ZnO. Thus, we conclude that Zn(0) surface defects reappear during photoreforming. As the deactivation was observed for any oxygenate photoreformed over Rh/GaN:ZnO, it is concluded to be caused by the presence of H₂ or conduction band electrons rather than being induced by a specific surface chemistry of an organic reactant.

The formation rate of CO decreased over time as manifested by the steadily rising H₂ to CO-ratio (Figure 2-14B) (note that the opposite trend was observed over Rh/TiO₂). The absence of CH₄ indicates that EG is not dehydrated to acetaldehyde, the precursor of acetic acid and concomitant CH₄ (chapter 2.4.2.2). As acetaldehyde

is induced by surface-bound $\cdot\text{O}(\text{H})$ -radicals over Rh/TiO_2 , the absence of dehydration pathways is a direct consequence of the less positively located valence band of $\text{GaN}:\text{ZnO}$. In addition, an increased degree of mineralization was observed on $\text{Rh}/\text{GaN}:\text{ZnO}$ (H_2 to $\text{CO}_2 = 2.9$; H_2 : $698 \mu\text{mol}$) compared to Rh/TiO_2 (H_2 to $\text{CO}_2 = 3.5$, H_2 : $757 \mu\text{mol}$).

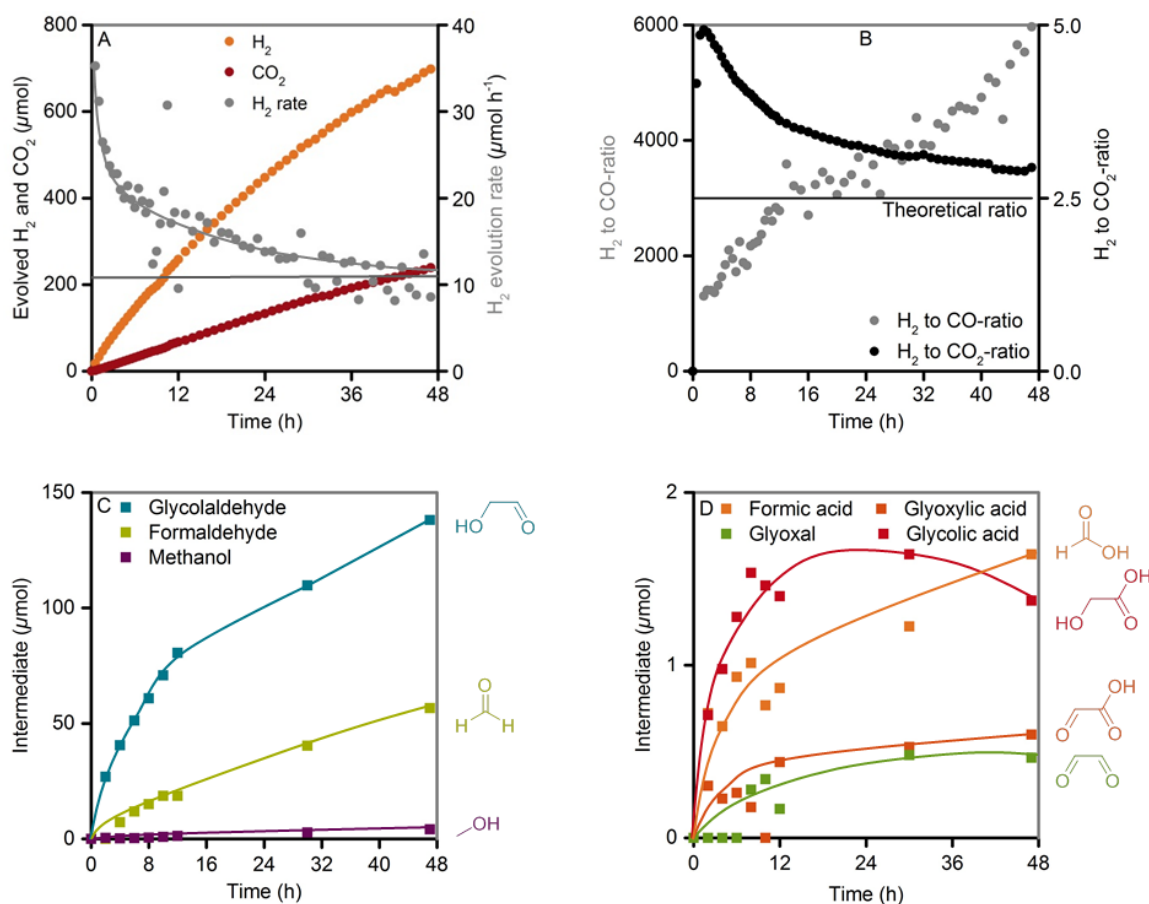


Figure 2-14. Analysis of gaseous and liquid species generated during ethylene glycol photoreforming. Course of (A) gaseous and liquid (C) main / (D) side intermediates as well as (B) H_2 to CO_2 - and H_2 to CO -ratio. Sloped lines serve to guide the eye. Reaction conditions: 75 mg Rh/TiO_2 , 100 mL aqueous ethylene glycol solution (20 mM), 288 K, 1 bar Ar, 300 W Xe-lamp (CM1).

In the liquid phase, glycolaldehyde ($138 \mu\text{mol}$ after 47 h) and formaldehyde ($57 \mu\text{mol}$ after 47 h) as well as a variety of C2-oxygenates, i.e., glycolic acid, glyoxal and glyoxylic acid (all $< 1.5 \mu\text{mol}$ after 47 h) were identified (Figure 2-14C-D). Thus, photoreforming of glycolaldehyde was explored to probe whether these higher oxidized C2-oxygenates are part of the main degradation pathways. Formaldehyde was the main intermediate, suggesting that glycolaldehyde was oxidized *via* C–C-

cleavage to formaldehyde and formic acid. In contrast to Rh/TiO₂, the amounts of formic acid and CO₂ exceeded the amounts of detected formaldehyde (Figure 2-15A). This was attributed to additional pathways, because the higher oxidized C₂-products (e.g., glyoxal (10 μmol after 47 h) or glycolic acid (27 μmol after 47 h)) showed that glycolaldehyde was not selectively converted to formaldehyde and formic acid (Figure 2-15B). The small concentration of formic acid, glycolic acid and glyoxylic acid during EG photoreforming (Figure 2-14C-D) was attributed to high adsorption constants in analogy to the observations over Rh/TiO₂.

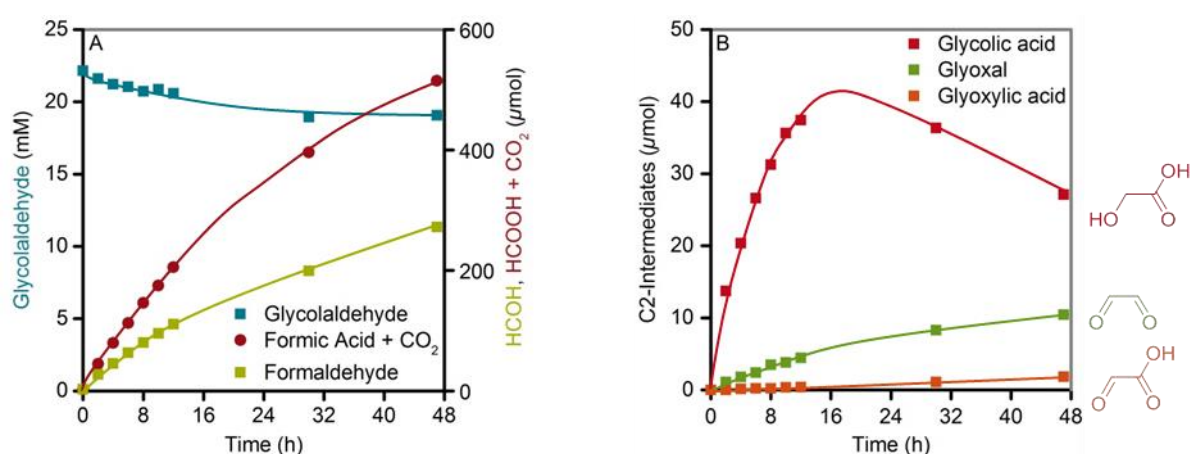
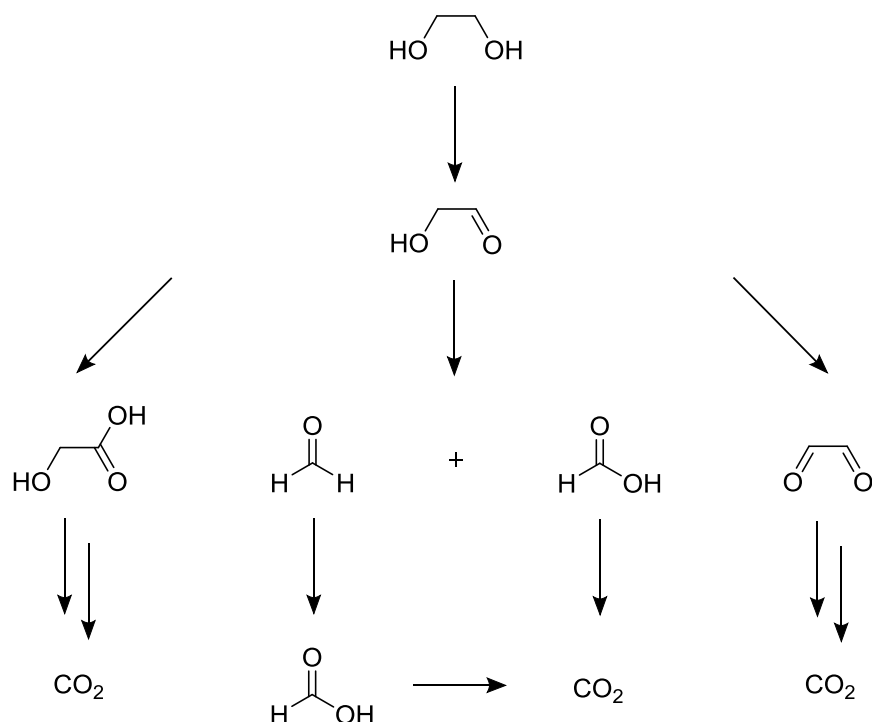


Figure 2-15. Analysis of gaseous and liquid species generated/transformed during glycolaldehyde photoreforming. (A) Course of concentration of glycolaldehyde and comparison of amounts of detected formaldehyde and totalized amounts of detected formic acid and CO₂. (B) Temporal profiles of minor intermediates. Reaction conditions: 75 mg Rh/GaN:ZnO, 100 mL aqueous glycolaldehyde solution (20 mM), 288 K, 1 bar Ar, 300 W Xe-lamp (CM1).

2.4.6.2. Impact of the Potential on Photoreforming - Catalysis on Rh/GaN:ZnO

Materials for visible-light driven photocatalytic H₂ evolution have a less positive valence band than TiO₂ (e.g., on GaN:ZnO, $V_{\text{GaN:ZnO}} = +1.72$ V vs. NHE).⁶⁸ In the case of GaN:ZnO, surface-bound hydroxyl radical mediated pathways are, therefore, excluded ($E^0(\cdot\text{OH}, \text{H}^+/\text{H}_2\text{O}) = +2.72$ V vs. NHE).⁶⁹ Rh/GaN:ZnO is, however, active for the overall water splitting reaction, implying that additional oxidizing species, such as free hydroxyl- ($\cdot\text{OH}$) or perhydroxyl-radicals ($\cdot\text{OOH}$), are formed. Thus, the lower anodic potential and additional oxidizing species induce a different anodic reaction network compared to Rh/TiO₂.

The proposed reaction network for the photoreforming of EG over Rh/GaN:ZnO is presented in Scheme 2-20.



Scheme 2-20. Deduced reaction network for photocatalytic ethylene glycol reforming on Rh/GaN:ZnO based on quantitative liquid and gas phase analysis.

The presence of higher oxygenated products of glycolaldehyde conversion over Rh/GaN:ZnO implies that additional mechanisms other than direct hole transfer exist. As no surface-bound $\cdot\text{O}(\text{H})$ -radicals can be formed, free perhydroxyl-radicals or hydroxyl-radicals resulting from reduced oxygen have to be responsible for the oxidation of ethylene glycol to glycolaldehyde and subsequently to glyoxal or glycolic acid. Thus, the free radicals open additional reaction pathways and glycolaldehyde is converted to higher oxidized C2-oxygenates. The generation of glyoxal and glyoxylic acid is of special interest as those species do not form formaldehyde (drawback for further applications due to its toxicity) after C–C-cleavage. In contrast, on Rh/TiO₂, α -oxygen functionalized sp²-hybridized C2-oxygenates interact selectively with terminal Ti^{IV}-OH groups and are oxidized *via* C–C-cleavage.

2.4.6.3. Comparison of CO-Evolution during EG Photoreforming on Rh/TiO₂ and Rh/GaN:ZnO

Photoreforming of EG over Rh/TiO₂ generates H₂ containing 975 ppm CO after 12 h, whereas a very CO-poor H₂ stream (180 ppm CO after 47 h) is obtained for the same reaction on Rh/GaN:ZnO (Figure 2-16). The course of CO evolution also strongly differs for these two photocatalysts. A steadily rising CO content is observed on Rh/TiO₂, whereas the opposite was observed on Rh/GaN:ZnO. After some accelerated initial formation, the CO evolution rate stabilizes on a very modest level ($\sim 0.1 \mu\text{mol CO h}^{-1}$). This low rate of CO formation is explained by the very low concentration of its intermediate precursor formic acid ($\sim 15 \mu\text{M}$) in contrast to Rh/TiO₂ ($\sim 60 \mu\text{M}$).

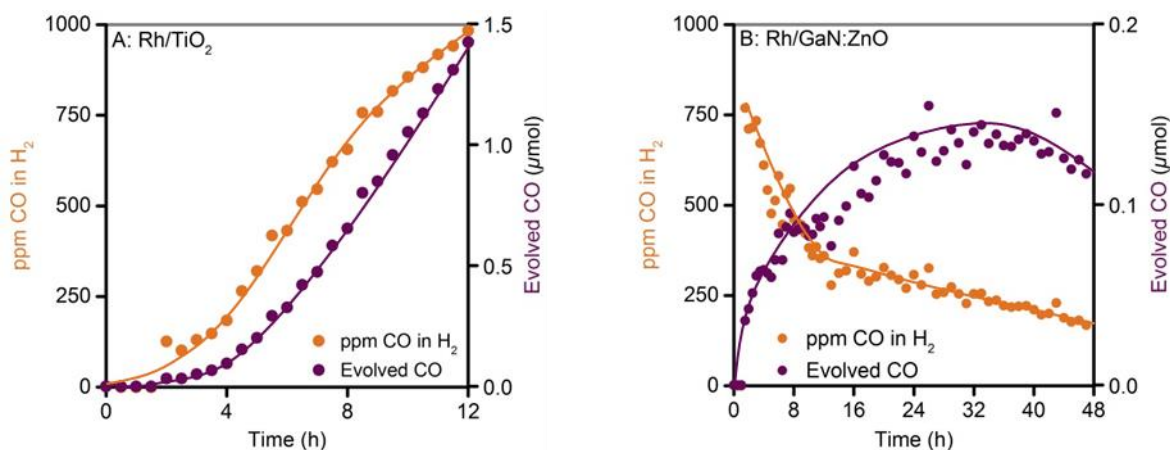


Figure 2-16. Course of CO-evolution and CO-content in evolved H₂ for photocatalytic ethylene glycol reforming on (A) Rh/TiO₂ and (B) Rh/GaN:ZnO. Reaction conditions: 75 mg Rh/GaN:ZnO, 100 mL aqueous ethylene glycol solution (20 mM), 288 K, 1 bar Ar, 300 W Xe-lamp (CM1).

2.4.7. Challenges for a Clean EG Photoreforming Process

Formaldehyde and CO, undesired byproducts for potential applications, were observed during EG photoreforming over Rh/GaN:ZnO and Rh/TiO₂. Thus, an experiment with increased photon flux on Rh/TiO₂ was performed in order to verify the course of both compounds at high EG conversions. The EG consumption followed first order kinetics (Figure 2-17A) because the chosen starting concentration (20 mM) led to a surface coverage in the Henry's regime (Figure 2-11). First order kinetics along the whole conversion range proved that

neither increasing CO concentration nor acetic acid (Figure-SI 2-7A, Table-SI 2-4), which is converted at slow rate, adsorb in appreciable concentration on cathode or anode.

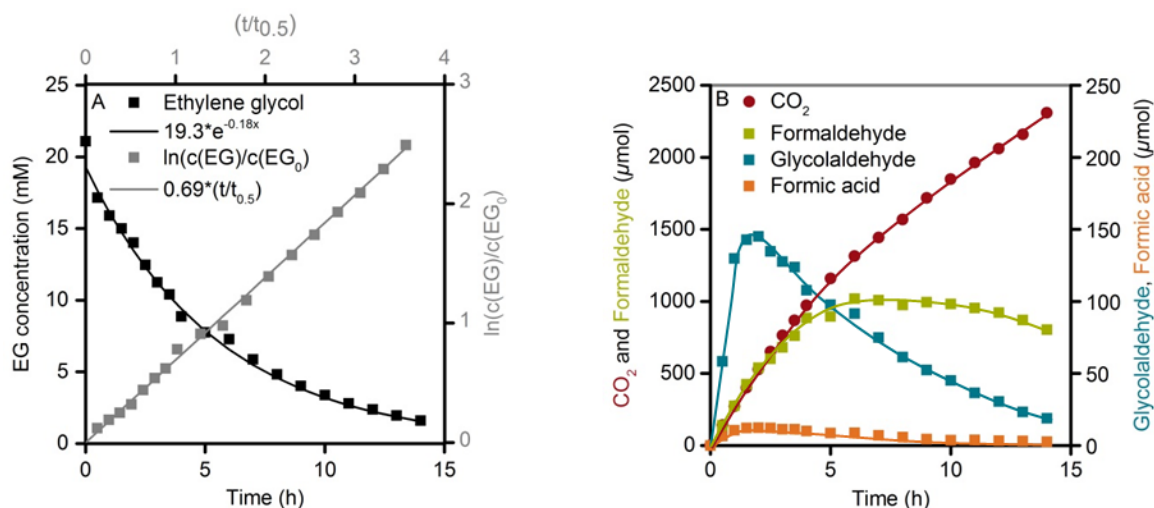


Figure 2-17. Ethylene glycol photoreforming with increased photon flux. **(A)** Course of ethylene glycol concentration and determination of reaction order. **(B)** Course of the main intermediates and CO_2 . Reaction conditions: 75 mg Rh/GaN:ZnO, 100 mL aqueous ethylene glycol solution (20 mM), 288 K, 1 bar Ar, 14 UV-LEDs (365 nm, 14.8 V, 400 mA).

During the first four hours of the experiment, almost equivalent amounts of formaldehyde (884 μmol) and CO_2 (973 μmol) were formed (Figure 2-17B). At this point, stoichiometric amounts of EG and formaldehyde were present and formation rate equaled the consumption rate. When most of the EG was converted (> 85%), the concentration of formaldehyde (~ 10 mM) declined. The decreasing competition of other reactants allowed a higher surface concentration of formaldehyde. Due to the small adsorption constant of formaldehyde, however, very low H_2 evolution rates were observed during the reaction even at high EG conversions (~ 200 $\mu\text{mol H}_2 \text{ h}^{-1}$ vs. initially 1100 $\mu\text{mol H}_2 \text{ h}^{-1}$). The CO content in relation to the evolved H_2 increased up to 5500 ppm before stabilization. The induction period (Figure-SI 2-7B) suggests that the active centers are formed during the illumination. In order to decrease CO formation, EG has to be selectively oxidized to oxalic acid which decarboxylates without CO formation.

2.5. Conclusions

Photoreforming of ethylene glycol (EG) has been found to be a process, in which the diol acts as sacrificial reductant at the anode to enable the reduction of H^+ . The anodic half reaction occurs *via* two pathways on Rh/TiO₂. The minor pathway proceeds *via* dehydration of EG to acetaldehyde, which is subsequently oxidized to acetic acid, which undergoes Photo-Kolbe reaction. In the dominant pathway EG is oxidized to glycolaldehyde or formaldehyde (*via* oxidative C–C-cleavage), with selectivities of 85% and 15%, respectively. Glycolaldehyde is subsequently converted *via* oxidative C–C-cleavage to formaldehyde and formic acid. Formaldehyde, on the other hand, oxidizes to formic acid, which dehydrogenates to CO₂. The sites proposed for the oxidative C–C-cleavage are terminal Ti^{IV}–OH groups, where the adsorbate is oxidized to an alkoxy-radical upon β -C–C-cleavage. Compounds with a sp²-hybridized α -oxygen interact with this reaction site converting to products that correspond to a Malaprade oxidation chemistry. On [Ti··O··Ti]⁺ oxidation occurs by abstracting an H-atom from the oxygenate producing a carbon centered radical, which is further oxidized causing current-doubling. CO evolves during the photoreforming of all C1- and C2-oxygenates (with the exception of oxalic acid).

The linear dependence of the surface coverage of formic acid and the rate of CO formation shows that the light-driven dehydration of formic acid is the source of CO. Identical, maximum H₂ evolution rates for the photoreforming of various C2-oxygenates, imply that the rates are independent of the nature of the reactant and the specific transformation of functional group, and C–C-cleavage under our reaction conditions. Together with the good fit of the experimental data to a Langmuir-type kinetic model led to conclude that H₂ evolution rates mainly depend on the concentration and adsorption strength of the specific oxygenate.

In the case of the EG photoreforming over Rh/GaN:ZnO the main conversion occurs *via* glycolaldehyde (as observed over Rh/TiO₂). Additional pathways *via* higher oxidized C2-oxygenates are induced by oxidizing radicals, e.g., ·OH, ·OOH, formed from oxygen due to the water-splitting reaction on Rh/GaN:ZnO. These new pathways avoid formaldehyde formation. Thus, while alcohols such as ethylene glycol can be readily oxidized at the photo-anode, under the present conditions

formaldehyde accumulates in the aqueous phase due to its small adsorption constant until all other compounds are consumed. Dehydration of the intermediate formic acid leads to considerable contents of CO in the H₂ produced.

2.6. Acknowledgements

Financial support from the Federal Ministry of Education and Research (BMBF) is gratefully acknowledged (project no. 01RC1106A). Productive discussions with Clariant within the framework of MuniCat and the iC⁴ PhotoCOO project were appreciated. Beam time at the BM25 station for XAFS experiments was thankfully provided by ESRF in Grenoble, France. The author thanks Kazuhiro Takanabe for fruitful discussions and scientific advice. Xaver Hecht is thanked for technical support as well as Christine Schwarz for assistance during NMR experiments, and Miriam Wehrle for her contributions to the graphical abstract.

2.7. References

- (1) Shimura, K.; Yoshida, H. *Energy Environ. Sci.* **2011**, *4*, 2467-2481.
- (2) Chen, X. B.; Shen, S. H.; Guo, L. J.; Mao, S. S. *Chem. Rev.* **2010**, *110*, 6503-6570.
- (3) Dionigi, F.; Vesborg, P. C. K.; Pedersen, T.; Hansen, O.; Dahl, S.; Xiong, A. K.; Maeda, K.; Domen, K.; Chorkendorff, I. *J. Catal.* **2012**, *292*, 26-31.
- (4) Kondarides, D. I.; Daskalaki, V. M.; Patsoura, A.; Verykios, X. E. *Catal. Lett.* **2008**, *122*, 26-32.
- (5) Nomikos, G. N.; Panagiotopoulou, P.; Kondarides, D. I.; Verykios, X. E. *Appl. Catal., B* **2014**, *146*, 249-257.
- (6) Panagiotopoulou, P.; Karamerou, E. E.; Kondarides, D. I. *Catal. Today* **2013**, *209*, 91-98.
- (7) Bahruji, H.; Bowker, M.; Davies, P. R.; Pedrono, F. *Appl. Catal., B* **2011**, *107*, 205-209.
- (8) Hara, M.; Nunoshige, J.; Takata, T.; Kondo, J. N.; Domen, K. *Chem. Commun.* **2003**, 3000-3001.
- (9) Lalitha, K.; Sadanandam, G.; Kumari, V. D.; Subrahmanyam, M.; Sreedhar, B.; Hebalkar, N. Y. *J. Phys. Chem. C* **2010**, *114*, 22181-22189.
- (10) Sakata, T.; Kawai, T. *Chem. Phys. Lett.* **1981**, *80*, 341-344.
- (11) Cargnello, M.; Gasparotto, A.; Gombac, V.; Montini, T.; Barreca, D.; Fornasiero, P. *Eur. J. Inorg. Chem.* **2011**, 4309-4323.
- (12) Minero, C.; Bedini, A.; Maurino, V. *Appl. Catal., B* **2012**, *128*, 135-143.
- (13) Ma, Y.; Xu, Q.; Zong, X.; Wang, D. G.; Wu, G. P.; Wang, X.; Li, C. *Energy Environ. Sci.* **2012**, *5*, 6345-6351.
- (14) Wu, G. P.; Chen, T.; Zong, X.; Yan, H. J.; Ma, G. J.; Wang, X. L.; Xu, Q.; Wang, D. G.; Lei, Z. B.; Li, C. *J. Catal.* **2008**, *253*, 225-227.
- (15) Xu, Q. A.; Ma, Y.; Zhang, J.; Wang, X. L.; Feng, Z. C.; Li, C. *J. Catal.* **2011**, *278*, 329-335.
- (16) Chiarello, G. L.; Aguirre, M. H.; Selli, E. *J. Catal.* **2010**, *273*, 182-190.
- (17) Maeda, K.; Hashiguchi, H.; Masuda, H.; Abe, R.; Domen, K. *J. Phys. Chem. C* **2008**, *112*, 3447-3452.
- (18) Maeda, K.; Teramura, K.; Lu, D. L.; Takata, T.; Saito, N.; Inoue, Y.; Domen, K. *Nature* **2006**, *440*, 295-295.
- (19) Maeda, K.; Teramura, K.; Domen, K. *J. Catal.* **2008**, *254*, 198-204.
- (20) Bamwenda, G. R.; Tsubota, S.; Kobayashi, T.; Haruta, M. *J. Photochem. Photobiol., A* **1994**, *77*, 59-67.
- (21) Yu, J. G.; Ran, J. R. *Energy Environ. Sci.* **2011**, *4*, 1364-1371.
- (22) Ollis, D. F.; Pelizzetti, E.; Serpone, N. In *Photocatalysis - Fundamentals and Applications*; Serpone, N., Pelizzetti, E., Eds.; John Wiley & Sons: New York, 1989, p 620-629.
- (23) Ollis, D. F. *J. Phys. Chem. B* **2005**, *109*, 2439-2444.
- (24) Mills, A.; O'Rourke, C.; Moore, K. *J. Photochem. Photobiol., A* **2015**, *310*, 66-105.
- (25) Maeda, K.; Sakamoto, N.; Ikeda, T.; Ohtsuka, H.; Xiong, A. K.; Lu, D. L.; Kanehara, M.; Teranishi, T.; Domen, K. *Chem. Eur. J.* **2010**, *16*, 7750-7759.
- (26) Kraeutler, B.; Bard, A. J. *J. Am. Chem. Soc.* **1978**, *100*, 5985-5992.

- (27) Gallo, A.; Marelli, M.; Psaro, R.; Gombac, V.; Montini, T.; Fornasiero, P.; Pievo, R.; Dal Santo, V. *Green Chem.* **2012**, *14*, 330-333.
- (28) Bowker, M.; Morton, C.; Kennedy, J.; Bahruji, H.; Greves, J.; Jones, W.; Davies, P. R.; Brookes, C.; Wells, P. P.; Dimitratos, N. *J. Catal.* **2014**, *310*, 10-15.
- (29) Davda, R. R.; Shabaker, J. W.; Huber, G. W.; Cortright, R. D.; Dumesic, J. A. *Appl. Catal., B* **2003**, *43*, 13-26.
- (30) Shabaker, J. W.; Davda, R. R.; Huber, G. W.; Cortright, R. D.; Dumesic, J. A. *J. Catal.* **2003**, *215*, 344-352.
- (31) Kim, H. J.; Choi, S. M.; Green, S.; Tompsett, G. A.; Lee, S. H.; Huber, G. W.; Kim, W. B. *Appl. Catal., B* **2011**, *101*, 366-375.
- (32) Wang, H.; Zhao, Y.; Jusys, Z.; Behm, R. J. *J. Power Sources* **2006**, *155*, 33-46.
- (33) Wang, H.; Jusys, Z.; Behm, R. J. *Electrochim. Acta* **2009**, *54*, 6484-6498.
- (34) Sato, S.; White, J. M. *J. Am. Chem. Soc.* **1980**, *102*, 7206-7210.
- (35) Panayotov, D.; Mihaylov, M.; Nihtianova, D.; Spassov, T.; Hadjiivanov, K. *Phys. Chem. Chem. Phys.* **2014**, *16*, 13136-13144.
- (36) Turchi, C. S.; Ollis, D. F. *J. Catal.* **1990**, *122*, 178-192.
- (37) Xu, Y. M.; Langford, C. H. *J. Photochem. Photobiol., A* **2000**, *133*, 67-71.
- (38) Meng, Y. B.; Huang, X.; Wu, Y. X.; Wang, X. M.; Qian, Y. *Environ. Pollut.* **2002**, *117*, 307-313.
- (39) Emeline, A. V.; Ryabchuk, V.; Serpone, N. *J. Photochem. Photobiol., A* **2000**, *133*, 89-97.
- (40) Martyanov, I. N.; Savinov, E. N. *J. Photochem. Photobiol., A* **2000**, *134*, 219-226.
- (41) Markham, E. C.; Benton, A. F. *J. Am. Chem. Soc.* **1931**, *53*, 497-507.
- (42) Milonjic, S. K. *J. Serb. Chem. Soc.* **2007**, *72*, 1363-1367.
- (43) Montoya, J. F.; Atitar, M. F.; Bahnemann, D. W.; Peral, J.; Salvador, P. *J. Phys. Chem. C* **2014**, *118*, 14276-14290.
- (44) Chowdhury, P.; Malekshoar, G.; Ray, M. B.; Zhu, J.; Ray, A. K. *Ind. Eng. Chem. Res.* **2013**, *52*, 5023-5029.
- (45) McMurray, T. A.; Byrne, J. A.; Dunlop, P. S. M.; Winkelman, J. G. M.; Eggins, B. R.; McAdams, E. T. *Appl. Catal., A* **2004**, *262*, 105-110.
- (46) Minero, C.; Mariella, G.; Maurino, V.; Pelizzetti, E. *Langmuir* **2000**, *16*, 2632-2641.
- (47) Salvador, P. *J. Phys. Chem. C* **2007**, *111*, 17038-17043.
- (48) Brookes, I. M.; Muryn, C. A.; Thornton, G. *Phys. Rev. Lett.* **2001**, *87*, 226103.
- (49) Howe, R. F.; Gratzel, M. *J. Phys. Chem.* **1987**, *91*, 3906-3909.
- (50) Henderson, M. A. *Surf. Sci. Rep.* **2002**, *46*, 1-308.
- (51) Imanishi, A.; Okamura, T.; Ohashi, N.; Nakamura, R.; Nakato, Y. *J. Am. Chem. Soc.* **2007**, *129*, 11569-11578.
- (52) McGinnis, B. D.; Adams, V. D.; Middlebrooks, E. J. *Chemosphere* **2001**, *45*, 101-108.
- (53) McGinnis, B. D.; Adams, V. D.; Middlebrooks, E. J. *Water Res.* **2000**, *34*, 2346-2354.
- (54) Dean, J. A. In *Lange's Handbook of Chemistry (15th edition)*; Dean, J. A., Ed.; McGRAW-HILL: New York, 1999, p 6.1-6.50.
- (55) Sklarz, B. Q. *Rev. Chem. Soc.* **1967**, *21*, 3-28.

-
- (56) Minella, M.; Faga, M. G.; Maurino, V.; Minero, C.; Pelizzetti, E.; Coluccia, S.; Martra, G. *Langmuir* **2010**, *26*, 2521-2527.
- (57) Shkrob, I. A.; Sauer, M. C.; Gosztola, D. *J. Phys. Chem. B* **2004**, *108*, 12512-12517.
- (58) Ingold, K. U. In *Free radicals, Vol. 1*; Kochi, J. K., Ed.; John Wiley & Sons: New York, 1973; Vol. 1, p 37-112.
- (59) Gu, X. D.; Zhang, W. J.; Salomon, R. G. *J. Org. Chem.* **2012**, *77*, 1554-1559.
- (60) Orlando, J. J.; Tyndall, G. S.; Wallington, T. J. *Chem. Rev.* **2003**, *103*, 4657-4689.
- (61) Micic, O. I.; Zhang, Y. N.; Cromack, K. R.; Trifunac, A. D.; Thurnauer, M. C. *J. Phys. Chem.* **1993**, *97*, 13284-13288.
- (62) Schneider, J.; Bahnemann, D. W. *J. Phys. Chem. Lett.* **2013**, *4*, 3479-3483.
- (63) Harada, H.; Ueda, T.; Sakata, T. *J. Phys. Chem.* **1989**, *93*, 1542-1548.
- (64) Hykaway, N.; Sears, W. M.; Morisaki, H.; Morrison, S. R. *J. Phys. Chem.* **1986**, *90*, 6663-6667.
- (65) Batchelor, S. N.; Heikkila, H.; Kay, C. W. M.; Mclauchlan, K. A.; Shkrob, I. A. *Chem. Phys.* **1992**, *162*, 29-45.
- (66) Wang, H.; Jusys, Z.; Behm, R. J. *J. Electroanal. Chem.* **2006**, *595*, 23-36.
- (67) Wu, G. P.; Chen, T.; Su, W. G.; Zhou, G. H.; Zong, X.; Lei, Z. B.; Li, C. *Int. J. Hydrogen Energy* **2008**, *33*, 1243-1251.
- (68) Hashiguchi, H.; Maeda, K.; Abe, R.; Ishikawa, A.; Kubota, J.; Domen, K. *Bull. Chem. Soc. Jpn.* **2009**, *82*, 401-407.
- (69) Schwarz, H. A.; Dodson, R. W. *J. Phys. Chem.* **1984**, *88*, 3643-3647.

2.8. Supporting Information

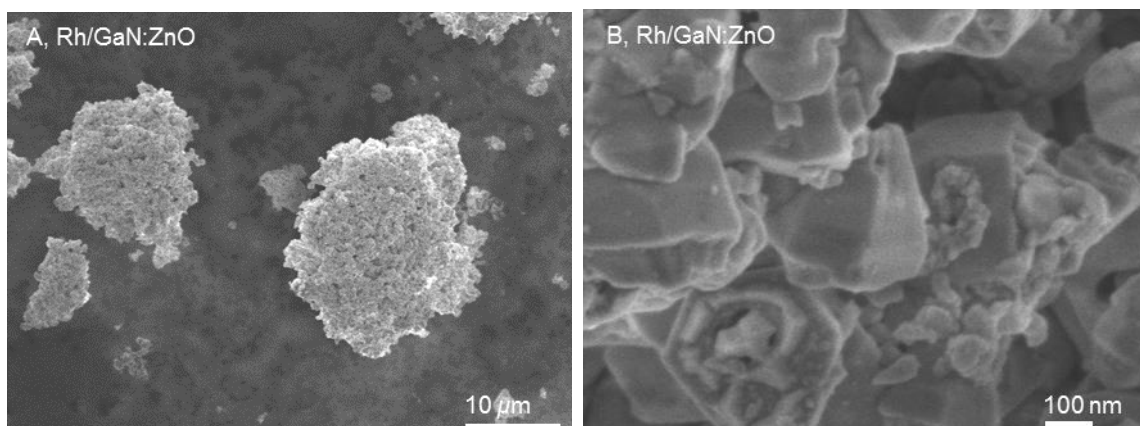


Figure-SI 2-1. HR-SEM of Rh/GaN:ZnO after photocatalysis test. **(A)** Typical particle consisting of agglomerated non-porous crystallites. **(B)** Shown in larger magnification.

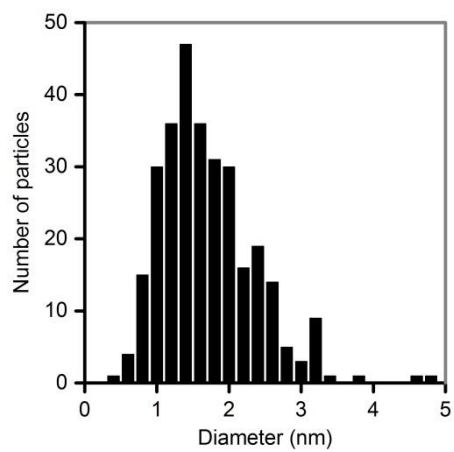


Figure-SI 2-2. Rh particle size distribution of 1 wt.% Rh/TiO₂ (300 measured Rh particles).

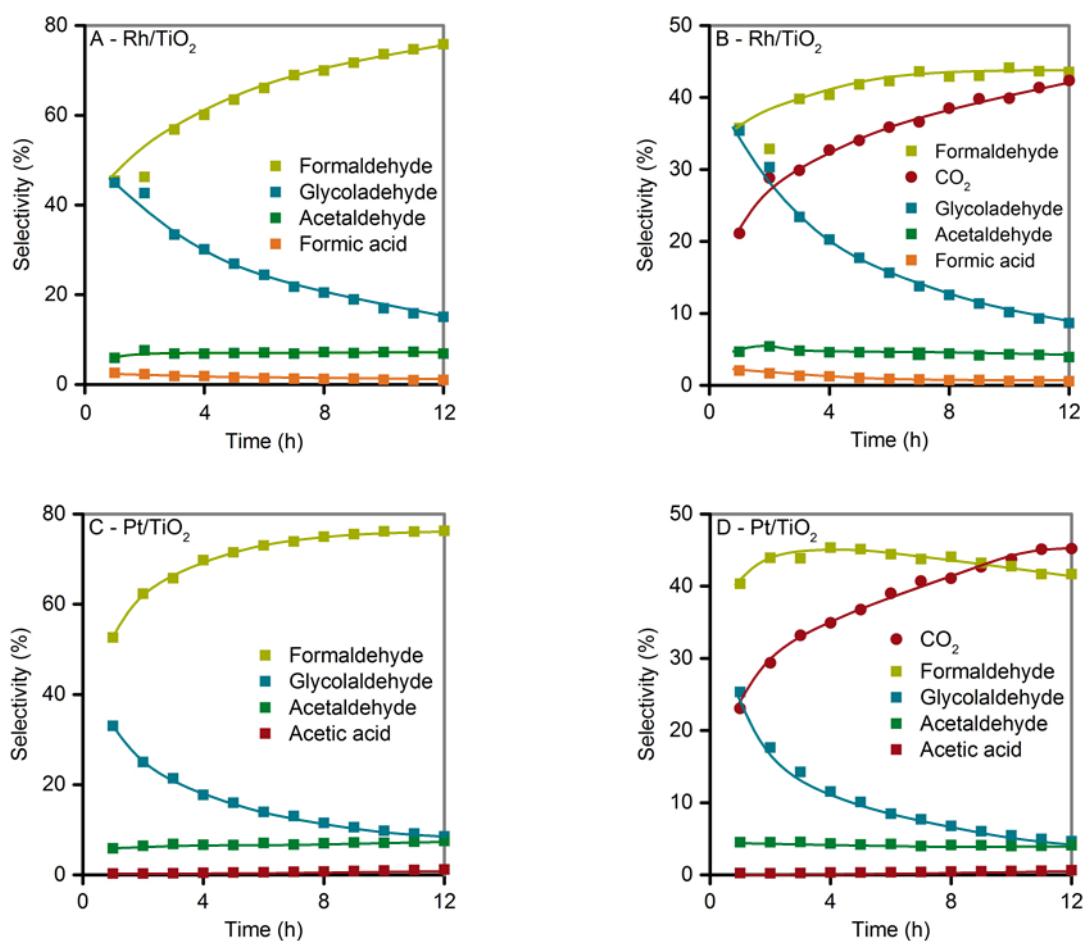


Figure-SI 2-3. Selectivities of intermediates (and CO₂) for ethylene glycol photoreforming on Rh/TiO₂ and Pt/TiO₂. (A, C) Selectivities of all relevant liquid intermediates (> 1%). (B, D) Selectivities of all relevant liquid intermediates (> 0.5%) and the reaction product CO₂. Reaction conditions: 75 mg Rh/TiO₂ or Pt/TiO₂, 100 mL aqueous ethylene glycol solution (20 mM), 288 K, 1 bar Ar, 300 W Xe-lamp (CM1).

Table-SI 2-1. Comparison of selectivities of formed organic intermediates and CO₂ for the photocatalytic ethylene glycol reforming on Rh/TiO₂ and Pt/TiO₂ at equivalent amounts of evolved H₂.

Photocatalyst		Rh/TiO ₂	Pt/TiO ₂	Rh/TiO ₂	Pt/TiO ₂	Rh/TiO ₂	Pt/TiO ₂
Reaction time	(h)	3	2	7	4	12	7
Evolved H ₂	(μ mol)	390	403	868	841	1449	1442
Acetaldehyde	(%)	4.8	4.5	4.4	4.3	3.9	4.1
Acetic acid	(%)	0.2	0.2	0.2	0.4	0.3	0.5
Glycolaldehyde	(%)	23.4	17.6	13.8	8.5	8.6	6.0
Formaldehyde	(%)	39.8	43.9	43.6	44.4	43.5	43.2
Formic acid	(%)	1.3	1.0	0.8	0.6	0.6	0.5
CO ₂	(%)	29.9	29.4	36.6	39.0	42.4	42.7
Methanol	(%)	0.8	3.2	0.8	2.7	0.8	2.9

Table-SI 2-2. Comparison of fitted apparent adsorption constants for formaldehyde and formic acid with reported values in the literature.

	Study	Formic acid	Formaldehyde	Description
Apparent adsorption constant [$\cdot 10^4$]	This study	48-77	0.26-0.34	1 wt.% Rh/TiO ₂ P 25, T = 288 K, $I_0 = 1.34 \mu\text{mol s}^{-1}$.
	Montoya <i>et al.</i> ⁴³	30	-	TiO ₂ (anatase, Sigma Aldrich), T = 296 K, dark.
	McMurray <i>et al.</i> ⁴⁵	12	-	TiO ₂ P 25, T = unknown, $I_0 (3.5 \cdot 10^{-4} \text{ Einstein m}^{-2} \text{ s}^{-1})$
	Chowdhury <i>et al.</i> ⁴⁴	-	0.10	0.25 wt.% Pt/TiO ₂ P 25, T = n.d., solar simulator (100 mW cm^{-2})

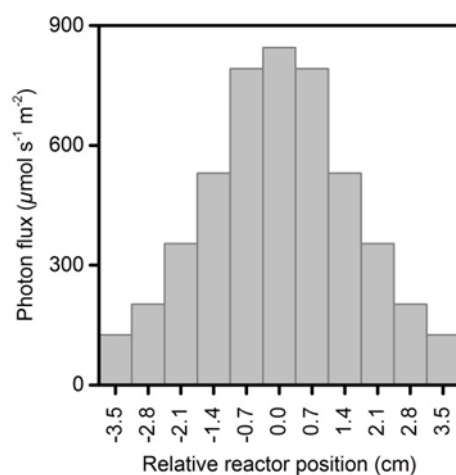


Figure-SI 2-4. Photon flux distribution of the used reactor configuration - averaged photon flux through aligned concentric rings with a width of 7 mm (200-390 nm). Conditions: 300 W Xe-lamp (CM1).

Table-SI 2-3. Calculated upper and lower time interval for e⁻/h⁺ pair generation for TiO₂ for the used photoreactor configuration.

	Photon flux cm ⁻² (nmol s ⁻¹ cm ⁻²)	Time interval for e ⁻ /h ⁺ - pair generation (ms)
Minimum	13	6.5
Average	30	2.7
Maximum	85	1.0

* $4.9 \cdot 10^{13}$ TiO₂ particles are estimated to be illuminated per square centimeter reactor area.

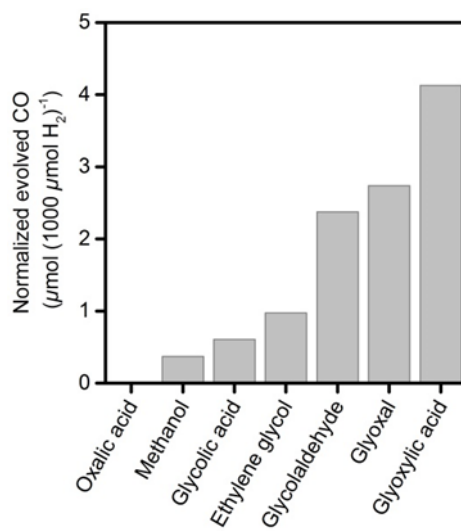


Figure-SI 2-5. Evolved CO normalized per 1000 μmol of evolved H_2 for various oxygenate photoreforming reactions. Reaction conditions: 75 mg Rh/TiO₂, 100 mL aqueous oxygenate solution (20 mM), 288 K, 1 bar Ar, 300 W Xe-lamp (CM1).

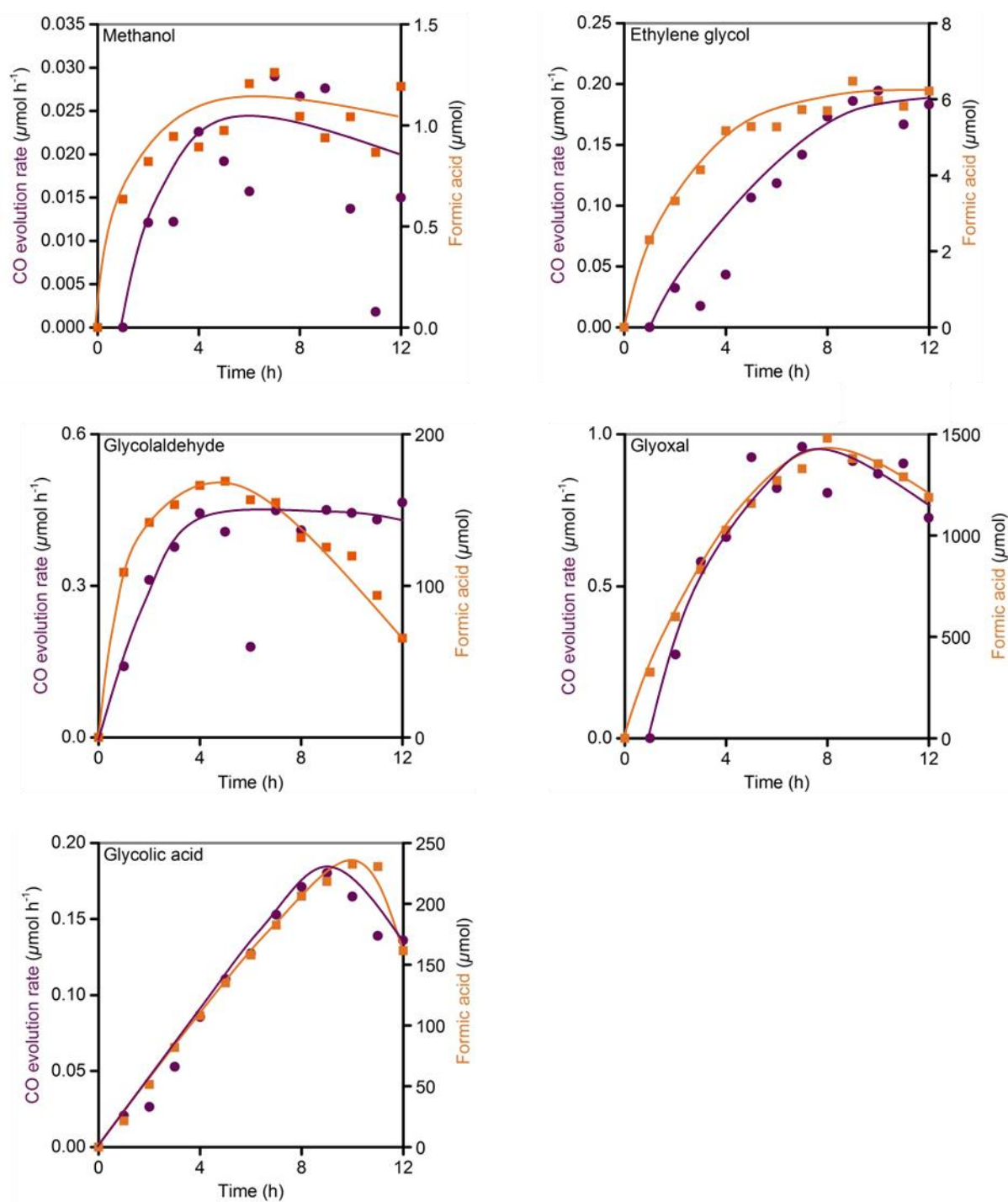


Figure-SI 2-6. Correlation of CO evolution rate with amounts of formed formic acid for various oxygenate photoreforming reactions. Reaction conditions: 75 mg Rh/TiO₂, 100 mL aqueous oxygenate solution (20 mM), 288 K, 1 bar Ar, 300 W Xe-lamp (CM1).

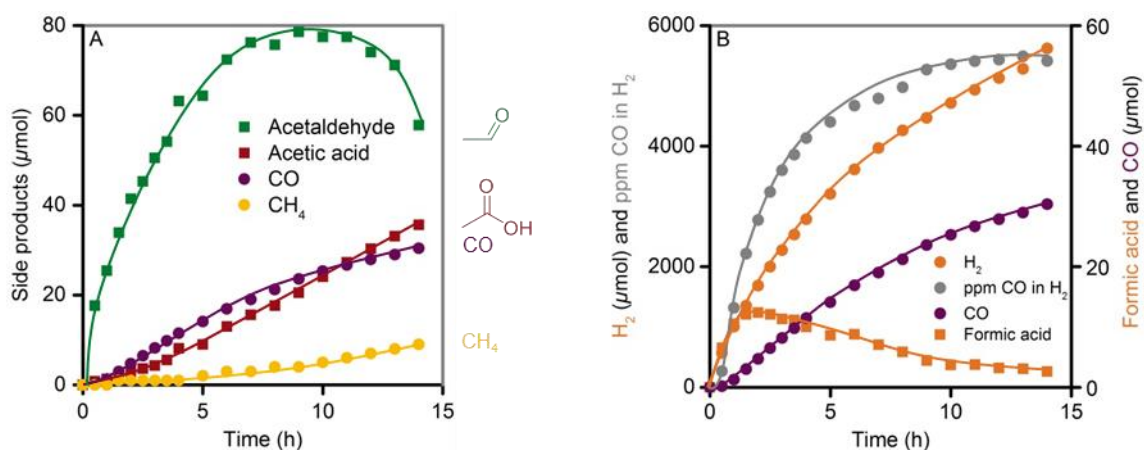
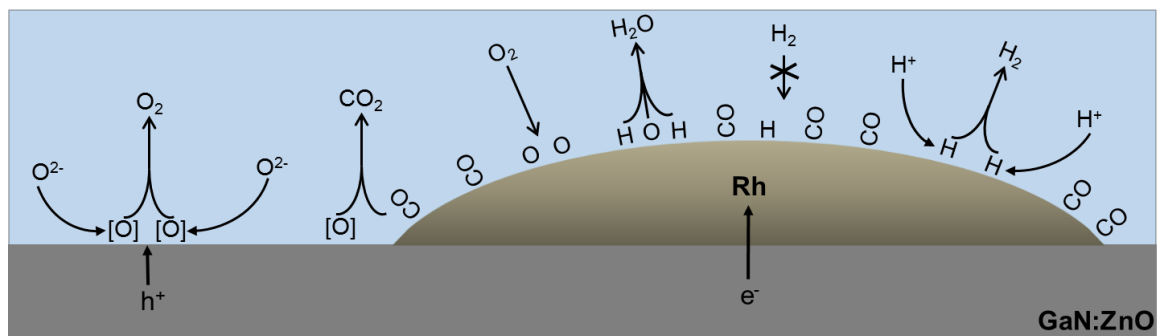


Figure-SI 2-7. Ethylene glycol photoreforming with increased photon flux. (A) Course of side intermediates. (B) Course of H₂, formic acid, CO and ppm CO in H₂. Reaction conditions: 75 mg Rh/TiO₂, 100 mL aqueous ethylene glycol solution (20 mM), 288 K, 1 bar Ar, 14 UV-LEDs (365 nm, 14.8 V, 400 mA).

Table-SI 2-4. Ethylene glycol photoreforming with increased photon flux. Remaining concentrations of reactant and intermediates after 14 h. Reaction conditions: 75 mg Rh/TiO₂, 100 mL aqueous ethylene glycol solution (20 mM), 288 K, 1 bar Ar, 14 UV-LEDs (365 nm, 14.8 V, 400 mA).

Compounds	Concentration after 14 h (mM)
Ethylene glycol	1.60
Formaldehyde	8.03
Methanol	0.58
Acetaldehyde	0.58
Acetic acid	0.36

Overall Water Splitting in the Presence of CO



Chapter 3

3. Overall Water Splitting over Photocatalysts with CO-Covered Nobel Metals: an Alternative to Core-Shell Approaches

This chapter is used as a draft for a publication from Berto, T.F.; Sanwald, K.E.; Buyers, J.P.; Browning, N.D.; Gutierrez, O.Y. and Lercher, J.A..³

Photocatalytic overall water splitting requires co-catalysts, which efficiently promote the generation of H₂ but do not catalyze its back reaction with O₂ to water. It is demonstrated, that CO, which is chemisorbed on precious metal based, cathodic acting co-catalysts (here: Rh, Pt, Pd), suppresses the back reaction while preserving the overall H₂ evolution reaction (HER). The mechanism of this novel protective effect has been studied over Rh/GaN:ZnO. The enhancing effect depends on the partial pressure of CO. Maximum water splitting rates are obtained between 4 and 40 mbar of CO. Lower or higher CO partial pressures hinder H₂ evolution by allowing the back reaction or hindering HER, respectively. Water oxidation proceeds *via* atomic O₂ intermediates competing for O₂ evolution or CO oxidation. The selectivity of these two routes depends on the surface oxygen concentration adjustable by photon flux or quantum efficiency of the photocatalyst. Rates of back reaction solely depend on O₂ partial pressure (above 7 mbar of O₂). The concentration of surface intermediates of HER and O₂ evolution reaction rises with increasing photon flux and with increasing quantum efficiency diminishing the rates of back reaction and CO oxidation. Thus, stability and effectiveness of the CO protection layer depend additionally on photon flux and quantum efficiency of the photocatalyst.

³ T.F.B. designed and performed the experiments (if not otherwise stated at the end of the chapter), did data analysis and wrote the manuscript. K.E.S., O.Y.G. and J.A.L. contributed with discussion of results and with correction of the manuscript. J.P.B. and N.D.B performed HR-TEM spectroscopy at the Pacific Northwest National Laboratory (PNNL), USA.

3.1. Introduction

Photocatalytic overall water splitting is an endergonic ($\Delta G = 237 \text{ kJ mol}^{-1} = 1.23 \text{ eV/e}$), carbon-free route to H_2 , which does not require thermal energy input as photogenerated charge carriers with appropriate chemical potential are used to drive the desired half reactions, i.e., H_2 evolution reaction (HER), and O_2 evolution reaction (OER) as explained in chapter 1.3. In order to achieve economic feasibility, visible light absorbing semiconductors with efficient electron hole separation and appropriate nanoparticulate co-catalysts for HER and OER are crucial.¹

Summarizing chapter 1.6.1, effective co-catalysts should enable efficient charge carrier transfer at the semiconductor/co-catalyst interface and low activation and desorption energy for the catalyzed half-reaction.¹ In addition, HER co-catalysts, must not catalyze the thermodynamical favored back reaction to water. Hence, selective reduction of protons to H_2 in presence of O_2 is required. Considering these boundary conditions, it does not surprise, that only few effective co-catalysts for the overall water splitting reaction are known.

Transition elements, e.g., Pt, Rh, Cu, Ni or Pd, are efficient metallic or oxidic HER co-catalysts in the presence of sacrificial compounds. The photocatalytic activity for HER follows the volcano plot of electrochemical H_2 evolution rate in function of H binding energy.¹ These elements fail for overall water splitting due to their ability to catalyze the back reaction with the exception of few cases.²⁻⁸ In order to prevent the back reaction, the most sweeping approach is to cover the HER-active co-catalyst with selective oxidic membranes. Redox inactive lanthanoid (III)⁹ and chromium (III)¹⁰ oxides have been successfully applied for these core-shell-type co-catalysts, whereas hydrated Cr_2O_3 forms the most effective and stable protective layers. The thin (~2 nm) layer shows selective permeability to protons and H_2 to/from the HER-active core as graphically illustrated in Figure 1-12B. However, reduction of O_2 is avoided, because its large kinetic diameter prohibits diffusion through the oxide layer.¹¹ However, the toxicity of the Cr(VI)-precursors and the potential danger of the Cr(III)-based co-catalyst itself demand the development of less harmful co-catalyst systems. Concerning this matter, Domen *et al.* recently reported the fabrication of core-shell-type photocatalysts, whereby the oxide shells,

made of group IV and V transition metal oxyhydroxides, cover the whole surface of the photocatalyst particle (Figure 1-12C).¹² The synthesis and properties of this system are described in detail in chapter 1.6.5. In this study we present a non-solid state approach to enhance H₂ production during overall water splitting by selectively blocking the sites active for the back reaction with a fragmented self-organized molecular layer. CO chemisorbed on precious metals is presented as the first co-catalyst of such kind and its mechanism of action for HER, OER and back reaction is explored.

3.2. Experimental Section

3.2.1. Materials

All chemicals were obtained from commercial suppliers and used as provided: alumina crucible (Coors), K_2CrO_4 (Aldrich, $\geq 99.5\%$), Ga_2O_3 (ABCR, 99.99 %, LOT: 1040437), H_2O (Wilhelm Werner GmbH, 18.2 M Ω cm), $PdCl_2$ (Aldrich, 5 wt.% solution in 10 wt.% HCl), H_2PtCl_6 (Alfa Aesar, solution, 20 wt.%), $RhCl_3 \cdot x H_2O$ (Aldrich, $\geq 99.9\%$), $SrCl_2 \cdot 6H_2O$ (Aldrich, $\geq 99.9\%$, LOT: SZBF170AV), $SrTiO_3$ (Wako, 99.9%, LOT: SAF5981) H_2SO_4 (Merck, 0.5 mol L $^{-1}$), ZnO (ABCR, 99.7%, LOT: 1121535), NH_3 (BASF, 5.0, anhydrous), D_2 (Westfalen, 2.1), O_2 (Westfalen, 5.0), $^{18}O_2$ (Isotec, 97%) H_2 (Westfalen, 5.0), CO (Westfalen, 3.7), synthetic air (Westfalen), Ar (Westfalen, 5.0), Al AAS-standard (Fluka, 1 g L $^{-1}$), Cr ICP-standard (Fluka, 10001 mg L $^{-1}$), Ga ICP-standard (Merck, 1000 mg L $^{-1}$), Pd AAS-standard (Fluka, 1003 mg L $^{-1}$), Pt AAS-standard (Fluka, 1001 mg L $^{-1}$), Rh AAS-standard (Fluka, 999 mg L $^{-1}$), Sr ICP-standard (Fluka, 1000 mg L $^{-1}$), Ti AAS-standard (Fluka, 998 mg L $^{-1}$), Zn ICP-standard (Merck, 1000 mg L $^{-1}$).

3.2.2. Synthesis of the Photocatalysts

3.2.2.1. Semiconductor Preparation

$(Ga_{1-x}Zn_x)(N_{1-x}O_x)$. $(Ga_{1-x}Zn_x)(N_{1-x}O_x)$ was synthesized according to a procedure adopted from Domen *et al.*¹³ and is described in detail in chapter 2.3.2.2. Shortly, powdered Ga_2O_3 and ZnO (1:2 stoichiometry) were nitrated at 1098 K for 16 h under NH_3 flow. The obtained solid solution was subsequently treated at 873 K for 1 h in a synthetic air flow (50 mL min $^{-1}$). Post-calcined $(Ga_{1-x}Zn_x)(N_{1-x}O_x)$ ($x = 0.14$) was modified with co-catalysts *via* different preparation methods and is denoted as GaN:ZnO.

Al-doped SrTiO₃: An 1:10 mixture of 0.75 g $SrTiO_3$ (4.1 mmol) and 10.99 g $SrCl_2 \cdot 6H_2O$ were thoroughly mixed in an agate mortar and transferred into an Al_2O_3 -crucible. The mixture was treated at 1323 K (5 K min $^{-1}$) for 10 h, cooled to 1073 K with a rate of 3 K min $^{-1}$ and subsequently cooled naturally to room temperature. $SrCl_2$

was removed by thoroughly washing the solid with bidistilled water. Completeness of Cl⁻-removal was tested by missing AgCl precipitation from an aliquot of the filtrate.

3.2.2.2. Deposition of HER-Active Co-Catalyst

Impregnation.^{14,15} 0.3 g of semiconductor were modified with MO_x (e.g., Rh, Pt, Pd) by wet impregnation technique using 1.5 mL of an aqueous solution containing the appropriate precursor. The impregnated powder was kept in static air at 623 K (5 K min⁻¹) for 1 h in order to obtain the MO_x-decorated photocatalyst. GaN:ZnO was loaded with 1 wt.% and Al-doped SrTiO₃ with 0.25 wt.%.

*Photodeposition.*¹⁶ 0.13 g of GaN:ZnO were dispersed in 100 mL of an aqueous 0.25 mM RhCl₃-solution, deaerated and irradiated with a 300 W Xe-lamp (CM1, L42) at 303 K for 4 h. Rh³⁺ is reduced to metallic nanoparticles. The sample was filtered and thoroughly washed with bidistilled water and dried overnight at 323 K. A Rh-loading of 0.75 wt.% was obtained.

*Deposition of Cr₂O₃-layer.*¹⁶ Rh(O_x)/Cr₂O₃/GaN:ZnO. 0.13 g of Rh(O_x)/GaN:ZnO were dispersed in 100 mL of an aqueous 20 mM K₂CrO₄-solution, deaerated and irradiated with a 300 W Xe-lamp (CM1, L42) at 303 K for 4 h. CrO₄²⁻ was reduced to Cr₂O₃. The sample was filtered and thoroughly washed with bidistilled water and dried overnight at 323 K. The Cr-loading was 0.3 wt.%.

3.2.3. Photocatalytic Tests

Overall water splitting experiments were conducted in a top irradiation photo-reactor closed by a quartz window. The vessel, tempered at 303 K, was connected to a gas-tight gas-circulation system (leakage rate < 5·10⁻⁴ Pa s⁻¹ L⁻¹, V = 330 mL). It comprised a two-position 6-port Valco gas sampling valve, which was connected to a 5 mL loop, a gas dosing line and a mass spectrometer / exhaust line (for details see chapter 6). In addition a two-position 10-port Valco gas sampling valve was installed for online gas chromatography. Typically 75 mg of GaN:ZnO- / 125 mg of Al-SrTiO₃-based photocatalyst were suspended in 100 mL of water ($\sigma = 18.2 \text{ M}\Omega \text{ cm}$), whereas the pH was adjusted to 4.5 (H₂SO₄) in the case of GaN:ZnO-based photocatalysts.

O₂ was removed by four subsequent evacuations and Ar filling turns up to 1 bar. Completeness of O₂ removal (< 0.3 μmol O₂ / detection limit) was verified by GC analysis. Prior illumination, defined volumes of CO and other probe gases were introduced into the gas-circulation system *via* the 6-port gas sampling valve. Subsequently, the suspension was illuminated with a 300 W Xenon lamp, equipped with a cold-mirror 1 (CM1). Experiments with visible light were performed by introducing a L42-filter into the beam path. High power UV-LEDs (Nichia NC4U133A, 365 nm) were used in order to determine quantum efficiencies and to alter the photon flux. The gas-phase was analyzed *online via* gas chromatography (Shimadzu, GC 2010 Plus equipped with a TCD, FID and a methanizer unit) on a Chromosorb 101 column connected with a MS-5Å column. The carrier gas was Ar. The concentrations of dissolved gases were accounted for by applying Henry's law. Rates were calculated by dividing the difference of amounts between two adjacent data points by the corresponding time interval. Isotopic experiments were accomplished by parallel use of a Pfeiffer Omni Star™ GSD 320 mass spectrometer and the described gas chromatograph. Gas chromatograph and mass spectrometer were calibrated for all analyzed isotopes excluding C¹⁶O¹⁸O, C¹⁸O¹⁸O, HD and ¹⁶O¹⁸O. As these isotopes were not detected or solely as side products, the significance of the experiments is not affected. For these gases the calibration factor of the appropriate sister isotope(s) (C¹⁶O¹⁶O, H₂ and D₂, ¹⁶O₂ and ¹⁸O₂) was used. CO and N₂ were exclusively quantified *via* gas chromatography.

3.2.4. Catalyst Characterization

Elemental analysis. Ga, Zn and Cr concentrations were determined by inductively coupled plasma atomic emission spectroscopy (ICP-AES) using a spectroflame-ICP spectrometer (Spectro Analytical Instruments Inc.). Atomic absorption spectroscopy (AAS) was applied in order to determine Rh, Pd, Pt and Al concentrations by using a Thermo Scientific – SOLAAR M Series AA Spectrometer. H-C-N elemental analyses were carried out by the Microanalytical Laboratory at the Technischen Universität München. Dissolution of Al-SrTiO₃ was performed using Na₂CO₃, B(OH)₃, tartaric acid (5%), HCl (conc.) and H₂O₂ (30 wt.%) according to literature procedures.^{17,18}

Textural properties. Specific surface area and average pore diameter were determined by N₂ adsorption-desorption measurements. After outgassing at 523 K for 20 h the measurements were carried out at 77 K using an automated PMI BET sorptometer. BET and BJH models were applied in order to calculate the specific surface area and the average pore diameter.

X-ray diffraction (XRD). XRD-patterns were collected on a STOE STADI-P diffractometer (Cu-K_{α1} radiation, $\lambda = 1.54051 \text{ \AA}$, Ge-monochromator) using a Dectris Mythen 1 K detector.

Diffuse reflectance UV-Vis (DR UV-Vis) spectroscopy. An Avantes Avaspec 2048 spectrometer equipped with a reflection probe (FCR-7UV200-2-ME) was used in order to perform DR UV-Vis measurements with a homemade sample holder. Prior plotting the Kubelka-Munk function, defined as $F(R) = (1-R)^2 (2R)^{-1}$ with $R = R_S/R_T$, where R_S is the reflectance of the sample and R_T is the reflectance of teflon used as a reference, was applied.

Transmission and scanning electron microscopy (TEM and SEM).

HR-TEM (PNNL). All HR-TEM imaging was done using an FEI Titan image corrected field emission gun (FEG) environmental (scanning) transmission electron microscope (ETEM) with accelerating voltage of 300 kV at the Environmental Molecular Sciences Laboratory (EMSL) at Pacific Northwest National Laboratory (PNNL). Prior measurement, the powdered sample was dispersed in a few drops of methanol and ground in a clean agate mortar and pestle. More methanol is added and the solution is agitated in a sonicator for two minutes. A small droplet is placed on a copper grid and allowed to air dry. The grid is heated gently for a minute over a hot plate at low heat, and before inserting into the microscope, it is plasma cleaned for 10-15 seconds in an Ar/O₂ gas mixture.

SEM. SEM images were taken on a JEOL JSM 5900 LV microscope operating at 2.0 kV. No sample pretreatment was applied.

TEM (TUM). The Pt/Al-SrTiO₃, Pd/Al-SrTiO₃, and Rh/Al-SrTiO₃ samples were imaged using a JEOL JEM-2010 transmission electron microscope. After grounding, suspending and ultrasonic dispersing in ethanol, a droplet of the suspension was placed on a copper-grid supported carbon film. Images were recorded with an accelerating voltage of 120 kV and a magnification of 200 k. Size of 100 particles was determined in order to calculate the averaged particle size.

3.2.5. Light Intensity Measurements

An Avantes Avaspec 2048 spectrometer equipped with a SMA terminated quartz fiber (FC-UV-200-1-ME-SR) equipped with a cosine corrector (CC-UV/Vis) was used to measure the photon flux. A calibrated light source (AvaLight DH-BAL-CAL) was used for calibration.

3.3. Results and Discussion

3.3.1. Photocatalyst Synthesis and Characterization

3.3.1.1. Rh/GaN:ZnO and Rh@Cr₂O₃/GaN:ZnO

The solid solution (GaN)_{0.86}(ZnO)_{0.14} (XRD: Figure 3-1A and Figure-SI 3-1A; denoted in the following as GaN:ZnO), is a visible light absorbing material with a band gap of 2.7 eV. (Figure 3-1B and Figure-SI 3-1B).

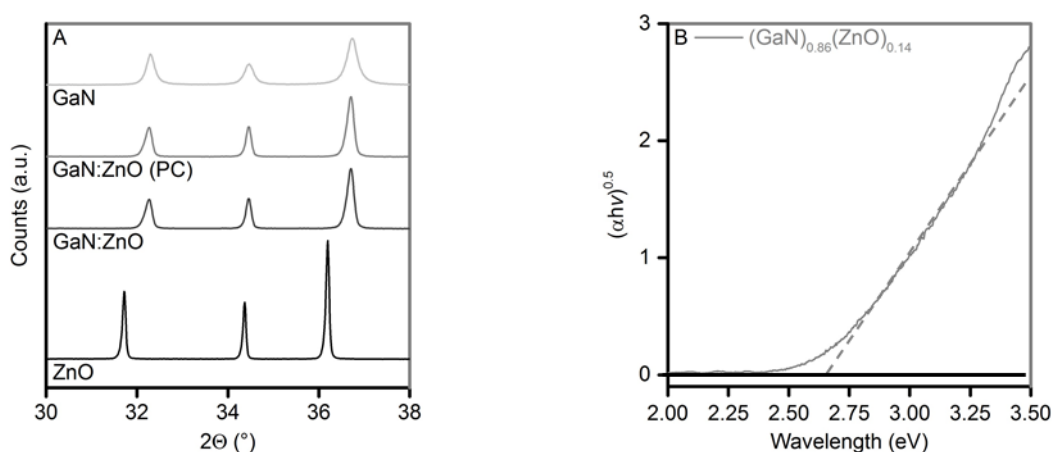


Figure 3-1: (A) Cut-out of x-ray diffractograms of GaN:ZnO (after nitridation and post-calcination (PC)) and the precursor materials GaN and ZnO. (B) Tauc plot of GaN:ZnO.

The surface area of GaN:ZnO was 9 m² g⁻¹. Post-calcined GaN:ZnO was loaded with Rh *via* impregnation or *via* photodeposition. The average Rh particle sizes were from 5 to 10 nm and from 2 to 5 nm (deposited *via* impregnation or *via* photodeposition, respectively). Formation of Rh@Cr₂O₃ core-shell particles was confirmed by HR-TEM (Figure-SI 3-2) in agreement with the findings of Maeda *et al.*¹⁴ In the case of impregnated materials, rough particle surfaces were observed after Cr₂O₃-deposition and the Rh-Cr₂O₃ interface was sometimes indistinct. In contrast, well-defined spherical Cr₂O₃ shells, which exhibited typical thicknesses from 2 to 3 nm, were observed surrounding photodeposited Rh particles.

3.3.1.2. M/Al-doped SrTiO₃ (M = Rh, Pt, Pd)

Agglomerated particles with truncated cubic shape of Al-doped SrTiO₃ (Figure 3-2) with sizes from 0.2 to 3 μm (Figure-SI 3-3) and $2.7 \text{ m}^2 \text{ g}^{-1}$ were obtained. Aluminum, which decreases the hole recombination rate by reducing the defect concentration,¹⁷ was incorporated with 0.07 wt.%. The band gap (3.2 eV) and absorption edge (390 nm) (Figure 3-2), were not altered by the flux treatment and are in agreement with previous measurements.¹⁷ The average particle sizes of Rh, Pt or Pd decorated Al-SrTiO₃ were $2.8 \text{ nm} \pm 1.5 \text{ nm}$, $3.8 \text{ nm} \pm 2.5 \text{ nm}$ and $4.4 \text{ nm} \pm 1.7 \text{ nm}$, respectively (Figure-SI 3-4). Rh nanoparticles possess the lowest averaged diameter and narrowest particle size distribution. Nevertheless, a number of those Rh nanoparticles formed large agglomerates.

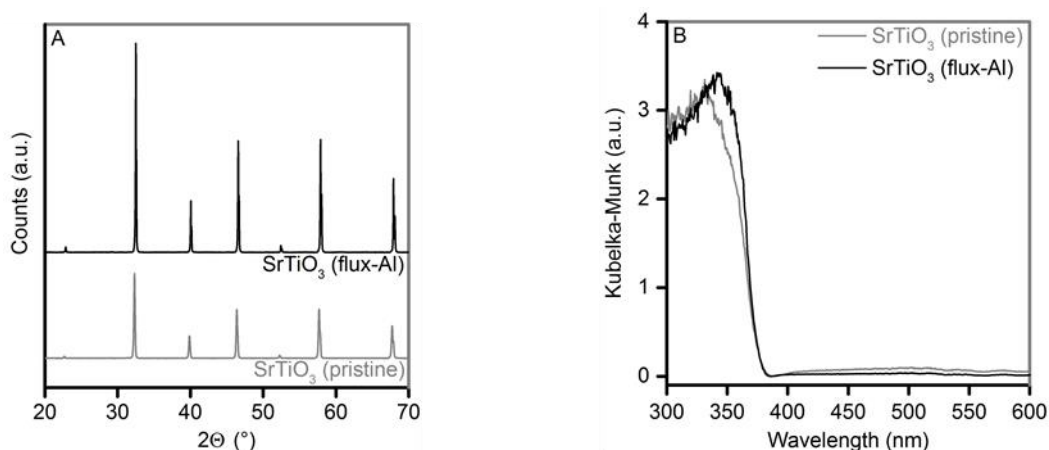


Figure 3-2: (A) XRD patterns and (B) diffuse reflectance UV-Vis spectra of pristine SrTiO₃ and Al-doped SrTiO₃ obtained from a SrCl₂ flux-treatment of SrTiO₃ in an Al₂O₃-crucible.

3.3.1.3. State of Co-Catalyst during Overall Water Splitting

The oxidation state of the co-catalysts prepared *via* impregnation is oxidic due to missing reductive treatment. However, the co-catalyst acts as a H₂ evolution site (cathode) and was hypothesized to undergo *in situ* photoreduction to a metallic state upon illumination. To test this hypothesis, 2:1 mixtures of H₂ and O₂ were reacted over Rh₂O₃/GaN:ZnO exposed to different illumination conditions (Figure 3-3). If the suspension of Rh₂O₃/GaN:ZnO was directly exposed to the H₂-O₂ atmosphere in the dark, negligible reactant consumption was observed. In contrast, reactants were quickly consumed in the dark and under illumination if the suspension had been

illuminated for 1 h in the presence of H_2 . Similarly, a suspension of $Rh_2O_3/GaN:ZnO$, which was exposed to light once the H_2-O_2 -mixtures was added, converted the reactants with accelerating rates after 0.5 hours of reaction.

Furthermore, considering the Pourbaix diagram of Rh¹⁹ and the potential of conduction band electrons of $SrTiO_3$ (-1.25 V vs. NHE, pH = 7)²⁰ and $GaN:ZnO$ (-1.19 V vs. NHE, pH = 7)²¹, in situ reduction of Rh_2O_3 to metallic Rh under illumination conditions is assumed for any of the investigated materials.

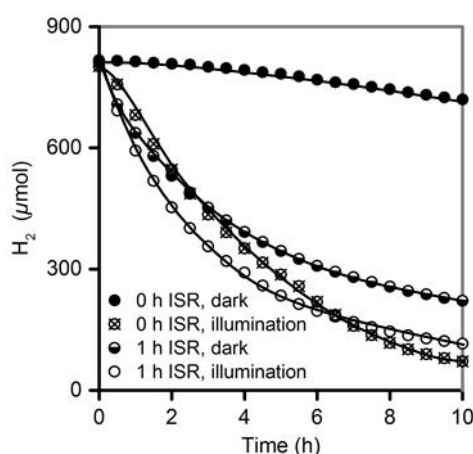


Figure 3-3: Comparison of kinetics of H_2-O_2 reaction under different reaction conditions in order to explore the co-catalyst oxidation state. $Rh_2O_3/GaN:ZnO$ was in situ reduced via illumination or not and subsequently exposed to a mixture of H_2 (60 mbar) and O_2 (30 mbar) under illumination or in the dark. Black lines serve to guide the eye. Reaction conditions: 75 mg photocatalyst, 100 mL H_2O (pH = 4.5, H_2SO_4), 303 K, 1 bar, 300 W Xe-lamp (CM1).

3.3.2. Influence of CO on Water Splitting over Rh/GaN:ZnO

We observed stable overall water splitting over Rh/GaN:ZnO in the presence of 40 mbar of CO at 303 K under UV-Vis- and Vis-light illumination ($\lambda > 420$ nm) as shown in Figure 3-4. As a higher number of photons generating e^- / h^+ -pairs are absorbed under UV-Vis illumination an increased activity is gained under UV-Vis- compared to Vis-light illumination. The contrasting O_2 to CO_2 -ratios (i.e., 1.9 (UV-Vis) and 0.3 (Vis) after five hours) in dependence of photon flux are explained in Chapter 3.3.6.1.

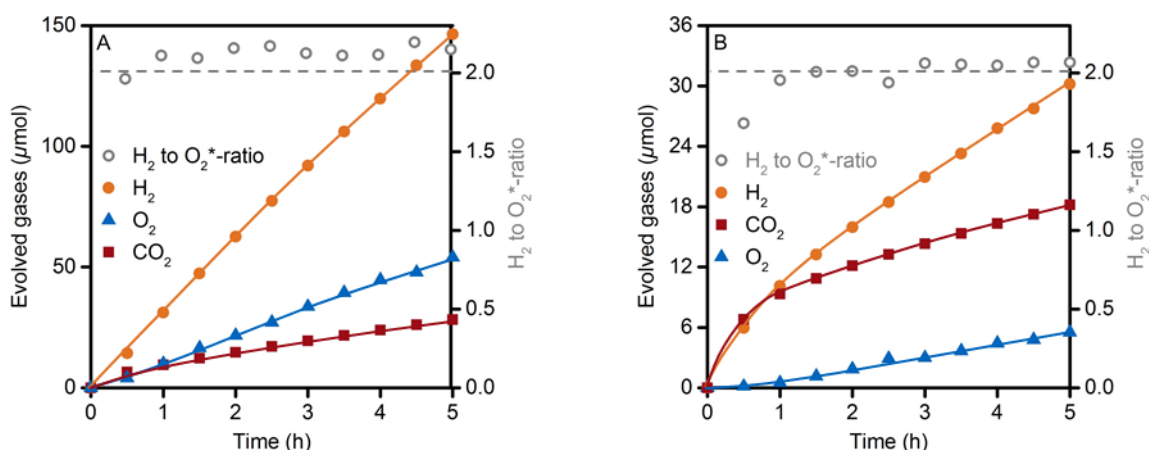


Figure 3-4: Overall water splitting over Rh/GaN:ZnO in the presence of 40 mbar CO. (A) UV-Vis and (B) visible light illumination. Dashed horizontal line represents the expected stoichiometric ratio of H₂ to O₂. Solid lines serve to guide the eye. Reaction conditions: 75 mg photocatalyst, 100 mL H₂O (pH = 4.5, H₂SO₄), 303 K, 40 mbar CO, 1 bar, 300 W Xe-lamp (CM1, Vis: L42).

In contrast, negligible H₂ and O₂ evolution (H₂: 6 μmol after 5 h, O₂: 3 μmol after 5 h) was obtained over the same photocatalyst in pure noble gas atmosphere (Figure 3-5A). After 0.5 hours the net rate was almost zero, which is explained due to equilibrated forward and backward rates as described in chapter 1.6.1.²² Chemisorption of CO on precious metal electrodes, e.g., rhodium,^{23,24} platinum^{24,25} or palladium²⁶ has been observed in aqueous phase over a large potential range. In analogy, it is proposed that CO chemisorbs on the Rh co-catalyst suppressing the back reaction. Clearly, whereas CO occupies the sites for the back reaction, the protons can still access metal sites for the HER and, thus, positive net rates are enabled.

The observed H₂ to O₂ ratio was higher than 2 (e.g., 2.7 after 5 h under UV-Vis illumination) because CO was oxidized *via* anodic or thermal CO oxidation to CO₂. The amount of consumed CO equaled the amount of detected CO₂ as depicted in Figure 3-5B. It is worth noting that methane formation from CO and hydrogen atoms was not observed. A corrected ratio (named as H₂ to O₂*-ratio) that accounts for the oxygen evolved as O₂ and CO₂ corresponds to the expected H₂ to O₂ ratio of 2 (Figure 3-4). In order to understand the mode of action in detail, the study is performed under UV-Vis illumination due to higher activities.

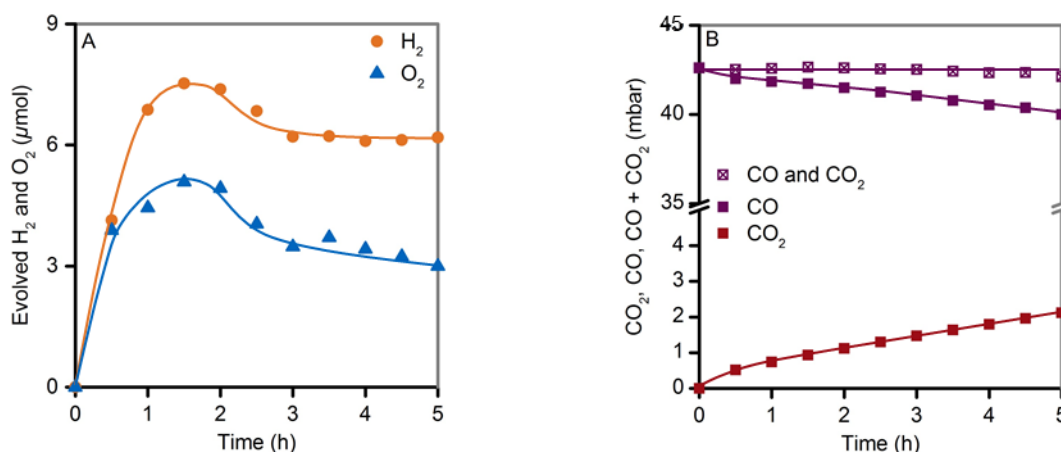


Figure 3-5: (A) Overall water splitting over Rh/GaN:ZnO in the presence of 0 mbar CO. (B) Consumed CO, formed CO₂ and summation of present CO and CO₂ during overall water splitting over Rh/GaN:ZnO in the presence of 40 mbar CO. Solid lines serve to guide the eye. Reaction conditions: 75 mg photocatalyst, 100 mL H₂O (pH = 4.5, H₂SO₄), 303 K, 0 or 40 mbar CO, 1 bar, 300 W Xe-lamp (CM1).

3.3.3. Comparison of Rh@Cr₂O₃ and Rh-CO Co-Catalysts

Table 3-1 compares the amounts of H₂ produced over Rh@Cr₂O₃ and Rh-CO co-catalysts decorated on GaN:ZnO with Rh being deposited by wet impregnation or photodeposition. All photocatalysts show similar activities for the overall water splitting reaction. Thus, the beneficial effects of the CO layer are independent from the preparation method. Comparable activities of GaN:ZnO loaded with Rh@Cr₂O₃ or Rh-CO co-catalysts demonstrate that the back reaction was efficiently suppressed during all experiments. Thus a layer of CO prevents the activation of O₂ as efficiently as a Cr₂O₃ layer acting as a selective membrane. Hence, the experiments demonstrate that selective blocking of metal sites by molecular adsorbates, here CO, is a potential substitute of oxide shells.

Table 3-1: Comparison of evolved H₂ after 5 h over CO-covered Rh/GaN:ZnO and Rh@Cr₂O₃/GaN:ZnO prepared *via* photodeposition and impregnation.

Photocatalyst	Photodeposition	Impregnation
	μmol H ₂ after 5h	
CO-Rh/GaN:ZnO	116	145
Rh@Cr ₂ O ₃ /GaN:ZnO	112	142

Reaction conditions: 75 mg photocatalyst, 100 mL H₂O (pH = 4.5, H₂SO₄), 303 K, 40 mbar CO in case of CO-Rh/GaN:ZnO, 1 bar, 300 W Xe-lamp (CM1).

3.3.4. Influence of CO Partial Pressure on Overall Water Splitting Rate

Partial pressure of CO was varied from 0 to 200 mbar in a series of experiments. The overall water splitting activity sharply increased in the presence of small amounts of CO (Figure 3-6). In contrast, a plateau in overall water splitting activity was observed between 8 to 40 mbar of CO followed by declining activities at higher CO partial pressures. The variations in H₂ evolution rates with CO partial pressure in the range of 0 to 200 mbar are expected to result from the varying CO coverages of Rh-sites.

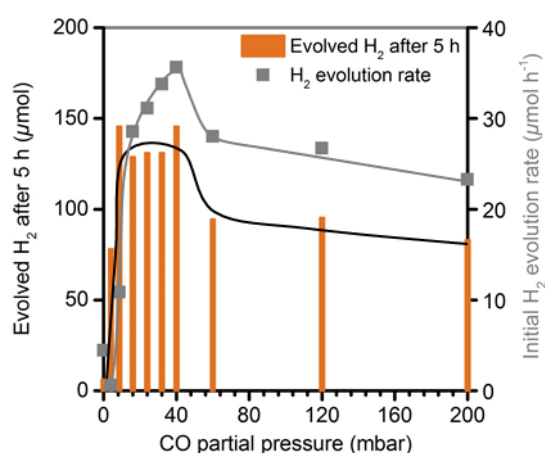


Figure 3-6: Amount of H₂ evolved after 5 h and initial H₂-evolution rate in function of CO partial pressure over Rh/GaN:ZnO. Black and grey lines serve to guide the eye. H₂ to O₂⁺-ratio is 2 in any experiment. Reaction conditions: 75 mg photocatalyst, 100 mL H₂O (pH = 4.5, H₂SO₄), 303 K, 0 – 200 mbar CO, 1 bar, 300 W Xe-lamp (CM1).

In the presence of approximately 4 mbar of CO we observed a H₂ production rate of approximately 28 μmol h⁻¹ after an induction period of 0.5 h (Figure 3-7), which is explained in chapter 3.3.5. This rate is within the range of the initial activities within the 8 to 40 mbar CO region (Figure 3-6). After 2.5 h the H₂ evolution rate decreased to < 10 μmol h⁻¹ due to continuous oxidative CO consumption, which decreased its partial pressure to 3.6 mbar and the CO coverage is not sufficient to cover all back reaction sites. Thus, under my experimental conditions, that CO partial pressure marks the lower boundary required in order to obtain maximum suppression of the back reaction (Figure 3-7). The decrease in activity above 40 mbar of CO is attributed to poisoning of H⁺-reduction sites, whereby all sites for the back reaction

are covered by CO. Between 4 and 40 mbar, CO preferentially covers sites for the back reaction without affecting the sites for the HER.

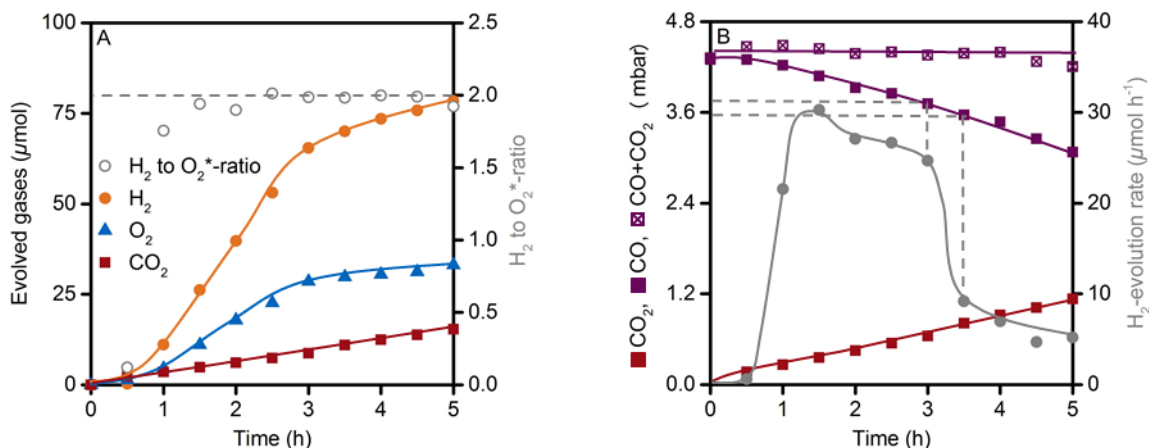


Figure 3-7: Overall water splitting over Rh/GaN:ZnO in the presence of 4 mbar CO. Solid lines serve to guide the eye. Dashed lines (**A**) represent the expected stoichiometric ratio of H_2 to O_2 and (**B**) mark the minimum required partial pressure of CO to suppress the O_2 reduction reaction. Reaction conditions: 75 mg photocatalyst, 100 mL H_2O (pH = 4.5, H_2SO_4), 303 K, 4 mbar CO, 1 bar, 300 W Xe-lamp (CM1).

3.3.5. Deduction of CO-Coverage

CO_2 evolution rates follow a Langmuir adsorption based rate equation (3-1) as a function of dissolved CO independently of the oxidation state of the Rhodium.

$$\frac{dc_{\text{CO}_2}}{dt} = \frac{k_{\text{CO}_2} \cdot K_{\text{CO}} \cdot c_{\text{CO}}}{1 + K_{\text{CO}} \cdot c_{\text{CO}}} \quad (3-1)$$

Here dc_{CO_2}/dt is the reaction rate of CO_2 -formation ($\mu\text{mol h}^{-1}$), k_{CO_2} is the apparent rate constant of CO_2 formation ($\mu\text{mol h}^{-1}$), K_{CO} is the apparent adsorption constant of CO ($\text{L } \mu\text{mol}^{-1}$) and c_{CO} is the concentration of CO ($\mu\text{mol L}^{-1}$). Note that CO is oxidized by water oxidation intermediates (shown in chapter 3.3.6.1), whose concentration cannot be directly determined but is considered to be constant. Therefore, the activity of oxygen is incorporated in k_{CO_2} . A linearized form²⁷ (3-2) of rate equation (3-1) was applied in order to verify the set hypothesis.

$$\frac{c_{\text{CO}}}{r_{\text{CO}_2}} = \frac{1}{K_{\text{CO}} \cdot k_{\text{CO}_2}} + \frac{c_{\text{CO}}}{k_{\text{CO}_2}} \quad (3-2)$$

The oxidation state of the Rh_2O_3 co-catalyst changes due to in situ photoreduction to metallic rhodium as indicated by declining CO_2 rates during the first 1.5 hours. Accordingly, O_2 evolution rates rise. In line with this conclusion, high thermal CO oxidation rates have been observed over oxidized Rhodium²⁸ compared to metallic,

which have been explained, inter alia, by weak chemisorption energies of CO on oxidized Rhodium.²⁹ The observed induction period at 4 mbar of CO (Figure 3-7) and the rising initial H₂ evolution rates within the 8 to 40 mbar CO partial pressure range (Figure 3-6) occur due to the oxidized Rh co-catalyst. At 4 mbar, CO coverage is insufficient to cover the back reaction sites, so that the rate of forward and backward reaction equal. With increasing CO partial pressure (up to 40 mbar) the share of CO-covered back reaction sites rises reflected by increasing initial H₂ evolution rates as shown in Figure 3-7. As soon as the Rh₂O₃ co-catalyst is reduced, the H₂ evolution rates between 4 and 40 are identical because all back reaction sites are covered due to the increased adsorption constant of CO over Rh compared to Rh₂O₃.

The observed Langmuir behavior (Figure 3-8) contrast the negative reaction orders in CO for thermal CO oxidation on metallic rhodium.²⁸ This discrepancy is explained by the competitive adsorption of CO and O₂ on the metal in thermal oxidation, whereas in photooxidation CO on the metal reacts with O-atomic species at the semiconductor-metal interphase (*vide infra*). According to the Langmuir model, varying CO partial pressure from 4 mbar to 40 mbar, increases the CO coverage from 20 - 60% to 30 - 85% depending on the reaction time frame (Figure 3-8 A, C, E). The deduced surface coverages are in good agreement with electrochemical H₂ evolution and adsorption studies on Pt in presence of CO. Kinetics of electrochemical H₂ evolution are not altered up to surface coverages of 60%³⁰ and the free energy of H₂ adsorption is not affected at CO coverages between 50% and 70%.³¹ Within this pressure range, the change in CO surface coverage does not affect the HER activity. In order to obtain stable overall water splitting rates CO coverages of at least 45% (8 mbar CO) are required due to continuous CO consumption.

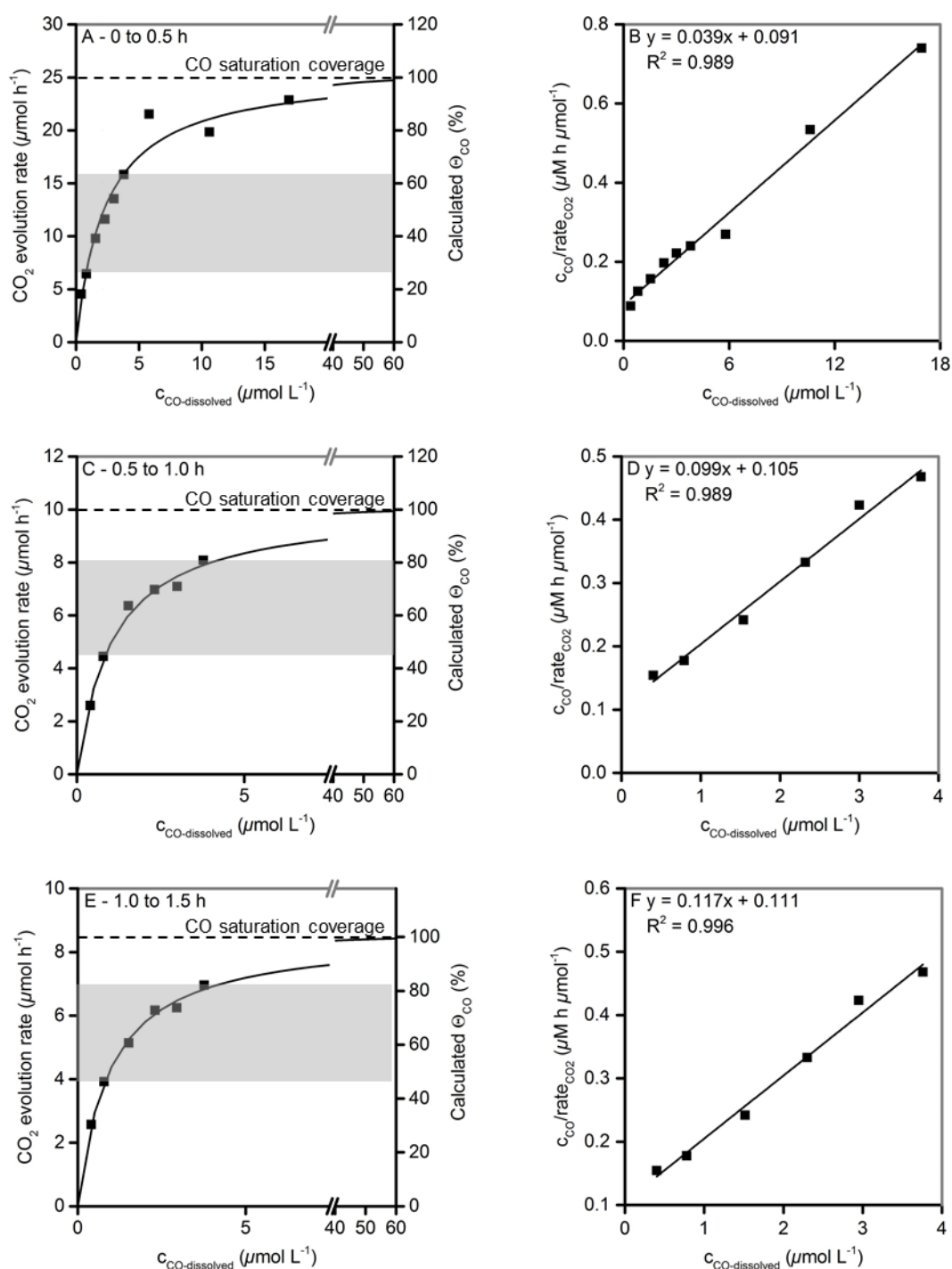
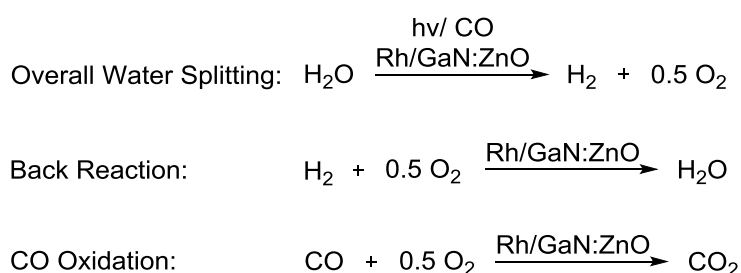


Figure 3-8: Dependence of CO₂ evolution rates on initial concentrations of dissolved CO. The points correspond to experimental values and the curves correspond to the Langmuir fittings within different time intervals ((A) 0 to 0.5 h, (C) 0.5 to 1.0 h, (E) 1.0 to 1.5 h). The grey areas mark the surface coverage corresponding to the CO partial pressure range of 8 to 40 mbar. The corresponding linear plots are shown on the right side ((B) 0 to 0.5 h, (D) 0.5 to 1.0 h, (F) 1.0 to 1.5 h). The time frames 0 to 0.5 h, and 1 to 1.5 h correspond to the reaction occurring mainly on Rh₂O₃ and Rh, respectively. This phase transition occurs *via* photochemical reduction as explained in chapter 3.3.1.3.

3.3.6. Elucidation of Reaction Mechanism

Overall water splitting over CO-covered Rh/GaN:ZnO is an interplay of three reactions, i.e., overall water splitting (coupled HER and OER), back reaction and CO oxidation (Scheme 3-1). The latter two are undesired as they lower the efficiency of the target reaction. In order to decouple their effect in the overall reaction, isotope-labeled co-feeding experiments ($^{18}\text{O}_2$, D_2), and experiments at varied light intensities were performed at fixed CO partial pressure (~ 40 mbar).



Scheme 3-1: Reactions occurring during overall water splitting over Rh/GaN:ZnO.

3.3.6.1. CO Oxidation

CO oxidation is a light driven process as CO conversion was not observed in the dark (Figure-SI 3-5). In principle, chemisorbed CO can be oxidized by atomic O-species originating from water oxidation or by activated molecular O_2 . When $^{18}\text{O}_2$ (60 mbar) was co-dosed to estimate the contribution of water oxidation and oxidation with O_2 , $\text{C}^{16}\text{O}^{16}\text{O}$ and $\text{C}^{16}\text{O}^{18}\text{O}$ were detected with $65 \mu\text{mol}$ and $1 \mu\text{mol}$, respectively, after five hours. Consequently, CO is mainly oxidized by atomic O-species generated from the water oxidation reaction.

There is a direct correlation between photon flux, concentration of photogenerated charge carriers and concentration of active O-species.^{1,32,33,34} Thus, to understand the influence of atomic O-species on the CO oxidation rate, overall water splitting was studied at varied photon flux at 365 nm. The H_2 evolution rate was first order in photon flux (Figure 3-9A) and the H_2 to O_2^* -ratio was close to 2 in all experiments. The first order for H_2 evolution reflects the quasi-first-order kinetics of charge carrier recombination rate.³⁵ However, the dependence of CO oxidation on photon flux was 0.5, whereas a factor of 1.3 was determined for O_2 evolution (Figure 3-9B). That is, O_2 evolution rate increases faster than CO oxidation rate with the concentration of

active O-species. Accordingly, the O_2 to CO_2 -ratio was not constant and changed from 1.9 to 5.6 with rising photon flux (Figure-SI 3-6).

The number of generated electron hole pairs, and concomitant concentration of atomic O-species, is also manipulated by the fraction of photons absorbed by the material. Accordingly, the O_2 to CO_2 -ratio increased from 0.3 to 1.4 over Rh/GaN:ZnO by changing from visible-light to UV-Vis illumination (compare Figure 3-4).

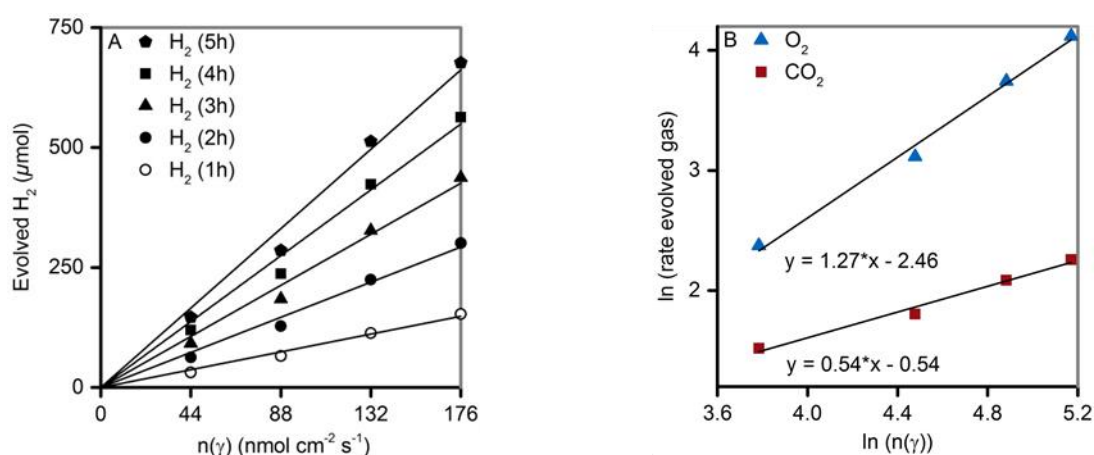


Figure 3-9: (A) Effect of incident light intensity on evolved H_2 for the overall water splitting reaction. (B) Dependence of competing O_2 evolution and CO oxidation reaction on incident light intensity. Solid lines represent linear fitting curves. Reaction conditions: 75 mg photocatalyst, 100 mL H_2O (pH = 4.5, H_2SO_4), 303 K, 40 mbar CO, system pressure 1 bar, UV-LEDs (50 – 200 mA, 365 nm).

The surface concentration of water oxidation intermediates rises with increasing quantum efficiency of the photoabsorber at constant photon flux. In order to test this hypothesis, the CO_2/O_2 selectivity was compared for two Rh decorated photoabsorbers, i.e., Al-doped $SrTiO_3$ ¹⁷ and GaN:ZnO, with different apparent quantum efficiencies under monochromatic illumination ($\lambda = 365$ nm). Associated with an increase of quantum efficiency (Rh/GaN:ZnO: 1.4%; Rh/Al- $SrTiO_3$: 10.9% at 365 nm, respectively), the O_2 to CO_2 -ratio increased from 1.9 to 14.8 after five hours of reaction time, respectively.

3.3.6.2. Back Reaction

Having established that positive net rates of overall water splitting are enabled on Rh with balanced coverage of CO, the performance of the CO-shell in respect to the back reaction was tested in dependence of H₂ and O₂ partial pressures. It was shown before, that CO is not oxidized by molecular O₂. H₂ evolution rates were indeed influenced by ¹⁸O₂ co-dosed prior to irradiation. Partial pressures up to 7 mbar of O₂ did not influence H₂ evolution, whereas increasing pressures in the range of 15 to 100 mbar of O₂ decreased the amount of evolved H₂ (Figure 3-10A). The reaction order of HER in O₂ was -1.3 (7 to 100 mbar).

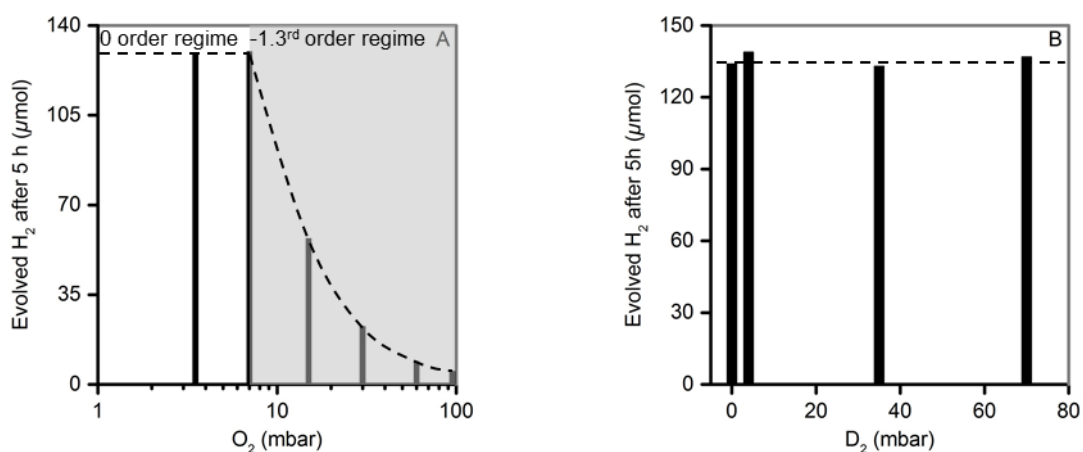


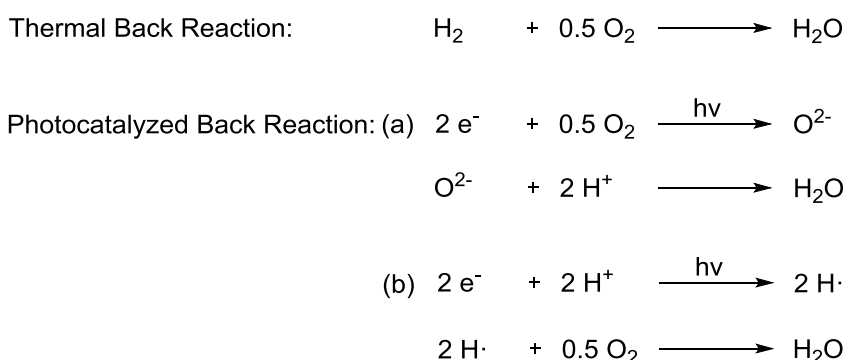
Figure 3-10: (A) Influence of O₂ and (B) D₂ partial pressure on H₂ evolution activity. Black dotted line serves to guide the eye. Reaction conditions: 75 mg photocatalyst, 100 mL H₂O (pH = 4.5, H₂SO₄), 303 K, 40 mbar CO, 0 - 100 mbar O₂ or 0 - 70 mbar D₂, 1 bar, 300 W Xe-lamp (CM1).

Comparison between a typical water splitting experiment in the presence of 40 mbar CO and an experiment where ¹⁸O₂ (60 mbar) was co-dosed revealed that in the presence of O₂, 130 μmol less H₂ was evolved. The missing H₂ matched almost stoichiometrically with the amount of consumed ¹⁸O₂ (55 μmol). The difference (10 μmol of O₂) can be assigned to the back reaction with evolved ¹⁶O₂ or ¹⁶O intermediates from the water oxidation reaction. As ¹⁶O₂ is evolved in close proximity to the Rh co-catalyst, an increased local partial pressure can be considered and the contribution of ¹⁶O intermediates turns to be negligible or non-existing.

Undesired back reaction can be limited by increasing the CO to O₂-ratio. The H₂ evolution rate raised by a factor of four by increasing CO partial pressure from 40 mbar to 120 mbar in presence of 60 mbar O₂ (Figure-SI 3-7). Molecular O₂ can

react *via* thermal or photocatalyzed pathways to water (Scheme 3-2). Note that 'photocatalyzed route' can imply that one of the reacting species is solely generated by a photocatalyzed reaction and therefore demands light, although the generated surface species react *via* a thermal pathway to water.

Various amounts of D₂ were co-dosed prior the experiments in order to interrogate these possibilities. D₂ was not consumed in any case (Figure-SI 3-8A) while the expected H₂ to O₂^{*}-stoichiometry was observed. Moreover HD was not formed (Figure-SI 3-8B) providing strong evidence that dissociative adsorption of D₂ over CO-covered Rh co-catalysts does not occur. This explains why the back reaction was not observed over CO-covered Rh/GaN:ZnO in the dark (Figure-SI 3-5) in contrast to experiments over naked Rh co-catalysts (Figure 3-5A). Suppressed H₂ oxidation due to CO poisoned Pt-catalysts (starting from 10 ppm of CO in diluted H₂ streams) is well known in fuel cell applications.³⁶ Here, we observe that CO prevents H₂-activation under a cathodic potential while the rate of HER was independent of the D₂ partial pressure (0 to 70 mbar, Figure 3-10B).



Scheme 3-2: Possible thermal and photochemical pathways for the back reaction occurring on cathodic acting Rh co-catalysts.

The back reaction is a light-driven reaction over CO-covered Rh co-catalysts and may proceed *via* two reaction pathways, i.e., O₂ anions are generated which capture protons to form water, or protons are reduced to H-atoms and react with dissociatively adsorbed O₂ to water (Scheme 3-2). In the latter case, the H-atom can pursue an additional reaction pathway, i.e., H₂ formation, in parallel to the back reaction. The selectivity is influenced, in case of different reaction orders, by H atom surface concentration. To explore these possibilities, overall water splitting was studied in presence of co-dosed O₂ at varied photon flux. H₂ followed a second order

dependence on photon flux (Figure 3-11, Figure-SI 3-9). This result, which contrasts the experiments without co-dosed O_2 (first order dependence, Figure 3-11A), supports the transfer of electrons to protons instead of to O_2 as main back reaction pathway. The amount of evolved H_2 significantly varies with O_2 partial pressure due to the back reaction consuming H_2 . H_2 evolution rate is first order in photon flux, if minor amounts of O_2 are present. In the presence of significant amounts of O_2 (60 mbar) the H_2 evolution rate exhibits a second order dependence in photon flux. This indicates that the HER and back reaction comprise the same surface intermediates (Scheme 3-2, pathway (b)), i.e., reduced protons. If the two reactions had proceeded *via* different surface intermediates, i.e., reduced proton (HER) and reduced O_2 (back reaction, Scheme 3-2, pathway (a)), a first order dependence in photon flux on HER and back reaction would have been observed. The author does not expect that the rate of charge carrier generation influences the selectivity of electron transfer to protons or O_2 . Therefore, it is the surface concentration of H-atoms which determines the selectivity towards HER or back reaction. Figure 3-11A shows that HER is preferred with increasing photon flux, which is equivalent to increasing H-atom concentration on the co-catalyst.

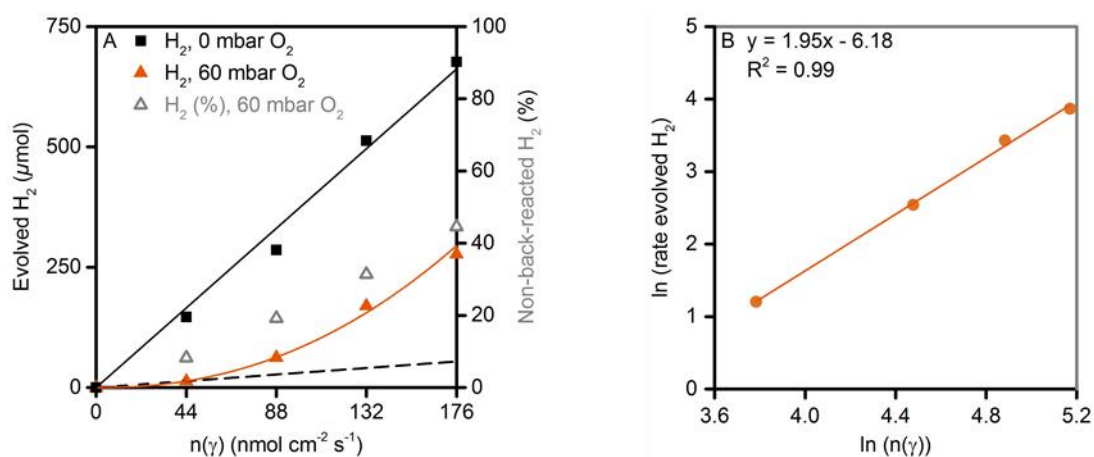


Figure 3-11: (A) Comparison of effect of incident light intensity on evolved H_2 after 5 h for the overall water splitting reaction in presence of 0 and 60 mbar of O_2 . (B) Dependence of H_2 evolution rate on incident light intensity in presence of 60 mbar co-dosed O_2 . Solid lines are fitting curves. Dashed line indicates first order H_2 evolution in presence of 60 mbar O_2 . Reaction conditions: 75 mg photocatalyst, 100 mL H_2O (pH = 4.5, H_2SO_4), 303 K, 40 mbar CO , 0 or 60 mbar of O_2 , 1 bar, UV-LEDs (50 – 200 mA, 365 nm).

In the presence of 30 mbar O_2 , the H_2 evolution rate over Rh/GaN:ZnO (Q.E. 1.4 %) was reduced to 15 % of the rate observed in the presence of less than 7 mbar O_2 ,

whereas the H₂ evolution rate over Rh/Al-SrTiO₃ (Q.E. 10.9 %) decreases to 40 % of the activity in the absence of O₂. Hence, the share of back reaction to the overall reaction can be diminished by increasing photon flux and / or quantum efficiency.

3.3.7. Water Splitting over Various Co-Catalysts

Upon metal semiconductor contact, the respective Fermi levels equilibrate upon formation of Schottky barriers. Efficient overall water splitting is believed to require minimized Schottky barrier heights down to ohmic contacts for efficient electron transfer.^{37,38} Therefore, different semiconductors require different metallic co-catalysts. Rh ($\Phi = 4.98$ eV)³⁹, Pt ($\Phi = 5.65$ eV)³⁹, and Pd ($\Phi = 5.12$ eV)³⁹ are commonly used as co-catalysts for HER in presence for sacrificial agents. All these elements adsorb CO strongly (Table-SI 3-1), which is a prerequisite for a stable CO layer in aqueous phase. Thus, the generality of our approach was tested by modifying SrTiO₃ with 0.25 wt.% of Rh, Pt and Pd, respectively. The preparation and photocatalysis test conditions were not completely optimized and therefore improved activities and selectivities might be obtained. Considerable H₂ evolution was observed over all co-catalysts only in the presence of CO, underlining that the back reaction was suppressed. The O₂ to CO₂-ratio of 13.5 on Rh/SrTiO₃ indicates that OER is favored over CO oxidation, whereas the opposite was observed over Pt and Pd (Table 3-2). Although the observed selectivities cannot be explained, the dominant influence of two factors, namely co-catalyst particle size and quantum efficiency, can be neglected. Pt and Pd exhibit a larger averaged particle size than Rh (chapter 3.3.1.2). Therefore a larger distance between water oxidation intermediates and CO chemisorbed on the co-catalyst can be considered for the Pt and Pd decorated co-catalyst. Accordingly, OER should be favored contrasted by the experimental observation. Compared to Rh/Al-SrTiO₃ (Q.E.: 10.4 %), the concentration of water oxidation intermediates should be lower for Pt/Al-SrTiO₃ (Q.E.: 4.2 %) and Pd/Al-SrTiO₃ (Q.E.: 1.0 %) due to their reduced quantum efficiency. The difference in quantum efficiency of Rh/GaN:ZnO (Q.E.: 1.4 %) and Rh/SrTiO₃ is similar to Pd/Al-SrTiO₃ and Pt/Al-SrTiO₃, although the change in O₂ to CO₂-ratio was less pronounced (chapter 3.3.6.1, Table 3-2). Considering this comparison, it is unlikely that the different concentration of water oxidation

intermediates is the solely factor for the observed selectivity of OER or CO oxidation on different M/SrTiO₃.

Table 3-2: Evolved H₂, O₂ to CO₂-ratios and quantum efficiencies after 5 h over different precious metal decorated Al-SrTiO₃ (M = Rh, Pt, Pd) and Rh/GaN:ZnO.

Photocatalyst	H ₂ (μ mol)	O ₂ to CO ₂ -ratio after 5 h	Quantum efficiency (Q.E., %)*
Rh/SrTiO ₃	625	13.5	10.4
Pt/SrTiO ₃	250	0.2	4.2**
Pd/SrTiO ₃	58	0.1	1.0**
Rh/GaN:ZnO	145	1.4	1.9

Reaction conditions: 125 mg photocatalyst, 100 mL H₂O, 303 K, 40 mbar CO, 1 bar, 300 W Xe-lamp (CM1). *Values determined from UV-LED experiments (365 nm). **Referenced to Rh/SrTiO₃.

3.4. Conclusions

Efficient overall water splitting was achieved by a molecular CO layer chemisorbed on precious metal co-catalysts (Rh, Pt, Pd). A detailed study focused on Rh/GaN:ZnO shows that the active sites for the back reaction are selectively poisoned by CO while the sites for hydrogen evolution are unaffected and result in performances similar to photocatalysts with a molecular sieve acting protection layer. Low O₂ concentrations and CO coverages of 40 - 80% are required to achieve quantitative suppression of back reaction over Rh/GaN:ZnO (Q.E.: = 1.4 %). The HER exhibits a negative dependence on O₂ partial pressure above 7 mbar O₂. CO₂ evolution is observed due to CO oxidation competing with O₂ evolution. In parallel, the H₂ evolution rate follows a first order dependence without O₂ and a second order one in the presence of O₂ with rising photon flux. Thus, the effectiveness of the CO protection layer rises with increased intermediate concentration of HER and OER intermediates. It was demonstrated that a molecular protection layer is a powerful tool to enable overall water splitting due to defeating a thermodynamic constraint by introducing kinetic control. The ease of formation opens its applicability to multiple precious metal based co-catalysts.

3.5. Acknowledgements

Financial support by the Federal Ministry of Education and Research (BMBF) (project no. 01RC1106A), and productive discussions with Clariant within the framework of MuniCat and the iC⁴ PhotoCOO project are gratefully acknowledged. HRTEM-imaging was funded by the Chemical Imaging Initiative at Pacific Northwest National Laboratory (PNNL), and the Environmental Molecular Sciences Laboratory (EMSL), a national scientific user facility sponsored by the DOE's Office of Biological and Environmental Research and located at PNNL. PNNL is a multiprogram national laboratory operated by Battelle for the DOE under Contract DE-AC05-76RL01830. Kazuhiro Takanabe, Garry Haller, and Hany El-Sayed is thanked for fruitful discussions, as well as Xaver Hecht, Martin Neukamm and Udishnu Sanyal for technical support, physicochemical characterization and TEM measurements.

3.6. References

- (1) Takanabe, K.; Domen, K. *Green* **2011**, *1*, 313-322.
- (2) Sato, S.; White, J. M. *Chem. Phys. Lett.* **1980**, *72*, 83-86.
- (3) Domen, K.; Naito, S.; Soma, M.; Onishi, T.; Tamaru, K. *J. Chem. Soc. Chem. Comm.* **1980**, 543-544.
- (4) Lehn, J. M.; Sauvage, J. P.; Ziessel, R.; Hilaire, L. *Isr. J. Chem.* **1982**, *22*, 168-172.
- (5) Inoue, Y.; Niiyama, T.; Asai, Y.; Sato, K. *J. Chem. Soc. Chem. Comm.* **1992**, 579-580.
- (6) Sayama, K.; Arakawa, H. *J. Chem. Soc. Chem. Comm.* **1992**, 150-152.
- (7) Kudo, A.; Sayama, K.; Tanaka, A.; Asakura, K.; Domen, K.; Maruya, K.; Onishi, T. *J. Catal.* **1989**, *120*, 337-352.
- (8) Domen, K.; Kudo, A.; Onishi, T. *J. Catal.* **1986**, *102*, 92-98.
- (9) Yoshida, M.; Maeda, K.; Lu, D. L.; Kubota, J.; Domen, K. *J. Phys. Chem. C* **2013**, *117*, 14000-14006.
- (10) Maeda, K.; Teramura, K.; Lu, D. L.; Saito, N.; Inoue, Y.; Domen, K. *Angew. Chem., Int. Ed.* **2006**, *45*, 7806-7809.
- (11) Yoshida, M.; Takanabe, K.; Maeda, K.; Ishikawa, A.; Kubota, J.; Sakata, Y.; Ikezawa, Y.; Domen, K. *J. Phys. Chem. C* **2009**, *113*, 10151-10157.
- (12) Takata, T.; Pan, C. S.; Nakabayashi, M.; Shibata, N.; Domen, K. *J. Am. Chem. Soc.* **2015**, *137*, 9627-9634.
- (13) Maeda, K.; Teramura, K.; Domen, K. *J. Catal.* **2008**, *254*, 198-204.
- (14) Maeda, K.; Sakamoto, N.; Ikeda, T.; Ohtsuka, H.; Xiong, A. K.; Lu, D. L.; Kanehara, M.; Teranishi, T.; Domen, K. *Chem. Eur. J.* **2010**, *16*, 7750-7759.
- (15) Berto, T. F.; Sanwald, K. E.; Eisenreich, W.; Gutierrez, O. Y.; Lercher, J. A. *J. Catal.* **2016**, *338*, 68-81.
- (16) Xiong, A. K.; Yoshinaga, T.; Ikeda, T.; Takashima, M.; Hisatomi, T.; Maeda, K.; Setoyama, T.; Teranishi, T.; Domen, K. *Eur. J. Inorg. Chem.* **2014**, 767-772.
- (17) Ham, Y.; Hisatomi, T.; Goto, Y.; Moriya, Y.; Sakata, T.; Yamakata, A.; Kubota, J.; Domen, K. *J. Mater. Chem. A* **2016**, 3027-3033.
- (18) Kato, H.; Kobayashi, M.; Hara, M.; Kakihana, M. *Catal. Sci. Technol.* **2013**, *3*, 1733-1738.
- (19) Colombo, C.; Oates, C. J.; Monhemius, A. J.; Plant, J. A. *Geochem.: Explor., Environ., Anal.* **2008**, *8*, 91-101.
- (20) Xian, T.; Yang, H.; Di, L. J.; Ma, J. Y.; Zhang, H. M.; Dai, J. F. *Nanoscale Res. Lett.* **2014**, *9*.
- (21) Hashiguchi, H.; Maeda, K.; Abe, R.; Ishikawa, A.; Kubota, J.; Domen, K. *Bull. Chem. Soc. Jpn.* **2009**, *82*, 401-407.
- (22) Dionigi, F.; Vesborg, P. C. K.; Pedersen, T.; Hansen, O.; Dahl, S.; Xiong, A. K.; Maeda, K.; Domen, K.; Chorkendorff, I. *J. Catal.* **2012**, *292*, 26-31.
- (23) Kunimatsu, K.; Lezna, R. O.; Enyo, M. *J. Electroanal. Chem.* **1989**, *258*, 115-126.
- (24) Beden, B.; Bewick, A.; Kunimatsu, K.; Lamy, C. *J. Electroanal. Chem.* **1982**, *142*, 345-356.
- (25) Lin, W. F.; Sun, S. G.; Tian, Z. Q.; Tian, Z. W. *Electrochim. Acta* **1993**, *38*, 1107-1114.

-
- (26) Kunitatsu, K. *J. Phys. Chem.* **1984**, *88*, 2195-2200.
- (27) Foo, K. Y.; Hameed, B. H. *Chem. Eng. J.* **2010**, *156*, 2-10.
- (28) Ligthart, D. A. J. M.; van Santen, R. A.; Hensen, E. J. M. *Angew. Chem., Int. Ed.* **2011**, *50*, 5306-5310.
- (29) Gong, X. Q.; Liu, Z. P.; Raval, R.; Hu, P. *J. Am. Chem. Soc.* **2004**, *126*, 8-9.
- (30) Breiter, M. W. *J. Electroanal. Chem. Interfacial Electrochem.* **1980**, *115*, 45-51.
- (31) Breiter, M. W. *Proc. Symp. Electrocatal.* **1974**, 115.
- (32) Zhang, M.; de Respinis, M.; Frei, H. *Nat. Chem.* **2014**, *6*, 362-367.
- (33) Tang, J. W.; Durrant, J. R.; Klug, D. R. *J. Am. Chem. Soc.* **2008**, *130*, 13885-13891.
- (34) Turchi, C. S.; Ollis, D. F. *J. Catal.* **1990**, *122*, 178-192.
- (35) Hisatomi, T.; Takanabe, K.; Domen, K. *Catal. Lett.* **2015**, *145*, 95-108.
- (36) Cheng, X.; Shi, Z.; Glass, N.; Zhang, L.; Zhang, J. J.; Song, D. T.; Liu, Z. S.; Wang, H. J.; Shen, J. *J. Power Sources* **2007**, *165*, 739-756.
- (37) Aspnes, D. E.; Heller, A. *J. Phys. Chem.* **1983**, *87*, 4919-4929.
- (38) Takanabe, K.; Domen, K. *ChemCatChem* **2012**, *4*, 1485-1497.
- (39) Michaelson, H. B. *J. Appl. Phys.* **1977**, *48*, 4729-4733.

3.7. Supporting Information

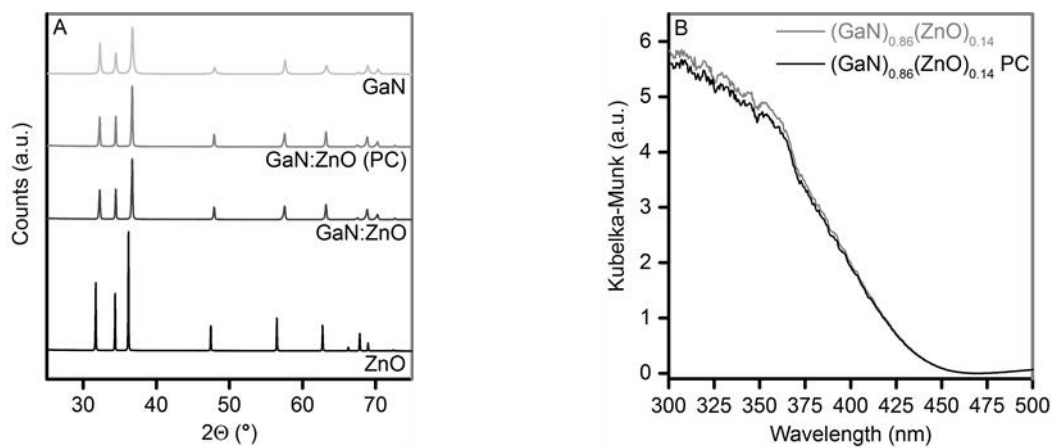


Figure-SI 3-1: X-ray diffractograms of (A) GaN:ZnO (after nitridation and post-calcination (PC)) and the precursor materials GaN and ZnO. (B) Diffuse reflectance spectra of GaN:ZnO before and after PC.

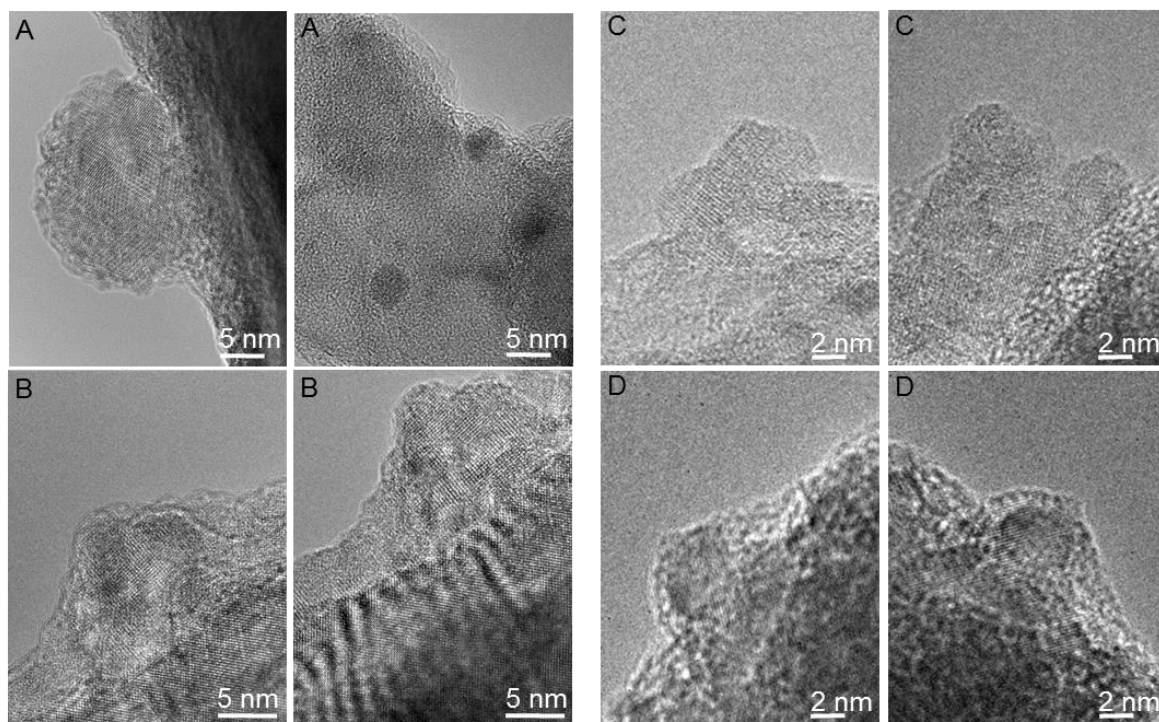


Figure-SI 3-2: HR-TEM images of Rh/GaN:ZnO, decorated *via* impregnation (A) or *via* photodeposition (C), before (A, C) and after (B, D) treatment with a neutral solution of K_2CrO_4 under visible light.

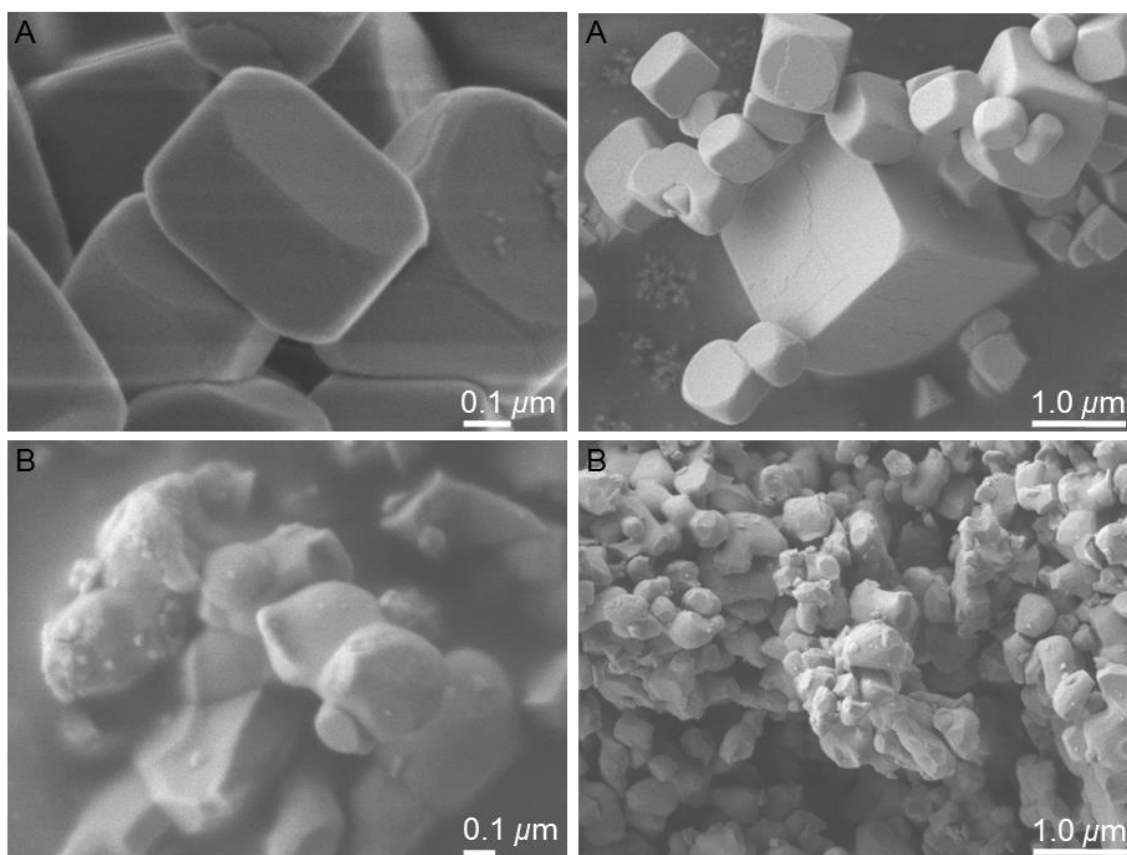


Figure-SI 3-3: HR-SEM images of SrTiO_3 after SrCl_2 flux-treatment in an Al_2O_3 crucible (A) and in its origin state (B) at different magnifications.

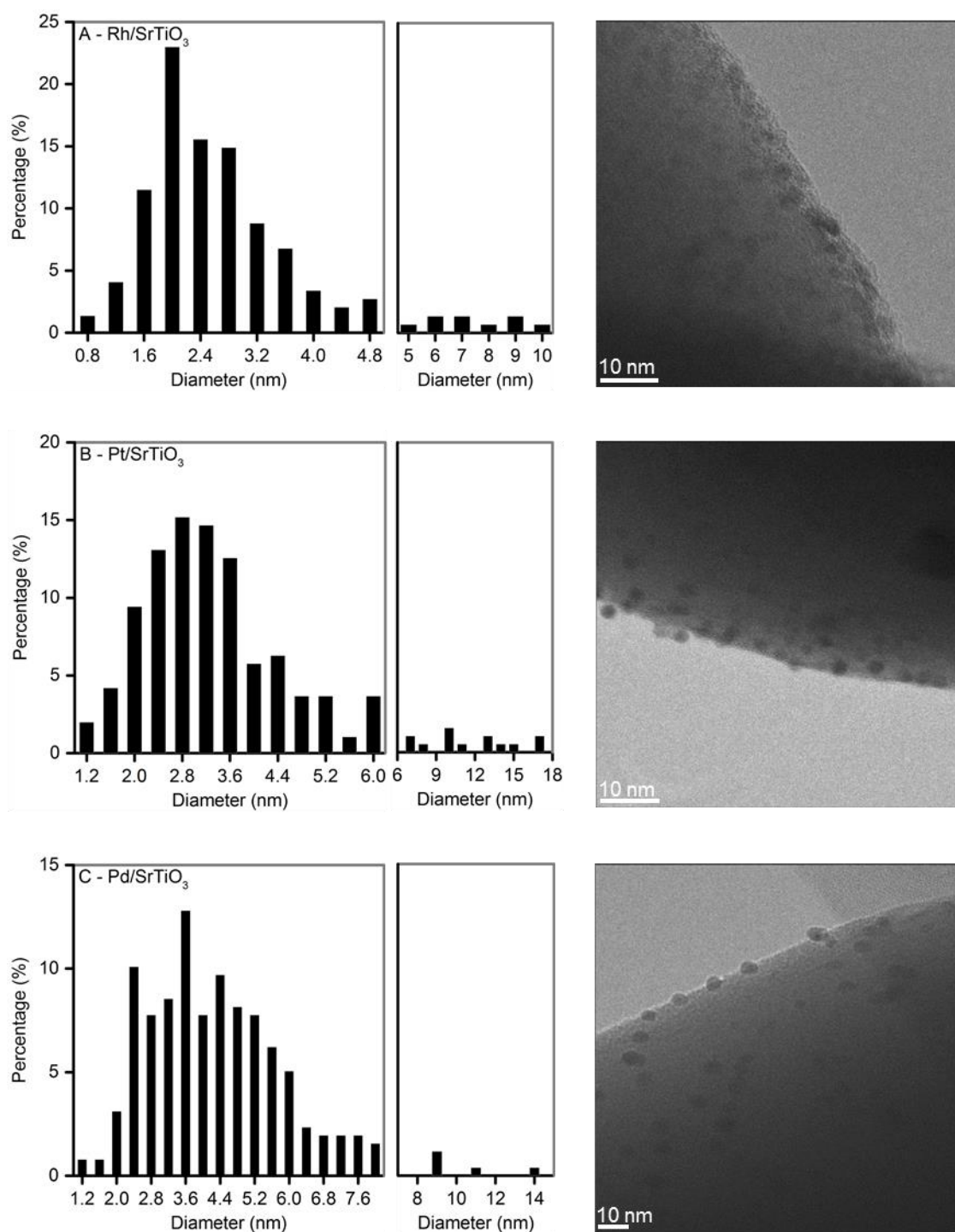


Figure-SI 3-4: Particle size distribution and typical TEM-image of 0.25 wt.% (A) Rh/Al-SrTiO₃, (B) Pt/Al-SrTiO₃ and (C) Pd/Al-SrTiO₃, respectively. Size distribution is based on 150 to 250 measured particles.

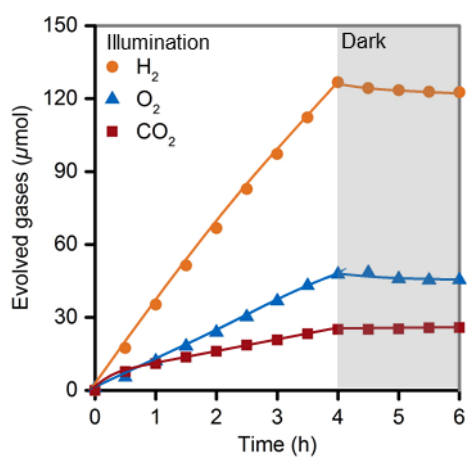


Figure-SI 3-5: Determination of CO oxidation and water formation rates in the dark after overall water splitting experiment. Black lines serve to guide the eye. Reaction conditions: 75 mg photocatalyst, 100 mL H₂O (pH = 4.5, H₂SO₄), 303 K, 40 mbar CO, 1 bar, 300 W Xe-lamp (CM1).

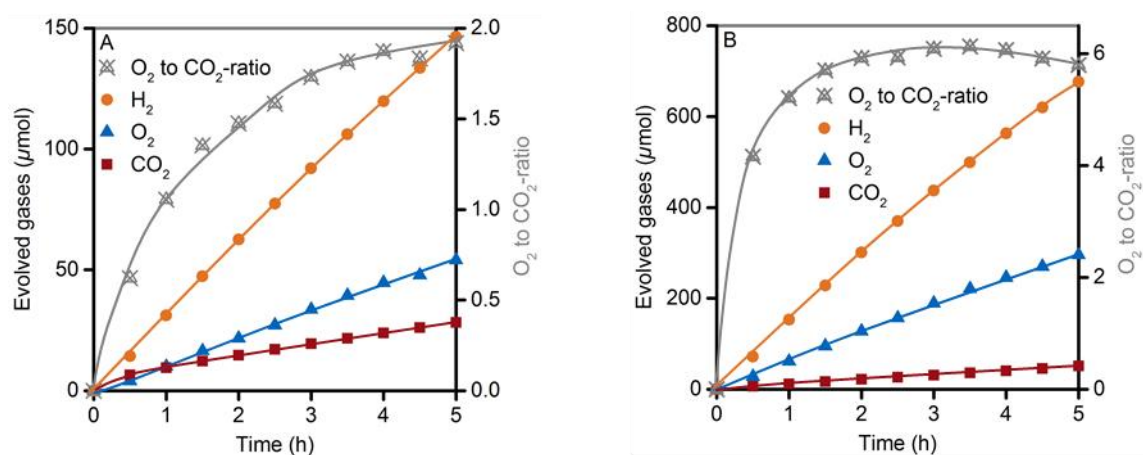


Figure-SI 3-6: Overall water splitting over Rh/GaN:ZnO in the presence of CO at different light intensities (**A:** $n(\gamma) = 44 \text{ nmol cm}^{-2} \text{ s}^{-1}$, **B:** $n(\gamma) = 176 \text{ nmol cm}^{-2} \text{ s}^{-1}$, 365 nm). Black and grey lines serve to guide the eye. Reaction conditions: 75 mg photocatalyst, 100 mL H₂O (pH = 4.5, H₂SO₄), 303 K, 40 mbar CO, 1 bar, UV-LEDs.

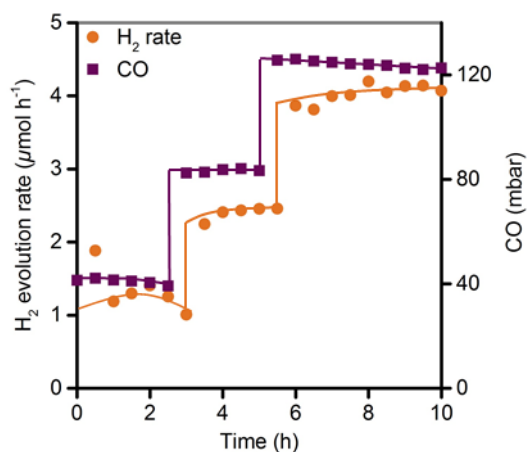


Figure-SI 3-7: Dependence of water splitting rate on CO partial pressure in presence of O₂. Lines serve as a guide for the eye. H₂ evolution rate is lagged by 30 min in respect to CO partial pressure. Reaction conditions: 75 mg photocatalyst, 100 mL H₂O (pH = 4.5, H₂SO₄), 303 K, 60 mbar O₂, 40 – 80 – 120 mbar CO, 1 bar, 300 W Xe-lamp (CM1).

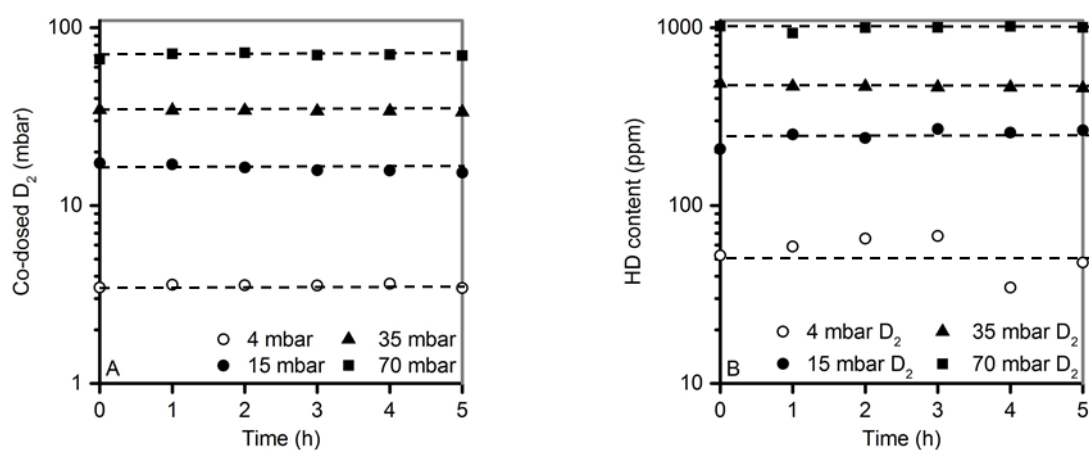


Figure-SI 3-8: Course of co-dosed D₂ (A) and HD (B) content during overall water splitting. Initial HD concentrations correspond to impurities in the co-dosed D₂ (content: circa 1.6 % HD). Dotted lines serve as a guide for the eye. Reaction conditions: 75 mg photocatalyst, 100 mL H₂O (pH = 4.5, H₂SO₄), 303 K, 40 bar CO, 0 to 70 mbar D₂, 1 bar, 300 W Xe-lamp (CM1).

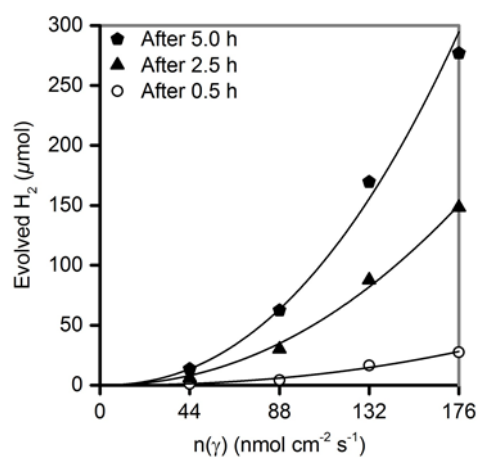


Figure-SI 3-9: Influence of photon flux on H₂ evolution activity in presence of 60 mbar O₂. Black lines serve to guide the eye. Reaction conditions: 75 mg photocatalyst, 100 mL H₂O (pH = 4.5), 303 K, 40 mbar CO, 60 mbar O₂, system pressure 1 bar, UV-LEDs (50 – 200 mA, 365 nm).

Table-SI 3-1. Heat of adsorption of CO on Rh, Pd and Pt dispersed on Al₂O₃ in the gas phase.¹⁻³

Metal	Adsorption site	Heat of adsorption (kJ mol ⁻¹)
Rhodium	Linear	195 ($\theta = 0$)
		103 ($\theta = 1$)
	Bridged	125 ($\theta = 0$)
		75 ($\theta = 1$)
Palladium	Linear	92 ($\theta = 0$)
		54 ($\theta = 1$)
	Bridged	168 ($\theta = 0$)
		92 ($\theta = 1$)
Platinum	Linear	195 ($\theta = 0$)
		103 ($\theta = 1$)

- (1) Chafik, T.; Dulaurent, O.; Gass, J.L.; Bianchi, D. *J. Catal.* **1998**, *179*, 503-514.
(2) Dulaurent, O.; Chandes, K.; Bouly, C.; Bianchi, D. *J. Catal.* **1999**, *188*, 237-251.
(3) Dulaurent, O.; Chandes, K.; Bouly, C.; Bianchi, D. *J. Catal.* **2000**, *192*, 262-272.

Chapter 4

4. Summary and Conclusions

Anaerobic heterogeneous photocatalysis is an attractive option to sustainably generate H_2 . On a metal decorated photoabsorber, H_2O is oxidized to O_2 (water splitting) or alternatively an oxygenate to CO_2 (photoreforming), meanwhile protons are reduced to H_2 . Most efforts focused on the development of efficient photocatalysts with small band gaps or with high quantum efficiency. It is also accepted that highly active and environmentally friendly photocatalysts demand defined adsorbate-surface interactions for selective chemical reactions. However, studies aiming to fully describe and rationalize the chemical transformations at the surface and their underlying mechanisms are scarce. The aim of this thesis is to elucidate the reaction mechanisms of the anodic half reaction of polyol reforming as well as of the water splitting reaction in presence of CO .

In respect to photoreforming, the simplest polyol, ethylene glycol, was chosen as a typical surrogate in biomass waste water streams. The reaction pathways of the oxidation of ethylene glycol were identified on Rh/TiO_2 and $Rh/GaN:ZnO$ through analysis of all reaction products in gas and liquid phase.

On Rh/TiO_2 , two reaction pathways have been identified. The dominant one proceeds *via* glycolaldehyde or formaldehyde (oxidative C–C-cleavage) with selectivities of 85% and 15%, respectively. The minor one is initiated by acetaldehyde formation. Glycolaldehyde is further converted *via* oxidative C–C-cleavage to formaldehyde and formic acid. Formaldehyde is oxidized to formic acid, which further decomposes to CO_2 and H_2 . Acetaldehyde is oxidized to acetic acid, which decarboxylates to CO_2 and CH_4 . These pathways of EG oxidation are initiated by direct or indirect hole transfer.

The sites proposed for direct hole transfer are terminal $Ti^{IV}-OH$ groups, where the adsorbate is oxidized to an alkoxy-radical, which undergoes β -C–C-cleavage. The

resulting carbon-centered radical is oxidized to a C1-oxygenate. C2-oxygenates with a sp^2 -hybridized α -oxygen, like glycolaldehyde, interact selectively with this reaction site while being converted to products that resemble Malaprade oxidation chemistry. The sites for indirect hole transfer are identified as bridged oxygen radicals $[\text{Ti}\cdot\text{O}\cdot\text{Ti}]^+$, which abstract a H-atom from the oxygenate producing a carbon centered radical, which is oxidized by the current doubling mechanism (transfer of the unpaired electron into the conduction band of the semiconductor). Independent of the nature of the hole transfer mechanism, identical maximum H_2 evolution rates for the photoreforming of various C1-/C2-oxygenates were observed. This observation, together with the excellent representation of the experimental data by a Langmuir-type kinetic model, allowed to conclude that H_2 evolution rates mainly depend on the concentration and adsorption strength of the oxygenate. Formaldehyde enriches in the liquid phase due to its small adsorption constant. CO evolution was observed during the photoreforming of all C1- and C2-oxygenates (with the exception of oxalic acid), which was attributed to the light-driven dehydration of intermediate formic acid.

In the case of photoreforming over Rh/GaN:ZnO, the main pathway for ethylene glycol conversion is *via* glycolaldehyde. Additional pathways *via* higher oxidized C2-oxygenates are induced by oxidizing radicals, e.g., $\cdot\text{OH}$, $\cdot\text{OOH}$, formed from O_2 or an intermediate of the overall water splitting reaction on Rh/GaN:ZnO. These pathways avoid formaldehyde formation.

In the absence of an organic electron donor, water is oxidized to O_2 at the anode. In order to obtain appreciable H_2 production rates, suppression of the thermodynamically preferred back reaction is mandatory. The strategy followed in this work was to avoid O_2 activation on sites located on the co-catalysts active for H_2 evolution. This was achieved by inducing the formation of a layer of CO chemisorbed on the precious metal co-catalysts (Rh, Pt, Pd). A detailed study focused on Rh/GaN:ZnO showed that CO covers selectively the active sites for the back reaction while the sites for H_2 evolution are unaffected. Low O_2 concentrations and CO coverages of 40% – 80% are required to achieve quantitative suppression of back reaction while maintaining efficient proton reduction over Rh/GaN:ZnO. Under these conditions, the performance of the photocatalyst was comparable to that

observed with protective oxide layers, which act as molecular sieves. In the presence of CO, CO oxidation competes with O₂ evolution. The H₂ evolution reaction exhibits a negative dependence on O₂ partial pressure above 7 mbar. The rates of CO oxidation and back reaction diminish, relative to the rates of water splitting, with rising photon flux or increasing quantum efficiency of the photoabsorber. The rationale is that rising concentration of H₂ and O₂ evolution reaction intermediates, caused by increasing electron–hole pair formation rates, leads to preferred H₂ and O₂ evolution.

Summing up, both strategies for photocatalytic H₂ production underline the importance of selective adsorption in order to control surface chemistry. The gained understanding can be used to optimize material design and to advance towards technological application. In respect to polyol reforming, formaldehyde is formed *via* oxidative cleavage of C2-oxygenates. Formaldehyde-free routes demand photocatalysts, which convert C2-oxygenates with a sp³-hybridized α -oxygen to fully sp²-hybridized oxygenates prior to C–C-cleavage. Regarding water splitting, CO was identified to selectively cover the sites of the back reaction without affecting H₂ evolution reaction sites. However, chemisorbed CO may be further stabilized towards competitive O₂ adsorption, whereas the effect of the metal on the tradeoff of CO oxidation and O₂ evolution remains to be explored.

Chapter 5

5. Zusammenfassung

Die anaerobe heterogene Photokatalyse stellt eine attraktive Möglichkeit für eine nachhaltige H₂-Herstellung dar. Auf einem metalldekorierten Photoabsorber werden Wasser zu O₂ (Wasserspaltung) oder alternativ ein Oxygenat zu CO₂ (Photoreformierung) oxidiert unter gleichzeitiger Reduktion von Protonen zu H₂. Die meisten Vorhaben zur Entwicklung effizienter Photokatalysatoren haben sich auf eine Verringerung der Bandlücke und Erhöhung der Quanteneffizienz fokussiert. Ferner ist unumstritten, dass hochaktive und umweltverträgliche Photokatalysatoren definierte Adsorbat-Oberflächenwechselwirkungen für selektive chemische Reaktionen verlangen. Forschungsarbeiten, die eine vollständige Beschreibung und Erklärung der chemischen Oberflächentransformationen und der ihnen zu Grunde liegenden Mechanismen zum Ziel haben, sind bisher kaum durchgeführt worden. Ziel dieser Arbeit ist die Aufklärung der Reaktionsmechanismen der anodischen Halbreaktion der Polyolreformierung sowie der Wasserspaltung in Gegenwart von CO.

Hinsichtlich der Photoreformierung wurde das einfachste Polyol, Ethylenglykol, als strukturtypisches Modellmolekül der in biomassehaltigen Abwässern vorkommenden Verbindungen gewählt. Durch die Identifikation aller Flüssig- und Gasphasenprodukte konnten die auf Rh/TiO₂ und Rh/GaN:ZnO ablaufenden Reaktionswege der Ethylenglykoloxidation entschlüsselt werden.

Auf Rh/TiO₂ wurden zwei Reaktionswege identifiziert. Der Hauptreaktionsweg führt mit Selektivitäten von 85% und 15% über die Bildung von Glykolaldehyd oder Formaldehyd (oxidative C–C-Spaltung). Der Nebenreaktionsweg wird durch die Bildung von Acetaldehyd eingeleitet. Die weitere Umsetzung von Glykolaldehyd erfolgt durch C–C-Spaltung zu Ameisensäure und Formaldehyd, dessen Oxidation wiederum Ameisensäure ergibt. Letztere wird nachfolgend zu CO₂ und H₂ zersetzt. Acetaldehyd wird zu Essigsäure oxidiert, welche unter Bildung von CO₂ und CH₄

decarboxyliert. Die Reaktionspfade für die Oxidation von Ethylenglykol werden durch direkten oder indirekten Lochtransfer eingeleitet.

Als Reaktionszentren für den direkten Lochtransfer werden terminale $\text{Ti}^{\text{IV}}\text{-OH}$ -Gruppen vorgeschlagen, an welchen das Adsorbat zu einem Alkoxyradikal oxidiert wird, welches anschließend einer $\beta\text{-C-C}$ -Spaltung unterliegt. Das resultierende kohlenstoffzentrierte Radikal wird zu einem C1-Oxygenat oxidiert. C2-Oxygenate mit einem sp^2 -hybridisierten α -Sauerstoff, wie Glykolaldehyd, wechselwirken selektiv mit diesem Reaktionszentrum, wobei die Reaktionsprodukte einer entsprechend ablaufenden Malaprade-Oxidationsreaktion gleichen. Die Reaktionszentren für den indirekten Lochtransfer werden verbrückten Sauerstoffradikalen $[\text{Ti}\cdot\text{O}\cdot\text{Ti}]^+$ zugeordnet, welche ein H-Atom unter Bildung eines kohlenstoffzentrierten Radikals abstrahieren, dessen nachfolgende Oxidation nach dem sogenannten Stromverdoppelungsmechanismus (Injektion des ungepaarten Elektrons in das Leitungsband des Halbleiters) erfolgt. Unabhängig von der Art des Lochtransfers wurden identische maximale H_2 -Entwicklungsraten für die Photoreformierung mehrerer C1-/C2-Oxygenate beobachtet. Diese Beobachtung sowie die exzellente Beschreibung der experimentellen Daten mittels eines kinetischen Langmuir-Modells, erlaubt die Schlussfolgerung, dass die H_2 -Entwicklungsraten maßgeblich von der Konzentration und Adsorptionsstärke des Oxygenats abhängen. Auf Grund seiner kleinen Adsorptionskonstante reichert sich Formaldehyd in der Flüssigphase an. Das Photoreformieren aller C1- und C2-Oxygenate (mit Ausnahme von Oxalsäure) führte zur Freisetzung von CO aufgrund einer lichtgetriebenen Dehydratisierung von intermediär gebildeter Ameisensäure.

Wird Ethylenglykol über Rh/GaN:ZnO photoreformiert, führt der Hauptreaktionsweg über Glykolaldehyd. Weitere Reaktionspfade über höher oxidierte C2-Oxygenate werden durch oxidierend wirkende Radikale, z.B. $\cdot\text{OH}$, $\cdot\text{OOH}$, eingeleitet. Diese werden aus O_2 oder einem Intermediat aus der Wasserspaltungsreaktion über Rh/GaN:ZnO gebildet. Diese zusätzlichen Reaktionswege vermeiden die Bildung von Formaldehyd.

In Abwesenheit eines organischen Elektronendonors, wird Wasser an der Anode zu O_2 oxidiert. Um ansprechende H_2 -Bildungsraten zu erhalten, ist eine Unterdrückung der thermodynamisch bevorzugten Rückreaktion unumgänglich. Die in dieser Arbeit

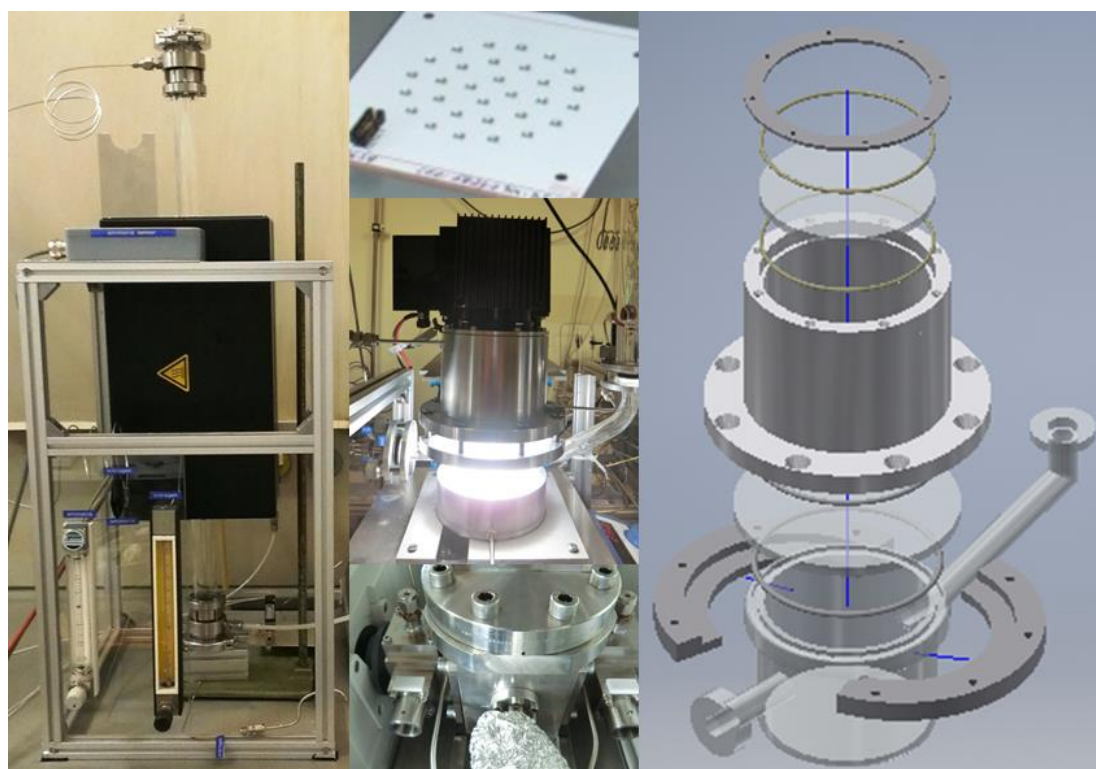
verfolgte Strategie zielt auf eine Unterdrückung der O₂-Aktivierung, welche an den für die H₂-Entwicklung aktiven Co-Katalysatoren abläuft. Die gewünschte Suppression wurde durch die Bildung einer auf den edelmetallhaltigen Co-Katalysatoren (Rh, Pt, Pd) chemisorbierten CO-Schicht erreicht. Eine detaillierte Studie, welche auf Rh/GaN:ZnO durchgeführt wurde, zeigte, dass CO selektiv die Reaktionszentren der Rückreaktion bedeckt, während die Zentren für die H₂-Entwicklung nicht beeinflusst werden. Geringe O₂ Konzentrationen sowie CO-Bedeckungsgrade von 40% - 80% sind notwendig, damit einerseits eine quantitative Unterdrückung der Rückreaktion und andererseits eine effiziente Protonenreduktion über Rh/GaN:ZnO gewährleistet ist. Unter diesen Bedingungen war die Aktivität dieses Photokatalysatorsystems vergleichbar zu jenen, welche auf oxidischen Schutzhüllen, die als molekulare Siebe fungieren, basieren.

In der Gegenwart von CO konkurrieren CO-Oxidation und O₂-Freisetzung. Außerdem weist die H₂-Entwicklungsreaktion eine negative Abhängigkeit bezüglich des O₂-Partialdruckes auf sobald dieser 7 mbar übersteigt. Verglichen mit den Raten der Wasserspaltung führt eine Erhöhung des Photonenflusses oder eine größere Quanteneffizienz zu einer relativen Verringerung der Raten der CO-Oxidation und der Rückreaktion. Die Erklärung hierfür ist, dass eine erhöhte Elektronen-Lochpaarbildungsrate eine steigende Oberflächenkonzentration an Intermediaten der H₂- und O₂-Entwicklungsreaktion hervorruft, woraus eine bevorzugte H₂- und O₂-Freisetzung resultiert.

Zusammenfassend unterstreichen beide Möglichkeiten der photokatalytischen H₂-Herstellung die Notwendigkeit einer selektiven Adsorption für eine kontrollierte Oberflächenchemie. Das erzielte Verständnis kann für ein verbessertes Materialdesign und weitere Entwicklungen hin zu einer technischen Anwendung dienen. In Bezug auf die Polyolphotoreformierung wird konstatiert, dass Formaldehyd aus der oxidativen C–C-Spaltung von C₂-Oxygenaten gebildet wird. Formaldehydfreie Reaktionspfade verlangen Photokatalysatoren, welche C₂-Oxygenate mit sp³-hybridisierten α -Sauerstoff vor Eintritt einer oxidativen C–C-Spaltung zu komplett sp²-hybridisierten Oxygenaten oxidieren. Im Hinblick auf die Wasserspaltung wurde festgestellt, dass CO selektiv die Zentren der Rückreaktion bedeckt ohne die H₂-Entwicklungszentren zu beeinflussen. Eine stärkere

Stabilisierung von chemisorbiertem CO gegenüber einer kompetitiven O₂-Adsorption wäre wünschenswert. Ferner gilt es den Effekt des Metalls auf die Selektivität von CO-Oxidation und O₂-Entwicklung zu untersuchen.

Setups for Investigations of Heterogeneous Photocatalysts



Chapter 6

6. Appendix

Careful design of setups for the synthesis of heterogeneous photocatalysts and their kinetic as well as spectroscopic investigation had been requested at the beginning of the present PhD work. Further commissioning and construction of the equipment constituted another important portion of the entire thesis. In the following, the design and operating principle of the most important devices are described.

Quartz tube furnace for the synthesis of (oxy)nitrides via ammonolysis

(Oxy)nitrides are commonly synthesized *via* ammonolysis from their oxidic precursors at temperatures between 1073 and 1473 K.¹ At these temperatures NH_3 decomposes *via* various reductive species, e.g., N_2H_4 , to N_2 and H_2 .² The formation of (oxy)nitrides from oxidic precursors causes water formation, whereas the water concentration rises along the reactant bed. In order to expose the reactant(s) to an identical gas atmosphere high space velocities and a vertical oven design are mandatory. Compared to a horizontal configuration, shorter reactant beds are obtained for a vertical synthesis oven, because the diameter of the reactant bed corresponds to the inner diameter of the synthesis tube. To meet these requirements a vertical synthesis oven was designed, built up and commissioned (Figure 6-1). The electric furnace (*HTM Reetz GmbH*) has a length of 40 cm and a maximal power of 1200 W. The inner diameter of the ceramic oven tube is 40 mm, so that a quartz tube (length: 750 mm, wall thickness: 2.5 mm) with an outer diameter of 32 mm can be inserted. The reactants are placed on a flat bed of quartz wool, which has been inserted into the quartz tube at a defined position before. The ends of the reaction tube are closed with stainless steel flanges (*HTM Reetz GmbH*). The bottom of the lower flange is flat and sits directly on the bench, so that a reproducible position of the reactants regarding the synthesis oven is ensured. The gas inlet of the upper flange is connected to the gas dosing line (1/16", stainless steel). The tube can be

flushed with NH_3 or N_2 by means of a three way valve as graphically illustrated in Figure 6-2.

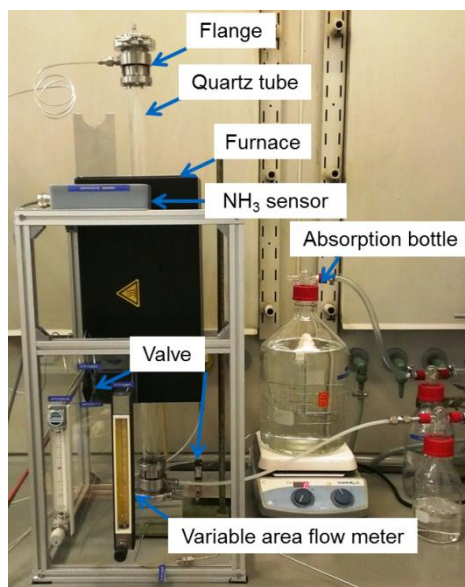


Figure 6-1: Vertical quartz tube furnace for the synthesis of (oxy)nitrides *via* ammonolysis (for the sake of clarity: prior modification with saturator).

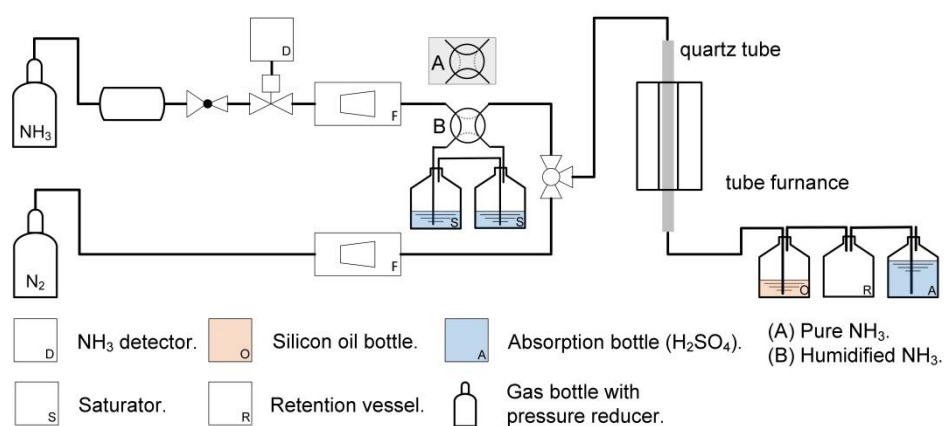


Figure 6-2: (Simplified) flow scheme of vertical quartz tube furnace for the synthesis of (oxy)nitrides *via* ammonolysis. (Saturator was realized by Kai Sanwald.)

N_2 is used in order to remove air prior and NH_3 after synthesis. The flow of each gas is adjustable by separate variable area meters (NH_3 : $75 - 350 \text{ mL min}^{-1}$, N_2 : $0 - 100 \text{ mL min}^{-1}$, *Wagner Mess- und Regeltechnik GmbH*). The NH_3 gas line comprises a solenoid valve coupled to a NH_3 sensor (*TBL Technisches Büro Lotter KG*), a small gas tank and an additional pressure reducer. The solenoid valve closes if the sensor detects more than 50 ppm NH_3 or in case of a blackout. The

evaporation of a liquified gas results in an oscillating volumetric flow. An additional pressure reducer can compensate these oscillations. For this purpose, the outlet pressure of the second pressure reducer has to be set to a smaller value than the outlet pressure of the pressure reducer of the gas bottle. A small gas tank between the two pressure reducers serves as a buffer volume. The synthesis of some oxynitrides, e.g., TaON, requires a humidified NH_3 stream in order to avoid overnitridation. By means of a two-position four-port valve NH_3 can be passed through a saturator prior entering the reaction tube as depicted in Figure 6-2. (Attention: Start with a small water level because the absorption of NH_3 in water causes volumetric expansion!) Non-reacted NH_3 is passed through a silicon oil bottle and a retention vessel prior entering an absorption bottle filled with diluted H_2SO_4 . Note that the volume of the retention bottle has to be larger than the volume of the absorption solution. The silicon oil bottle protects gas line and flanges from corrosion. Due to the corrosive effect of the absorption solution the entire outlet tubing is made of glass or plastics (inner diameter: 1/4") and connected *via* GL fittings. Compression fittings are used for all other connections (Figure 6-1).

Liquid phase photoreactor setup for kinetic investigations

A setup for the kinetic characterization of heterogeneous photocatalysts was designed, built and commissioned. The design follows the general rules of such a setup given in reference 3. The built system comprises a liquid and a gas phase top irradiation photoreactor which are connected to separate gas-circulation systems and gas-dosing lines. As this thesis focuses solely on investigations in the liquid phase, the design of the gas phase reactor (Figure 6-3B) is not further discussed. The liquid phase reactor is schematically illustrated in Figure 6-3A. The reactor chamber (inner height: 65 mm, inner diameter: 75 mm) is made of borosilicate glass. The bottom is a circular float glass disc (*Schott AG*, Borofloat[®] 33) which is merged with a glass flange (*Gebr. Rettberg GmbH*). This manufacturing technique (suggested and carried out by *Gaßner Glastechnik GmbH*) ensures a flat bottom which prevents settling of photocatalyst particles and guarantees good heat transfer between the reactor and the tempered cooling/heating unit, which covers the bottom and the lower part of the side walls of the reactor. The top of the reactor is covered

with a circular quartz disc (QSil GmbH), which serves as an optical window, and is closed with a self-designed flange clamp.

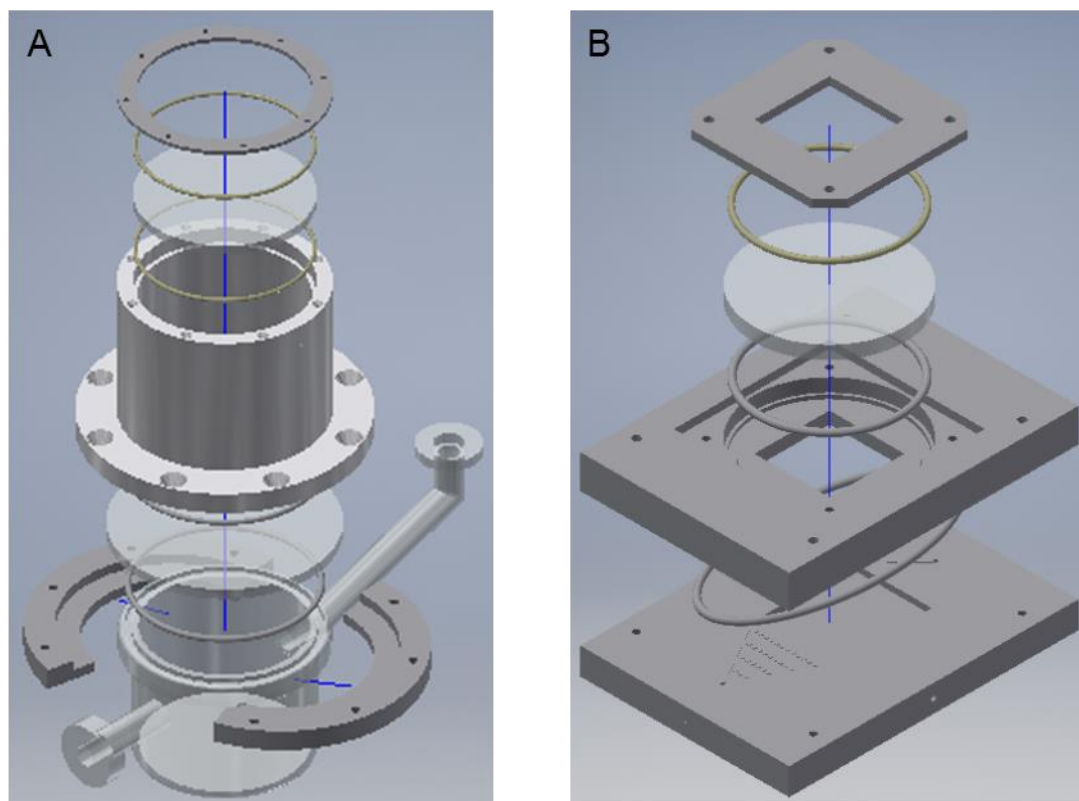


Figure 6-3: Schematic collocation of all essential components of (A) the aqueous phase photoreactor comprising reactor chamber, quartz windows, water filter, flange and seal rings and (B) the gas phase photoreactor comprising photoreactor, seal rings and quartz window. Note, heating chamber with heating element as well as water filter is not shown for the sake of simplicity.

Gas discharge lamp units (e.g., Xe-lamp, *LOT-Quantum Design GmbH*, *Peccell Technologies, Inc.*) as well as Vis- or UV-LEDs mounted on circuit boards (*LUMITRONIX LED-Technik GmbH*) with self-designed water-cooling and current control device can be used as illumination sources. The diameter of the light cone is adjusted to the dimensions of the reactor, whereas the photon flux distribution for the reactor chamber is shown for a 300 W Xe-lamp and UV-LEDs (365 nm, 50 mA) in Figure-SI 2-4 and Figure 6-4, respectively. If gas discharge lamps are used as illumination sources, a so-called ‘water filter’ within the beam path is obligatory. Water runs through the water filter and absorbs the emitted infrared radiation. For this purpose, the top part of the flange clamp continues with a hollow metal cylinder

(inner height: 75 mm, inner diameter: 75 mm) as depicted in Figure 6-3. Note that the inlet and outlet fittings for the cooling system are not shown for simplicity.

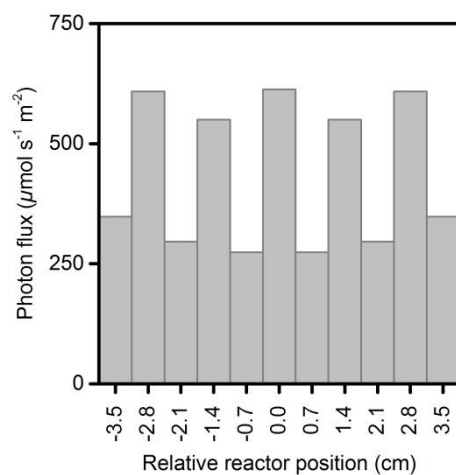


Figure 6-4: Photon flux distribution of the used reactor configuration - averaged photon flux through aligned concentric rings with a width of 7 mm (200-390 nm). Conditions: 365 nm UV-LEDs (50 mA). Note, that the alternating photon flux reflects circular positioning of UV-LEDs on the circuit board.

Stirring of the photocatalyst suspension is ensured with a magnetic stirrer unit placed beneath the tempering unit of the photoreactor as shown in Figure 6-5.

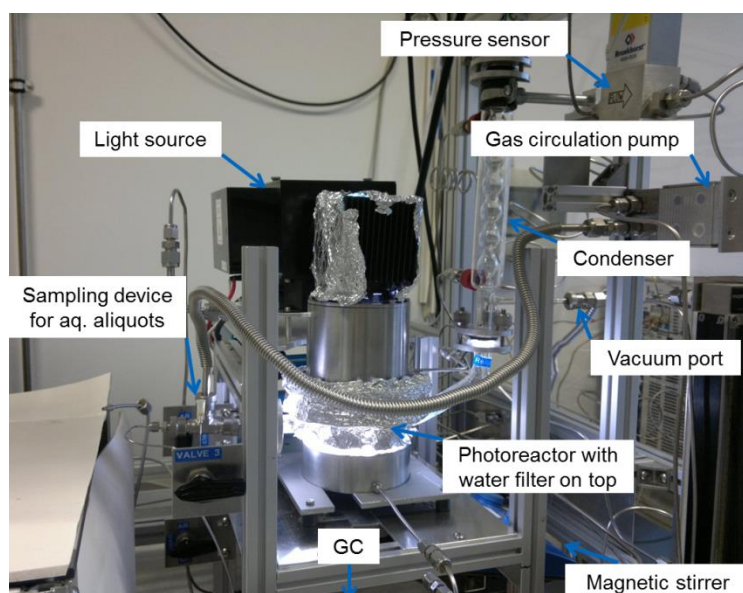


Figure 6-5: Photocatalysis setup for kinetic investigations of powdered photocatalysts in aqueous phase with sampling ports for liquid and gaseous aliquots.

Two KF10 flanges (*Gebr. Rettberg GmbH*) serve as joints to the gas circulation systems, being oppositely fixed at the side walls of the photoreactor. The outlet tube of the reactor is connected to an Allihn condenser and is curved upwards to ensure back flow of condensed water into the reactor chamber. The gas circulation system comprises a pressure sensor (*Bronkhorst High-Tech B.V.*), a double membrane gas pump (*KNF Neuberger GmbH*), a manually controlled vacuum port and sampling ports for liquid and gas phase sampling. The sampling device for removing liquid phase aliquots from the photoreactor is depicted in Figure 6-6. A simplified flow scheme of the setup is shown in Figure 6-7.

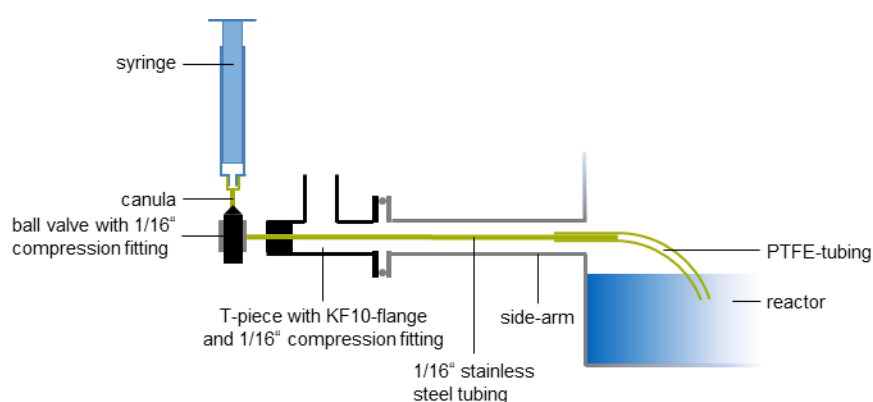
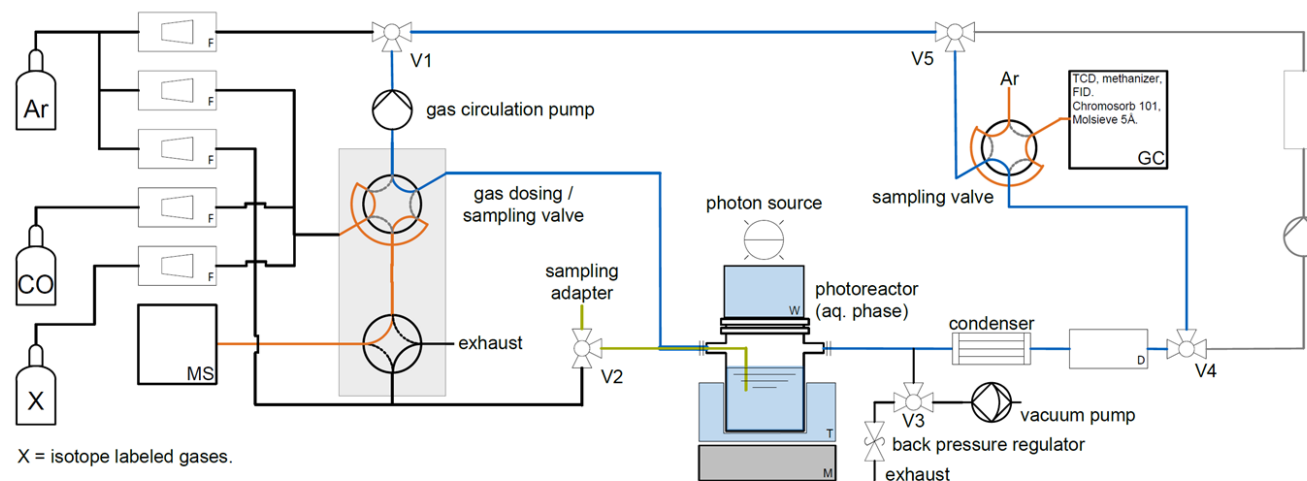
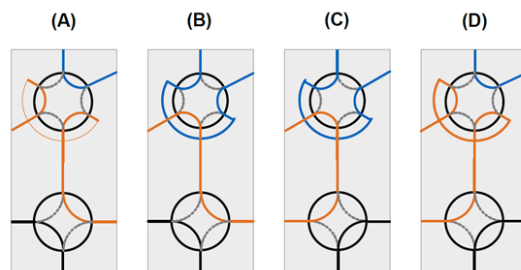


Figure 6-6: Schematic outline of sampling device for withdrawing liquid phase ‘aliquots’ from the photoreactor for *offline* analysis.

Sampling is performed manually with a syringe inserted into the sampling port (canula). The sampling line (1/16", stainless steel, $V = 0.4$ mL) is opened / closed by a ball valve. The inlet of the sample line is made of plastics, i.e., PTFE, in order to avoid metal poisoning of sensitive photoabsorbers. Sampling of gas phase aliquots is performed with remote controlled six-port two-position valves (*VICI AG*) for *online* analysis *via* gas chromatography and mass spectroscopy, respectively. The volume of the sample loop is 0.3 mL for gas chromatography and 5.0 mL for mass spectroscopy. During the circulation period the sample loops are part of the gas circulations system (Figure 6-7C). The six-port valve switches for sample taking and the content of the sample loop is flushed out with Ar towards the analysis instrument. The analysis of photoreforming gas mixtures demands a two column configuration (*Chromosorb 101* and *MS-5Å* column, configured by *Shimadzu Deutschland GmbH*)

(SIMPLIFIED) FLOW SCHEME OF AQUEOUS PHASE PHOTOREACTOR**VALVE POSITIONS FOR DOSING AND SAMPLING**

Prior reaction – gas dosing:

(A): Filling period of gas loop with gas mixture.

(B): Dosing period of filled gas loop into gas circulation system.

During reaction – gas sampling:

(C): Gas circulation period.

(D): Gas analysis period.

LEGEND

	Pressure sensor.		Gas dosing lines.
	Mass flow controller.		Gas circulation lines (aq. phase reactor).
	Gas chromatograph.		Gas circulation lines (gas phase reactor).
	Gas phase reactor.		Liquid phase sampling lines.
	Magnetic stirrer.		Gas phase sampling lines for GC or MS.
	Mass spectrometer.		Gas bottle with pressure reducer.
	Tempered cooling tank.	V1: (1) Ar flushing, (3) gas circulation. (1) (3)	
	Water filter.	V2: (1) Ar flushing, (3) aq. phase sampling. (2)	
		V3: (1) vacuum, (3) exhaust.	
		V4: (1) circulation gas phase reactor, (3) circulation aq. phase reactor.	
		V5: (1) circulation aq. phase reactor, (3) circulation gas phase reactor. (2) in any case closed position.	

Figure 6-7. (Simplified) flow scheme of liquid phase photoreactor. Note that the sampling valve for gas chromatography is operated in analogy to the sampling valve for mass spectroscopy. (Valve operation modes (C) and (D))

with a six-port two-position column-switching valve. With the exception of CO₂ permanent gases can be analyzed on a MS-5Å column. Therefore a Chromosorb 101 column is used as a guard column retaining CO₂. As soon as all other permanent gases than CO₂ are transferred onto the MS-5Å column, the column sequence is reversed by turning the column switching valve and the analytes are back flushed. Accordingly CO₂ is eluted first from the column. Table 6-1 lists the retention time of all analytes.

Table 6-1: Retention times of photoreforming / overall water splitting analytes on a two column configuration (Chromosorb 101 and MS-5Å column for thermal conductivity (TCD) and flame ionization detector (FID)).

Analyte	TCD (min)	FID (min)
CO ₂	2.91	2.98
H ₂	3.73	-
O ₂	5.20	-
N ₂	8.34	-
CH ₄	12.12	12.17
CO	-*	23.47

* The sensitivity is very low for CO due to the similar thermal conductivity of this analyte and the used carrier gas (Ar).

The analytes are analyzed by a serially connected TCD and FID. In order to increase the detection limit of CO and CO₂ a methanizer unit is installed between the two detectors. The sample switching valve for mass spectroscopy is also used as a gas dosing valve for inserting defined volumes of (isotope) labeled gases, e.g., CO, D₂, ¹⁸O₂, into the gas circulation system. A two-position four-port guard valve prevents that pure dosing gases, e.g., 100 % D₂, enter the mass spectrometer and thus ensures small baseline currents. The appropriate positions for dosing and sampling of the four-port valve are graphically depicted in Figure 6-7A-D. The gas dosing system consists of five mass flow controllers for Ar, isotope labeled gases and CO with optimal inlet pressures of 2 bar. The maximum flow rates are between 3 mL and 600 mL depending on the purpose of the gas dosing line (e.g., flushing of gas circulation system or dosing of isotope labeled gases). All connections are based on

compression, metal gasket face seal, FKM O-ring vacuum or KF10 flange fittings resulting in a leakage rate of less than $5 \cdot 10^{-4} \text{ Pa s}^{-1} \text{ L}^{-1}$ ($V_{\text{system}} \sim 330 \text{ mL}$).

IR spectroscopy setup with in situ UV-Vis-illumination of self-supported wafers.

Conduction band electrons of TiO_2 can be observed by a transient absorption in the IR from 3000 cm^{-1} ($\sim 0.37 \text{ eV}$) to 900 cm^{-1} ($\sim 0.15 \text{ eV}$) after band gap excitation with conventional light arc sources, e.g., Xe-lamp.^{4,5} Currently used vacuum infrared cells are made of stainless steel as shown in Figure 6-8B-C. In order to perform similar studies an optical device for the coupling of UV-Vis-light into stainless steel based vacuum IR-cells was developed, which is schematically outlined in Figure 6-9. Germanium was identified as a material that shows good transmission properties for infrared light and additionally excellent reflection properties for UV-Vis-light. Therefore, two holders for circular Ge-wafers (*LOT Quantum Design GmbH*) were designed (Figure 6-8A), which are positioned between the cell and the in- and outlet windows of the infrared spectrometer as shown in Figure 6-8B. This arrangement enables front- and back-side illumination of self-supported wafers. The diameter of the Ge wafers is equivalent to the diameter of the CaF_2 -windows of the infrared cell. As photon source, conventional light arc lamps are used, which are connected to branched quartz fibers with collimating optics. Two circular openings serve as holder for the collimating optics, forwarding the emitted light of fiber bundles onto the entire diameter of the Ge-wafer, which then reflects the UV-Vis-beam onto the self-supported wafer as schematically illustrated in Figure 6-9.



Figure 6-8: (A) Schematic collocation of all essential components of an optical device for holding a Ge-mirror, which reflects UV-Vis-light into a vacuum infrared cell made of stainless steel for in situ investigations of self-supported wafers. (B) Photograph of the infrared cell and the Ge-mirror holders and (C) of the whole infrared spectroscopy setup.

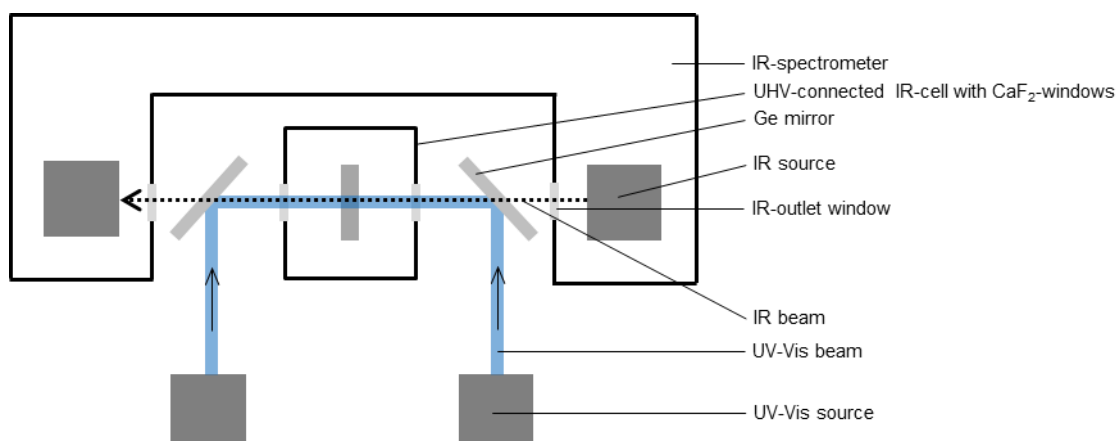


Figure 6-9: Schematic outline of an optical device based on Ge-mirrors, which reflects UV-Vis light into a vacuum IR-cell made of stainless steel for in situ investigations of self-supported wafers.

Acknowledgement

I am very thankful to the staff of the workshop for fruitful discussions on setup design and appreciate the gainful assistance of Xaver Hecht, Kai Sanwald, José Moya Cancino and Andreas Marx during construction and commissioning. I thank Thomas Obereisenbuchner for his contributions to the computer aided design of the devices.

References

- (1) Brophy, M. R.; Pilgrim, S. M.; Schulze, W. A. *J. Am. Ceram. Soc.* **2011**, *94*, 4263-4268.
- (2) Dirtu, D.; Odochian, L.; Pui, A.; Humelnicu, I. *Cent. Eur. J. Chem.* **2006**, *4*, 666-673.
- (3) Kudo, A.; Miseki, Y. *Chem. Soc. Rev.* **2009**, *38*, 253-278.
- (4) Panayotov, D. A.; Burrows, S. P.; Morris, J. R. *J. Phys. Chem. C* **2012**, *116*, 6623-6635.
- (5) Berger, T.; Sterrer, M.; Diwald, O.; Knozinger, E.; Panayotov, D.; Thompson, T. L.; Yates, J. T. *J. Phys. Chem. B* **2005**, *109*, 6061-6068.

Curriculum Vitae

Personal Data

Date / place of birth: October 4, 1986, Augsburg
 Citizenship: German

Education

Since 01/2012 **Technische Universität München – Doctoral Dissertation in Chemistry**
Chair for Technical Chemistry II, Prof. Dr. J. A. Lercher
 Topic: Heterogeneous Photocatalysis

03/2013 – 05/2013 **King Abdullah University of Science and Technology (Saudi Arabien)**
 Research under *Prof. K. Takanabe (KAUST Catalysis Center)*

03/2011 – 11/2011 **Georgia Institute of Technology (Atlanta, USA) – Master's Thesis**
School of Chemical & Biomolecular Engineering, Prof. Dr. C. W. Jones
 Topic: Polymer-supported molecular catalysts

10/2006 – 11/2011 **Technische Universität München – Studies in Chemistry**
 Main subject: Inorganic and metalorganic chemistry
 Subsidiary subject: Catalysis and reaction engineering

09/1996 – 06/2005 **Justus-von-Liebig-Gymnasium Neusäß – University Entrance Exam**

Working Experience and Internships

08/2010 – 10/2010 **Umicore AG & Co. KG (Hanau) – Internship**
Precious Metals Chemistry (R&D)
 Synthesis and characterization of metalorganic Ru-compounds

08/2006 **Clariant Produkte (Deutschland) GmbH (Gersthofen) – Internship**
Technical Marketing Waxes/Polymer Additives
 Plastics testing and converting in pilot-plant scale

04/2006 – 07/2006 **Osram GmbH (Augsburg) – Temporary Student Employment**
Development Glass Augsburg
 Optimization of process parameters of a pilot coating setup

Civilian Service

07/2005 – 03/2006 Elder care and nursing at the Congregatio Jesu, Maria-Ward Sisters Augsburg

Scholarship / Honors

03/2008 – 11/2011 **Cusanuswerk** (Scholarship Body of the Catholic Church)
 01/2008 – 09/2009 **Max Weber-Programm Bayern** (Elite Network of Bavaria)
 06/2005 Prize of the city Neusäß for the best university entrance exam

List of Publications

Publications in peer-reviewed journals

T.F. Berto, K.E. Sanwald, W. Eisenreich, O.Y. Gutiérrez and J.A. Lercher, Ethylene Glycol Photoreforming of Ethylene Glycol over Rh/TiO₂ and Rh/GaN:ZnO, *Journal of Catalysis* **2016**, 338, 68-81.

T.F. Berto, K.E. Sanwald, J.P. Byers, N.D. Browning, O.Y. Gutiérrez and J.A. Lercher, Overall Water-Splitting with CO-Covered Noble Metals: an Alternative to Core-shell Approaches, in preparation.

K.E. Sanwald, T.F. Berto, W. Eisenreich, O.Y. Gutiérrez and J.A. Lercher, Catalytic routes in photoreforming of polyols and aldose sugars, submitted.

Oral presentations

K.E. Sanwald, T.F. Berto, W. Eisenreich, O.Y. Gutiérrez and J.A. Lercher, "Photocatalytic transformations of biomass-derived oxygenates for hydrogen generation", 9th European Meeting on Solar Chemistry and Photocatalysis, **2016**, Strasbourg, France.

J.A. Lercher and T.F. Berto, K.E. Sanwald, O.Y. Gutiérrez, "Elucidation of Reaction Pathways of Polyol and Aldose Photoreforming", Catalysis Research Center (CRC) Graduate Academy, **2016**, Raitenhaslach, Germany.

K.E. Sanwald, T.F. Berto, W. Eisenreich, O.Y. Gutiérrez and J.A. Lercher, "Photocatalytic Pathways for H₂-Production from Biomass over UV- and Visible-Light Responsive Materials", XII European Congress on Catalysis, **2015**, Kazan, Russia.

T.F. Berto, K.E. Sanwald, W. Eisenreich, O.Y. Gutiérrez and J.A. Lercher, "Pathways for Biomass Photoreforming over UV- and Visible-Light Responsive Materials", 27th International Conference on Photochemistry (ICC), **2015**, Jeju-do, South Korea.

J.A. Lercher and T.F. Berto, K.E. Sanwald, O.Y. Gutiérrez, "Reaction Pathways of Selective Photocatalytic Oxidation of Diols and Triols", Irsee VII Symposium „New Insights in Selective Oxidation Catalysis, Electrocatalysis and Catalysis of Biomass“, **2015**, Kloster Irsee, Germany.

T.F. Berto, K.E. Sanwald, W. Eisenreich, O.Y. Gutiérrez and J.A. Lercher, "Photocatalytic Ethylene Glycol Reforming on Rh/GaN:ZnO and Rh/TiO₂-P25", 48th Annual Meeting of the German Catalysis Society, **2015**, Weimar, Germany.

T.F. Berto, K.E. Sanwald, W. Eisenreich, O.Y. Gutiérrez and J.A. Lercher, "Photochemical H₂-Production from Biomass and Water over Heterogeneous Catalysts", SoITech - "Workshop on Catalysis for Solar Fuels – Fundamental Concepts and Applications", **2015**, Garching bei München, Germany (Invited lecture).

T.F. Berto, K.E. Sanwald, M.C. Sanchez-Sanchez, O.Y. Gutiérrez and J.A. Lercher, "Photocatalytic Ethylene Glycol Reforming over GaN:ZnO-Based and TiO₂-Based Photocatalysts", Les Rencontres Scientifiques d'IFP Energies Nouvelles „Photo4E“, **2014**, Lyon, France.

Poster presentations

T.F. Berto, K.E. Sanwald, O.Y. Gutiérrez, J.A. Lercher “Overall Water Splitting over Photocatalysts with CO-Covered Noble Metals“, Catalysis Research Center (CRC) Graduate Academy, **2016**, Raitenhaslach, Germany.

K.E. Sanwald, T.F. Berto, W. Eisenreich, O.Y. Gutiérrez and J.A. Lercher, “Towards H₂ Generation Through Photocatalytic Reforming of Biomass Surrogates“, 48th Annual Meeting of the German Catalysis Society, **2015**, Weimar, Germany.

K.E. Sanwald, T.F. Berto, W. Eisenreich, O.Y. Gutiérrez and J.A. Lercher, “Kinetic Study of Reaction Pathways in Photocatalytic Biomass Reforming“, 48th Annual Meeting of the German Catalysis Society, **2015**, Weimar, Germany.

T.F. Berto, K.E. Sanwald, O.Y. Gutiérrez and J.A. Lercher, “Photocatalytic Glycerol Reforming with Co-catalyst Modified GaN:ZnO Solid Solutions“, 562nd WE-Heraeus Seminar „From Sunlight to Fuels“, **2014**, Bad Honnef, Germany.

T.F. Berto, K.E. Sanwald, O.Y. Gutiérrez and J.A. Lercher, “Photocatalytic Glycerol Reforming with Co-catalyst Modified GaN:ZnO Solid Solutions“, 47th Annual Meeting of the German Catalysis Society, **2014**, Weimar, Germany.